



A NEAR INFRARED TULLY-FISHER SURVEY BEHIND THE GALACTIC PLANE

Wendy L. Williams

*Thesis presented for the degree of Master of Science
in the
Department of Astronomy
University of Cape Town*

February 2011

Abstract

This thesis presents a first look at the directly measured peculiar velocity flow field within the Southern Zone of Avoidance. Large peculiar velocity surveys are hampered by the low detection rates and poor data quality of galaxies in the Zone of Avoidance (ZoA) where the obscuring effects of dust and stars in the Milky Way prevent the detection of galaxies across 10 – 20% of the sky. Moreover, dynamically significant structures lie hidden behind the Galactic plane. Dedicated surveys have been conducted to unveil the mass distribution within the ZoA. The ZoA peculiar velocity survey presented here makes use of deep systematic HI survey data, new high resolution HI observations and new deep near infrared (NIR) observations to provide high fidelity measurements for use with the NIR Tully-Fisher relation.

HI observations reveal galaxies where both optical and NIR surveys fail. The HIZOA deep HI survey conducted at the 64m Parkes telescope revealed ~ 1000 galaxies in the southern ZoA (Henning et al. 2005, Donley et al. 2005, Shafi 2008). Accurate HI linewidths are required for the measurement of Tully-Fisher distances. The fidelity of the HI linewidths depends both on the velocity resolution and signal-to-noise ratio of the spectrum. New HI data were therefore acquired at Parkes for 82 galaxies, providing a mean factor ~ 3.4 improvement in the fractional uncertainties in the 50% linewidth.

A deep NIR follow-up survey of HIZOA galaxies within 6000 km s^{-1} was conducted using the 1.4m IRSF telescope using the SIRIUS camera for simultaneous imaging in the near infrared J , H and K_s bands. These deep, high resolution NIR observations are able to penetrate the dust and deblend foreground stars making it possible to detect the NIR counterparts for the HI-detected galaxies. The survey images have an exposure time of 10 min resulting in a limiting magnitude approximately 2^m deeper than the 2MASS survey and the SIRIUS camera has a $0''.45 \text{ pix}^{-1}$ pixel scale and 7.7×7.7 field of view. The three-colour images were searched by eye for possible NIR-HI counterparts resulting in a galaxy catalogue containing 567 galaxies in 422 fields. Of these fields the NIR counterparts were confirmed for 356 HI galaxies. Algorithms for the subtraction of foreground stars were developed and used to obtain accurate surface photometry of each source.

The NIR galaxy colours were used to investigate the nature of extinction in the ZoA. The results show that on average across the southern ZoA, the true extinction is 82% of the DIRBE/IRAS values provided by Schlegel et al. (1998). There is no significant variation in

the correction factor as a function of Galactic longitude but there is variation with Galactic latitude. The DIRBE/IRAS overestimation is greater within $\pm 1^\circ$ of and $1^\circ - 3^\circ$ above the Galactic plane.

A preliminary peculiar velocity flow field within the southern ZoA is derived by combining the HI and NIR data. A strong flow towards the Great Attractor (GA) is observed. This flow field also shows possible indications of backside infall onto the GA, showing that the GA does indeed play an important role in the motion of the Local Group. The success of this study demonstrates the feasibility of further TF peculiar velocity studies in the ZoA, notably the extension of this survey to greater distances and an improved calibration of the TF relation for use in the ZoA.

Acknowledgements

First and foremost I would like to thank my supervisor Professor Renée Kraan-Korteweg for her insight into and enthusiasm for this work, for her many hours of reading my drafts and adding to the depth of this thesis. I would also like to thank my co-supervisor, Associate Professor Patrick Woudt, for his invaluable assistance particularly for the near infrared observations and photometry.

My thanks also go to the Japanese collaborators on the Norma Wall Survey, particularly to Drs Matsunaga and Nagayama who developed the scripts for calibration and star-subtraction, and to the Japanese IRSF team for the allocation of observing time. I am grateful also for the input by Dr Tom Jarrett on my photometry, Professor Lister Stavely-Smith for teaching me the HI data reduction and Stacey Mader who taught me how to observe with the Parkes telescope. The staff at SAAO, Sutherland and at CSIRO, Parkes all deserve my thanks for helping my observing runs go smoothly, particularly when the telescopes suffered technical problems.

I am also indebted to my colleagues and friends in the UCT Astronomy Department and at SAAO who made this a pleasant and productive environment for work. In particular, to Ihab from whom I learned a lot about star-subtraction and photometry and without his work on the Norma Wall, much of my work would have been a lot more difficult. Thanks also to Paul for his help with my photometry when I encountered problems. Many other people have added to this thesis from general discussions.

On a personal note, I would like to specifically thank Kosma who has been an awesome friend and partner in crime! It certainly helped having you there. My family have supported me throughout my career thus far. My parents have always encouraged me and have made it possible for me to get this far. Also to my sisters who have had to bear with me when things have been rough (particularly to Heather who ensured I always had a clean flat and food to eat). I thank you all for your support and kind words, in particular over the last few months.

I am grateful for the financial support of the South African SKA project for Human Capacity development during this thesis as well as the travel funding provided by the UCT Astronomy multi-wavelength grant.

This publication makes use of data products from the Two Micron All Sky Survey, which is a joint project of the University of Massachusetts and the Infrared Processing and Analysis

Center/California Institute of Technology, funded by the National Aeronautics and Space Administration and the National Science Foundation.

We acknowledge the use of the Legacy Archive for Microwave Background Data Analysis (LAMBDA). Support for LAMBDA is provided by the NASA Office of Space Science.

Plagiarism Declaration

I, Wendy L. Williams, know the meaning of plagiarism and declare that all of the work in the document, save for that which is properly acknowledged, is my own.

Contents

1	Introduction	1
1.1	The Zone of Avoidance	3
1.1.1	Galactic Extinction	4
1.1.2	Stellar Density	7
1.2	Galaxies in the ZoA	9
1.2.1	The Importance of Mapping Structures in the ZoA	9
1.2.2	Multi-wavelength Searches	10
1.3	The Cosmic Peculiar Velocity Flow-Field	13
1.3.1	Peculiar Velocities	13
1.3.2	The Local Peculiar Velocity Flow Field	14
1.3.3	The Problem of the ZoA	14
1.3.4	The Near Infrared Tully-Fisher Relation	15
1.4	Motivation for follow-up NIR survey	16
1.5	Outline of this Thesis	17
2	Deep HI Survey	19
2.1	The HI Parkes Deep Zone of Avoidance Survey	19
2.1.1	HIZOA Survey Parameters	20
2.1.2	Source Detection and Parameterisation	22
2.1.3	Source Distribution	22
2.1.4	Large-Scale Structures	24
2.2	Near Infrared Counterparts	26
2.3	Target Selection for NIR Follow-up	29
3	Narrowband HI Observations and Data Reduction	31
3.1	Observations and Data Reduction	31
3.2	HI Parametrisation	33
3.2.1	Results	34
3.3	Comparison to HIZOA	50
3.3.1	Improvement in Linewidth Errors	52

4 NIR Follow-up Survey	55
4.1 Infrared Survey Facility	55
4.1.1 Comparison of the IRSF to Contemporary Instruments	56
4.1.2 Comparison of IRSF/SIRIUS to 2MASS Imaging	56
4.2 Observations	58
4.2.1 Imaging	60
4.3 Image Processing with the SIRIUS Pipeline	62
4.3.1 Dark Current Subtraction	62
4.3.2 Determination of the Master Flat and Flat Correction	63
4.3.3 Sky Determination and Subtraction	64
4.3.4 Dither Combine	65
4.4 Image Calibration	65
4.4.1 Calibration Standard	66
4.4.2 Astrometric Calibration	66
4.4.3 Photometric Calibration	66
4.4.4 Image Statistics	68
4.5 Galaxy Identification	68
4.6 Star-subtraction	70
4.6.1 PSF Determination	72
4.6.2 Background Cleaning	72
4.6.3 Star Removal	72
4.6.4 Residual Cleaning	74
4.6.5 Postage Stamp Creation	74
4.7 Surface Photometry	77
4.7.1 Astrometric Parameters	78
4.7.2 SELF-sky Correction for Large Galaxies	78
4.7.3 Photometric Parameters	79
5 NIR Galaxy Catalogue	83
5.1 Catalogue Parameters	83
5.2 Quality Control	86
5.2.1 Comparison with 2MASX	86
5.2.2 Comparison with Other IRSF Observations in the ZoA	88
5.2.3 Internal Consistency	88
5.3 Extinction and NIR Colours	90
5.3.1 Variation with Galactic Latitude and Longitude	93
5.4 Catalogue Statistics	94
5.4.1 Detection Rates	94
5.4.2 Magnitude and Colour Distribution	95
5.5 H α Counterpart Identification	100
5.5.1 Reliability	100

5.6	Stellar and HI Properties	101
6	Tully-Fisher Analysis	105
6.1	Previous Work	105
6.1.1	Early Work	105
6.1.2	Large TF Samples	106
6.1.3	The 2MASS Tully-Fisher Survey	107
6.2	The Tully-Fisher Relation	108
6.2.1	Tully-Fisher Observables	109
6.2.2	2MTF Template	111
6.2.3	Derivation of Peculiar Velocities	115
6.3	The Peculiar Velocity Sample within the ZoA	116
6.3.1	TF Sample	116
6.3.2	Peculiar Velocity Sample	119
6.4	The Local Peculiar Velocity Field in the ZoA	124
6.4.1	One Attractor or Two?	127
6.5	Discussion	129
6.5.1	Extinction	130
6.5.2	Comparison to 2MASS TF Relation	130
6.5.3	Further Work	134
7	Conclusions and Future Work	135
7.1	Summary	135
7.2	Future Prospects	136
A	Catalogue and Postage Stamps	139
B	Tully-Fisher Sample	149

List of Figures

1.1	All-sky dust extinction map	6
1.2	All-sky 2MASS stellar number density map	8
1.3	Stellar number density and confusion noise	8
1.4	Optical ZoA	11
1.5	2MASX ZoA	12
1.6	Comparison between 2MASS and IRSF/SIRIUS images	17
2.1	MB beam sensitivity pattern	19
2.2	HIZOA survey area	21
2.3	Filling in the ZOA with HIZOA detections	23
2.4	Velocity distribution of HIZOA sources	23
2.5	Mass sensitivity of the HIZOA survey.	24
2.6	Redshift slices of HIZOA	25
2.7	HIZOA source distribution by Galactic longitude	27
2.8	Velocity histograms by Galactic longitude	27
2.9	2MASS counterparts to HIZOA galaxies.	28
2.10	Near-infrared field selection from HIZOA	30
3.1	Spatial distribution of narrowband HI observations	32
3.2	Examples of two cases of baseline fits	33
3.3	New HI spectra	39
3.4	Histograms of offsets between narrowband and HIZOA systemic velocities and linewidths	50
3.5	Comparison of narrowband and HIZOA systemic velocities	51
3.6	Comparison of narrowband and HIZOA 50% velocity widths	51
3.7	J1149-64 an asymmetric profile poorly fitted in HIZOA	52
3.8	Example spectra with bad baselines	53
3.9	Comparison of narrowband and HIZOA 50% velocity width errors	53
3.10	Improvement of fractional linewidth errors from HIZOA to narrowband	54
3.11	Example spectra with good widths	54
4.1	Comparison of IRSF and 2MASS imaging at high extinction	57

4.2	Near-infrared survey completeness	59
4.3	Survey completeness per longitude	59
4.4	Dither pattern	61
4.5	Typical dark frames	63
4.6	Typical master differential flat fields	63
4.7	Typical sky frames in low and high stellar density	64
4.8	SIRIUS/2MASS transmission curves	68
4.9	Histogram of image FWHM as a measure of the seeing.	69
4.10	Histogram of magnitude zero points as a measure of the image quality.	69
4.11	Galaxy search and identification output	71
4.12	Flowchart of star subtraction algorithm	75
4.13	Improved performance of star-subtraction routine	76
4.14	Examples of star-subtracted images	77
4.15	Intensity profile showing SELF-sky correction	79
4.16	Example of Radial SBP plots and fits	81
5.1	Comparison of IRSF and 2MASX aperture and isophotal magnitudes	87
5.2	Comparison of IRSF and NWS aperture magnitudes	88
5.3	Internal comparison of 5'' aperture magnitudes	89
5.4	Extinction-corrected NIR colours as a function of A_{K_s}	92
5.5	DIRBE/IRAS extinction correction factor as a function of l	94
5.6	DIRBE/IRAS extinction correction factor as a function of b	94
5.7	Spatial distribution of detected possible NIR counterparts	95
5.8	Extinction distribution	96
5.9	Stellar density distribution	96
5.10	Magnitude distribution	98
5.11	Colour distribution	99
5.12	Positional offsets between H α positions and IRSF positions	101
5.13	H α mass as a function of K band magnitude	102
5.14	H α mass as a function of stellar mass	103
6.1	Global TF relation in the NIR	114
6.2	Tully-Fisher Relation in J , H and K_s	118
6.3	Peculiar velocities in the ZoA	120
6.4	Histogram of peculiar velocities: GA region	121
6.5	Histogram of peculiar velocities: Narrowband	122
6.6	Histogram of peculiar velocities: Mass limit	122
6.7	Peculiar velocities and errors as a function of observed velocity.	123
6.8	Smoothed peculiar velocity flow field: limited velocities	125
6.9	Smoothed peculiar velocity flow field: all velocities	126
6.10	Peculiar velocity vector field	128
6.11	Model attractors	130

6.12 Comparison of IRSF and 2MASX extrapolated total magnitudes	132
6.13 Comparison to the 2MASS TF data	133

List of Tables

2.1	HIZOA Survey parameters	21
3.1	HI properties	36
4.1	Specifications of current/proposed NIR surveys and their instruments	56
4.2	IRSF/SIRIUS observations	58
4.3	Mean magnitude zeropoints and average seeing for all 580 images	68
5.1	Comparison of 2MASX and IRSF/SIRIUS 5'' and isophotal magnitudes	87
5.2	Comparison of NWS and IRSF/SIRIUS 5'' aperture magnitudes	89
5.3	Internal consistency: 5'' aperture magnitudes	90
5.4	Mean observed and extinction-corrected magnitudes	97
5.5	Mean observed and extinction-corrected colours	97
5.6	Counterpart detection rates	100
6.1	Comparison of 2MASX and IRSF/SIRIUS total magnitudes	132
6.2	Comparison of 2MASX and IRSF/SIRIUS TF offsets	132
A.1	The brightest, $K_{s20} < 11^m$ galaxies in the NIR catalogue sorted by K_{s20} magnitude from the brightest to the faintest.	140
A.2	NIR postage stamps	143
B.1	TF Sample	150
B.2	Peculiar Velocity Sample	157

Chapter 1

Introduction

Over the last few decades, the emerging picture of the Universe is that of a “cosmic web”, with galaxies lying along filaments and walls with voids in between (Shapley 1930, Joeveer & Einasto 1978, Davis et al. 1982, de Lapparent et al. 1986). Cosmological studies have shown that these sponge-like structures are born out of the tiny density fluctuations in the early universe (Bardeen et al. 1983, Guth & Pi 1982, Hawking 1982, Starobinsky 1982). Gravitational instability caused these fluctuations to grow into the large-scale structure observed in the present-day Universe (e.g. Bond & Efstathiou 1987, Holtzman 1989, Springel et al. 2005). On scales of a few hundred Mpc, the asymmetric gravitational influence of this inhomogeneous distribution of matter results in the motions of galaxies. These “peculiar motions” are superimposed on the smooth Hubble flow of the expanding Universe. In the nearby Universe, the mass distribution around the Local Group (LG) results in its own peculiar motion. The peculiar motion of the LG, the motion of our Galaxy in the LG and the motion of the Sun within our Galaxy give rise to the observed dipole in the Cosmic Microwave Background (CMB; Kogut et al. 1993). While the CMB anisotropy provides a direct and accurate measurement of the peculiar velocity of the LG (Conklin 1969, Henry 1971), the underlying gravitational acceleration caused by the mass distribution is contested (cf. Strauss et al. 1992, Lynden-Bell et al. 1989, Erdoğdu et al. 2006a, Kocevski & Ebeling 2006, Scaramella et al. 1991).

The mass distribution, and hence the LG acceleration, can be measured by the direct detection and three-dimensional mapping of galaxies in large surveys. This hinges on the assumption that galaxies trace the total mass distribution, i.e. that the relationship between visible and dark matter is well constrained. Several estimates of the density field and the LG acceleration have been made using measured redshifts from the IRAS Galaxy Catalogue (e.g. Rowan-Robinson et al. 1990, Strauss et al. 1992), optical catalogues (e.g. Lynden-Bell et al. 1989, Hudson 1993a;b) and 2MASS (Erdoğdu et al. 2006b). Alternatively, the mass density field can be inferred from the peculiar velocities of a sample of galaxies, independently of any a priori knowledge of the bias between visible and dark matter (Bertschinger & Dekel 1989, Dekel et al. 1990, Dekel 1994). The peculiar velocities of every galaxy respond to the

underlying gravitational potential field generated by the overall local mass distribution. As such, each galaxy can be considered as a test particle on the gravitational potential field. Large mass overdensities act as “attractors” whereas voids appear to repel nearby galaxies. Bertschinger & Dekel (1989) developed a method to reconstruct the density field from the peculiar velocity field (POTENT; see also Dekel et al. 1990, Dekel 1994) using the assumption of irrotationality of gravitational flows. The measurement of peculiar velocities, however, relies on a large uniform sample of galaxies with high fidelity distance measurements. Moreover, redshift-independent distances (e.g. the Tully-Fisher relation; Tully & Fisher 1977) are needed in order to extract the peculiar velocities from the recession velocities.

Peculiar velocity surveys are hampered by the low detection rates of galaxies in the Zone of Avoidance (ZoA) where the obscuring effects of dust and stars in the Milky Way prevent the detection of galaxies across 10 – 20% of the sky. The apparent lack of galaxies within the ZoA has serious implications for peculiar velocity analysis; this unfilled part of the sky acts as a void and may artificially produce an outflow unless it is accounted for. This problem has been circumvented by statistical interpolation of the adjacent mass distribution and filling in the ZoA. Yahil et al. (1991) employ a simple linear interpolation across the 10° wide ZoA of the IRAS redshift survey. The optical surveys used by Lynden-Bell et al. (1989) exhibit a larger 30° wide exclusion zone which is filled by duplicating galaxies from higher latitudes into the Galactic plane. Lahav et al. (1994) apply a noise-reducing Weiner filter to the interpolated spherical harmonics of the angular distribution of galaxies in adjacent regions. Kolatt et al. (1995) advocate interpolating the observed potential field as opposed to the mass distribution. They used this method to specifically study the derived mass density field within the ZoA. Their study and that by Loeb & Narayan (2008) suggest that the largely unknown mass distribution within the ZoA contributes significantly to the motion of the LG. Several dynamically important structures, including the Great Attractor (Lynden-Bell et al. 1988) and Local Void (Tully & Fisher 1987) lie within the ZoA. Moreover, the Pisces-Perseus and Hydra-Centaurus Superclusters, two of the largest superclusters within the nearby Universe, lie near the Galactic plane.

The motivation for mapping structures within the ZoA is twofold. The first is to produce a complete map of structures within the local Universe. The second reason is the importance of these structures in dynamical studies, in particular studies of the origin of the motion of the LG. To this end, it is necessary to first detect large numbers of galaxies within the ZoA. Kraan-Korteweg & Lahav (2000) and Kraan-Korteweg (2005) describe the complementary multi-wavelength work aimed at revealing galaxies behind the Galactic plane. The blind H α surveys pioneered by Kerr & Henning (1987) which used the 1.42 GHz (21 cm) hyperfine emission line of neutral hydrogen provide an efficient and unbiased means of penetrating the dust and stars of the Milky Way to detect galaxies. Recently, the HIZOA deep H α survey conducted at the Parkes telescope (Henning et al. 2005) revealed ~ 1000 galaxies in the southern ZoA. The survey covered the region of the sky that is most obscured by dust, i.e. where the optical ZoA is particularly prominent. The extension of HIZOA around the Galactic bulge covers the regions where near infrared (NIR) surveys such as 2MASS

become increasingly incomplete due to prohibitive stellar densities. Complementary, deep, high resolution NIR imaging which is able to overcome most of the effects of extinction and stellar density can be used to shed light on the stellar properties of the HI galaxies. Importantly, the NIR data combined with the HI information can be used to determine distances to these galaxies using the NIR Tully-Fisher relation (e.g. Aaronson et al. 1980a, Masters et al. 2008).

This thesis describes a deep NIR follow-up survey of HI galaxies detected in the HIZOA survey. These data are used to measure directly, for the *first time*, preliminary peculiar velocity flow fields within the southern ZoA. This can be used as a feasibility study for further such work. This dataset will be valuable in quantifying the mass distribution within the ZoA and will aid in our understanding of the origin of the motion of the LG.

This introductory chapter describes the background information pertaining to the measurement of peculiar velocities within the Zone of Avoidance. In Sect. 1.1, the ZoA is described in detail and the effects of extinction and stellar density at different wavelengths are discussed. Section 1.2 outlines why it is important to map the mass within the ZoA and describes the multi-wavelength searches that have been undertaken to reduce the ZoA. I explain the advantages of HI observations to detect galaxies in the ZoA and the usefulness of subsequent NIR follow-up observations. Section 1.3 describes how the determination of peculiar velocities can unveil the mass distribution. Here I discuss how observations in the ZoA can contribute to our understanding of the mass distribution in the Local Universe and then describe the NIR Tully-Fisher relation as an ideal method for distance determination of spiral galaxies in the ZoA. Finally, in Sect. 1.4, I emphasize the necessity for dedicated follow-up NIR observations which are significantly deeper than those available with current NIR surveys.

1.1 The Zone of Avoidance

It was Proctor (1887) who first noticed that the nebulae in Herschel’s General Catalogue (Herschel 1864) seemed to avoid the region of the sky near the Galactic plane. The detection of Cepheids in these nebulae allowed their distances to be determined and so they were identified as galaxies (Hubble 1925). However, at that time, there was no explanation why these galaxies would avoid part of the sky. It was only after the discovery of the obscuration of starlight by interstellar dust (Trumpler 1930), that it was understood that this “Zone of few Nebulae” was caused by dust in our own Galaxy (Hubble 1936). This region came to be known as the “Zone of Avoidance” because galaxies appeared to avoid it and because of the greater difficulty in observing galaxies within it. The ZoA was first quantified as the region delineated by “the isopleth of five galaxies per square degree from the Lick and Harvard surveys” (Shapley 1961). For comparison, the density of galaxies in the unobscured sky is observed to be 54 galaxies per square degree (Shane & Wirtanen 1967). The ZoA is not caused solely by dust extinction; the increase in stellar density near the Galactic plane creates further problems for the detection and parametrisation of galaxies in the ZoA.

The extent of the ZoA depends on wavelength. It encompasses more than $\sim 20\%$ of the optical extragalactic sky, but only $\sim 10\%$ of the infrared extragalactic sky (Kraan-Korteweg & Lahav 2000). The optical ZoA is mainly a result of dust extinction, which increases strongly towards the Galactic plane, reaching up to 70 mag in the B -band ($\lambda_c = 445 \mu\text{m}$) (Schlegel, Finkbeiner, & Davis 1998). The NIR ZoA is largely due to the high stellar density in the Galactic plane and around the Galactic bulge. The increase in the number of stars increases the background noise and causes confusion where stars appear ‘blended’ and are misidentified as extended sources. The following two sections (Sect. 1.1.2 and Sect. 1.1.1) give a full discourse on the causes and effects of extinction and star density, including how they are parametrised and measured. An understanding of these processes is needed to understand their limitations to photometry and how to correct for their effects.

1.1.1 Galactic Extinction

Dust in the interstellar medium (ISM) scatters and absorbs light, thereby reducing the flux of stellar sources. This process is known as *extinction*. Extinction is wavelength dependent and increases towards shorter wavelengths. Moreover, objects appear redder because the bluer wavelengths suffer more extinction. The extinction in the NIR wavebands, J ($\lambda_c = 1.25 \mu\text{m}$), H ($1.62 \mu\text{m}$) and K_s ($2.14 \mu\text{m}$)*, is typically 21%, 13% and 9% respectively of the optical B band extinction (Cardelli, Clayton, & Mathis 1989). It is therefore advantageous to work at longer wavelengths where the extinction is reduced. The extinction, A_λ , at a given wavelength λ is expressed in magnitudes,

$$m_\lambda = m_\lambda^0 + A_\lambda, \quad (1.1)$$

where m_λ is the observed and m_λ^0 is the extinction-corrected magnitude of a stellar source at the wavelength λ .

Extinction Laws

The amount of the scattering depends on the relative sizes of the dust grains, their composition and the wavelength of the light. The size of the grains depends on the density of the environment (Cardelli et al. 1989) and so the variation in the density of the ISM means the amount of extinction is different for each line of sight. The extinction can be quantified via the parameter R_V :

$$R_V \equiv \frac{A_V}{E(B-V)}. \quad (1.2)$$

This represents the ratio of the total, A_V , to the selective extinction or colour-excess, $E(B-V)$. R_V is dependent on the environment, thus line-of-sight. The typical value of R_V is 3.1, increasing up to ~ 5 in regions of recent star formation where the dust grains are likely to be larger (Glass 1999). The extinction at a specific wavelength, A_λ , can usually be expressed

*where λ_c , given in brackets, is the central wavelength of each band

as a function of R_V . Cardelli et al. (1989) find an empirical extinction law,

$$\left\langle \frac{A_\lambda}{A_V} \right\rangle = a(x) + \frac{b(x)}{R_V}, \quad (1.3)$$

where $x \equiv 1/\lambda$. Over the wavelength range $0.9 \mu\text{m} \leq \lambda \leq 3.3 \mu\text{m}$ they find:

$$\begin{aligned} a(x) &= 0.574x^{1.61}, \\ b(x) &= -0.527x^{1.61}. \end{aligned} \quad (1.4)$$

The extinction in a given bandpass is calculated by integrating the extinction law over the filter response curve and thus depends on the telescope and filters used. For example Schlegel et al. (1998) calculate the extinction values for the optical Landolt B and NIR UKIRT J , H and K bands using the extinction laws of Cardelli et al. (1989) in the NIR and O'Donnell (1994) in the optical. Their results, listed in their Table 6, are:

$$\begin{aligned} A_B &= 4.315E(B-V), \\ A_J &= 0.902E(B-V), \\ A_H &= 0.576E(B-V), \\ A_K &= 0.367E(B-V). \end{aligned} \quad (1.5)$$

Provided the selective extinction is known, the extinction in any waveband covered by the extinction law can be determined.

Extinction Maps

The dust maps of Schlegel, Finkbeiner, & Davis (1998) are widely used for determining the selective extinction for a given line of sight. Figure 1.1 shows the all-sky reddening map of Schlegel et al. (1998). The map gives $E(B-V)$ in logarithmic units from $0^{\text{m}}004$ (dark blue) to $6^{\text{m}}3$ (red), plotted in Galactic coordinates. This all-sky reddening map is based on the $100 \mu\text{m}$ observations of the Differential InfraRed Background Explorer (DIRBE) on the COsmic Background Explorer satellite (COBE; Hauser et al. 1991) and the InfraRed Astronomy Satellite (IRAS; Neugebauer et al. 1984) Sky Survey Atlas (ISSA; Wheelock et al. 1994). Dust emits strongly at these wavelengths so the intensity can be transformed to a map of dust column density. Schlegel, Finkbeiner, & Davis (1998) calibrated the column-density map for reddening with the colours of elliptical galaxies.

The original infrared DIRBE maps have a coarse resolution of $0^{\circ}7$ which fails to resolve small-scale variations of the dust column density across the Galactic plane. The higher resolution, $5'$, all-sky IRAS/ISSA map was used to improve the resolution of the DIRBE dust map to $6^{\circ}0$. However, within the Galactic plane, extinction can vary on scales smaller than this.

Due to the high density and bright-source contamination in the Galactic plane, Schlegel

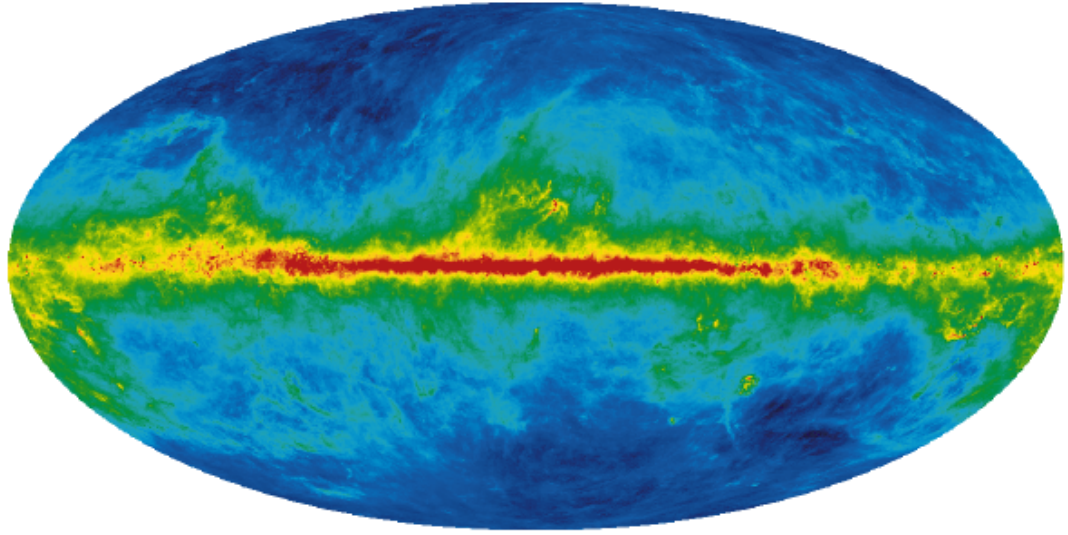


Figure 1.1: All-sky extinction map of Schlegel et al. (1998). The map gives $E(B - V)$ in logarithmic units from 0^m004 (dark blue) to 6^m3 (red), plotted in Galactic coordinates. Image from LAMBDA data products.

et al. (1998) warn that their dust maps are not properly calibrated and are thus poorly constrained for $|b| \lesssim 5^\circ$, where b is Galactic latitude. In the Zone of Avoidance, both the Schlegel map and the older reddening maps of Burstein & Heiles (1982) overestimate the reddening by $\sim 13\text{--}33\%$ (see for example Burstein 2005, Dutra et al. 2002, Schröder et al. 2005).

Effect of Extinction on Galaxy properties

Intervening dust causes galaxies to appear fainter and redder. Additionally, extended objects will appear smaller since the fainter outer parts will drop below the detection limit. This effect was first rigorously quantified by Cameron (1990) in the optical B band and later in the NIR J , H and K_s bands by Riad et al. (2010). While the extinction correction for simple dimming is linear, the additional dimming because of the decreased isophotal radii is non-linear and depends on the surface brightness profile of the source (see for example Cameron 1990, Riad et al. 2010).

Internal Extinction

Dust within galaxies causes *internal* extinction, A^i , as well. The amount of internal extinction depends on the inclination of the galaxy: a line of sight through a more inclined galaxy will have a higher dust column density and thus experience more extinction. It also depends on the morphology: late-type irregular galaxies have a higher fractional dust content, however, they are smaller and thus have less total dust and lower internal extinction. The internal extinction is often determined statistically from a very large sample of galaxies.

In a study of 2MASS spiral galaxies, Masters, Giovanelli, & Haynes (2003) parametrise the NIR internal extinction as:

$$A_\lambda^i = \gamma \log(a/b), \quad (1.6)$$

where a and b are the semi-major and -minor axes respectively. a/b is the axis ratio of the galaxy which is a proxy for the inclination. For low inclination, $\log(a/b) \leq 0.5$, they find a linear relation with:

$$\begin{aligned} \gamma_J &= 0.48 \pm 0.15, \\ \gamma_H &= 0.39 \pm 0.15, \\ \gamma_{K_s} &= 0.26 \pm 0.15. \end{aligned}$$

For high inclinations, $\log(a/b) > 0.5$, they find:

$$\begin{aligned} \gamma_J &= (1.6 \pm 0.2) + 0.24/\log(a/b), \\ \gamma_H &= (1.4 \pm 0.2) + 0.20/\log(a/b), \\ \gamma_{K_s} &= (1.1 \pm 0.2) + 0.13/\log(a/b). \end{aligned}$$

1.1.2 Stellar Density

The exponential increase in the surface density of stars near the Galactic plane and Bulge causes an increase in source confusion. Unresolved, spatially co-incident stars appear ‘blended’ and mimic extended objects. These stars can be mistakenly identified as galaxies, particularly by automated routines. The completeness and reliability of a galaxy catalogue thus deteriorates with increasing stellar density. Figure 1.2 shows the 2MASS Point Source Catalogue (2MPSC) stellar number density metric, $\log(N_{K_s<14}/\text{deg}^2)$, where $N_{K_s<14}$ is the number of stars brighter than $14^{\text{m}}0$ in K_s . The Galactic bulge has a stellar density, $\log(N_{K_s<14}/\text{deg}^2) > 4.5$. There is a significant increase in density across the Galactic plane increasing towards the Galactic bulge.

In addition, the stellar density contributes an additional ‘noise’ component to the total background noise. This is known as *confusion noise*. This is due to the increased number of stars fainter than the detection limit that contribute to the background sky (Jarrett et al. 2000b). This is illustrated in Fig. 1.3, taken from Jarrett et al. (2000b) who quantified the confusion noise for the 2MPSC. The plot shows the relationship between Galactic latitude (left axis) and star density for two regions along the Galactic plane at longitudes 50° and 130° . The cross-hatched area gives the confusion noise in magnitude units (right axis) as a function of the stellar number density. There is a strong correlation between the increase in confusion noise and the increase in stellar density.

Finally, the inability to resolve faint stars and the need to remove a greater number of foreground stars results in larger errors in galaxy photometry.

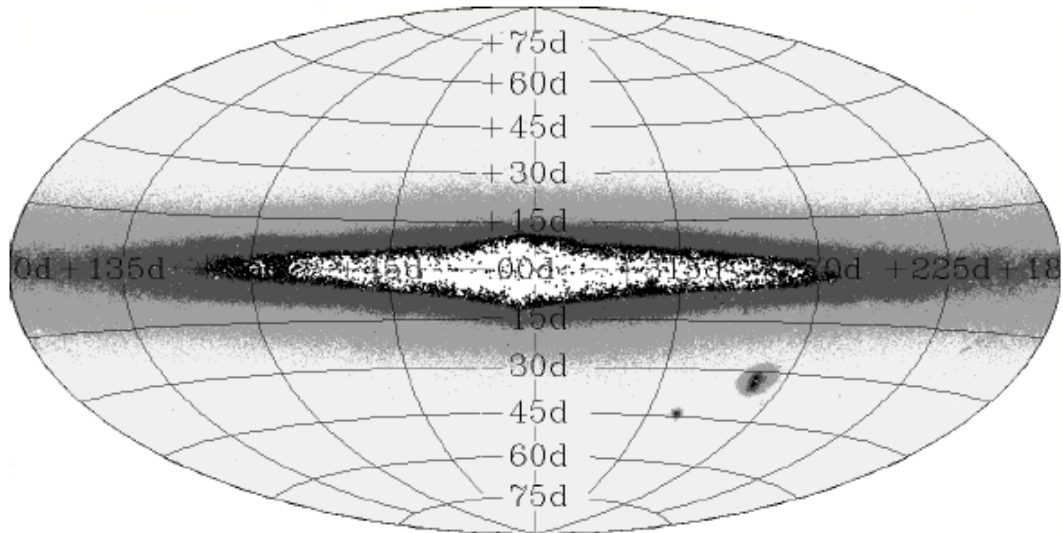


Figure 1.2: 2MPSC stellar number density for stars brighter than $14^{\text{m}}0$ in K_s plotted in Galactic coordinates. The number density metric is $\log(N_{K_s < 14}/\text{deg}^2)$, where $N_{K_s < 14}$ is the number of stars brighter than $14^{\text{m}}0$ in K_s . The light grey region has $\log(N_{K_s < 14}/\text{deg}^2) < 3.2$ and the white region (Galactic bulge) has $\log(N_{K_s < 14}/\text{deg}^2) > 4.5$. Image from Jarrett et al. (2000b).

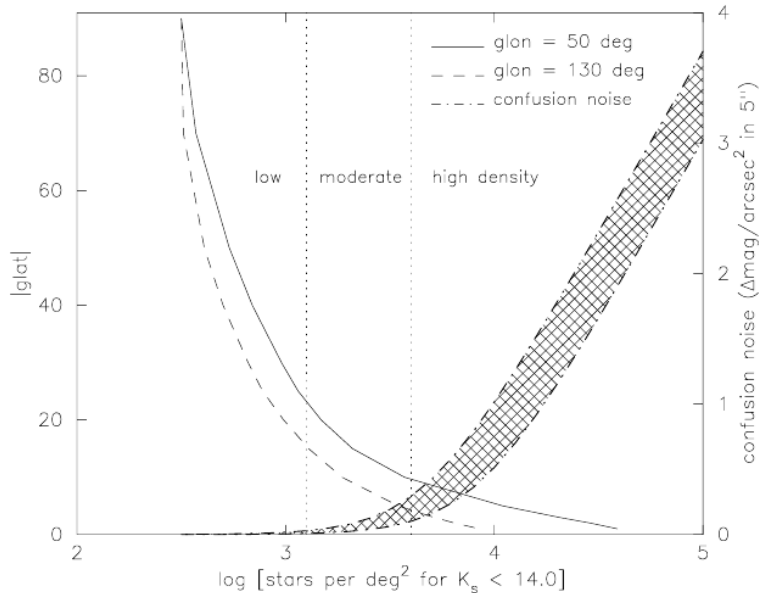


Figure 1.3: Predicted stellar number density, $\log(N_{K_s < 14}/\text{deg}^2)$, as a function of Galactic latitude for 50° Galactic longitude (solid line) and 130° Galactic longitude (dashed line). The dashed lines demarcate regions of low (< 3.1), moderate ($3.1 – 3.6$), and high (> 3.6) stellar number density. The estimated confusion noise as a function of the stellar number density is denoted by two dot-dashed lines with cross-hatching in between. Image from Jarrett et al. (2000b).

1.2 Galaxies in the ZoA

The intrinsic properties of galaxies in the ZoA are no different to those of the population in the unobscured sky. Studies of the properties of galaxies are therefore best accomplished outside of the ZoA where the measurements are largely unaffected by foreground dust and stars. However, in studying the large-scale distribution of matter in the Universe, and in particular, the effects this matter distribution has on the dynamics of the Milky Way and nearby galaxies, it is important to include the distribution within the ZoA. A multi-wavelength survey approach is necessary to unveil and characterise this distribution.

1.2.1 The Importance of Mapping Structures in the ZoA

Large-scale galaxy redshift surveys reveal complex web-like structures in the three-dimensional distribution of galaxies. Galaxies tend to be grouped together in clusters and super-clusters joined by filaments and separated by voids (Fairall 1998). Analysis of these large-scale structures (LSS) helps us understand the formation of structure in the Universe and allows for the determination of fundamental cosmological parameters. Moreover, the distribution of matter, both dark and visible, induces the peculiar motions of galaxies and is responsible for the motion of the Local Group and the resulting dipole in the CMB. The incompleteness of the distribution of galaxies in the ZoA has hampered our progress in understanding these cosmological problems, in particular:

- The determination of the size, extent and connectivity of nearby large-scale structures. Several nearby structures are bisected by the Milky Way, including the Perseus-Pisces Chain (Chamaraux et al. 1990), the Centaurus Wall (Fairall et al. 1998), the Hydra-Antlia extension (Kraan-Korteweg et al. 1994a) and the Great Attractor region (Woudt 1998).
- The origin of the motion of the Local Group. The CMB dipole is very accurately measured and implies a LG velocity of 622 km s^{-1} towards Galactic longitude $l = 277^\circ$, and latitude $b = 30^\circ$ (Kogut et al. 1993). However, the source of the motion remains poorly constrained and it is debated whether it is caused by distant structures or nearby massive structures hidden by the ZoA. Strauss et al. (1992, IRAS sample), Lynden-Bell, Lahav, & Burstein (1989, optical surveys) and Erdo\u{g}du et al. (2006a, 2MRS) concluded that the mass within $\sim 6000 \text{ km s}^{-1}$ causes the motion, with the major contributions due to Virgo (Jerjen & Tammann 1993), the GA (Lynden-Bell et al. 1988) and the LV (Tully 2007). On the other hand, Kocevski & Ebeling (2006, X-ray clusters) and Scaramella, Vettolani, & Zamorani (1991, Abell/ACO clusters) show that there are contributions to the motion from beyond 6000 km s^{-1} , with the major contributor being the Shapley supercluster concentration (SC; Shapley 1930).
- The relative importance of the GA and SC to the local dynamics remains contended. The nature of the dynamics around the GA will help resolve this issue. If the GA is an isolated structure and the large positive peculiar motions in front of it are indeed

generated by the GA there should be present behind the GA significant negative peculiar velocities or *backside infall*. Evidence for this was first reported by Dressler & Faber (1990), but Mathewson, Ford, & Buchhorn (1992a) found no evidence for such infall using an independent dataset. Recently, using data from the 2MASS Redshift Survey, Erdoğdu et al. (2006a) find a backside infall of $v_{infall} = 127 \pm 409 \text{ km s}^{-1}$ in the CMB frame in the reconstructed velocity fields. The infall is strongest at a distance of 5000 km s^{-1} and the highest back-falling velocity they find is $800 \pm 600 \text{ km s}^{-1}$ in the CMB frame. However, their results remain inconclusive.

1.2.2 Multi-wavelength Searches

The degree and extent of the ZoA depends on the wavelength of observation. A multi-wavelength approach is most effective at detecting galaxies within the ZoA and provides complementary information from the different wavebands. A number of systematic surveys have been conducted using different parts of the electromagnetic spectrum. The following subsections give a brief overview of the searches undertaken at various wavelengths to reduce the ZoA. For a more detailed overview, see Kraan-Korteweg & Lahav (2000) and a more recent update by Kraan-Korteweg (2005).

Optical

Nearly two decades of deep optical studies of the ZoA have revealed tens of thousands of galaxies behind the plane of the Milky Way (see for example Kraan-Korteweg & Lahav 2000, Wakamatsu et al. 1994). Although the optical wavelengths are most affected by dust extinction, a significant reduction of the ZoA has been achieved through systematic deep surveys covering most of the low latitudes. These surveys have been particularly effective for moderate extinction and have reduced the optical ZoA from $A_B \lesssim 1 \text{ mag}$ ($|b| \gtrsim 10^\circ$) to $A_B \lesssim 3 \text{ mag}$ ($|b| \gtrsim 5^\circ$) (Kraan-Korteweg 2000). Optical surveys are unbiased towards any specific morphological type.

Figure 1.4 (reproduced from Kraan-Korteweg & Lahav 2000) shows an extinction-corrected diameter-limited ($D^0 \geq 1.3'$) sample of optical galaxies in Galactic coordinates. The ZoA is obviously void of galaxies. The completeness of the sample follows approximately the $A_B = 3^{m0}$ extinction contour (plotted in red).

Near Infrared

The longer wavelength NIR ($0.75 - 5 \mu\text{m}$) searches become more efficient where deep optical surveys become incomplete ($A_B \gtrsim 3 \text{ mag}$) because extinction in the NIR is much lower than the optical. The sensitivity of the NIR to the old stellar population makes NIR surveys particularly sensitive to early type galaxies.

There have been two major systematic surveys in the NIR: the DEep Near Infrared Southern Sky Survey (DENIS; Epchtein et al. 1997) and the 2 Micron All Sky Survey (2MASS; Strutskie 2006) which imaged the whole sky in J , H and K_s . DENIS observed the

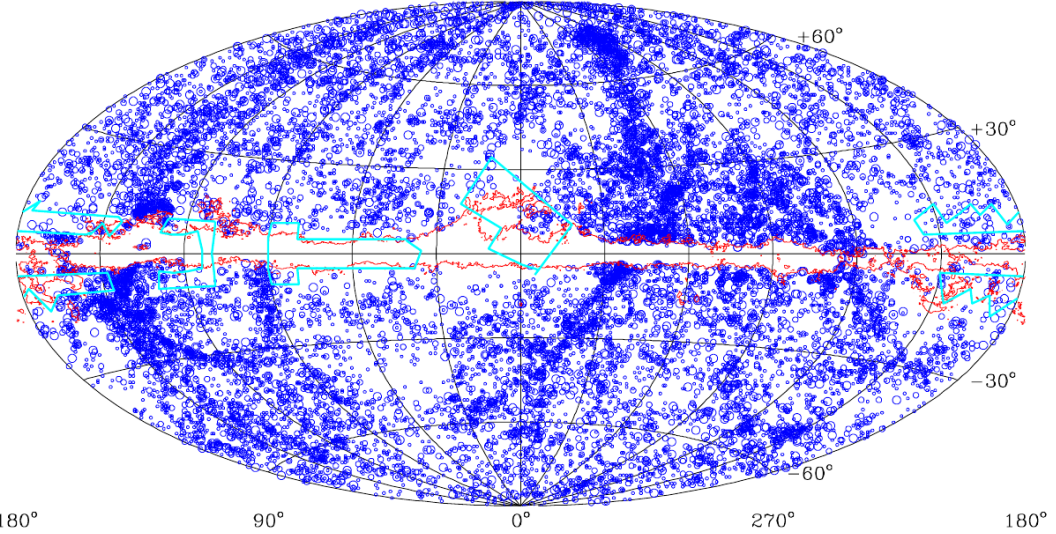


Figure 1.4: Optical galaxies with extinction-corrected diameter $D^0 \geq 1.3'$ in Galactic coordinates. The size of the circles indicates the diameter of each galaxy. The ZoA is obvious as a lack of galaxies with $b \lesssim 5^\circ$ which follows closely the $A_B = 3m0$ (Schlegel et al. 1998) extinction contour (red line). Reproduced from Kraan-Korteweg & Lahav (2000).

southern sky in the three NIR bands I ($\lambda_c = 0.82 \mu\text{m}$), J and K_s , while 2MASS observed the northern and southern skies in J , H and K_s going $\sim 1^{\text{m}}$ deeper in K_s than DENIS. 2MASS produced a catalogue of 0.5 billion Milky Way stars and 1.65 million extended sources (mostly galaxies) (Jarrett et al. 2000b). The 2MASS extended source catalogue (2MASX) has been used to map large scale structure in the ZoA (Jarrett 2004, Jarrett et al. 2000a). However, galaxies near the Galactic bulge are still largely obscured due to the high stellar density and confusion (Kraan-Korteweg & Jarrett 2005). Figure 1.5 shows an Aitoff equal area plot of integrated flux along the line of sight for ~ 1 million sources in the 2MASX in Galactic coordinates. The ZoA follows the Galactic plane flaring up around the bulge.

Radio

The neutral hydrogen (H I) emission line at 21 cm has shown to be the most effective at penetrating the most obscured parts of the ZoA. Galactic H I emission was first detected by Ewen & Purcell (1951) and extragalactic H I emission by Kerr & Hindman (1953). The weak 21 cm or 1.42 GHz emission results from the neutral hydrogen undergoing a hyperfine transition between spin states. Despite the fact that an average hydrogen atom would take 11 million years to undergo this transition spontaneously (Landowitz & Marshall 1960), there are enough hydrogen atoms in galaxies for these transitions to occur. The absorbing dust in the Milky Way is fully transparent to radiation at 21 cm, making gas-rich galaxies easy to detect in the ZoA. Moreover, the emission line nature makes it possible to determine the redshift as well as the maximum rotational speed of the gas of the detected source.

The search for galaxies behind the Milky Way in H I was pioneered by Kerr & Henning

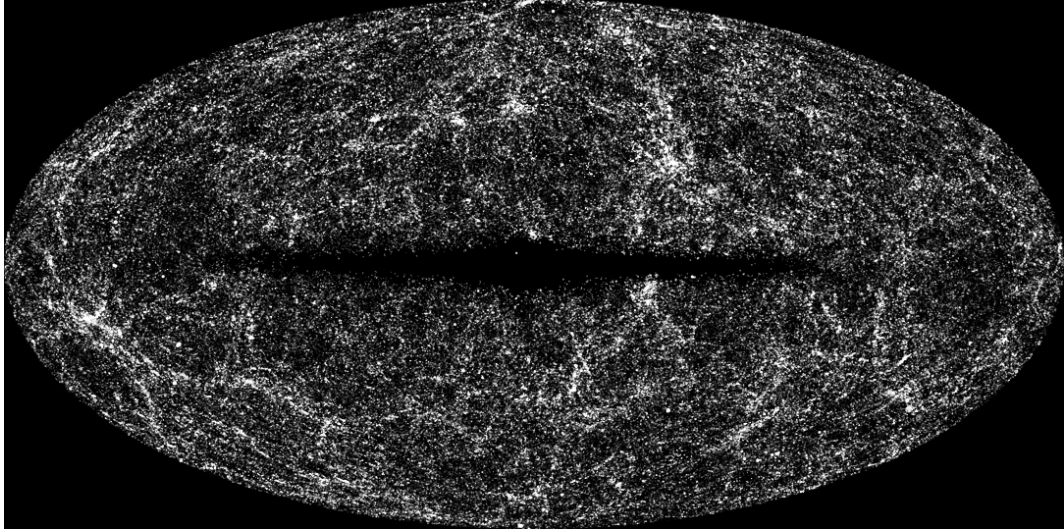


Figure 1.5: 2MASX integrated flux along the line of sight for ~ 1 million sources in Galactic coordinates. The ZoA flares up around the Galactic bulge due to the increase in stars. (Jarrett, priv. comm.)

(1987) using the Greenbank 91 m radio telescope. The first systematic survey in the northern ZoA was the Dwingeloo Obscured Galaxies Survey (Henning et al. 1998). The introduction of the Multibeam (MB; Staveley-Smith et al. 1996) receiver on the 64 m Parkes* telescope in 1997 brought with it the capability for more sensitive larger systematic surveys with higher survey speed (see for example Staveley-Smith et al. 1998). The MB receiver, consisting of 13 beams in a focal plane array (Staveley-Smith et al. 1996), has uncovered thousands of galaxies in two key surveys: a southern all sky survey (HIPASS; Meyer et al. 2004) with an rms noise of 13 mJy beam^{-1} and another deeper survey covering the southern ZoA (HIZOA; Henning et al. 2005) with an rms noise of 6 mJy beam^{-1} . The HI observations reveal galaxies where both optical and NIR surveys fail (see Figs. 1.4 and 1.5) due to high extinction and stellar density. In fact, the HIZOA survey region was chosen in order to cover this specific region of the sky. However, no information is available on the stellar content of these galaxies. Deep, high resolution NIR observations are able to penetrate the dust and deblend foreground stars making it possible to detect the NIR counterparts for the HI-detected galaxies. These complementary data are extremely valuable in the determination of distances, in particular via the NIR Tully-Fisher relation.

*The Parkes telescope is part of the Australia Telescope which is funded by the Commonwealth of Australia for operation as a National Facility managed by CSIRO

1.3 The Cosmic Peculiar Velocity Flow-Field

1.3.1 Peculiar Velocities

The expansion of the Universe results in the well-known Hubble (1929) law

$$v = H_0 d, \quad (1.7)$$

where H_0 is the Hubble constant, taken to be $75 \text{ km s}^{-1} \text{ Mpc}^{-1}$ * throughout this thesis. However, in addition to this smooth Hubble flow, galaxies exhibit a *peculiar motion* as a direct result of the gravitational influence of the inhomogeneous mass distribution within their local environment. These large scale structures in the Universe are born out of the initial quantum density fluctuations in the early universe which collapse and coalesce under gravitational instability.

Peebles (1976) showed that, in the linear regime, where both the perturbations and the velocities are small, the peculiar velocities, \mathbf{v}_{pec} , are directly proportional to the underlying gravitational acceleration, \mathbf{g} . At position \mathbf{x} the peculiar velocity is

$$\mathbf{v}_{\text{pec}}(\mathbf{x}) = \frac{2f}{3H_0\Omega_M} \mathbf{g}(\mathbf{x}). \quad (1.8)$$

The symbols in boldface represent vector quantities. The constant of proportionality depends only on cosmological parameters: the Hubble constant, H_0 , the matter density, Ω_M , and the rate of growth of structure, which can be approximated as $f \sim \Omega_M^{0.6}$ for ΛCDM cosmologies Percival (2005). The gravitational acceleration is simply the divergence of the gravitational potential, directly proportional to the mass density. Therefore, the peculiar velocity field can be used to either investigate the fundamental cosmological parameters for a known potential field or, assuming a cosmological model, reveal the underlying gravitational potential or mass distribution field.

Observationally, only the scalar radial component of the peculiar velocities, v_{pec} , can be measured. Provided a *redshift-independent* distance is known, the peculiar velocity can be calculated from the difference between the measured recession velocity, v_{obs} , and the expected Hubble flow, $H_0 d$:

$$v_{\text{pec}} = v_{\text{obs}} - H_0 d. \quad (1.9)$$

For a sample of galaxies, it is theoretically possible to reconstruct the three-dimensional velocity field from the measured radial velocity field. This is because the velocity is proportional to the gradient of a potential field. Reconstruction methods (e.g. POTENT; Dekel et al. 1990) have been developed to implement this but they suffer two main problems: large errors on individual measurements and sparse, uneven sky coverage.

Peculiar velocities are typically of the order of a few hundred km s^{-1} and their errors are

*The error in H_0 is represented by the dimensionless value h_{75} which is related to the usual Hubble parameter $h \equiv H_0/100 \text{ km s}^{-1} \text{ Mpc}^{-1}$ by $h = 0.75h_{75}$. A factor of h_{75} therefore is present in all distance dependent results.

largely dominated by the uncertainties in the distances. This means that they can only be measured in the Local Universe, within a few thousand km s^{-1} . At $v_{obs} = 1000 \text{ km s}^{-1}$, a 10% distance error corresponds to a peculiar velocity error of 100 km s^{-1} , while at $v_{obs} = 10\,000 \text{ km s}^{-1}$ the corresponding error is 1000 km s^{-1} , which is larger than the typical magnitude of the peculiar velocity.

The study of cosmic flows is only possible with the ability to measure distances for many galaxies. In the 1970's several methods for the determination of redshift independent distances were discovered, providing distances for much larger numbers of galaxies. These methods include the Tully-Fisher relation (TF; Tully & Fisher 1977) for spiral galaxies and the $D_n - \sigma$ relation (Dressler et al. 1987) and the Fundamental Plane (FP; Djorgovski & Davis 1987) for elliptical galaxies. Recently, methods using Surface Brightness Fluctuations (Tonry & Schneider 1988) and surveys for Type Ia supernovae (Gibson et al. 2000, Riess et al. 2004) have provided complementary distance measurements. However, the workhorses of peculiar velocity determinations remain the TF and FP relations.

1.3.2 The Local Peculiar Velocity Flow Field

De Vaucouleurs (1958) first noticed the presence of an overdensity of galaxies in the Local Universe ($cz \lesssim 3000 \text{ km s}^{-1}$). He described this flattened local supercluster as a ‘supergalaxy’ and defined the supergalactic plane (for a recent review see Lahav et al. 2000). He also noted that this mass overdensity could perturb the motions of galaxies. Early work in measuring the flow fields was aimed at determining the amplitude of the infall towards the Virgo cluster, what de Vaucouleurs (1958) considered to be the center of the local supercluster (Tonry & Davis 1981, Aaronson et al. 1982). Since then, it has been recognised that the local velocity field is more complex. There are many nearby attractors and voids as well as distant mass concentrations. See Willick (2000) for a review on flow fields.

1.3.3 The Problem of the ZoA

While the ZOA has been greatly reduced in the last decade, it is still too poorly sampled and the determination of the velocity fields is severely hampered in this region. Methods of statistically interpolating either the mass density distribution (Lahav et al. 1994) or the underlying gravitational potential (Kolatt et al. 1995) have been used to ‘fill in’ this region. However, it is uncertain whether they truly model the hidden dynamics. By interpolating the surrounding peculiar velocities into the ZoA, Kolatt et al. (1995) show that the inclusion of the $\pm 20^\circ$ around the Galactic plane changes the direction of the gravitational acceleration vector by $\sim 35^\circ$. Clearly, the mass distribution in the ZoA is of crucial importance to the motion of the Local Group. Recent work by Loeb & Narayan (2008), comparing the CMB dipole and that of the 2MASS Redshift Survey (2MRS; Huchra et al. 2005), suggests a significant contribution to the motion by hidden mass within the ZoA, particularly around the Galactic centre. Direct measurement of the peculiar velocity flow field within the ZoA will help resolve a number of these questions, including that of the nature and extent of the

GA (Tully et al. 2008).

1.3.4 The Near Infrared Tully-Fisher Relation

The Tully-Fisher relation (TF; Tully & Fisher 1977) is a general empirical correlation between the luminosity and the rotation velocity of spiral galaxies. The rotation velocity (measured either by the H_I line width or by the optical rotation curve) is independent of distance, while the luminosity falls off as the square of the distance, so the relation provides a natural means for determining distances for spiral galaxies. A consensus on the physical origins of the TF relation is yet to be reached, but it can be explained by several sub-relations between:

- the total luminosity and luminous mass;
- the distributions of luminous mass and total mass (including dark matter); and
- the total mass distribution and rotation speed.

A simple derivation leads to the relation

$$L \propto v_{max}^4, \quad (1.10)$$

where v_{max} is the maximum rotational speed of the gas in the galaxy. Observationally, it is convenient to express the relation in terms of absolute magnitude, $M \propto -2.5 \log L$, and the H_I linewidth, $W = 2v_{rot}$. The TF relation can then be written as

$$M = a + b(\log W - 2.5), \quad (1.11)$$

where $b/2.5$ is the measured exponent. The slope and intercept depend on wavelength, morphological type and the choice of observational parameters; in particular the exponent may have a value between 3 and 4. Several different measurements can be made of the magnitude (e.g. total or isophotal magnitude) and the rotational velocity (e.g. 20%-linewidth w_{20} , 50%-linewidth w_{50} , circular velocity v_{circ}) which provide different TF relations. It is important to use consistent measurements in calibrating the relation and measuring distances. Several homogeneous datasets have been compiled from various samples, including the SCI sample (Giovanelli et al. 1997b) and the Mark III catalogue (Giovanelli et al. 1997a, Willick et al. 1997).

Shortly after the adoption of the TF relation as a distance indicator, it was realised that the NIR wavebands would provide several advantages over optical wavelengths (Aaronson et al. 1979) for the following reasons:

1. The extinction, both internal and Galactic, is significantly reduced in the NIR. This results in smaller uncertainties introduced by extinction corrections and more robust photometric measurements.

2. The spectral energy distribution of all galaxies peaks in the NIR, where it is dominated by the old, red stellar population. The long-lived low mass stars provide the best indicator of the total stellar mass which governs the kinematics of galaxies and is unperturbed by recent short-term star formation which is significant at bluer wavelengths.

3. The distribution of old stars is smoother, resulting in a smooth light profile. This makes it easier to fit smooth elliptical isophotes resulting in cleaner photometry.

Importantly, it is the low extinction in the NIR compared to shorter wavelengths that makes the NIR TF relation most ideal for use in the ZoA. Firstly, because it means that the galaxies can be detected and secondly because the photometric corrections and uncertainties are much smaller.

1.4 Motivation for follow-up Near Infrared observations of HI galaxies

The HIZOA survey was very successful in identifying new galaxies in the most obscured part of the ZoA. However, while the HI data provide information on the redshift, galaxy rotation and HI mass, no information on the stellar content is known. The NIR is ideally suited for this: it is an excellent tracer of the stellar mass of galaxies. Moreover, and of particular importance to this work, the effects of dust extinction are significantly lower in the NIR and the HI galaxies are more likely to be detected in the NIR than in the optical. In fact many of the HIZOA sources are optically invisible and can only be detected in the NIR. Imaging in the NIR can therefore provide the necessary information on their morphologies, luminosities and inclinations.

While all-sky NIR surveys such as 2MASS already exist, they lack the depth and resolution to either detect or accurately measure the parameters of these low-latitude HI galaxies. We have therefore conducted follow-up NIR observations in the J , H and K_s bands using the SIRIUS camera on the IRSF telescope in Sutherland. With images deeper than currently available with 2MASS (10 min compared to ~ 8 s) and a factor ~ 4.5 times improvement in resolution, we can detect fainter targets and mitigate some of the effects of stellar confusion. Figure 1.6 shows a comparison between postage stamps of the same galaxy in 2MASS and with the IRSF. HIZOA sources can be detected to higher levels of extinction and stellar density. In addition, the deep, high resolution images allow for improved photometry because we can resolve, and therefore remove, fainter stars.

The high fidelity IRSF photometry can be used to obtain Tully-Fisher distances, which will allow for the determination of peculiar velocities.

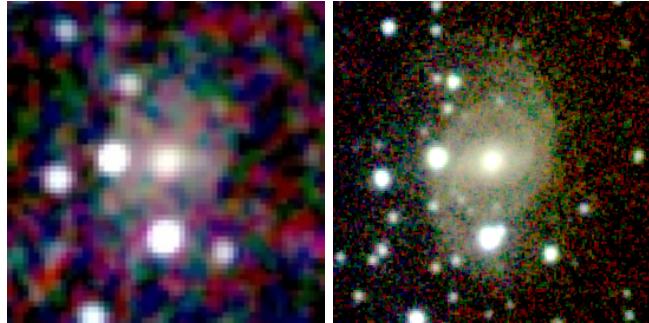


Figure 1.6: A comparison between the 2MASS image (*left*) and the IRSF/SIRIUS image (*right*) of HIZOA galaxy J0730-28. The deeper 10 min exposure with IRSF/SIRIUS reveals the fainter outer parts of the disk than the \sim 10 s exposure of 2MASS. The higher resolution of the IRSF/SIRIUS ($0.^{\prime\prime}45 \text{ pix}^{-1}$) compared to 2MASS ($2.^{\prime\prime} \text{ pix}^{-1}$) allows for fainter stars to be seen and resolved particularly on the faint disk of the galaxy. Both images are $1' \times 1'$ with North at the top and East to the left.

1.5 Outline of this Thesis

The remainder of the thesis is structured as follows. Chapter 2 summarises the HIZOA survey and the basis for selection for the follow-up NIR photometric survey. In Chapter 3 the results of follow-up narrowband HI observations are presented. These observations provide improved HI parameters for low signal-to-noise and/or narrow profiles in the HIZOA survey. The deep NIR follow-up survey is described in Chapter 4. The stages from observations and data reduction to source detection and parametrisation are discussed. Chapter 5 presents the NIR catalogue. The quality of the NIR data is assessed and the photometry is used to investigate the nature of extinction in the ZoA. Some of the combined gas and stellar properties of the galaxies are analysed for the sample of HI galaxies with confirmed NIR counterparts. The determination of Tully-Fisher distances and peculiar velocities is presented in Chapter 6. Details of the sample selection are given. The preliminary peculiar velocity flow field within the ZoA is presented and discussed. Possible systematic uncertainties in the flow field are also highlighted. Finally, Chapter 7 provides a summary of the results presented and outlines the prospects for future work.

Chapter 2

Deep HI Survey

This chapter describes the systematic HI survey conducted in the Zone of Avoidance. This survey serves as the basis for our selection for the follow-up NIR survey. We discuss here the completeness and characteristics of the HI survey and describe the large-scale structures evident in the survey.

2.1 The HI Parkes Deep Zone of Avoidance Survey

The development of the Multibeam receiver (MB; Staveley-Smith et al. 1996) on the 64 m Parkes Radio Telescope has allowed rapid large-area but sensitive blind HI surveys to be carried out for the first time. The MB receiver has 13 beams with two orthogonal polarisations in the focal plane array, arranged in a hexagonal grid. Each beam has a FWHM of 14.3' and the individual beams are separated by about two beamwidths. The beam sensitivity pattern is shown in Fig. 2.1. The receiver has a system temperature of 20 K.

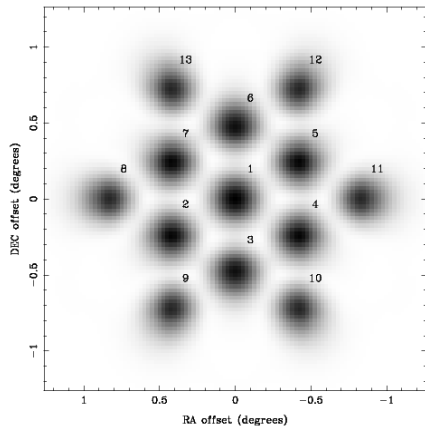


Figure 2.1: Beam sensitivity pattern of the Parkes Multibeam receiver at 1370 MHz (Staveley-Smith 1997). The footprint of the receiver on the sky is $\sim 1^{\circ}7$. Each beamsize is 14.3' and they are separated by about twice that beamwidth.

As mentioned in Chapter 1, two large, deep surveys have been conducted with the MB receiver:

HIPASS The HI Parkes All Sky Survey

The largest HI survey carried out thus far was a blind survey of the southern sky with an rms noise of 13 mJy beam^{-1} , covering a velocity range of $-1200 \lesssim cz \lesssim 12700 \text{ km s}^{-1}$. A total of 5317 galaxies were found: the original survey produced a catalogue of 4315 galaxies for $\delta < +2^\circ$ (Meyer et al. 2004), while the Northern Extension ($2^\circ < \delta < +25^\circ$) produced a further 1002 galaxies (Wong et al. 2006).

HIZOA The HI Parkes Deep Zone of Avoidance Survey

This systematic survey ran with an exposure time five times longer than HIPASS, resulting in an average rms noise of 6 mJy beam^{-1} and covering $196^\circ \leq l \leq 52^\circ$ over the same velocity range (Henning et al. 2005). The original survey ($212^\circ \leq l \leq 36^\circ$, $|b| < 5^\circ$) was extended to include a northern region, the Northern Extension (NE) covering $36^\circ < l < 52^\circ$ and $196^\circ < l < 212^\circ$ with $|b| < 5^\circ$ (Donley et al. 2005). In addition, it has been further extended into the Galactic Bulge region (GB extension) covering $332^\circ < l < 36^\circ$, $5^\circ < |b| < 10^\circ$ and $352^\circ < l < 24^\circ$, $10^\circ < |b| < 15^\circ$ (Shafi 2008).

The following sections describe the HIZOA survey and data products in detail.

2.1.1 HIZOA Survey Parameters

The survey was conducted with a correlator bandwidth of 64 MHz across 1024 channels, resulting in a 13.2 km s^{-1} channel spacing. It covers a velocity range of $-1200 < v < 12700 \text{ km s}^{-1}$. The full HIZOA survey was conducted in three parts: The initial part of the survey (ZOA) covered the entire southern ZoA ($\delta < 0^\circ$) within 5° of the Galactic plane (Henning et al. 2005). In Galactic coordinates this covers $212^\circ \leq l \leq 36^\circ$, $|b| < 5^\circ$. This was extended to the northern declinations visible from Parkes ($0^\circ < \delta < 27^\circ$). The so-called Northern Extension (NE) covers $36^\circ < l < 52^\circ$ and $196^\circ < l < 212^\circ$, $|b| < 5^\circ$ (Donley et al. 2005). Finally, higher Galactic latitudes around the Galactic Bulge were surveyed in the GB extension covering $332^\circ < l < 36^\circ$, $5^\circ < |b| < 10^\circ$ and $352^\circ < l < 24^\circ$, $10^\circ < |b| < 15^\circ$ (Shafi 2008). Hereinafter the HIZOA survey is taken to mean the combination of the ZOA survey and the NE and GB extensions (ZOA+NE+GB). The full survey area is plotted in Galactic coordinates in Fig. 2.2, overlaid with equatorial coordinates. The ZOA survey area is shown in blue, the NE extension in green and the GB extension in red.

The observations were made by scanning the telescope across the sky at constant Galactic latitude. Each scan covered 8° in Galactic longitude, offset by $35'$ in latitude, with the receiver rotated to achieve maximum sky coverage. Each scan maps out a strip $8^\circ \times 1.7'$. The ZOA and NE regions had 25 scans, while the GB extension was slightly less deep with only an average of 20 scans. The data were bandpass-corrected, calibrated and Doppler-corrected using LIVEDATA, a component of the Astronomical Image Processing System

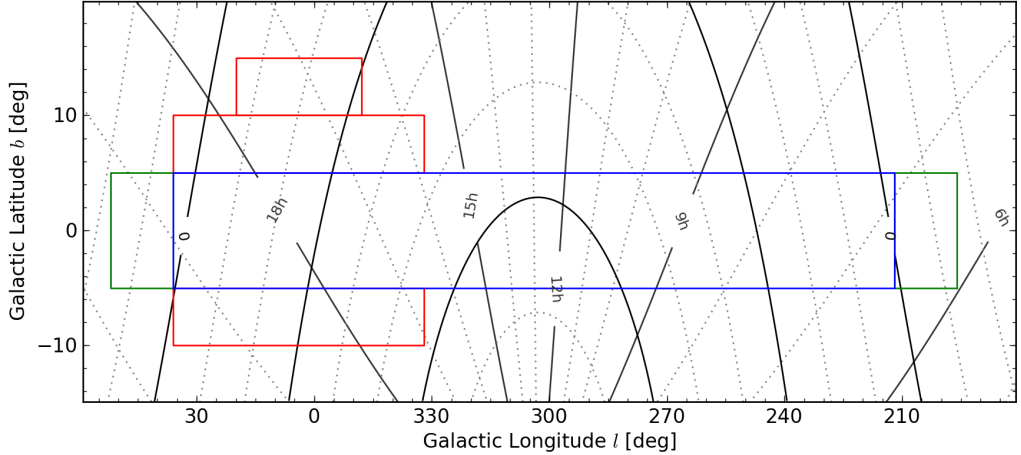


Figure 2.2: HIZOA survey area plotted in Galactic coordinates, overlayed with equatorial coordinates. The three subcomponents of the HIZOA are plotted in blue (ZOA), green (NE) and red (GB).

(AIPS++; Barnes et al. 2001). The calibrated, processed spectra were imaged using the GRIDZILLA component of AIPS++, using a top-hat median gridding algorithm with a tophat radius of $6'$ (Barnes et al. 2001). The resulting data products are three-dimensional (Right Ascension – Declination – Velocity) cubes of $8^\circ \times 10^\circ$ across the Galactic plane and $8^\circ \times 5^\circ$ in parts of the GB extension. The pixel size is $4' \times 4'$ and beamsize of the gridded data is $15\farcs5$. The cubes are Hanning smoothed to reduce the effects of ringing by strong continuum emission. This reduces the velocity resolution to 27 km s^{-1} . The survey parameters are summarised in Table 2.1.

Table 2.1: HIZOA Survey parameters

Parameter	Value
Area coverage	$212^\circ \leq l \leq 36^\circ, b < 5^\circ$ (1840 deg^2 ZOA) $36^\circ < l < 52^\circ$ and $196^\circ < l < 212^\circ, b < 5^\circ$ (320 deg^2 NE) $332^\circ < l < 36^\circ, 5^\circ < b < 10^\circ$ and $352^\circ < l < 24^\circ, 10^\circ < b < 15^\circ$ (800 deg^2 GB)
Velocity coverage	$-1200 < v < 12700 \text{ km s}^{-1}$
Telescope FWHP resolution	$14\farcs3$
Data cube FWHP resolution	$15\farcs5$
Integration time per beam	25 min (ZOA+NE) 20 min (GB)
rms noise	$\sim 6 \text{ mJy beam}^{-1}$
Velocity resolution	27 km s^{-1}

2.1.2 Source Detection and Parameterisation

The data cubes were searched visually by three independent searchers to identify galaxy candidates. A total of 1107 candidates were identified in the survey. At the time of this work, the ZoA catalogue was not completely finalised so this number may be subject to minor adjustment. A semi-automated procedure was used to determine the HI parameters of each source using a script developed by L. Staveley-Smith. The script uses the *mbspect* task in the MIRIAD package (Sault et al. 1995). The first step is determining the spatial position and extent of each source. This is done by spatially fitting a Gaussian to the velocity-integrated emission, the central coordinates defining the source coordinates. This position is used in the spectral analysis. A first-order baseline was fit to each spectral profile, however in some cases this is unrealistic and the lowest order that gave a reasonable fit was used. The maximum flux above the fitted baseline was determined as the peak flux density, S_{peak} . The total flux, I_{HI} , was determined by integrating the flux over the galaxy profile. The systemic velocity was taken to be the midpoint of the profile at 50% of the peak flux. The maximum width of the profile at 20% and 50% (w_{20} and w_{50} respectively) were measured. The extent of the HI emission for most of the sources is less than the resolution of the gridded data and can be treated as point sources.

Derived Parameters

The distance, D , in Mpc, was calculated from the Hubble law, based on the velocity in the Local Group standard of rest,

$$D = \frac{v_{LG}}{H_0}. \quad (2.1)$$

The Local Group velocity is derived using the IAU convention: $v_{LG} = v_{hel} + 300 \sin l \cos b$. The HI mass, in M_\odot , is derived from

$$M_{HI} = 2.356 \times 10^5 D^2 I_{HI}, \quad (2.2)$$

where I_{HI} is in Jy km s⁻¹ (Martin et al. 2010, Zwaan et al. 2005).

2.1.3 Source Distribution

The spatial distribution of the HIZOA sources (open circles) are plotted colour-coded by redshift bins in Fig. 2.3, which also shows galaxies with known velocities in and around the ZoA (small points). These are taken from LEDA. The non-uniform distribution of the LEDA sources is partly due to the fact that it is a non-homogeneous dataset, compiled from all available redshifts. The velocity distribution of the HIZOA sources is plotted in Fig. 2.4; 75% of the sources lie within 6000 km s⁻¹.

For the Northern Extension, Donley et al. (2005) find a mean flux density completeness limit of 22 mJy, where the mean flux density is defined to be the integrated flux divided by the 50% velocity width. This mean flux density limit corresponds roughly to a peak flux density limit of 29 mJy, which is $\sim 5\sigma$ above the rms noise of 6 mJy for the survey.

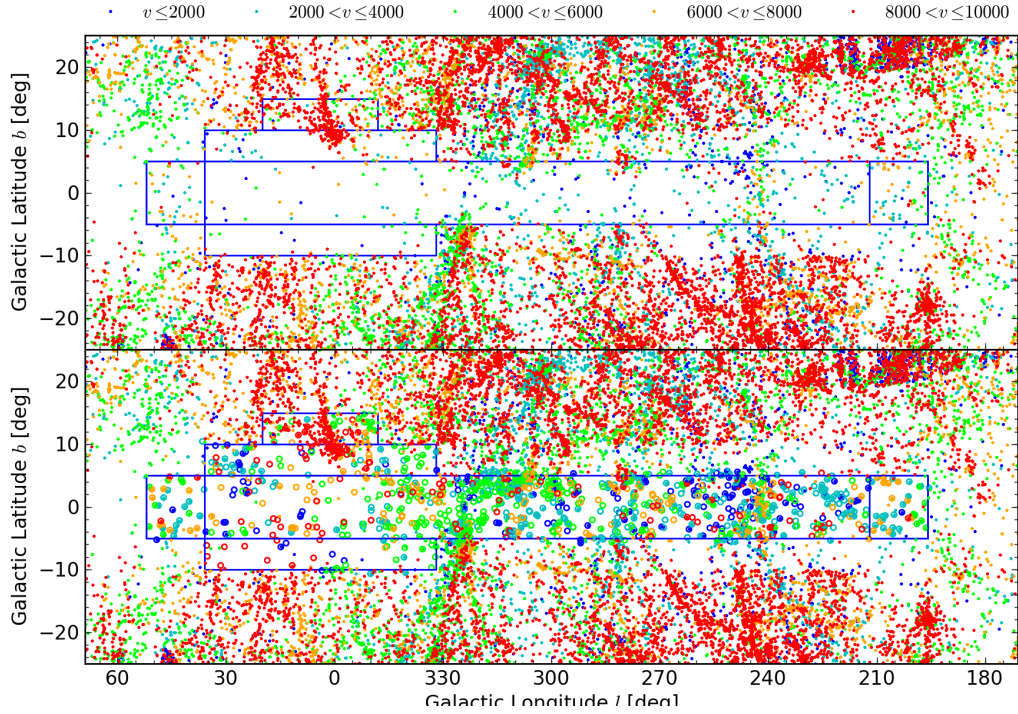


Figure 2.3: Sources detected in HIZOA compared to literature galaxies with known velocities. The top panel shows only sources in LEDA (small points) while the bottom panel shows also the new HIZOA detections (large open circles). The blue rectangles mark the boundary of the survey. Sources are plotted in Galactic coordinates and binned by velocity. Galaxies with $v \leq 2000 \text{ km s}^{-1}$ are plotted in blue, $2000 < v \leq 4000 \text{ km s}^{-1}$ in cyan, $4000 < v \leq 6000 \text{ km s}^{-1}$ in green, $6000 < v \leq 8000 \text{ km s}^{-1}$ in orange and $v > 8000 \text{ km s}^{-1}$ in red.

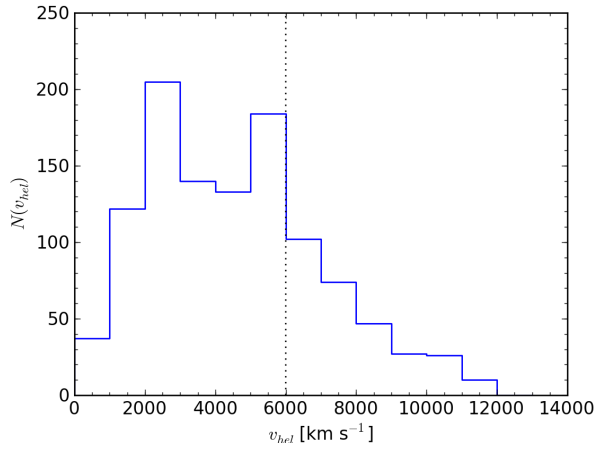


Figure 2.4: Velocity distribution of HIZOA sources. The vertical dotted line shows 6000 km s^{-1} within which $\sim 75\%$ of the sources lie.

Assuming a mean linewidth of $150 - 200 \text{ km s}^{-1}$ for a typical spiral galaxy, the HI mass limit, in M_{\odot} , at the 5σ level is

$$M_{HI} = (1.1 - 1.4) \times 10^6 D^2. \quad (2.3)$$

The HI mass limit serves as an indication of the lowest HI mass of the galaxies that can be detected in the survey. At 6000 km s^{-1} , this corresponds to a lower limit of $M \approx (7.2 - 9.2) \times 10^9 h_{75}^2 M_{\odot}$ for a mean linewidth of $150 - 200 \text{ km s}^{-1}$, while at the Great Attractor distance ($v = 4500 \text{ km s}^{-1}$) the lower limit is $M \approx (4.1 - 5.2) \times 10^9 h_{75}^2 M_{\odot}$. However, at the edge of the HIZOA survey ($v \approx 12000 \text{ km s}^{-1}$) this corresponds to a $\sim 4\times$ larger lower mass limit of $M \approx (1.4 - 3.7) \times 10^{10} h_{75}^2 M_{\odot}$. For comparison, the HI mass function derived from HIPASS by Zwaan et al. (2005) has a characteristic mass of $M_{HI}^* = 6.5 \times 10^9 h_{75}^2 M_{\odot}$. HIZOA is therefore sensitive to M_{HI}^* galaxies at GA distances. This is illustrated in Fig. 2.5, which shows the HI masses of the detected sources as a function of their recession velocities. The two blue lines show the mass, as a function of velocity, for a 5σ detection with mean linewidths of 100 km s^{-1} (dotted) and 200 km s^{-1} (solid). $M_{HI}^* = 6.5 \times 10^9 h_{75}^2 M_{\odot}$ is represented by a horizontal black line. For distances beyond $\sim 6000 \text{ km s}^{-1}$, HIZOA is sensitive only to the most massive galaxies.

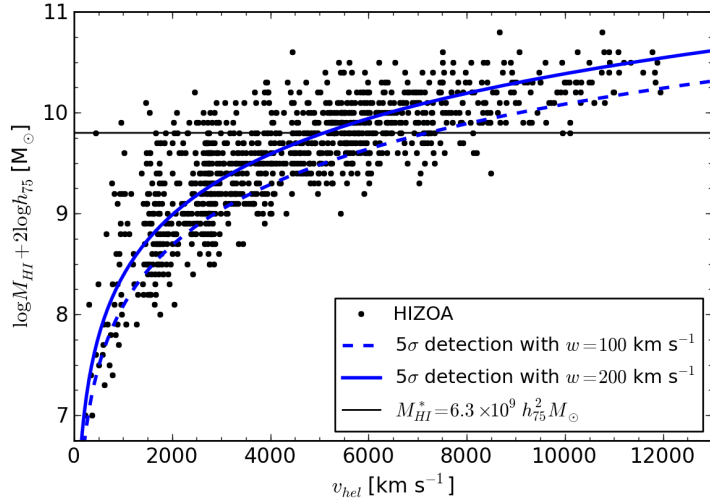


Figure 2.5: Mass sensitivity of the HIZOA survey: HI mass as a function of recession velocity. The horizontal black line shows an $M_{HI}^* = 6.3 \times 10^9 h_{75}^2 M_{\odot}$ (Zwaan et al. 2005). The solid and dotted blue lines show the mass as a function of velocity for galaxies with mean linewidths of 100 km s^{-1} and 200 km s^{-1} respectively for a 5σ detection.

2.1.4 Large-Scale Structures

As can already be seen in Fig. 2.3, the new HIZOA sources show the extension of several

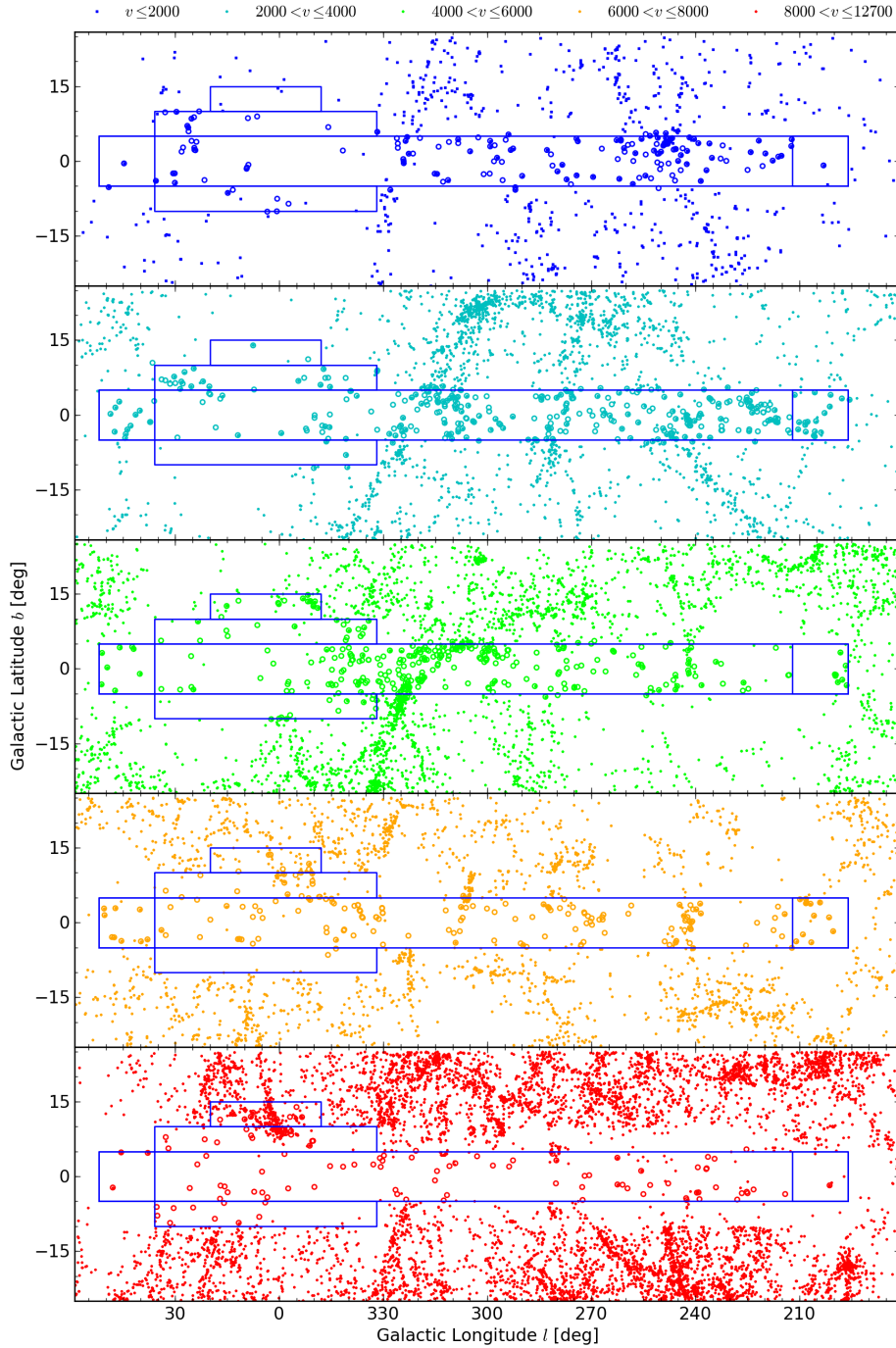


Figure 2.6: Five redshift slices of sources within 25° of the Galactic plane. Redshift slices are from *top to bottom*: $v \leq 2000 \text{ km s}^{-1}$ (blue), $2000 < v \leq 4000 \text{ km s}^{-1}$ (cyan), $4000 < v \leq 6000 \text{ km s}^{-1}$ (green), $6000 < v \leq 8000 \text{ km s}^{-1}$ (orange) and $8000 < v \leq 12700 \text{ km s}^{-1}$ (red). The HIZOA survey area is outlined in blue. Sources in LEDA are small dots. HIZOA sources are plotted with large open circles. HIZOA sources that have been previously detected and appear within LEDA appear as large filled circles. Note that LEDA constitutes an inhomogeneous dataset.

large-scale structures (LSS) into the ZoA. The apparent underdensity around the Galactic bulge (GB) is not a result of an observational bias, but is due to the Local Void (LV; Tully & Fisher 1987). Figure 2.6 shows the same plot, but subdivided into various velocity ranges. The small points are LEDA sources within 25° of the Galactic plane and the open circles are the HIZOA galaxies. The *top* panel (dark blue) shows galaxies with $v \leq 2000 \text{ km s}^{-1}$. The Puppis filament (Kraan-Korteweg & Huchtmeier 1992) is clearly visible crossing the Galactic plane at $l \sim 250^\circ$. The LV is evident as an underdensity around the GB. The *second* panel, $2000 < v \leq 4000 \text{ km s}^{-1}$ (cyan), shows the Centaurus Wall (Fairall et al. 1998) running diagonally across the Galactic plane at $l \sim 320^\circ$ and connecting to the Centaurus cluster at $(l, b) \sim (310^\circ, 20^\circ)$. Structures visible at $l \sim 240^\circ$ and $l \sim 280^\circ$ are respectively the Puppis filament and the Hydra-Antlia extension (Kraan-Korteweg et al. 1994b). The latter connects to the Antlia cluster at $(l, b, v) = (272^\circ 95, +19^\circ 19, 2797 \text{ km s}^{-1})$ after crossing the Galactic plane and extends further to the Hydra cluster centred at $(l, b, v) = (269^\circ 63, +26^\circ 51, 3777 \text{ km s}^{-1})$ (outside this plot). The *middle* panel ($4000 < v \leq 6000 \text{ km s}^{-1}$ in green) shows the Norma wall entering the plane from below at $l \sim 330^\circ$, bending over at $l \sim 310^\circ$ to join the Centaurus-Crux cluster (Woudt & Kraan-Korteweg 2001) and appearing to extend toward the Vela cluster, $(l, b) \sim (280^\circ, 15^\circ)$, (Abel S0639; Stein et al. 1997) at larger redshifts. The Norma wall is thought to be a dominant part of the Great Attractor (GA; Lynden-Bell et al. 1988). The *fourth* panel ($6000 < v \leq 8000 \text{ km s}^{-1}$ in orange) and the *bottom* panel ($v > 8000 \text{ km s}^{-1}$ in red) are relatively incomplete and only HI-bright galaxies are detected (see Fig. 2.5). These HI-massive galaxies are often found in less dense regions and are thus poorer tracers of the LSS. However, some structure behind the LV is visible. The back end of the Vela cluster is visible, as is a possible connection from the back of the Norma Wall towards the Ophiucus (Wakamatsu & Malkan 1981) cluster located behind the LV at $(l, b) \sim (350^\circ, 15^\circ)$. An additional structure located behind the Puppis filament is traced out at $l \sim 240^\circ$.

Figure 2.7 shows the distribution by Galactic longitude of all HIZOA sources. The dropoff at $l > 350^\circ$ is due to the LV. The peak near $l \sim 320^\circ$ is the Norma Wall and the broad peak around $l \sim 250^\circ$ are the Hydra-Antlia and Puppis filaments. The velocity distributions for three Galactic longitude slices are shown in Fig. 2.8. The *left* panel shows the GB ($l > 340^\circ$) and the underdensity of the LV. The *middle* panel shows the Norma Wall area ($300^\circ < l < 340^\circ$) with a clear peak around $3000 - 4000 \text{ km s}^{-1}$. The Puppis/Hydra-Antlia region ($l < 300^\circ$) is plotted in the *right* panel showing a peak around $2000 - 3000 \text{ km s}^{-1}$ corresponding to the Puppis and Hydra-Antlia filaments and a second peak at $5000 - 6000 \text{ km s}^{-1}$ corresponding to the Vela cluster.

2.2 Near Infrared Counterparts

The HI spectra provide information on the neutral gas properties of the galaxies as well as dynamical information via the width of the HI line. It does not provide any information on the stellar properties of the galaxies. NIR imaging is able to provide this information, whilst

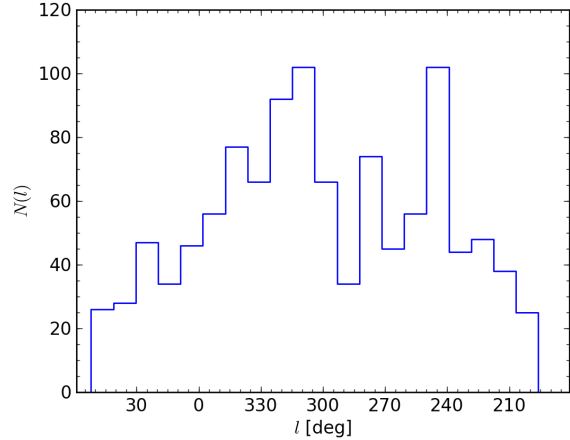


Figure 2.7: HIZOA source distribution by Galactic longitude. The peak around $l \sim 320^\circ$ is due to the Norma wall/GA, and the broad peak around $l \sim 230 - 260$ shows the Hydra-Antlia extension and the Puppis overdensity. The low counts around $l > 350^\circ$ are due to the LV.

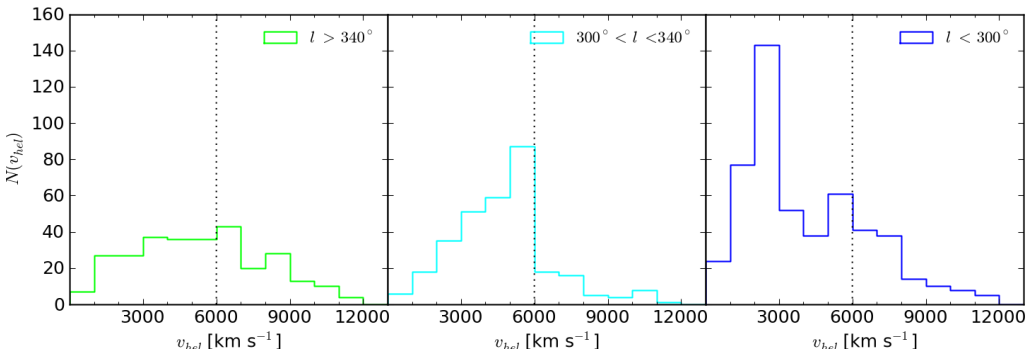


Figure 2.8: Velocity histograms for three Galactic longitude slices. The *left* panel shows the GB region ($l < 300^\circ$), the *middle* panel shows the GA region ($300^\circ < l < 340^\circ$) and the *right* panel shows the Hydra-Antlia region ($l > 340^\circ$).

overcoming some of the effects of extinction and star crowding that hamper observations in the ZoA. Importantly, NIR photometry allows for the determination of distances via the Tully-Fisher relation. 2MASS covered the entire sky in the NIR J , H and K_s bands. While the shallow depth and relatively low resolution of the 2MASS survey limits the detectability of galaxies behind the Galactic plane, some 2MASX counterparts are found for the HIZOA sources.

HI surveys favour the detection of gas-rich spirals and irregular galaxies. The NIR, being particularly sensitive to the old stellar population, is more sensitive to elliptical and normal spiral galaxies and misses faint disks and blue, low surface brightness (LSB) galaxies.

Fig 2.9 shows the HIZOA sources with confirmed counterparts in the 2MASS extended source catalogue. The plot shows all the HIZOA sources with green points and the ones with 2MASX counterparts with large blue points. Overlaid are contours of constant stellar density in the 2MASS PSC for $\log N_{(K_s < 14^m)} = 3.5, 4.0$ and 4.5 in yellow, orange and red respectively, where the stellar density, $\log N_{(K_s < 14^m)}$, is defined to be the number of stars per square degree brighter than $K_s = 14^m$. The distribution of HIZOA galaxies with 2MASX counterparts is strongly dependent on the 2MASS stellar density with almost no counterparts present where the stellar density is higher than $\log N_{(K_s < 14^m)} > 4.5$. As discussed in Sect. 1.1.2 the stellar density is the limiting factor causing the ZoA in the NIR. The fact that only 130 of the 1107 HIZOA galaxies have counterparts in 2MASS motivates the need for deeper, higher resolution NIR photometry of these sources. This will improve the identification of NIR counterparts as well as the photometry available for these counterparts.

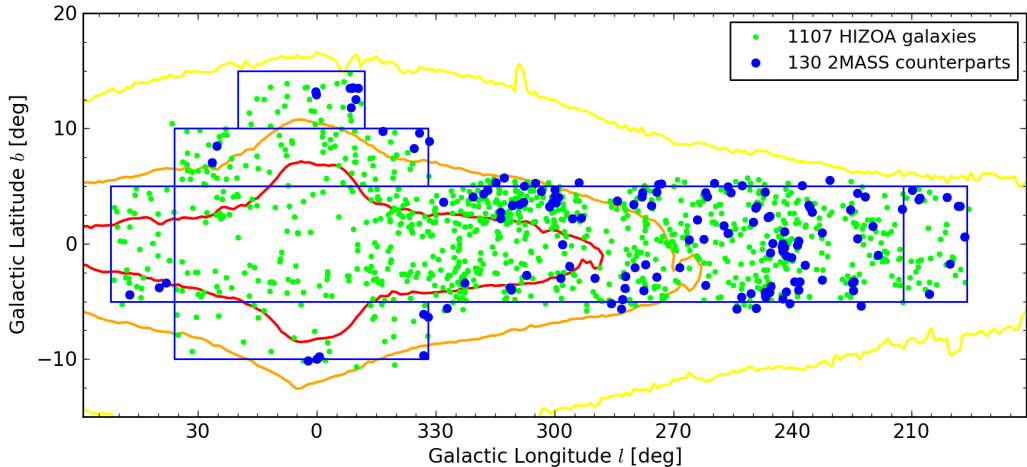


Figure 2.9: 2MASS counterparts to HIZOA galaxies. The small green points show all the sample galaxies while the large blue points show the sources with confirmed 2MASX counterparts. 2MASS PSC stellar density contours are overplotted on both plots with values of $\log N_{(K_s < 14^m)} = 3.5, 4.0$ and 4.5 plotted in yellow, orange and red respectively. The blue rectangles show the HIZOA survey area.

2.3 Target Selection for NIR Follow-up

Targets for the dedicated follow-up NIR survey are HIZOA galaxies within a volume delimited by $v = 6000 \text{ km s}^{-1}$. The reasons for this choice are:

- this volume encompasses most of the LSS in the nearby universe, including Centaurus, the Norma wall/GA and the Hydra clusters;
- at the limit of this volume we are sensitive to M_{HI}^* galaxies (see Sect. 2.1.3);
- an $M_{K_s}^* = -24.16$ galaxy (Kochanek et al. 2001) at 6000 km s^{-1} will have a apparent magnitude of $10^m 35$. 2MASX has a limiting magnitude in the K_s band of $13^m 1$ (at high Galactic latitudes; Jarrett et al. 2000b), while the limiting magnitude of the Norma wall with the same instrumental set-up as here has a limiting magnitude of $15^m 0$ (Riad 2010). Even with extinction of $A_{K_s} = 1^m$ ($A_B \approx 10^m$), we should be able to detect galaxies up to $3^m 5$ fainter than $M_{K_s}^*$; and
- the mass density out to this distance and within the ZoA may have a significant effect on the motion of the Local Group (Kolatt et al. 1995, Loeb & Narayan 2008).

Figure 2.10 shows the spatial distribution of HIZOA candidate galaxies; the targets selected for NIR follow-up observations, i.e. those within 6000 km s^{-1} , are plotted in the *top* panel (blue) and the more distant galaxies which are not observed are shown in the *bottom* panel (red).

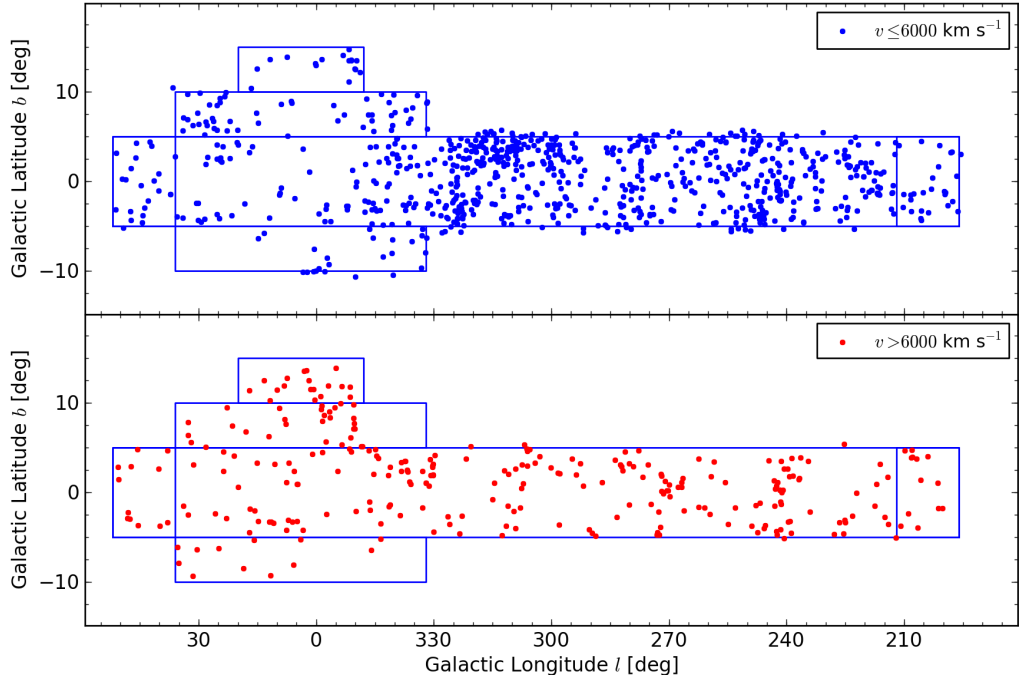


Figure 2.10: The distribution of all the HIZOA galaxies showing those selected for NIR follow-up observations. The blue rectangles mark the boundary of the HIZOA survey region. 821 galaxies with $v < 6000 \text{ km s}^{-1}$ are selected for observation with the IRSF. They are plotted in blue the *top* panel. The *bottom* panel, in red, shows the galaxies excluded from the follow-up survey.

Chapter 3

Narrowband HI Observations and Data Reduction

The measurement of TF distances not only requires accurate photometry, but also accurate HI linewidths. The fidelity of the HI linewidths depends both on the velocity resolution and S/N ratio of the spectrum. We have undertaken narrowband HI observations for a sample of HIZOA galaxies with low S/N and/or narrow linewidths in order to provide higher fidelity linewidths for the TF analysis. This chapter describes the new narrowband HI observations and the subsequent data reduction and spectral parameterisation.

3.1 Observations and Data Reduction

Observations

Follow-up HI line observations were carried out for 82 galaxies using the 64 m Parkes Radio Telescope with the Multibeam receiver (MB; Staveley-Smith et al. 1996) installed at the prime focus. Given the limited observing time, these galaxies were selected based on the identification of a likely NIR counterpart (see Chapter 4 for a description of the NIR observations) and to cover a wide range of velocity widths and HI masses.

Observations were acquired on five nights in the period 2010 February 15 – 20, with a total allocated observing time of 70 hours. The multibeam receiver allows both ON source and OFF (background) source measurements to be taken simultaneously, thereby halving the effective exposure time for a single target and significantly reducing the noise in the OFF measurement. In narrowband mode the MB receiver uses the inner 7 beams. The method of beam-switching was employed whereby the target is switched between each of the 7 beams. The ON source integration time per beam is then 1/7th of the total integration time. The OFF source observation is averaged from the other 6 beams which reduces the noise in the OFF measurement by a factor $\sqrt{6}$.

The individual exposure times of 10 – 50 min and the specific correlator configuration

for each target were optimised based on the average flux and velocity width measured from the HIZOA spectra. The narrowband correlator was used for nearly all the galaxies. This correlator has a bandwidth of 8 MHz across 1024 channels, which gives a channel separation of 1.65 km s^{-1} . The spectra were later binned to provide sufficient S/N for broader profiles. Some broad profiles were observed with the wideband ZOA correlator* (64 MHz over 2048 channels with 13.2 km s^{-1} channel width). Figure 3.1 shows the positions of the targets observed; the 82 new observations are plotted in large blue points. The remaining HIZOA galaxies within 6000 km s^{-1} are shown in small red points. Since the narrowband observations were done before the NIR follow-up survey, this sample does not constitute the entire sample used for Tully-Fisher analysis in Chapter 6. Some galaxies remain with large linewidth errors.

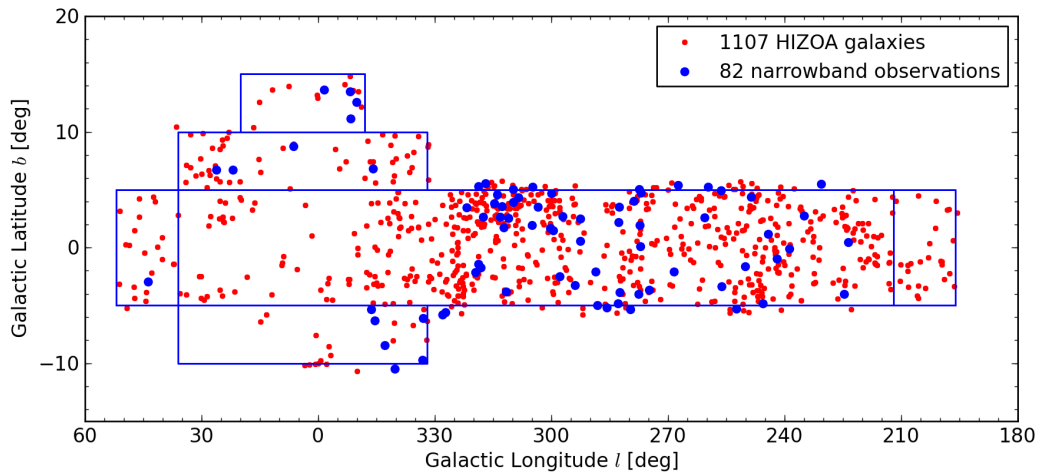


Figure 3.1: Distribution of narrowband HI observations of HIZOA galaxies, plotted in Galactic coordinates. HIZOA galaxies with $v \leq 6000 \text{ km s}^{-1}$ are plotted in small red points, the positions of the 82 new narrowband observations are shown in large blue points.

Data Reduction

The data were bandpass-corrected, calibrated and Doppler-corrected using LIVEDATA, a component of the Astronomical Image Processing System (AIPS++; Barnes et al. 2001). The calibrated and processed spectra were imaged using the GRIDZILLA component of AIPS++ (Barnes et al. 2001), using the WGTMED statistic. The extent of all sources is less than $15\farcs5$, the angular resolution of the gridded data. The sources can therefore be treated as point sources and the final spectrum is extracted from the entire “cube”.

There are two main causes of baseline ripples in the spectra: *ringing* due to strong Galactic H_I emission and continuum emission across the $20 - 22$ cm from Galactic sources (Barnes et al. 2001). Ripples caused by spectral ringing decay roughly as $1/n$, where n is the

*The choice of configuration was initially made based on the trade-off between velocity resolution and S/N . However, observations showed that the narrowband correlator provided more stable baselines and the choice was made to use the narrowband correlator and bin the spectra to improve the S/N .

channel number away from the strong narrow line. These ripples are commonly suppressed by smoothing the spectrum with an appropriate kernel. The spectra were smoothed with a Hanning filter of three channels. However, in many spectra, some significant residual baseline ripples remain which cannot easily be removed. This ripple is a result of a nearby continuum source which can set up standing waves in the telescope structure depending on the location and strength of the continuum emission and geometry of the telescope.

3.2 HI Parametrisation

The HI parameters of the galaxies were determined in a way consistent with the HIZOA parameters.

The *mbspect* task in the MIRIAD package (Sault et al. 1995) was used to measure the HI spectral parameters. A low order polynomial was fit to the baseline of each spectrum. In most cases, a first or second order fit was insufficient due to the strong baseline ripples. In these cases, a higher order fit was made. Examples showing two baseline-fitted spectra are shown in Fig. 3.2. The left panel shows a profile to which a first order baseline is fit, while the right panel shows a profile with a highly variable baseline which was fit with a fourth order polynomial over a restricted velocity range of the spectrum.

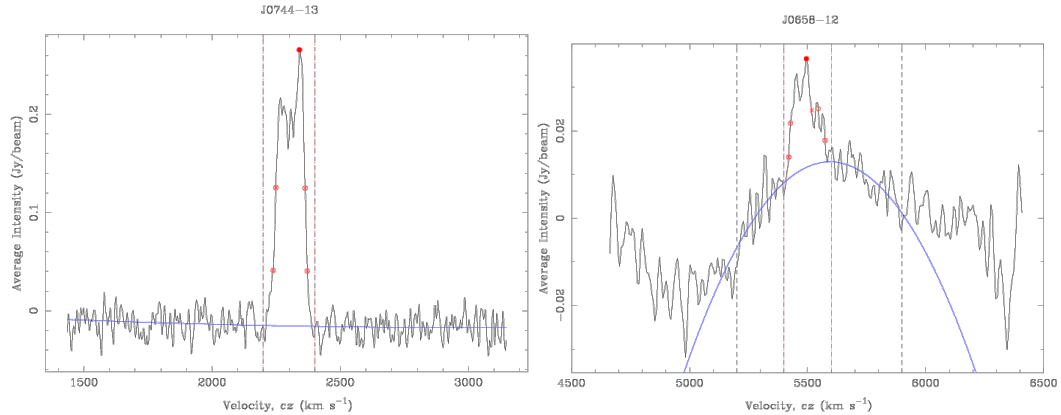


Figure 3.2: Examples of two cases of baseline fits. The (inner) vertical lines in the plots demarcate the HI profile which is masked from the baseline fit. Outer vertical lines show the velocity range within which the baseline was fit. The *left* panel shows a profile to which a first order baseline is fit. The *right* panel shows a profile with a highly variable baseline which was fit with a fourth order polynomial over a restricted velocity range of the spectrum.

The peak flux density (S_{peak}) above the baseline and the integrated flux (I_{HI} , robust moment 0) were determined with *mbspect*. The 20% and 50% velocity widths (w_{20} and w_{50} respectively) were usually taken to be the maximum fits returned by *mbspect*. The heliocentric velocity (v_{hel} , in the optical convention) was taken to be the centre point of the 20% velocity width. The HI mass was calculated from Eq. 2.2.

3.2.1 Results

The final parameters for all observed galaxies are given in Table 3.1, including the observation and the baseline fit parameters. The resulting H_I profiles for all galaxies are given in Fig. 3.3. The spectra show the fitted baseline; the velocity regions inside the inner two vertical lines (H_I profile) and outside the outer two vertical lines (where applicable) were disregarded in the baseline fit. The peak H_I flux is marked with a filled circle. The w_{20} and w_{50} velocity widths are shown with open circles (maximum fit) and crosses (minimum fit).

Uncertainties

Uncertainties on the H_I parameters were calculated according to Koribalski et al. (2004). The uncertainty in the peak flux density, $\sigma(S_{peak})$ is dominated by the rms noise in the spectrum and, additionally, increases with peak flux density. We take

$$\sigma(S_{peak})^2 = \text{rms}^2 + (0.05S_{peak})^2. \quad (3.1)$$

We adopt

$$\sigma(I_{HI}) = 4 \left(\frac{S_{peak}}{\sigma(S_{peak})} \right)^{-1} (S_{peak} I_{HI} \Delta v)^{1/2}, \quad (3.2)$$

where Δv is the velocity resolution of the spectrum, for the uncertainty in the integrated flux. The uncertainty in the systemic velocity is given by

$$\sigma(v_{sys}) = 3 \left(\frac{S_{peak}}{\sigma(S_{peak})} \right)^{-1} (P \Delta v)^{1/2}, \quad (3.3)$$

where $P = 0.5(w_{20} - w_{50})$ measures the steepness of the profile edges. Finally, the uncertainties in the 50% and 20% linewidths are

$$\sigma(w_{50}) = 2\sigma(v_{sys}), \text{ and} \quad (3.4)$$

$$\sigma(w_{20}) = 3\sigma(v_{sys}), \quad (3.5)$$

respectively. Finally, the error on the H_I mass is calculated by propagating the errors on the integrated flux and systemic velocity. From Eqs. 2.2 and 2.1, we have

$$\log M_{HI} = 5.372 - 2 \log H_0 + 2 \log v_{LG} + \log I_{HI}, \quad (3.6)$$

where the velocity has been transformed to the Local Group frame ($v_{LG} = v_{sys} + 300 \sin l \cos b$). The error is then given by

$$\sigma(\log M_{HI}) = \left[\left(\frac{2}{\ln 10} \right)^2 \left(\frac{\sigma(v_{sys})}{v_{LG}} \right)^2 + \left(\frac{1}{\ln 10} \right)^2 \left(\frac{\sigma(I_{HI})}{I_{HI}} \right)^2 \right]^{1/2}. \quad (3.7)$$

The dominant term is the uncertainty in the integrated flux, $\sigma(I_{HI})$ and errors in the transformation between the heliocentric and Local Group frames are negligible. Uncertainties in the distances due to peculiar velocities have been ignored.

Table 3.1: H α properties.

Name	v_{hel} [km s $^{-1}$]	w_{50} [km s $^{-1}$]	w_{20} [km s $^{-1}$]	S_{peak} [mJy beam $^{-1}$]	I_{HI} [Jy km s $^{-1}$]	$\log M_{HI}^*$ M_\odot	bin size †	rms [mJy]	order ‡
J0658-12	5497 ± 4	117 ± 9	154 ± 13	25 ± 1	2.3 ± 0.3	9.43 ± 0.14	4	3.3	2
J0712-09	2441 ± 2	97 ± 4	143 ± 6	60 ± 3	5.4 ± 0.3	9.03 ± 0.06	4	3.1	5
J0736-18	4349 ± 9	413 ± 17	520 ± 26	59 ± 3	17.2 ± 1.6	10.08 ± 0.09	2	4.5	2
J0737-31	2240 ± 6	127 ± 12	212 ± 18	65 ± 3	7 ± 0.8	9.07 ± 0.12	1	5.5	1
J0740-22	3049 ± 6	138 ± 12	186 ± 18	65 ± 3	8.1 ± 1.2	9.42 ± 0.15	1	7.5	3
J0743-18	3337 ± 3	172 ± 6	201 ± 9	56 ± 3	7.1 ± 0.7	9.5 ± 0.1	1	4.2	2
J0744-13	2305 ± 1	114 ± 1	133 ± 2	282 ± 14	27.6 ± 0.7	9.7 ± 0.03	2	10.4	2
J0744-26	2736 ± 2	278 ± 5	313 ± 7	53 ± 3	10.6 ± 0.6	9.45 ± 0.06	4	4.1	2
J0751-37	2806 ± 1	83 ± 1	100 ± 2	188 ± 9	14.5 ± 0.5	9.59 ± 0.04	2	8.4	2
J0757-26	952 ± 2	80 ± 4	99 ± 6	50 ± 3	3.6 ± 0.4	7.88 ± 0.1	4	4.3	5
J0801-33	1901 ± 3	177 ± 6	198 ± 9	58 ± 3	8.3 ± 0.9	8.99 ± 0.1	4	7	1
J0810-39	1421 ± 2	123 ± 4	149 ± 6	71 ± 4	6.3 ± 0.5	8.53 ± 0.08	1	3.8	2
J0820-28	4240 ± 2	222 ± 5	239 ± 7	54 ± 3	8 ± 0.7	9.71 ± 0.09	4	6	3
J0844-34	2167 ± 6	295 ± 12	350 ± 18	31 ± 2	8.6 ± 0.8	9.14 ± 0.09	8	3.2	3
J0848-39	1831 ± 1	171 ± 2	185 ± 3	100 ± 5	12.8 ± 0.6	9.11 ± 0.04	2	7	1
J0856-37	2500 ± 2	250 ± 4	271 ± 5	73 ± 4	13.6 ± 0.7	9.44 ± 0.05	4	5.2	1
J0856-48	2666 ± 3	268 ± 6	286 ± 10	48 ± 2	6.9 ± 0.8	9.25 ± 0.12	4	6.7	2
J0858-45A	2713 ± 6	450 ± 11	510 ± 17	58 ± 3	18.1 ± 1.4	9.69 ± 0.08	4	7.6	3
J0916-54B	4105 ± 5	188 ± 10	339 ± 14	91 ± 5	16.3 ± 0.9	10 ± 0.05	4	6.5	1
J0923-42	2979 ± 2	137 ± 4	155 ± 5	48 ± 2	5.1 ± 0.4	9.19 ± 0.08	4	3.8	5
J0928-56	4572 ± 3	188 ± 6	217 ± 9	48 ± 2	7.8 ± 0.6	9.79 ± 0.08	4	4.7	1
J0933-58	4450 ± 6	147 ± 13	208 ± 19	57 ± 3	6.5 ± 0.9	9.67 ± 0.14	4	8.5	3
J0944-53	5726 ± 12	163 ± 24	245 ± 35	31 ± 2	3.8 ± 0.8	9.68 ± 0.22	2	3.7	2
J0953-51	2754 ± 2	53 ± 4	75 ± 5	52 ± 3	2.3 ± 0.3	8.82 ± 0.11	2	5.2	1
J0955-60	3295 ± 2	253 ± 4	268 ± 6	48 ± 2	10 ± 0.7	9.61 ± 0.07	4	4.5	2
J0956-59	3417 ± 2	252 ± 5	288 ± 7	82 ± 4	11.5 ± 0.8	9.68 ± 0.07	1	4.4	1
J1003-49	2410 ± 1	105 ± 1	118 ± 2	109 ± 5	8.6 ± 0.3	9.21 ± 0.04	2	5.2	2
J1006-49	2402 ± 1	125 ± 2	143 ± 3	105 ± 5	8.9 ± 0.4	9.28 ± 0.05	2	6.1	3
J1009-51	2818 ± 4	146 ± 7	175 ± 11	32 ± 2	3.5 ± 0.4	8.99 ± 0.12	4	3.9	2

Continued on Next Page...

Table 3.1 – Continued

Name	v_{hel} [km s $^{-1}$]	w_{50} [km s $^{-1}$]	w_{20} [km s $^{-1}$]	S_{peak} [mJy beam $^{-1}$]	I_{HI} [Jy km s $^{-1}$]	$\log M_{HI}^*$ M_\odot	bin size †	rms [mJy]	order ‡
J1012-62	3450 ± 5	207 ± 10	335 ± 15	87 ± 4	12.6 ± 0.9	9.72 ± 0.07	4	7.1	3
J1024-54	1079 ± 1	135 ± 2	156 ± 4	143 ± 7	16.5 ± 0.7	8.63 ± 0.04	2	9.5	1
J1028-53	2721 ± 3	81 ± 5	122 ± 8	54 ± 3	3.6 ± 0.3	9.05 ± 0.09	2	5.5	2
J1031-63	3760 ± 4	316 ± 7	350 ± 11	66 ± 3	11.8 ± 1.1	9.78 ± 0.09	4	7.7	3
J1047-61	4461 ± 2	167 ± 5	178 ± 7	41 ± 2	6 ± 0.7	9.65 ± 0.11	4	5.3	2
J1059-66	1846 ± 3	147 ± 6	331 ± 9	248 ± 12	33.1 ± 1.1	9.54 ± 0.03	1	6.8	1
J1125-60	4566 ± 5	168 ± 10	251 ± 15	41 ± 2	6.1 ± 0.5	9.68 ± 0.09	4	4.2	3
J1126-64	5898 ± 4	172 ± 8	208 ± 12	41 ± 2	5.7 ± 0.6	9.88 ± 0.1	4	4.9	1
J1130-58	1842 ± 1	149 ± 2	163 ± 3	154 ± 8	18 ± 0.8	9.26 ± 0.04	2	10.1	1
J1149-64	2082 ± 1	291 ± 1	327 ± 2	383 ± 19	73.9 ± 1.1	9.99 ± 0.02	2	11	1
J1203-64	5519 ± 3	352 ± 6	373 ± 9	58 ± 3	10.3 ± 1	10.07 ± 0.1	2	3.6	1
J1204-59B	5726 ± 5	185 ± 9	203 ± 14	32 ± 2	4.2 ± 0.8	9.73 ± 0.18	4	6.4	1
J1223-61	3845 ± 4	163 ± 8	221 ± 12	68 ± 3	9.8 ± 0.8	9.72 ± 0.08	4	6.4	1
J1229-58	5651 ± 2	293 ± 4	307 ± 7	56 ± 3	9.3 ± 0.8	10.07 ± 0.09	4	6	3
J1229-61	5387 ± 2	328 ± 4	340 ± 6	67 ± 3	10.6 ± 0.9	10.06 ± 0.08	4	6.7	2
J1255-59	2296 ± 3	162 ± 6	190 ± 9	65 ± 3	9.4 ± 0.8	9.19 ± 0.09	4	6.7	1
J1305-57	5908 ± 2	195 ± 3	252 ± 5	81 ± 4	12.7 ± 0.4	10.23 ± 0.03	4	3	3
J1308-60	1621 ± 3	179 ± 5	222 ± 8	82 ± 4	12.4 ± 0.8	8.99 ± 0.06	2	8.5	2
J1332-58	1473 ± 1	104 ± 1	120 ± 2	190 ± 10	16.2 ± 0.5	8.98 ± 0.03	2	7.8	1
J1342-57	3727 ± 4	182 ± 7	208 ± 11	32 ± 2	3.2 ± 0.4	9.23 ± 0.13	4	4.2	4
J1344-58	5430 ± 3	240 ± 6	280 ± 9	58 ± 3	10.2 ± 0.7	10.05 ± 0.07	4	4.9	4
J1355-59A	5495 ± 2	329 ± 5	359 ± 7	48 ± 2	8.7 ± 0.5	9.99 ± 0.06	4	3.9	2
J1406-57	5551 ± 2	293 ± 5	313 ± 7	54 ± 3	11.3 ± 0.8	10.12 ± 0.07	4	5.2	2
J1406-59	3804 ± 3	189 ± 7	214 ± 10	59 ± 3	9.6 ± 0.9	9.73 ± 0.1	4	7.2	2
J1411-58	5260 ± 2	81 ± 4	100 ± 6	60 ± 3	3.9 ± 0.4	9.61 ± 0.11	2	7.1	1
J1412-56A	3769 ± 2	276 ± 4	292 ± 6	47 ± 2	8.1 ± 0.6	9.67 ± 0.08	4	4.6	3
J1416-65	2859 ± 2	337 ± 5	359 ± 7	50 ± 3	11.9 ± 0.7	9.59 ± 0.06	4	4.4	2
J1419-57	3849 ± 4	167 ± 7	205 ± 11	62 ± 3	7.7 ± 0.7	9.61 ± 0.1	4	6.5	2
J1429-54	3018 ± 1	122 ± 2	134 ± 3	160 ± 8	15.8 ± 0.8	9.69 ± 0.05	2	11.1	4

Continued on Next Page...

Table 3.1 – Continued

Name	v_{hel} [km s ⁻¹]	w_{50} [km s ⁻¹]	w_{20} [km s ⁻¹]	S_{peak} [mJy beam ⁻¹]	I_{HI} [Jy km s ⁻¹]	$\log M_{HI}^*$ M_{\odot}	bin size [†]	rms [mJy]	order [‡]
J1441-57	3384±2	151±4	165±6	49±2	5.6±0.5	9.43±0.09	4	4.7	5
J1442-54	2778±2	185±4	205±6	42±2	6.5±0.4	9.24±0.07	4	3.4	3
J1501-60	4436±1	124±3	153±4	211±11	23.1±1.1	10.24±0.05	2	14	1
J1504-60	4733±2	104±3	117±5	73±4	5.8±0.5	9.68±0.09	4	5.8	1
J1506-54	2938±1	135±2	152±3	155±8	13.1±0.7	9.59±0.05	2	10.1	3
J1512-60	5162±3	134±7	153±10	50±3	4.7±0.7	9.68±0.15	4	7	1
J1617-38	2767±2	240±4	261±6	82±4	15.5±0.9	9.63±0.06	4	6.2	2
J1621-53	4853±4	262±7	329±11	77±4	14.5±0.9	10.1±0.06	4	6.2	2
J1621-58	1404±1	73±1	92±2	292±15	19.6±0.7	9.03±0.04	1	16.4	1
J1632-29B	4820±2	276±3	310±5	84±4	16±0.7	10.14±0.04	4	4.6	-5
J1634-27	4226±3	88±7	113±10	52±3	3.7±0.5	9.39±0.14	4	6.2	2
J1639-36	1817±4	158±7	172±11	33±2	3±0.6	8.5±0.19	4	5.8	3
J1642-29	2596±1	155±3	187±4	72±4	8.3±0.4	9.31±0.05	2	4.8	3
J1648-54	4656±2	253±4	307±6	65±3	12.9±0.5	10.02±0.04	4	3.5	3
J1651-22	5853±2	119±3	136±5	66±3	6.3±0.5	9.92±0.08	4	4.8	3
J1708-56	4692±4	114±8	150±11	56±3	6±0.7	9.69±0.12	4	6.6	3
J1727-18B	4179±3	192±7	214±10	48±2	7.7±0.8	9.7±0.1	4	6.1	3
J1732-43	2539±4	111±7	224±11	134±7	13.6±0.9	9.55±0.06	4	8.2	1
J1734-44	5825±3	219±6	243±9	49±2	5.8±0.6	9.88±0.1	4	5.2	2
J1736-47	5878±2	328±4	356±6	69±3	15±0.7	10.3±0.05	4	4.9	3
J1739-51	3810±1	133±3	152±4	92±5	10±0.6	9.73±0.06	2	7.4	3
J1807-06	3298±2	113±4	126±6	59±3	5.6±0.6	9.35±0.1	4	5.8	5
J1815-02	1786±2	308±5	319±7	52±3	8±0.9	9.03±0.11	4	6.7	5
J1921+08	3111±2	146±4	166±5	91±5	9.6±0.7	9.51±0.07	4	6.6	5

NOTES:

*The quoted error on $\log M_{HI}$ is the formal error.

†Bin size is the number of channels that were binned to improve the S/N.

‡Polynomial order of the baseline fit.

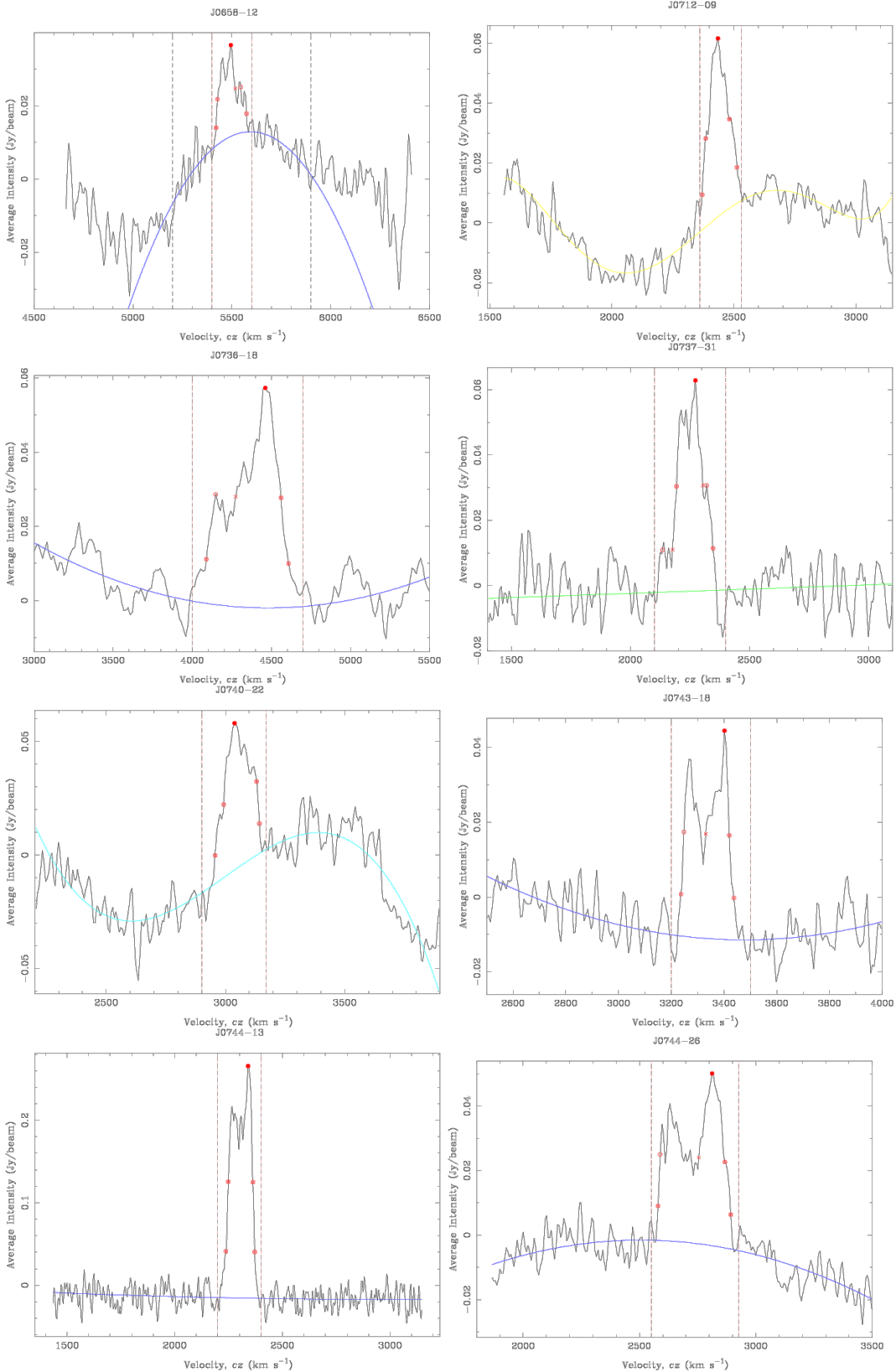


Figure 3.3: New HI spectra obtained for 82 galaxies. The fitted baseline is shown and the peak Hiflux is marked with a filled circle. The w_{20} and w_{50} velocity widths are shown with open circles (maximum fit) and crosses (minimum fit). The velocity regions between the inner two vertical lines and outside the outer two vertical lines (where applicable) were disregarded in the baseline fit. Spectra follow the order in Table 3.1.

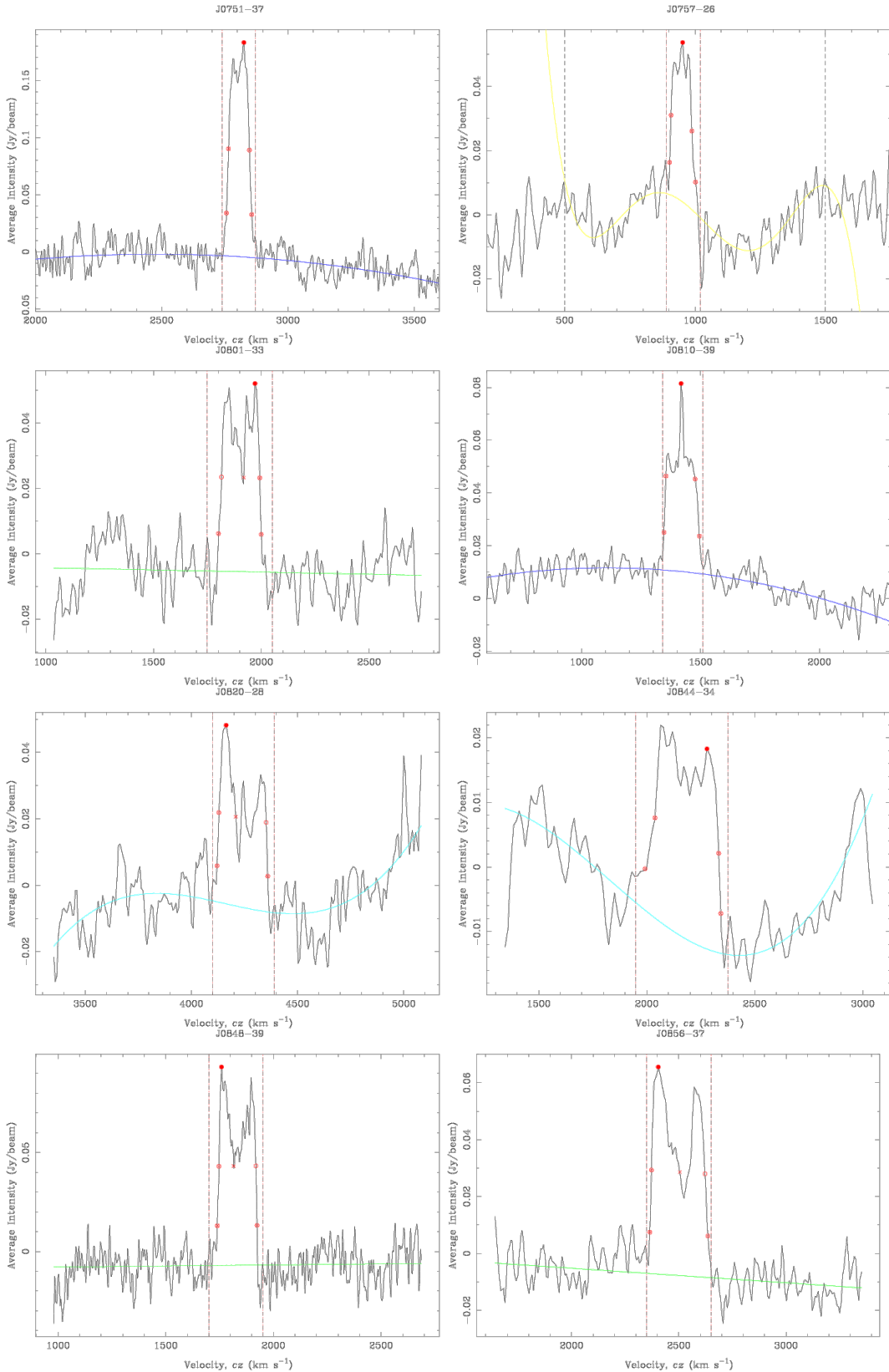


Figure 3.3: Continued

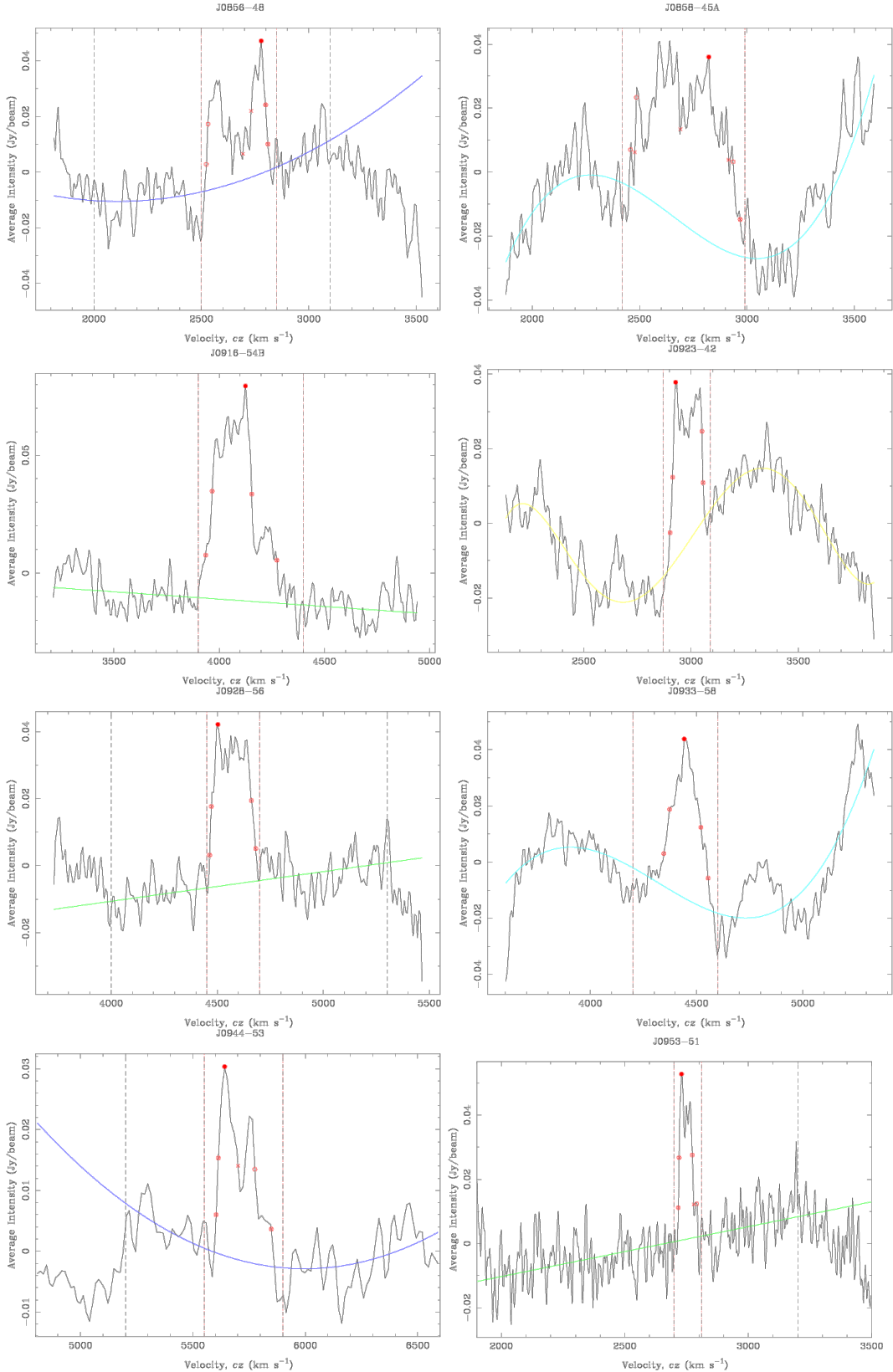


Figure 3.3: Continued

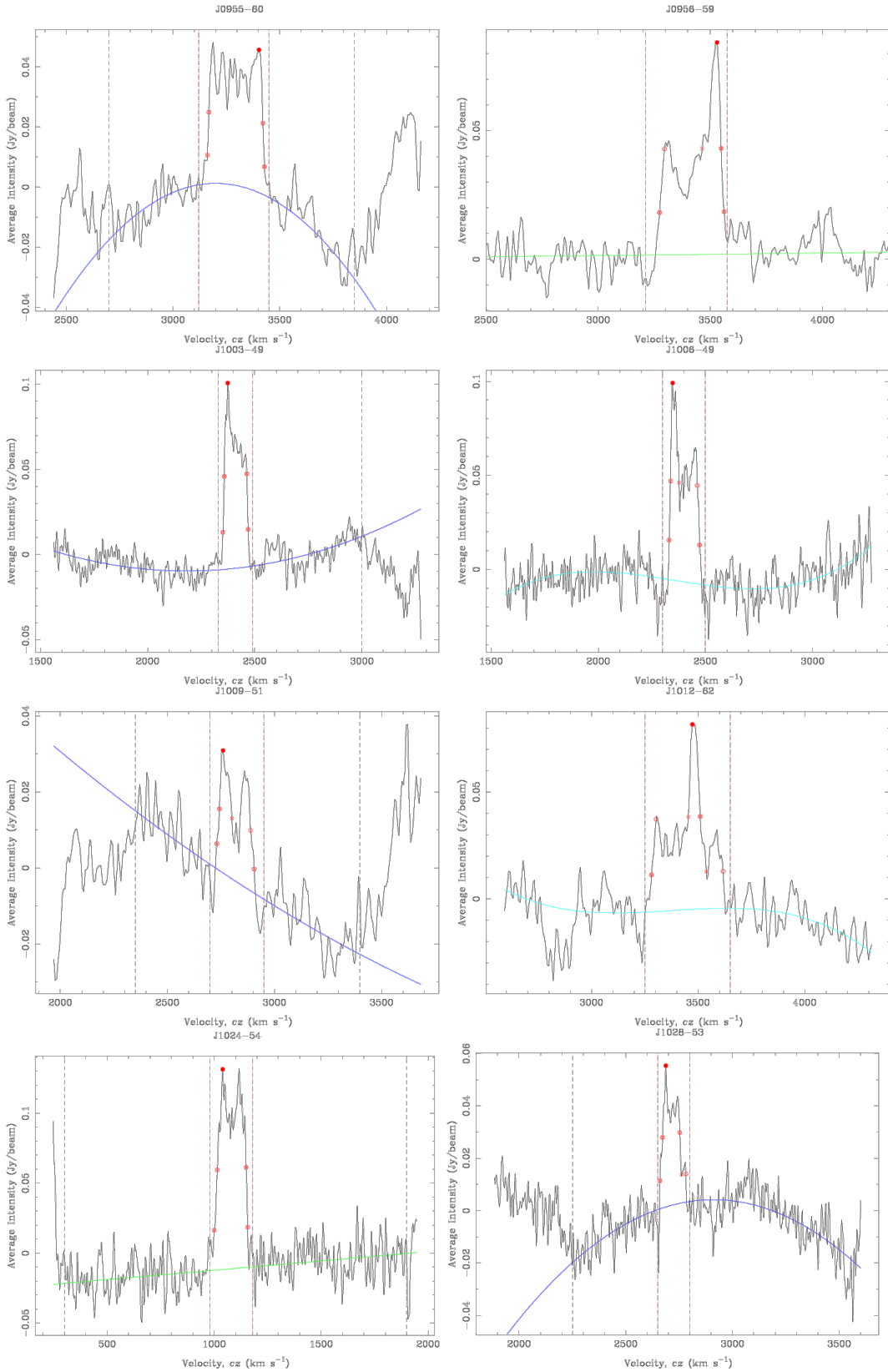


Figure 3.3: Continued

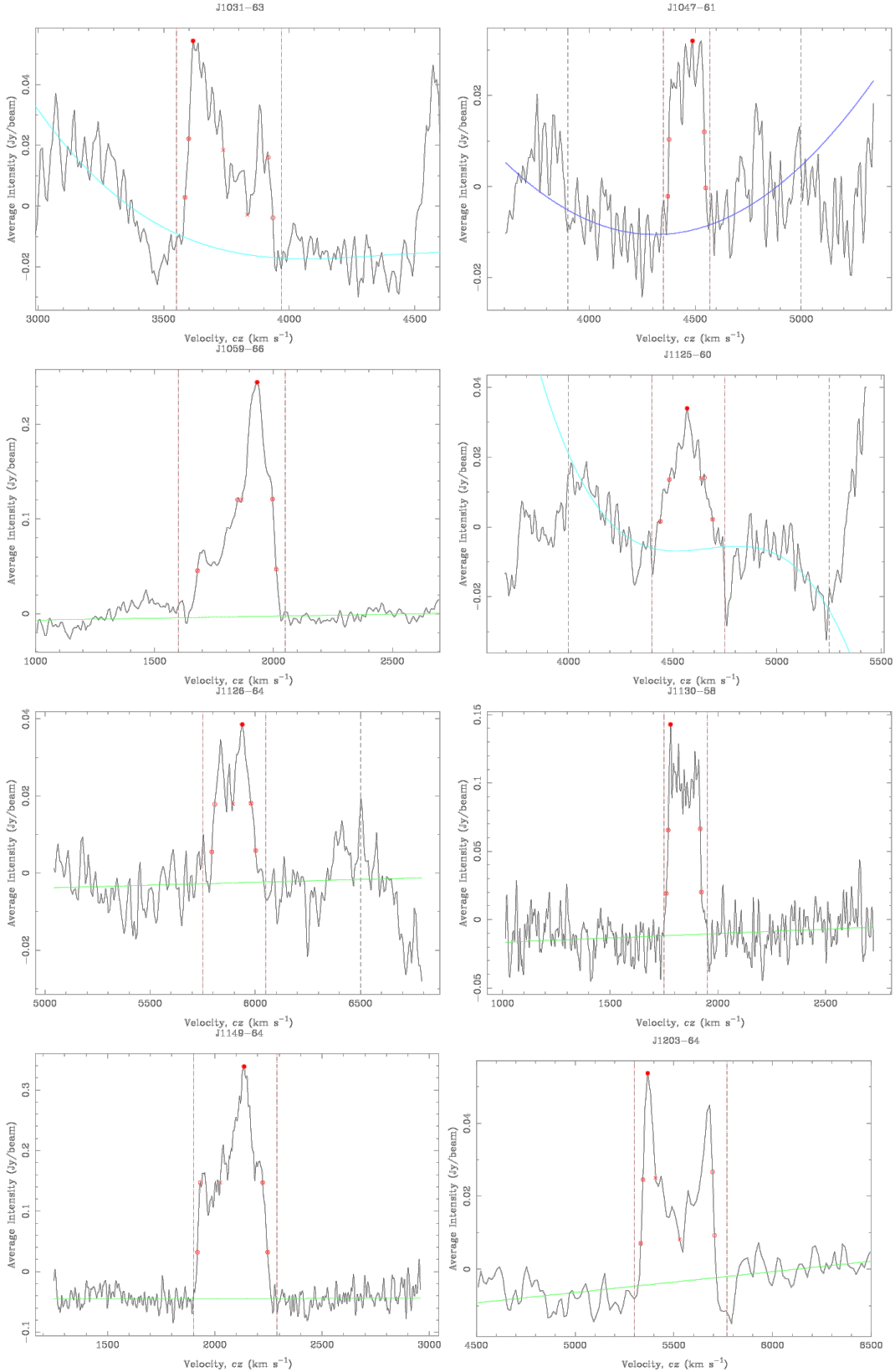


Figure 3.3: Continued

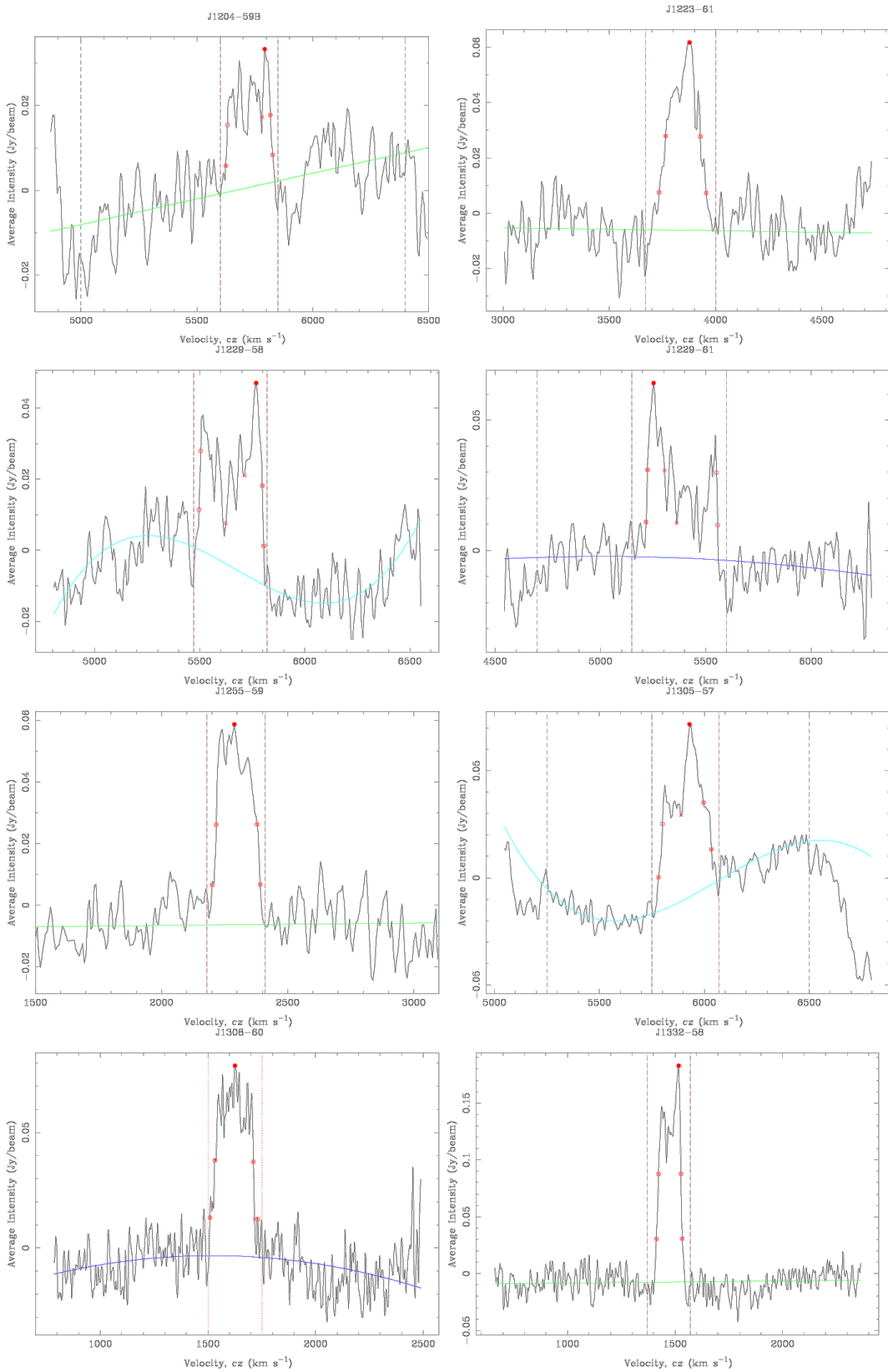


Figure 3.3: Continued

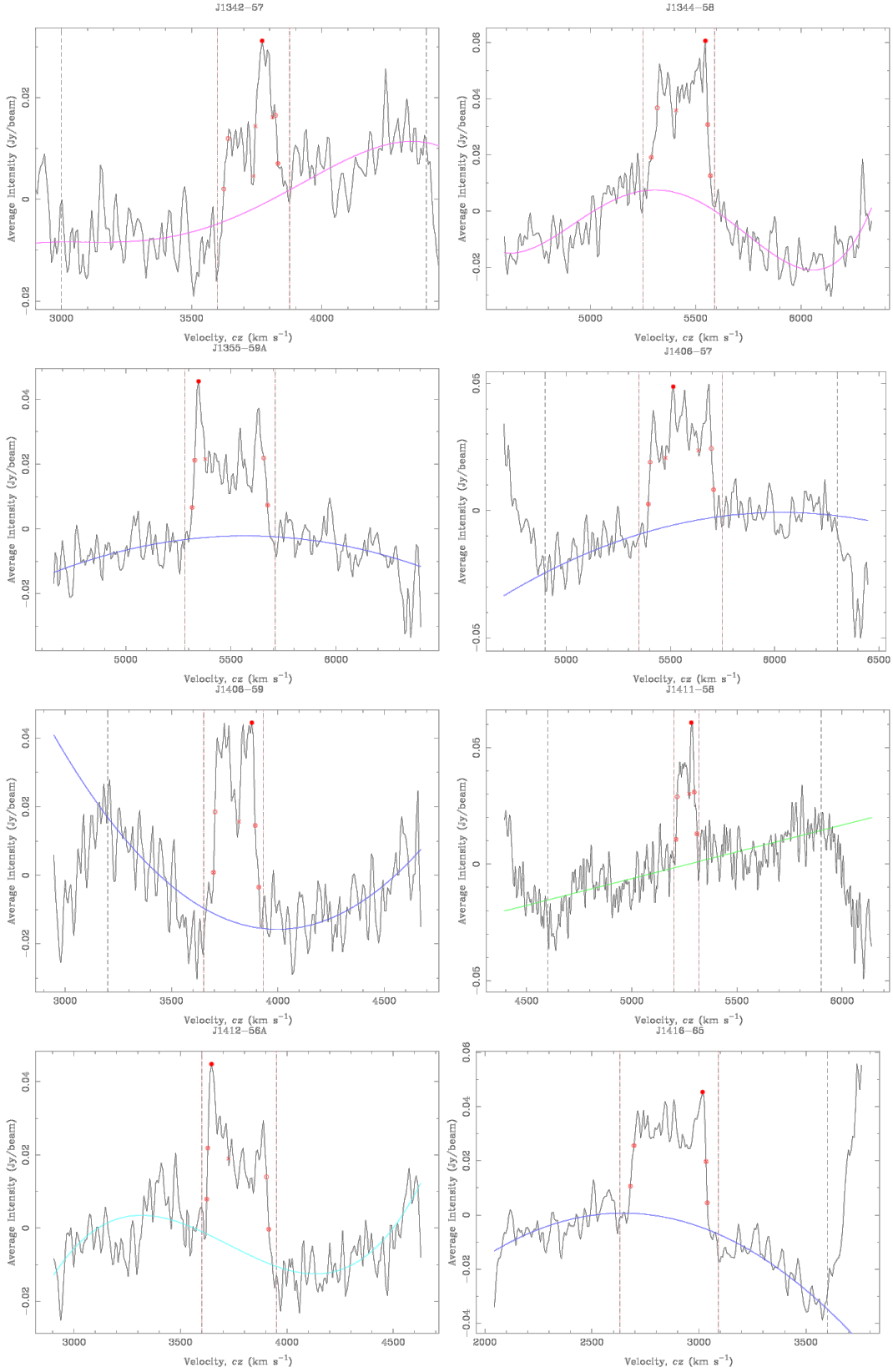


Figure 3.3: Continued

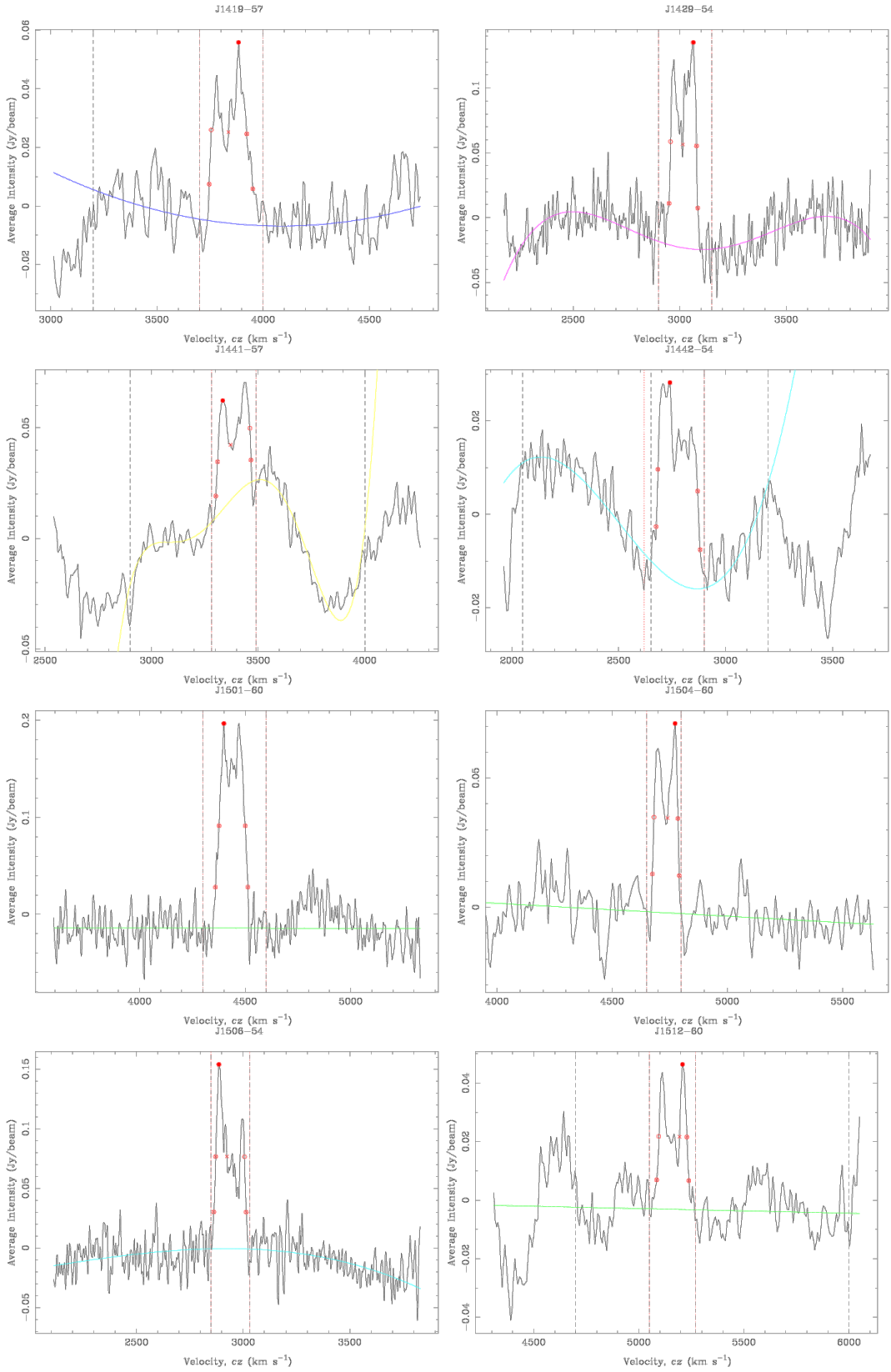


Figure 3.3: Continued

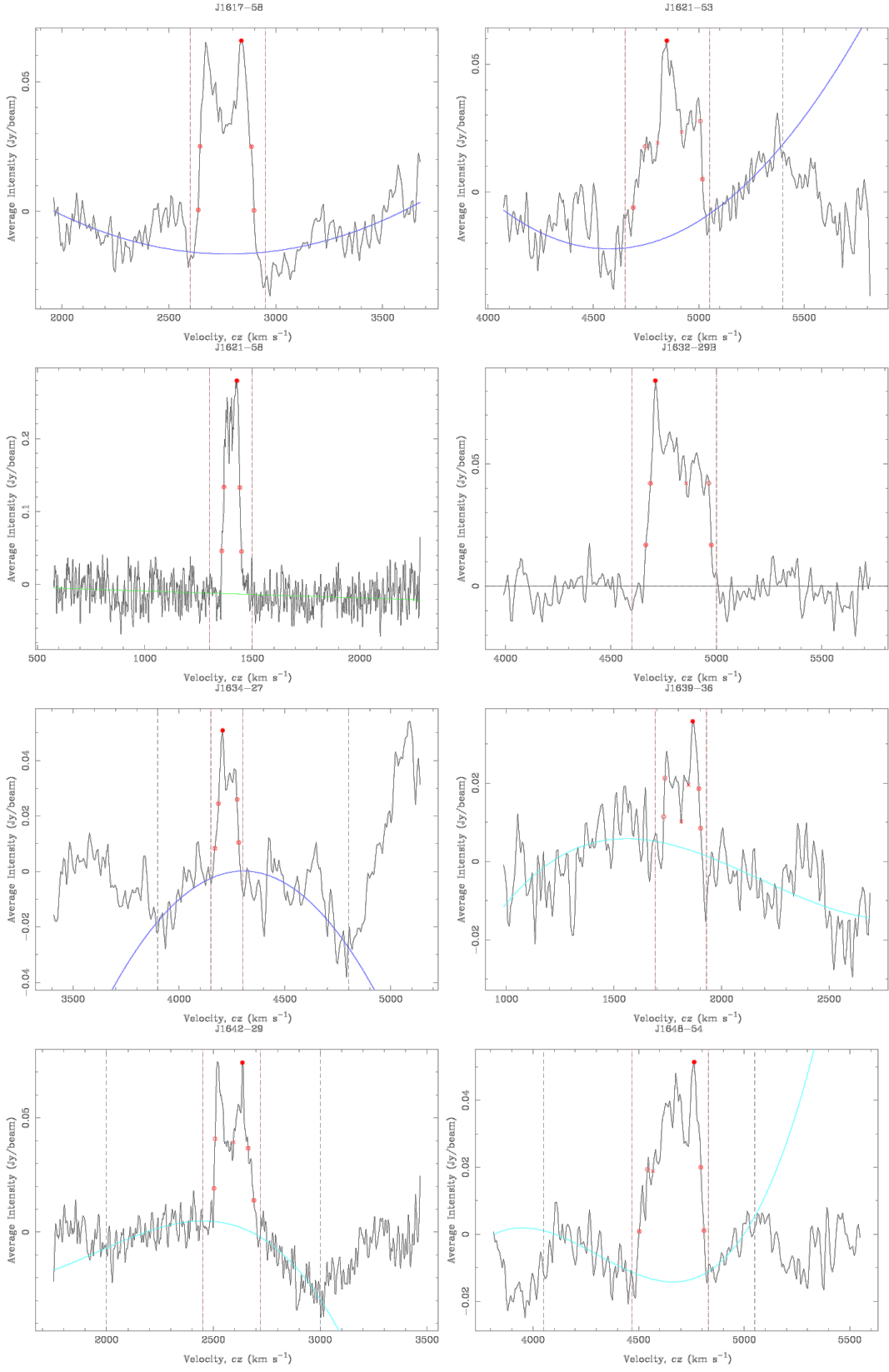


Figure 3.3: Continued

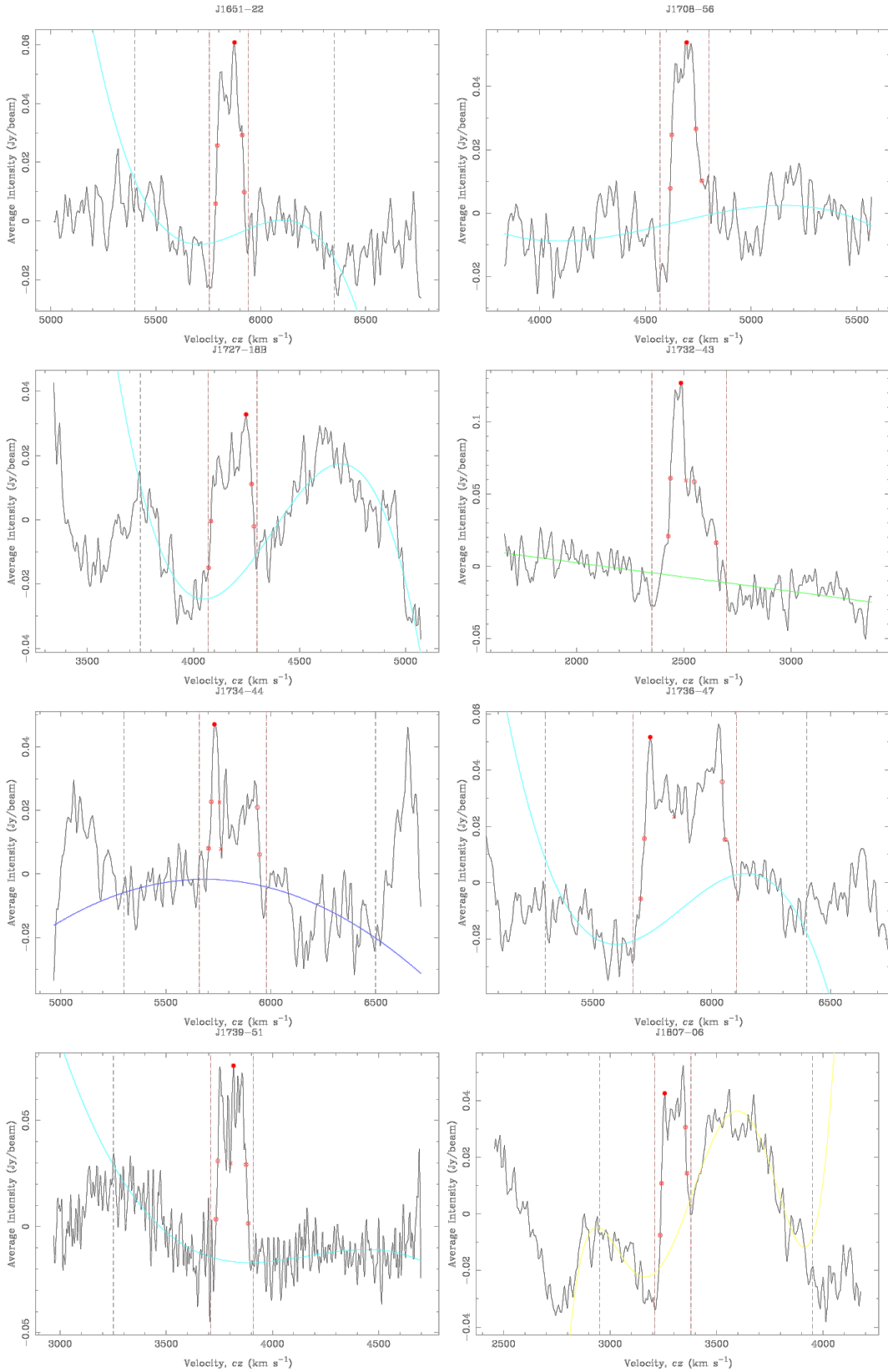


Figure 3.3: Continued

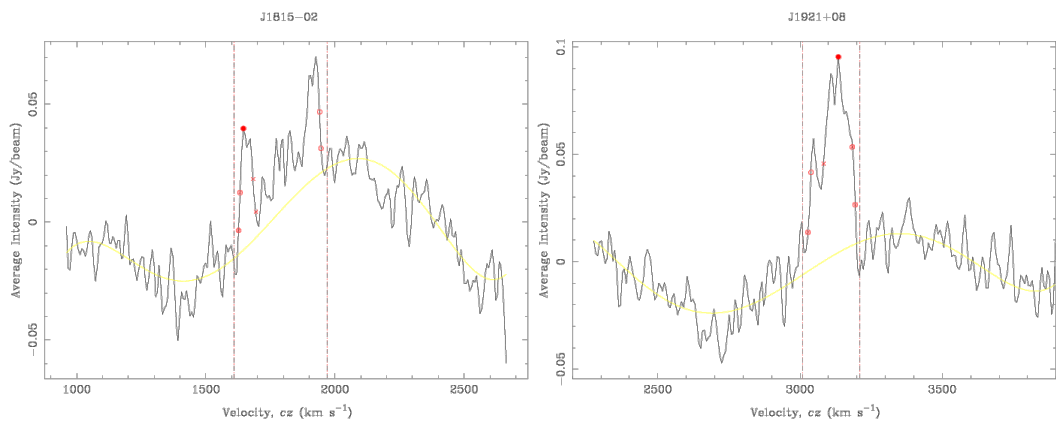


Figure 3.3: Continued

3.3 Comparison to HIZOA

At the time of this writing, the full set of HIZOA parameters were not available for all the cubes, specifically the w_{20} and w_{50} parameters. Five of the galaxies observed with the narrowband correlator do not have HIZOA w_{50} parameters. We use the remaining 77 galaxies to compare the newly derived parameters with those in HIZOA. The differences between our measured systemic velocities and the HIZOA H_I velocities given by HIZOA are plotted as a histogram in the *left* panel of Fig. 3.4. The distribution of velocity offsets has a mean of 1 km s^{-1} (shown by the vertical dotted line) and a dispersion of 14 km s^{-1} . The *right* panel of Fig. 3.4 illustrates the differences between our 50% linewidths and the HIZOA values. The mean offset is -5 km s^{-1} (shown by the vertical dotted line) with a dispersion of 13 km s^{-1} . The narrowband linewidths are marginally smaller than the HIZOA widths.

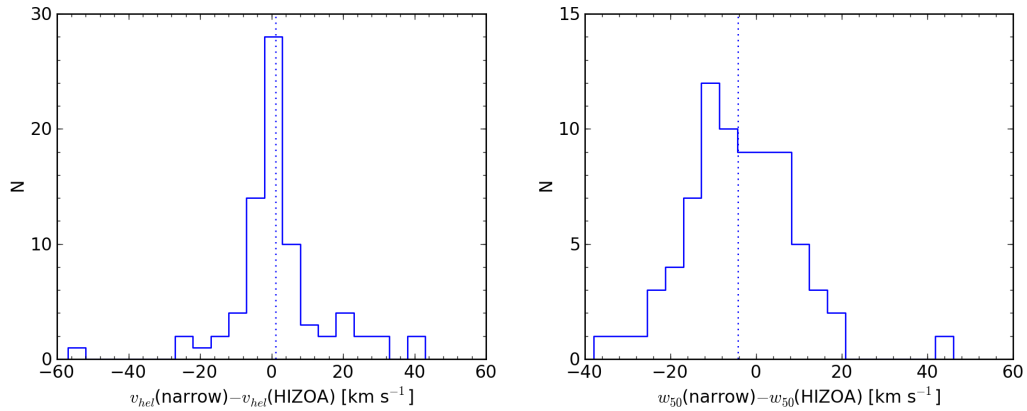


Figure 3.4: Histograms of offsets between narrowband and HIZOA systemic velocities and linewidths. The *left* panel shows the distribution of offsets between the narrowband and the HIZOA systemic velocities. The *right* panel gives the distribution of offsets between the narrowband and HIZOA 50% linewidths. In both panels the vertical dotted lines show the mean value of each distribution.

Both the 20% and 50% linewidths are needed for the computation of the uncertainty in the widths and velocities (see Sect. 3.2.1). We therefore select a sample of galaxies that have full HIZOA parameters and new narrowband observations in order to quantify the improvement in the errors of parameters obtained with the narrowband observations. For the 53 galaxies that have both w_{20} and w_{50} parameters in HIZOA we derive the errors on the systemic velocity, $\sigma(v_{sys})$, and the 50% linewidth, $\sigma(w_{50})$. Figure 3.5 shows a comparison of HIZOA and narrowband systemic velocities. Figure 3.6 shows a comparison of HIZOA and narrowband 50% linewidths. In both figures, the x -errors show the narrowband uncertainties and the y -errors are the quadrature sum of the narrowband and HIZOA uncertainties.

Figures 3.7 and 3.8 show examples of galaxies that have very large offsets between the narrowband and HIZOA parameters. These three galaxies were excluded from the previous plots. J1149-64 (Fig 3.7) has an asymmetric profile with a much weaker second peak. Our 50% width is measured at the second peak which is brighter in our profile. The HIZOA width

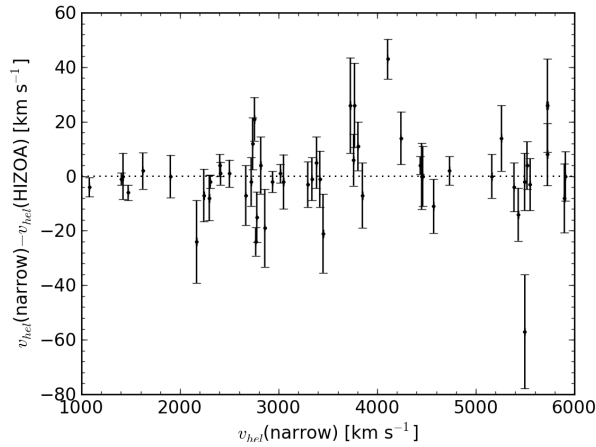


Figure 3.5: Comparison of narrowband and HIZOA systemic velocities.

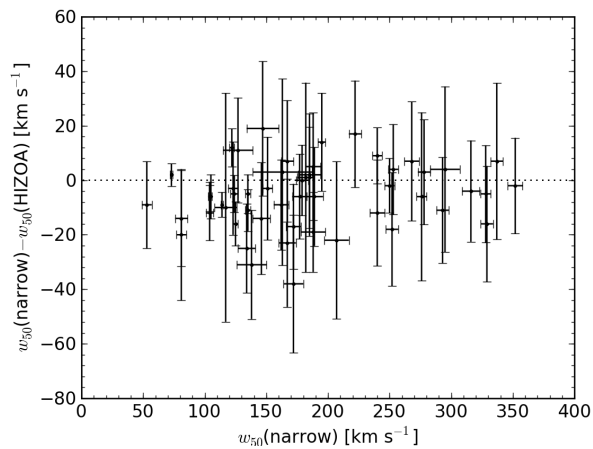


Figure 3.6: Comparison of narrowband and HIZOA 50% velocity widths.

is measured on a single peak. Figure 3.8 shows the spectra of two galaxies (J1621-53 and J0858-45A) that have very poor baselines in the narrowband observations. The baselines prevent the identification and accurate measurement of the H_I profile.

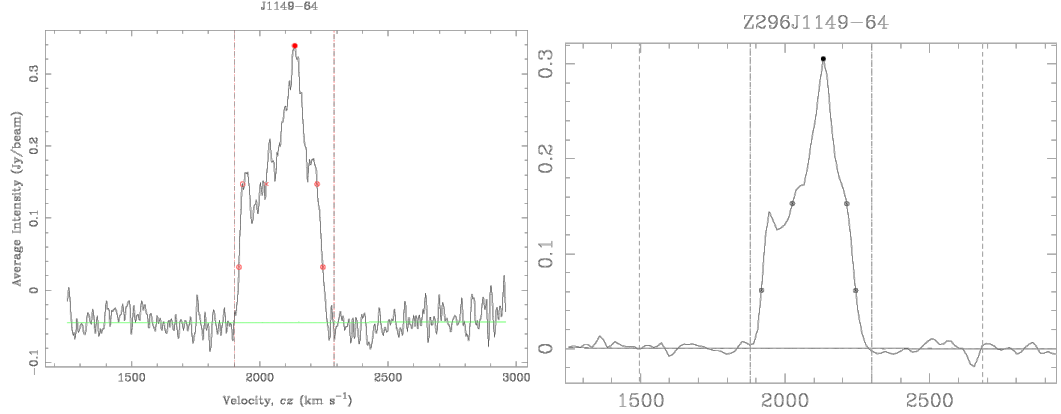


Figure 3.7: J1149-64: an asymmetric profile that is poorly fitted in HIZOA. The *left* panels show the narrowband spectrum and the *right* panels the HIZOA spectrum.

3.3.1 Improvement in Linewidth Errors

The error on the 50% linewidth is important for Tully-Fisher analysis. The improvement in the uncertainties obtained from the new observations compared to the HIZOA values is shown in Fig 3.9. The HIZOA fractional uncertainties, $\sigma(w_{50})/w_{50}$, are plotted against the narrowband fractional uncertainties. The dotted line is the line of equality and the dashed line is $y = 5x$, i.e. where the HIZOA fractional uncertainty is 5× the narrowband fractional uncertainty. The HIZOA uncertainties are clearly always much larger than the new values. Figure 3.10 shows a histogram of the ratio of $\sigma(w_{50})/w_{50}$ for HIZOA to $\sigma(w_{50})/w_{50}$ for the narrowband observations. The mean value of 3.4 is shown with a vertical dotted line.

Figure 3.11 shows the narrowband and HIZOA spectra of two galaxies (J1305-57 and J1003-49) with the best improvement over HIZOA.

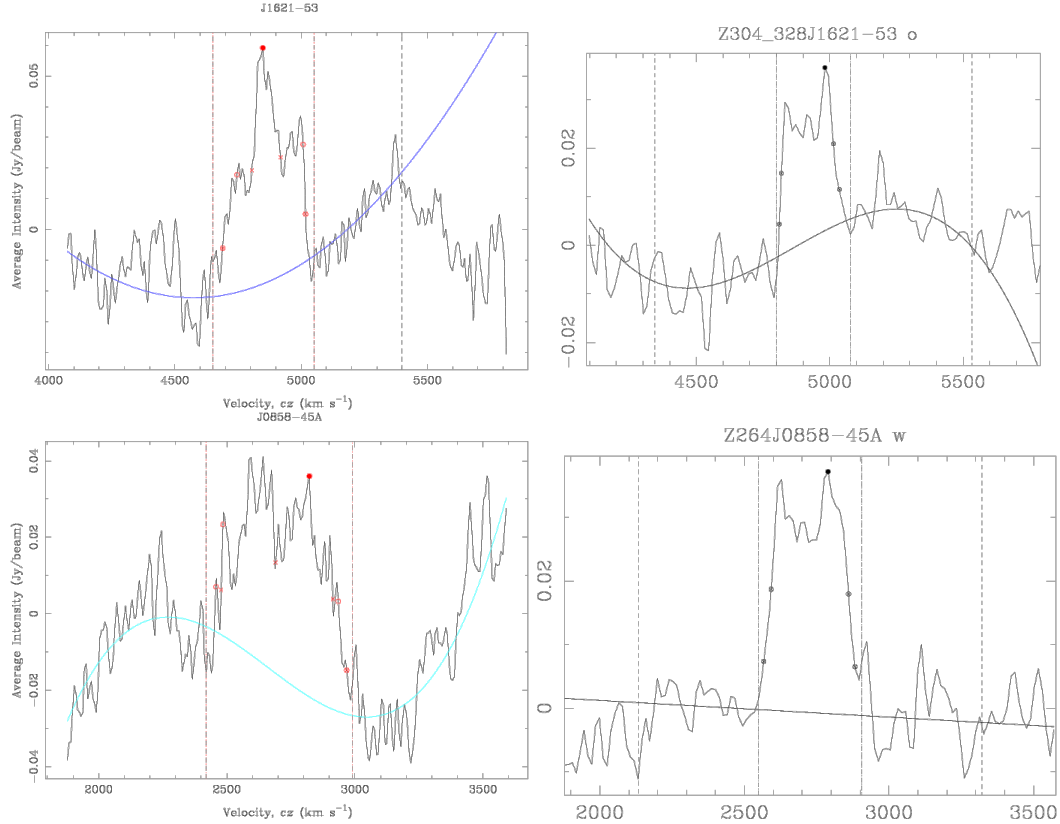


Figure 3.8: The two galaxies with very bad baselines in the narrowband spectra. The *left* panels show the narrowband spectra and the *right* panels the HIZOA spectra for J1621-53 (*top*) and J0858-45A (*bottom*).

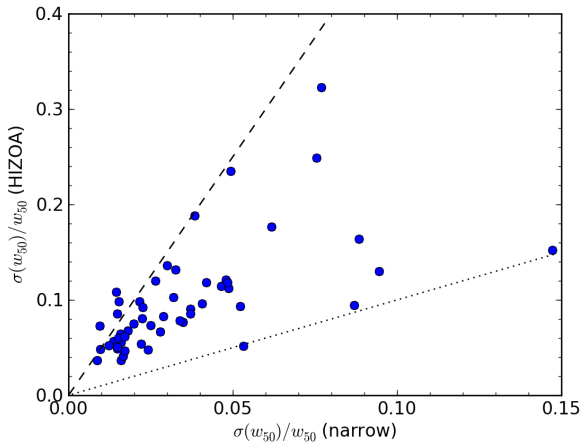


Figure 3.9: Comparison of narrowband and HIZOA 50% velocity width errors. The dotted line is the line of equality and the dashed line is $y = 5x$, i.e. where the HIZOA fractional uncertainty is 5× the narrowband fractional uncertainty.

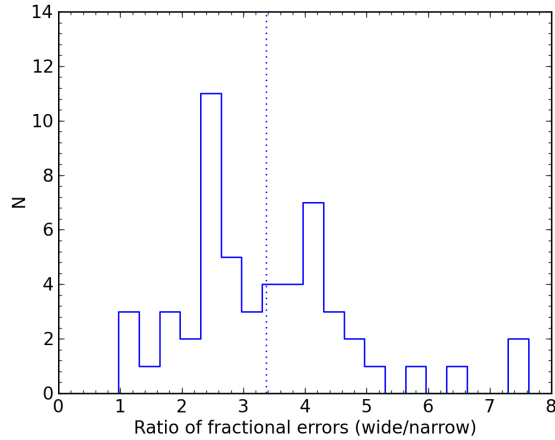


Figure 3.10: Comparison of narrowband and HIZOA 50% velocity width errors. The vertical dotted line shows the mean value of 3.4.

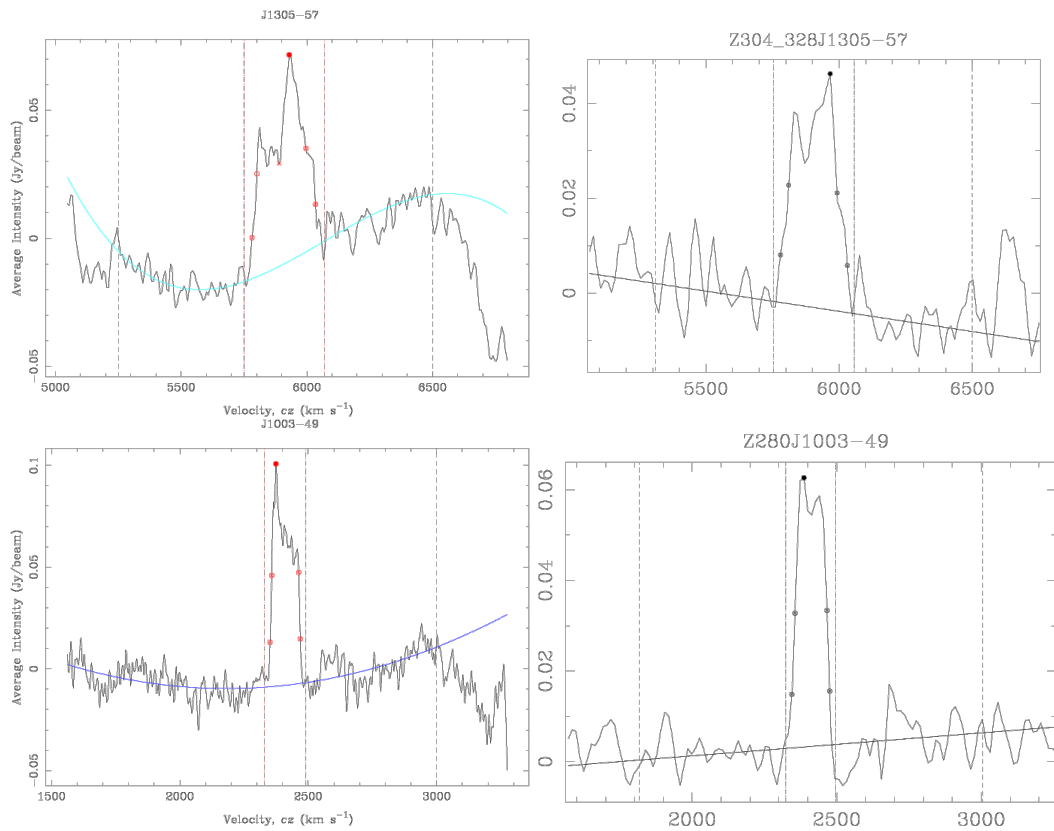


Figure 3.11: Two galaxies with very good narrowband spectra that provide improved parameters. The *left* panels show the narrowband spectra and the *right* panels the HIZOA spectra for J1305-57 (*top*) and J1003-49 (*bottom*).

Chapter 4

Near Infrared Follow-up Survey

This chapter describes the deep NIR follow-up survey of HI sources selected from the HIZOA survey. The survey was conducted under photometric conditions with the 1.4 m IRSF telescope using the SIRIUS camera for simultaneous imaging in the near infrared J , H and K_s bands. The survey images have an exposure time of 10 min resulting in a limiting magnitude approximately 2^m deeper than the 2MASS survey. The deeper images and the superior resolution of the IRSF ($0''.45 \text{ pix}^{-1}$) allow for the detection of galaxies to greater levels of Galactic extinction and stellar density.

The telescope and detector are first described, following which the reasons for their choice for a dedicated follow-up survey are given (Sect. 4.1). The details of the observations and the image reduction and calibration process are discussed in detail in Sect. 4.2.

This chapter also describes the process of identifying the most likely HI counterpart galaxies in the near infrared survey images. The detection rate and its dependence on extinction and stellar density is discussed. The routines and algorithms used to subtract foreground stars from the images are presented in detail in Sect. 4.5.

Finally, the surface photometry that was performed to extract the magnitudes is explained. The photometric parameters derived are described in Sect. 4.7.

4.1 Infrared Survey Facility

The imaging data were acquired with the Japanese InfraRed Survey Facility (IRSF), a 1.4 m Alt-Azimuth Cassegrain telescope situated at the South African Astronomical Observatory (SAAO) site in Sutherland, South Africa. The IRSF is equipped with the Simultaneous InfraRed Imager for Unbiased Surveys (SIRIUS), a detector capable of simultaneous imaging in the three near infrared atmospheric windows: J , H and K_s . The camera consists of three 1024×1024 pixel HgCdTe (HAWAII) arrays each with a gain of $5.5 e^-/\text{ADU}$ and a read-out-noise of $30e^-$ (Nagashima et al. 1999, Nagayama et al. 2003) and which are cooled to 80 K. The field-of-view of the telescope is $7\text{'}7 \times 7\text{'}7$ resulting in a pixel scale of $0''.45 \text{ pix}^{-1}$. Built for surveys, the IRSF has a speed of $f/10$, compared to that of $f/13.5$ for 2MASS.

The small pixel scale and fast speed makes the IRSF ideal for a follow-up survey of this nature.

4.1.1 Comparison of the IRSF to Contemporary Instruments

SIRIUS has a higher angular resolution than contemporary large-area NIR surveys such as 2MASS (Strutskie 2006) and DENIS (Epchtein et al. 1997). Table 4.1 gives a comparison between the IRSF/SIRIUS and 2MASS and DENIS. Also included in the table are the specifications of the forthcoming VISTA Hemisphere Survey (VHS). The Visible and Infrared Survey Telescope for Astronomy (VISTA) is 4 m class telescope currently under commissioning at Paranal (Emerson et al. 2004; 2006, Arnaboldi et al. 2007). The IRSF/SIRIUS provides improved resolution compared to current NIR surveys with large sky-coverage. It will be a few years before surveys like VISTA become available for this kind of work.

Table 4.1: Specifications of current/proposed near infrared surveys and their instruments

Telescope/ Survey	Diameter [m]	FoV [']	Filters	Pixel Scale [" pix ⁻¹]	Effective Exposure [s]
IRSF/SIRIUS	1.4	7.7 × 7.7	<i>J, H, K_s</i>	0.45	600
DENIS	1.0	12 × 12	<i>I, J, K_s</i>	3.0*	9.0
2MASS	1.3	8.5 × 8.5	<i>J, H, K_s</i>	2.0	7.8
VISTA/VHS	4.0	60 × 90	<i>J, H, K_s</i>	0.34	60

NOTES:

*DENIS pixel scale in the *I* band is 1."0 pixel⁻¹.

The higher resolution of the IRSF greatly helps in identifying and deblending foreground stars, allowing them to be removed more accurately and improving the surface photometry of galaxies. Our survey uses an effective exposure time of 10 min which results in a $\sim 1 - 2^{\text{m}}$ deeper survey depth than currently available with either 2MASS or DENIS (Riad 2010). This exposure time is long enough for the detection of fainter extragalactic objects while not so long the field is saturated with the fainter old stellar population. The VHS, which will start this year, will image $\sim 2^{\text{m}}$ fainter than our survey, but may in fact be too deep and be limited by confusion noise due to numerous faint foreground stars.

The field-of-view of the IRSF, 7.7' × 7.7', is ideally suited to this survey given the positional accuracy of the HI sources of $\sim 4'$ (Donley et al. 2005).

4.1.2 Comparison of IRSF/SIRIUS to 2MASS Imaging

A comparison of the quality of the IRSF images compared to 2MASS is shown in Fig. 4.1, which shows three-color image of a single field imaged both with the IRSF (*left*) and 2MASS (*right*). The field is centred on $l = 319^{\circ}756$, $b = 1^{\circ}226$, in a heavily extinguished ($A_V = 8^{\text{m}}51$) high star-density ($\log(N_{K_s < 14}/\text{deg}^2) = 4.74$) region. Two galaxies (denoted a and b in Fig. 4.1) that are not detected in 2MASX can be identified in the IRSF images. This clearly

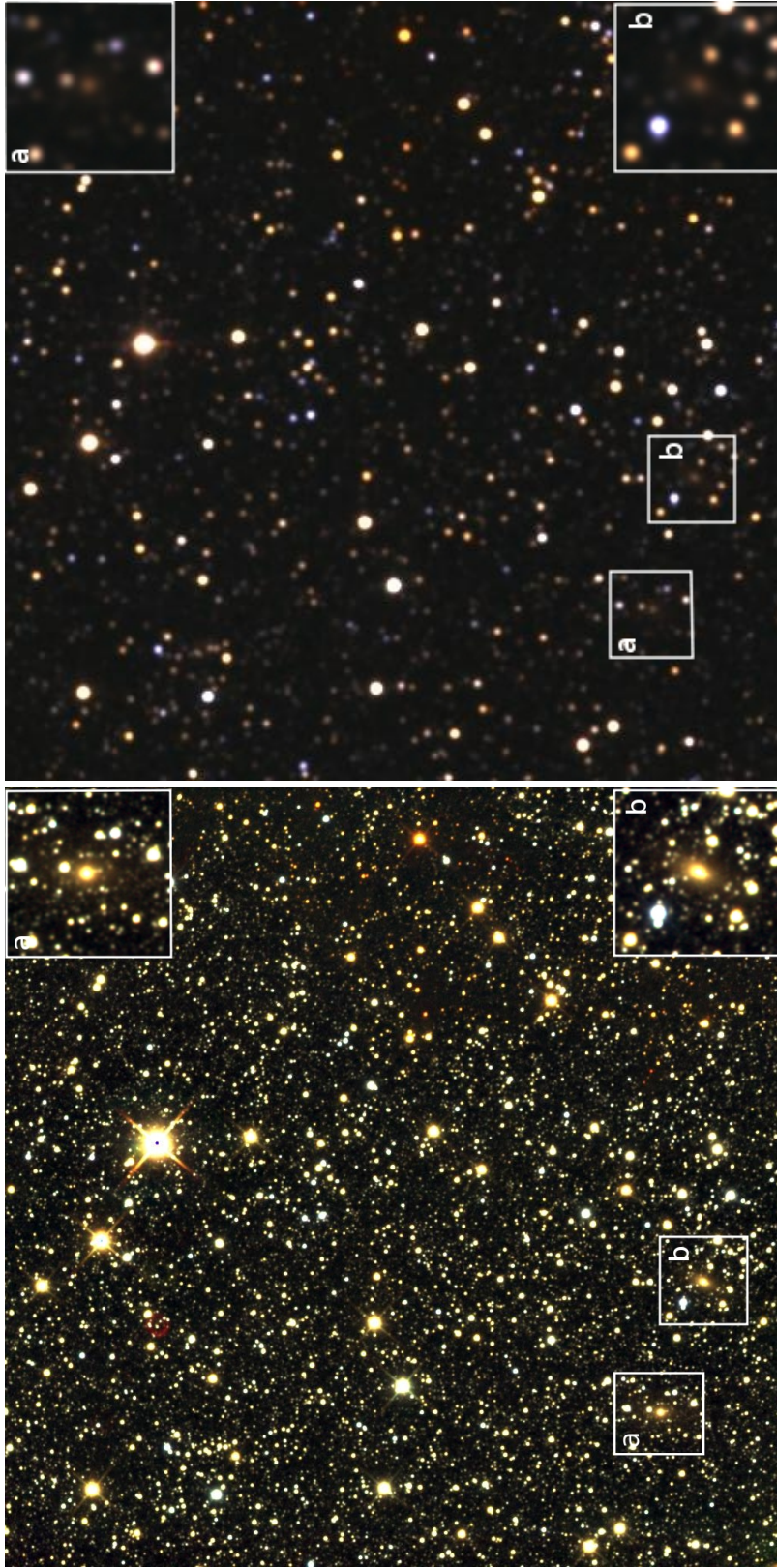


Figure 4.1: Comparison of IRSF (*left*) and 2MASS (*right*) images. The fields are centred on $l = 319^{\circ}756, b = 1^{\circ}226$ and the image size is $7\farcm7 \times 7\farcm7$. The field is heavily extinguished with an average V band extinction across the field of $A_V = 8\text{m}51$ and dust lanes can be seen across the image. The 2MPSC stellar density in the field is $\log(N_{K_s < 14}/\text{deg}^2) = 4.74$. Two galaxies are clearly visible in the IRSF field and can be identified in the 2MASS field, however they are not identified in 2MASX. The $50'' \times 50''$ insets show a $2\times$ magnification of each of these galaxies. Galaxy **a** (top inset) is located at $l = 319^{\circ}767, b = 1^{\circ}171$. Galaxy **b** (bottom inset) is located at $l = 319^{\circ}745, b = 1^{\circ}175$. In both images North is up and East is left.

demonstrates the improved sensitivity and resolution of the IRSF/SIRIUS data. Comparison of the insets (magnified postage stamps of each galaxy) show that, while no galaxies were detected by the 2MASS pipeline, the bright bulges of these two galaxies are visible in the 2MASS image, but are indistinguishable from stars. Furthermore, it is clear that many faint small stars are resolved with the IRSF, in particular on the outer edges of the galaxies, which are not visible in the 2MASS image. This means that we are better able to deblend these sources and obtain reliable photometry.

4.2 Observations

The observations for the follow-up survey were started in 2006 and were continued through to 2010. The bulk of these observations were done by myself in 2009 and 2010. Table 4.2 lists the progress of the observations and the observers who contributed to the survey. A total of 7 weeks were allocated exclusively to this project, however a significant amount of time ($\sim 60\%$) was lost due to bad weather and serious problems with the detector cooling system in 2010. This cooling problem led to an increase in the temperature of the detectors and the development of hot pixels, following which the repair process lasted five days.

Table 4.2: IRSF/SIRIUS observations

Year	Month(s)	Allocated weeks	Fields	Observer(s)*
2006	March – June	-	7	NWS
2007	March – May	-	50	NS/JT/NWS
2007	August/September	-	8	NWS
2008	January	-	7	EE
2008	March/April	-	7	NWS
2009	March/April	2	297	WW
2009	June	2	67	WW
2010	February	1	13	PK
2010	June/July	2	124	WW

NOTES:

*Norma Wall Survey (NWS), Nebiha Shafi (NS), James Tagg (JT), Ed Elson (EE), Wendy Williams (WW), Paul Kotze (PK)

Figure 4.2 shows the 580 ($\sim 70\%$) of the 821 HIZOA galaxies within 6000 km s^{-1} that have been observed to date; observed galaxies are plotted in blue while unobserved galaxies are marked in red. The remaining galaxies were not observed due to time constraints. The targets that were observed, however, constitute a representative sample of H α properties. The uneven spatial coverage of observations is largely a result of the allocated observing time lost due to poor weather and technical problems falling in June/July ($\alpha \gtrsim 18^{\text{h}}$) and February ($\alpha \lesssim 9^{\text{h}}$). The distribution of the target galaxies across Galactic longitude is shown in the left panel of Fig. 4.3 in red with those that could be observed in blue. The right panel shows the completeness fraction per longitude. The relative incompleteness of the observations at both $l < 270^{\circ}$ ($\alpha \lesssim 9^{\text{h}}$, Puppis/Hydra-Antlia filaments) and $l > 0^{\circ}$ ($\alpha \gtrsim 18^{\text{h}}$, Local Void) is again evident. The observations in the Norma region ($270^{\circ} < l < 360^{\circ}$) are nearly complete

which is excellent for studying the flow fields around the Great Attractor. Unfortunately the completeness is $\sim 50\%$ or less around the Local Void and Puppis regions. The impact of the low coverage for $l \lesssim 250^\circ$ is somewhat compensated for by the better detection rate in the 2MASX in this region due to the lower stellar density (see Sect. 2.2).

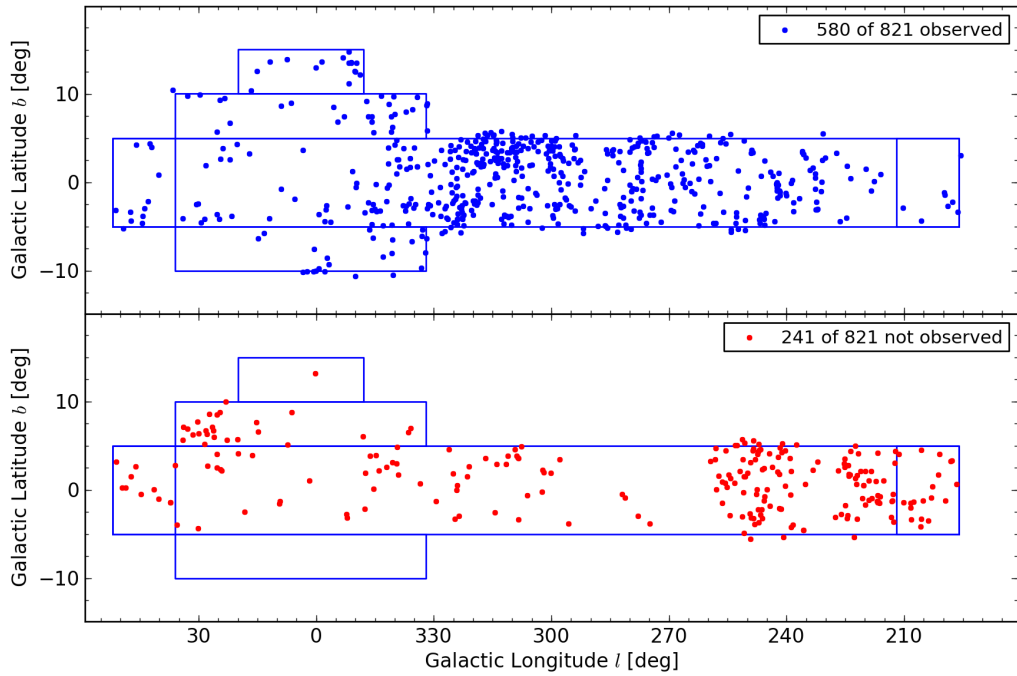


Figure 4.2: Observations completed within the allocated observing runs. The blue rectangles mark the HIZOA survey region. Of the 821 galaxies with $v < 6000 \text{ km s}^{-1}$ selected for observation 580 (70%) have been observed and are plotted with blue points in the *top* panel. The remaining 241 are plotted in red in the *bottom* panel.

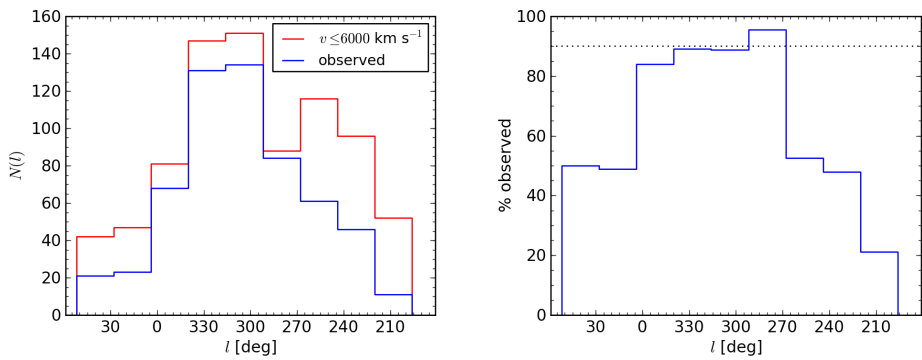


Figure 4.3: The numbers (*left*) and fraction (*right*) of galaxies observed (blue) out of the sample with $v < 6000 \text{ km s}^{-1}$ (red) plotted in 20° bins of Galactic longitude. The dotted line in the right panel shows 90% completeness.

4.2.1 Imaging

NIR imaging employs two dimensional arrays to count photons, which while similar to optical CCD's suffer some problems inherent to the NIR. Firstly these arrays need to be sensitive to the low energy of NIR photons and often their construction results in imperfections and defects known as bad pixels. Secondly the radiation from objects at room temperature (~ 300 K) is strong in the NIR, hence observations at these wavelengths suffer from very high thermal noise. Even with the cooling of the detectors, the thermal background remains high. Furthermore the atmosphere emits strongly in the NIR and the measured NIR sky background is about $5 - 10$ mag arcsec $^{-2}$ brighter than in the optical. Riad (2010) measured sky-background levels of approximately 16.3, 14.2 and 12.5 mag arcsec $^{-2}$ for J , H and K_s respectively at Sutherland which is comparable to the values measured for the Paranal Observatory (16.5, 14.5 and 13.0 mag arcsec $^{-2}$ for J , H and K_s respectively)*. This sky-background, most strongly in the K_s band, shows a seasonal variation with the changes of the site temperature. Additionally, the NIR sky emission has structure at all size scales, primarily because of upper atmospheric aerosol and hydroxyl emission known as airglow (Ramsay et al. 1992). The OH airglow is the dominant background component at J and H , while thermal continuum emission dominates the K_s background. Airglow emission frequently has a high degree of substructure on scales of tens of arcseconds.

Exposure Times

Exposure times above $\sim 30 - 40$ s result in saturation whereas short exposures have insufficient signal-to-noise for the detection of faint galaxies. To counter this, we take multiple short exposures and combine them. For N combined frames, the signal-to-noise ratio increases by \sqrt{N} . Based on previous experience with SIRIUS in the ZoA (Riad 2010, Skelton et al. 2009, Nagayama et al. 2006; 2004) we decided on 25 frames, each of 24 s exposures resulting in an effective exposure time of 600 s. This allows for the detection of faint galaxies without too much contamination by faint stars.

Dithering

These 25 frames are slightly offset from each other such that each part of the field is imaged on a different part of the detector in each frame. This process of *dithering* overcomes the problem of faulty pixels. The input from bad pixels is averaged out when the individual frames are aligned and median-combined. The dither pattern is shown in Fig. 4.4. Dithering is determined by the telescope controller which constructs the right ascension and declination offsets based on the number of frames and the dither radius, chosen to be $15''$ which defines the individual spacing in the 5×5 grid of pointings. An anomaly in the controller code results in the eleventh frame deviating from the pattern. All other frames lie on two concentric squares. Individual dithered frames, known as **self** frames are aligned and combined in the pipeline reduction process. Dithering increases the field size to $\sim 8.6' \times 8.6'$.

*www.eso.org/gen-fac/pubs/astclim/paranal/skybackground/

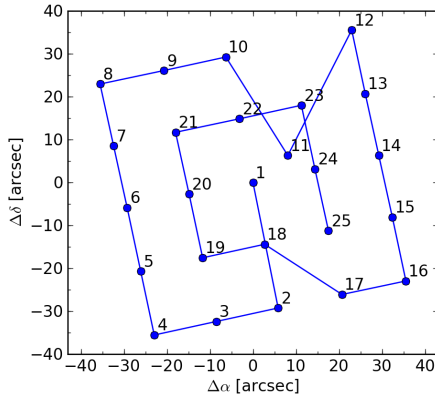


Figure 4.4: The dither pattern used for all the observations for the 25 dithered frames. The numbers refer to the frame number. The outer square is $60'' \times 60''$ and the inner square is $30'' \times 30''$. Frame 1 occupies the target coordinates. Frame 11 is offset due to an error in the flow of the control software.

Sky Observations

Atmospheric emission is not constant in time, it varies over scales of a few minutes. Moreover, the presence of substructure leads to strong gradients across a few arcminutes of sky. It is therefore essential to accurately measure the sky level across the detector. There are generally two methods of determining the sky. The first is to obtain images of empty sky adjacent to the object and switch rapidly between this sky field and the object. This method works well in regions of low star density where blank sky is easy to observe. It does, however, require as much time spent observing the sky as observing the object and makes a large survey inefficient. A second method involves generating a *self-sky* image when doing a dithered exposure. Here, instead of realigning the dithered frames, one simply stacks and median combines them. Because detector artifacts remain fixed on the detector while astronomical sources move with the dither pattern, any features (e.g. stars) with scale less than the spacing between dithered frames will be removed, leaving only the structure of the sky. Note that extended astronomical objects with scales larger than the field separation will leave a residual on the sky image.

Flat-fields

In addition to dead pixels, the sensitivity or response to light varies from pixel-to-pixel across the array. These pixel-to-pixel variations in sensitivity are corrected for by flat-fielding. An exposure taken of a uniformly illuminated source (flat-field), directly represents the response of each pixel. The twilight sky provides a good source of uniform light over the field-of-view of the IRSF. On each observing night 100 frames of 5 s exposures were taken both at evening and morning twilight (weather permitting). For each observing run (usually 1 or 2 weeks), all the twilight flats were combined into a single master flat for that run and used to correct all

the raw images from that run. In some instances, due to poor weather and when observing was done outside of the dedicated observing time, the master flat was constructed from only 1 or 2 twilights. However the stability of the SIRIUS detectors has been well established (Riad 2010).

Dark Frames

The relative low energy of NIR photons means that the detectors are particularly susceptible to thermal noise. This results in the build-up of charge on the detector even when the shutter is closed. Clearly this thermal noise depends on the exposure time. A dark frame taken with the shutter closed with the same exposure time as the object exposures, allows for the determination of the thermal noise. Therefore ten dark frames were taken at the end of each observing night. These are averaged and subtracted from all raw images in the pipeline reduction.

4.3 Image Processing with the SIRIUS Pipeline

All raw images were reduced using the SIRIUS pipeline developed and maintained by Yasushi Nakajima*. SIRIUS is a dedicated Image Reduction and Analysis Facility (IRAF)[†] package for automated reduction of SIRIUS images. The high-level steps that encompass the image reduction include:

1. dark current subtraction
2. determination of master flat fields and flat correction
3. sky determination and subtraction
4. frame to frame offset determination and combination

These steps are explained in detail in the following sections. The pipeline is executed in IRAF with the tasks `pipeneolist` which generates all the ASCII files containing the necessary information to run the reduction, which is executed with the task `pipeneo`. We start with N dithered frames `self(i)`.

4.3.1 Dark Current Subtraction

The first step in `pipeneo` generates the dark frame for the night and corrects all frames for thermal noise. The 10 dark frames from each night are median combined into a master dark frame which is subtracted from each `self(i)` frame. The new individual frames are named `self_d(i)`. Figure 4.5 shows typical dark frames. Faulty pixels show up in the dark frames as bright pixels while the horizontal gradients are a result of the *reset anomaly* due to the charge readout across four quadrants.

*Department of Astrophysics, Nagoya University, Chikusa-ku, Nagoya, Japan

[†]IRAF is distributed by the National Optical Astronomy Observatory, which is operated by the Association of Universities for Research in Astronomy, Inc, under cooperative agreement with the National Science Foundation

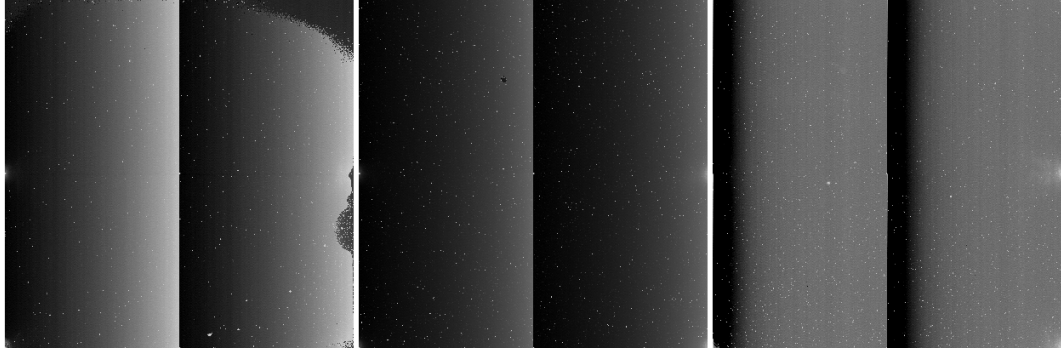


Figure 4.5: Typical dark frames in the J , H and K_s bands (*left to right*). Faulty pixels show up as bright white points. The horizontal gradients are a result of the detector readout.

4.3.2 Determination of the Master Flat and Flat Correction

A separate task, `autotwflat`, within SIRIUS is used to create the master flat field for each observing run. `autotwflat` takes as input the dates the twilight flats were taken, the frame numbers and whether they were morning or evening flats. The task then creates individual flat fields by selecting from within each twilight run pairs of frames with a mean flux less than 6000 counts ($\sim 30\%$ of the saturation level) and a mean flux difference of less than 2000 counts. Each of these pairs is combined differentially and normalised by the median flux. Finally these differential flats are median combined to produce a single master flat field, `twilight`.

Riad (2010) shows that the variation in the quantum efficiency of the detectors over about a month is negligible. In fact it is stable over time scales of over a year. A sample master flat for J , H and K_s is given in Fig. 4.6.

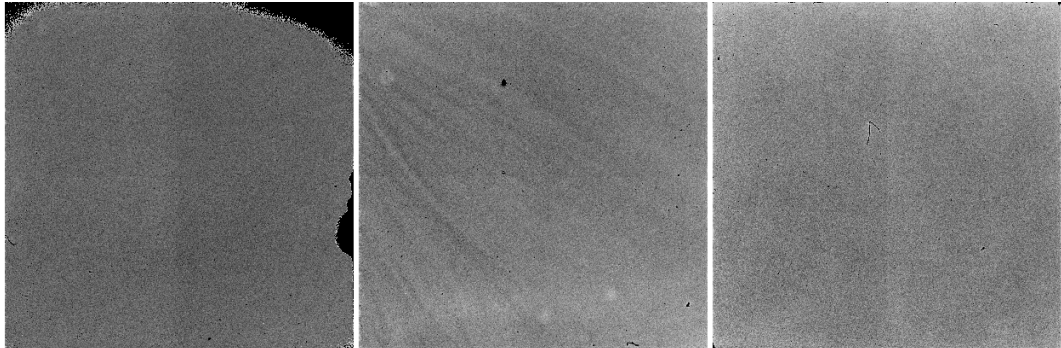


Figure 4.6: Typical master flat frames in the J , H and K_s bands (*left to right*). The dark regions around the edge of the J band flat field are faulty pixels.

The name of the `twilight` frame is passed as input to `pipeneolist`. Individual object frames throughout that observing run are corrected for pixel-to-pixel variations of quantum

efficiency of the detector by dividing each by this master flat:

$$\text{self}_d^f(i) = \frac{\text{self}_d(i)}{\text{twilight}}$$

4.3.3 Sky Determination and Subtraction

The next step in `pipeneo` is to generate sky frames for each dither set. In addition to sky emission, imperfections in the telescope optics and dust create patterns visible in each frame. Generally the J band is free of these patterns and has little sky structure. The H band is affected strongly by the OH emission which manifests as ripples across the image. Dust on the detector window radiates strongly in the K_s band producing out-of-focus rings and spots in the K_s images. Sample sky frames, in which these characteristics are visible, are shown in Fig. 4.7. Furthermore there is an effect of high stellar density on the sky frames. The overlap of different stars in the undithered combine results in a hatchwork residual pattern.

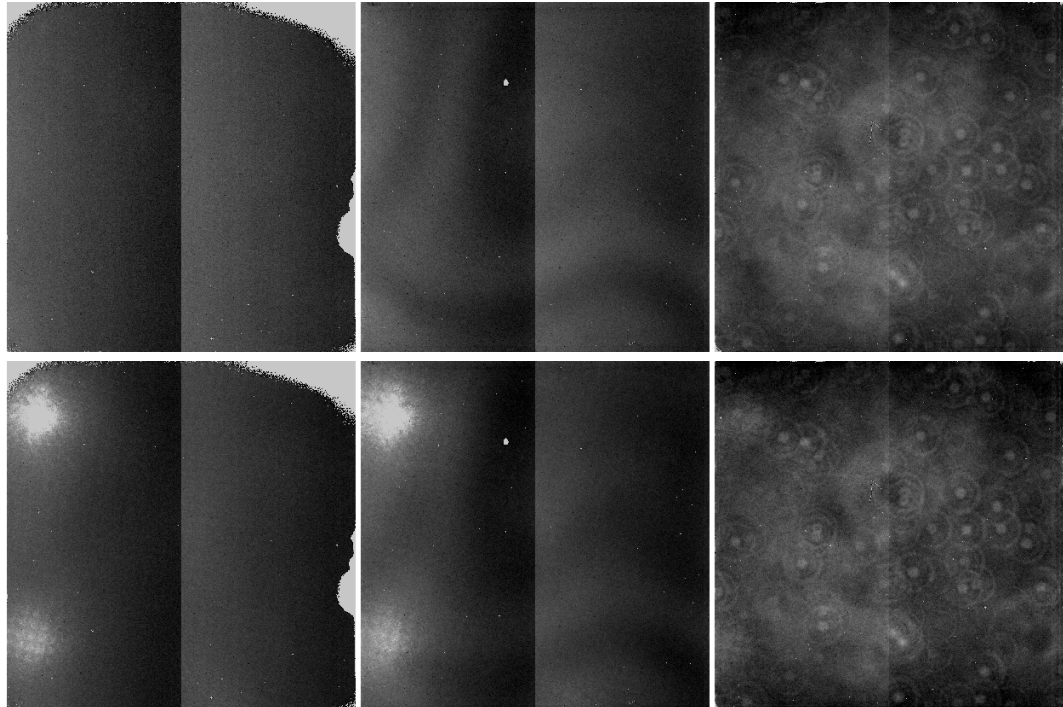


Figure 4.7: Typical sky frames in the J , H and K_s bands (*left to right*). The J band shows little or no structure. Structure from OH emission is evident in the H band. Rings due to dust emission from the detector window is seen in the K_s sky emission. The top panel shows a sky field in a region of relatively low stellar density, while the bottom panel shows sky fields from a region of high stellar density. Residuals from two saturated stars remain in all three sky frames and a faint hatchwork pattern due to the high stellar density is evident in the lower panel.

The sky frame is made by additively scaling each frame, $\text{self}_d^f(i)$, to have the same

median flux as the first frame in that dither sequence, $\text{self}_d^f(1)$:

$$\text{self}_d^{f'}(i) = \text{self}_d^f(i) + (\langle \text{self}_d^f(1) \rangle - \langle \text{self}_d^f(i) \rangle)$$

ensuring all frames in the sequence have the same median flux. These frames are median combined *without* correcting the dither offsets generating the `sky` image. Because any astronomical source will appear in different positions in each frame, their flux does not contribute to the median. This removes any astronomical sources in the image, leaving only the structure of the sky and detector artifacts. However, in regions of high star density, different stars may overlap in many frames and the median does not fully account for this. The result is a cross-hatched pattern in the `sky` frame as can be seen in the lower panels of Fig. 4.7. Also, for extended sources larger than the dither radius, the source overlaps with itself in the individual frames, resulting in a locally higher measure of the sky value. The bright residual in the upper left corner of the bottom panel of Fig. 4.7 is a result of a saturated star. Finally this `sky` image is subtracted from all frames in the dither sequence and the median flux of the `sky` image is added back, leaving a uniform sky level in each frame.

$$\text{SELF}(i) = \text{self}_d^{f'}(i) - \text{sky} + \langle \text{sky} \rangle$$

4.3.4 Dither Combine

The last step in `pipeneo` is to generate a single image from each dither set. A list of sources in each $\text{SELF}(i)$ frame is generated with IRAF tasks `daophot` and `daofind`. Stars are selected where the flux exceeds 10σ and the magnitude error $\epsilon \leq 0^{\mathrm{m}}1$ within the central region [51 : 900, 51 : 900]. The edges of the images are avoided due to the faulty pixels especially on the J band array. The initial dither offsets are applied to each frame list and sources in each field are matched, thereby refining the actual offsets between images. These offsets are used to align the images. Once aligned, the frames are median combined, removing any effects of bad pixels. The final image has a factor N enhancement in gain and a reduced noise by a factor of $1/\sqrt{N}$.

4.4 Image Calibration

The output images from the `SIRIUS` pipeline require astrometric calibration to transform image coordinates to the World Coordinate System (WCS) and photometric calibration to convert instrumental fluxes to a standard magnitude system. We use the 2MASS Point Source Catalogue (2MPSC Strutskie 2006) as a standard for these calibrations. The calibration is done with a combination of IRAF and python scripts developed by one of our Japanese collaborators Dr. N. Matsunaga* and modified by Riad (2010).

The following sections describe the calibration standard catalogue and the astrometric and photometric calibration procedures.

* Institute of Astronomy, School of Science, University of Tokyo

4.4.1 Calibration Standard

The 2MPSC contains 0.5 billion stars and provides an excellent standard for calibration purposes. It matches all the filters that we use in our survey, it covers our entire survey region and its calibration is smooth over the whole sky. The 2MPSC itself is calibrated from the Tycho 2 Point Source Catalogue (Høg et al. 2000). The mean astrometric offsets between 2MPSC and Tycho 2 were found to be $\langle \Delta\alpha \rangle = -0.09 \pm 8.06 \times 10^{-2}$ arcsec in right ascension and $\langle \Delta\delta \rangle = 0.48 \pm 8.85 \times 10^{-2}$ arcsec in declination. Stars with $S/N > 20$ have a photometric accuracy of 0^m054 (Cohen et al. 2003). See the 2MASS Explanatory Supplement* for a detailed description of the calibration of the 2MASS images.

4.4.2 Astrometric Calibration

In order to transform the image coordinates to WCS, we match sources in the image to an astronomical catalogue. While detecting sources in the image and extracting sources from a catalogue is relatively easy, the process of cross-identifying them is non-trivial and computationally expensive, particularly for large source numbers. However greater source counts significantly increase the accuracy of the transformation. The scripts developed by Dr. N. Matsunaga use a routine based on the Optimistic Pattern Matching (OPM) technique proposed by (Tabur 2007). This technique utilises the fact that for any two nearby stars, triangular combinations with a distant star are less frequent than with a third nearby star. This means that fewer triangles are required to provide a good match between the image and calibration catalogues. The astrometric solution is obtained by solving the following

$$\begin{aligned} X &= C_0x + C_1y + C_2 \\ Y &= C_3x + C_4y + C_5 \end{aligned} \quad (4.1)$$

where (x, y) are the image coordinates of each object, (X, Y) the WCS coordinates of each object in the calibration catalogue and C_i are the coefficients defining the transformation. The solution is found using the IRAF task `ccmap`. We use J2000 coordinates.

4.4.3 Photometric Calibration

The use of different filters and optical and electronic systems means that the flux of an object will differ with the optical system with which it is measured. However, this instrumental magnitude can be corrected for such effects and converted to a standard system. The instrumental magnitude is simply the counts expressed on a log scale:

$$m_\lambda^i = -2.5 \log \left(\frac{F_\lambda}{t} \right) \quad (4.2)$$

*<http://www.ipac.caltech.edu/2mass/releases/allsky/doc/expsup.html>

where m_λ^i is the instrumental magnitude, F_λ is the background-subtracted source flux in counts and t is the exposure time. This is transformed to a standard magnitude by

$$m_\lambda = ZP_\lambda^i + m_\lambda^i + c_1 X + c_2 m_{\text{col}}, \quad (4.3)$$

where m_λ is the object's magnitude in the standard system, ZP_λ is the calibration constant or magnitude zero-point, c_1 and X are the airmass extinction coefficient and airmass respectively, $c_2 m_{\text{col}}$ is a colour term. Following Riad (2010) we neglect the colour term as it is assumed to be small. The magnitude zero-point is usually determined by measurements of *standard stars* (near-infrared standard star catalogues Persson et al. 1998, Carter & Meadows 1995) with the same instrumental setup. However this requires additional observation time and where there are many stars within the field-of-view for which standardised magnitudes are available one can easily use these to determine the zero-points. Additionally this has the advantage that changes in the photometric conditions are readily tracked. We use the 2MPSC as a standardized magnitude catalogue. We do, however, need to correct for any differences in the instruments used, notably in the detector filters. SIRIUS uses broad-band J , H and K_s filters that, while very similar to the 2MASS standard, are sufficiently different that we cannot compare directly our magnitudes with those in the 2MASS system. However, there exist colour-dependent transformation equations between the two photometric systems. Nakajima (priv. comm.) shows

$$\begin{aligned} J_{\text{sirius}} &= J_{\text{2mass}} + (-0.045 \pm 0.008)(J - H)_{\text{2mass}} - (0.001 \pm 0.008) \\ H_{\text{sirius}} &= H_{\text{2mass}} + (0.027 \pm 0.007)(J - H)_{\text{2mass}} - (0.009 \pm 0.008) \\ K_{s,\text{sirius}} &= K_{s,\text{2mass}} + (0.015 \pm 0.008)(J - K_s)_{\text{2mass}} - (0.001 \pm 0.008) \end{aligned} \quad (4.4)$$

which are valid over a wide range in colour $0.0 \leq (J - H) \leq 3.9$, $0.0 \leq (H - K_s) \leq 2.8$ and $0.0 \leq (J - K_s) \leq 4.9$. A comparison on the transmission curves of the 2MASS and SIRIUS filter systems is given in Fig. 4.8. Thus, in the SIRIUS magnitude system:

$$m_{\lambda,\text{sirius}} = ZP_\lambda + m_\lambda^i \quad (4.5)$$

where the zero-point now incorporates the airmass term.

The photometric calibration makes use of an IRAF script developed by Riad (2010) which matches sources within $1.^{\prime\prime}35$ (3 pixels) in each image with sources in the 2MPSC. Only photometric quality stars (marked with AAA in the 2MPSC) and with colour ($J - H$ and $J - K$) errors of $\leq 0^m.1$ are considered for calibration. The code implements SExtractor (Bertin & Arnouts 1996, Bertin 1996) for measuring instrumental magnitudes and cross-identifying them with sources in the 2MPSC. The 2MPSC magnitudes are first converted to the SIRIUS system via the above transformations. For each matched pair the zero-point is calculated and the median of all pairs determined as the zero-point of the field.

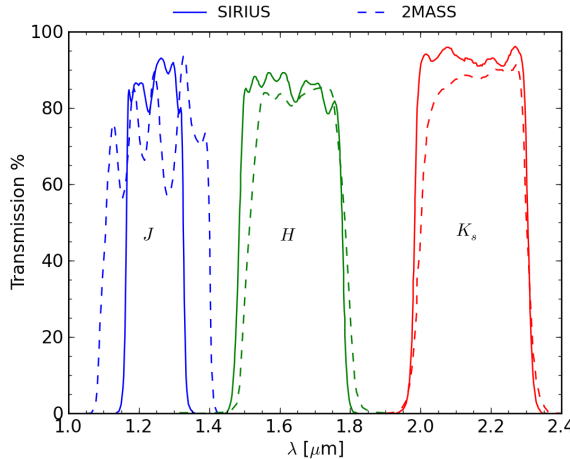


Figure 4.8: Comparison of SIRIUS (solid) and 2MASS (dashed) transmission curves for the J , H and K_s filters.

4.4.4 Image Statistics

Two measures of the photometric conditions are determined for each field: the seeing, or FWHM, of stars in the field, and the magnitude zeropoint. Fig. 4.9 shows the distribution of seeing values for all of the final 580 images. 65% of the images were observed with K_s seeing less than 1.5 and 85% less than 1.75. The distribution of magnitude zeropoints is shown in Fig. 4.10. The median zeropoints are consistent with values previously determined by Riad (2010) and Cluver et al. (2008a). The medians and standard deviations of both the magnitude zeropoints and seeing values in all three bands are given in Table 4.3.

Table 4.3: Mean magnitude zeropoints and average seeing for all 580 images

	$\langle ZP \rangle$ [mag]	σ [mag]	seeing ['']	σ ['']
J	20.84	0.06	1.49	0.35
H	21.02	0.06	1.47	0.33
K_s	20.24	0.06	1.39	0.30

4.5 Galaxy Identification

While the large number of images in our survey makes individual identification of sources time consuming, their location within the ZoA makes the use of automatic routines unreliable. The advent of large surveys brought the need for automated routines for the detection and parameterisation of sources. Programmes like FOCAS (Jarvis & Tyson 1981), COSMOS (Beard et al. 1990) and SExtractor (Bertin & Arnouts 1996) have been developed to identify and extract parameters of sources in images. These methods have been shown to be

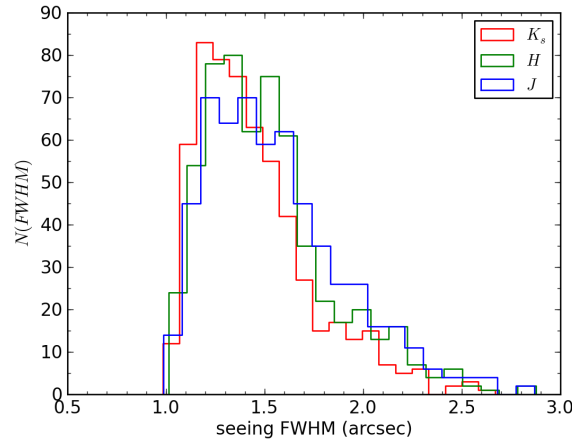


Figure 4.9: Histogram of image FWHM as a measure of the seeing.

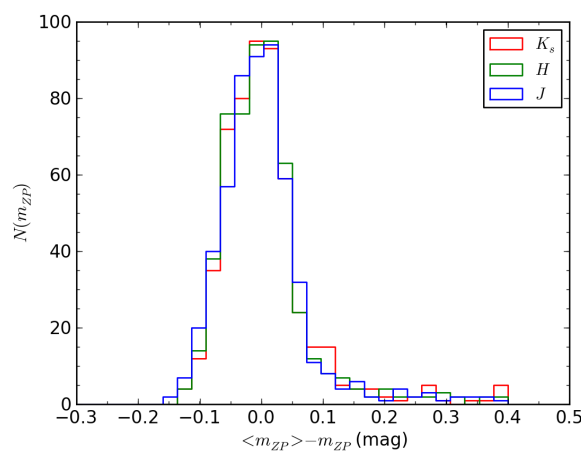


Figure 4.10: Histogram of magnitude zero points as a measure of the image quality.

efficient at high galactic latitudes. However, closer to the Galactic plane, it becomes more complicated to deblend and separate fluxes of nearby sources and the reliability of these algorithms severely degenerates (Beard et al. 1990). Identification and classification by eye remains the best choice and is not prohibitive for this survey.

Having the three NIR bands is particularly useful, as they allow for the generation of false colour images. Each band contributes one channel of the RGB image where blue is the shorter wavelength J and red is K_s . Galaxies are intrinsically red and their colours are different (redder) to the colours of foreground stars and Galactic sources. Their different colour and their extended nature allows the eye to rapidly identify galaxies in the field colour images of each field.

For this survey I developed a python script, *findgal*, that uses the pyDS9* module that interfaces with SAOImage DS9†, an astronomical imaging and data visualisation tool. The script is available online‡. DS9 is used to interactively display a three-colour RGB composite image (K_s : red, H : green and J : blue). The user is able to mark the approximate centre of each galaxy candidate on the DS9 image as well as the semi-major and -minor axes. The program interface provides information on the HI properties of each target to ease the visual identification of the HI counterpart. If any 2MASX sources lie within the field, they are marked with magenta circles allowing for quick identification and possible confirmation as the HI counterpart. Each field is systematically searched at a higher magnification for smaller sources.

Figure 4.11 shows an example of the DS9 display and HI information for HI source J1053-62. Identified in the field is a large ($\sim 2'$) spiral galaxy. The source is also marked as a 2MASS galaxy (2MASXJ10534560-6250026), however, the position is offset with respect to the IRSF position. This illustrates the susceptibility of 2MASS to identify a foreground star as the centre of faint galaxies lacking a strong bulge (i.e. later type spirals or irregulars). This source lies in a region of moderate extinction ($A_V = 2.^m76$) which explains the reddish colour of the galaxy.

Once the sources have been detected and before any meaningful photometry can be extracted, it is necessary to remove any foreground contamination by stars. The following sections describe the methods used for the subtraction of foreground stars from the images.

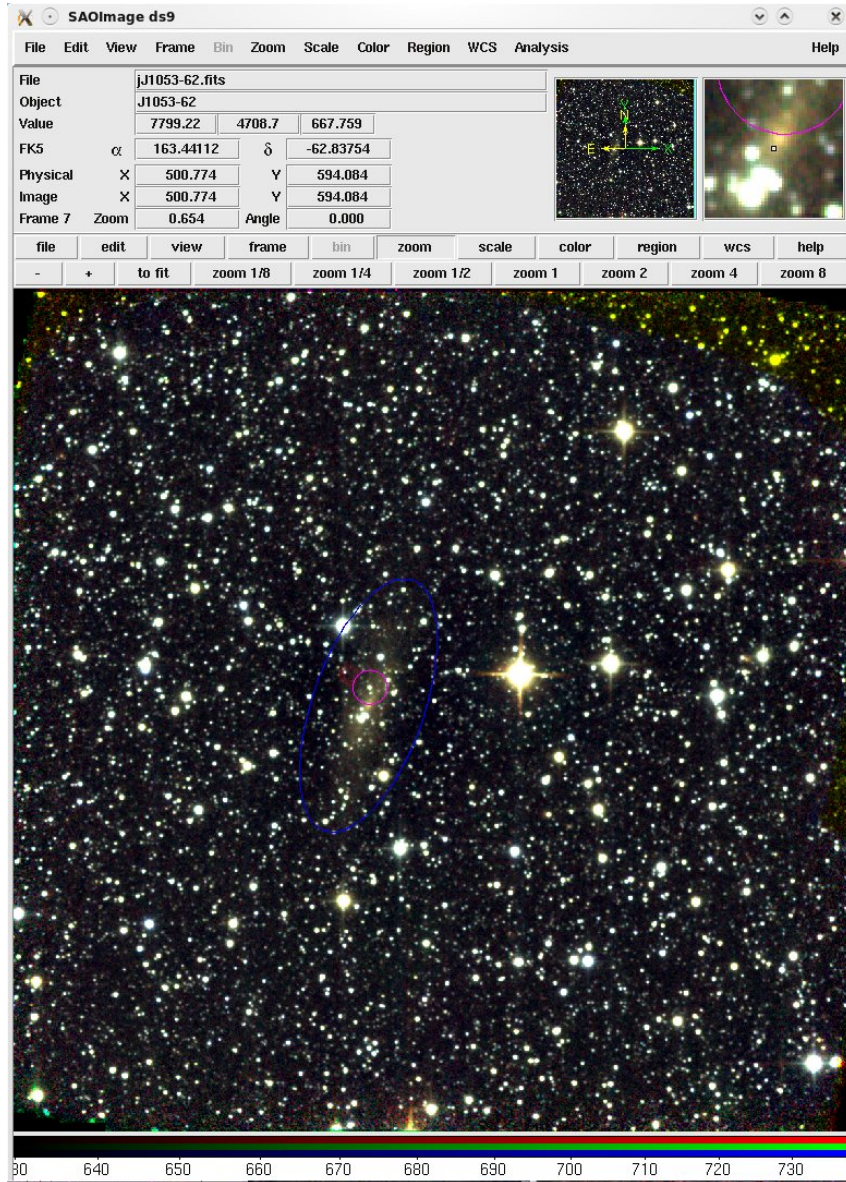
4.6 Star-subtraction

The increase in stellar density near the Galactic plane results in the contamination of extragalactic sources by foreground stars. It is important to remove the flux contribution of the foreground stars from the galaxy flux. A method of star-subtraction via PSF-fitting is employed to achieve this. This is implemented in two steps: First, the point spread function (PSF) is determined for the field, this is the “shape” of a point source (star) in the image.

*<http://hea-www.harvard.edu/saord/ds9/pyds9/>

†This research has made use of SAOImage DS9, developed by Smithsonian Astrophysical Observatory.

‡password-protected at www.ast.uct.ac.za/~wendy/zoatf/findgal.py



```

displaying field J1053-62
load catalogue: /home/wendy/masters/IRSFdata/calibrated/hicats/J1053-62.hicat
*****
Name: J1053-62          flux: 35.1
l,b: 289.952596, -2.973763   HI mass: 9.7
E(B-V): 0.83           velocity: 1837
A(V): 2.76            w50: 271

```

2MASXJ10534560-6250026

Figure 4.11: Sample output from *findgal*, showing the $\sim 8'.6 \times 8'.6$ three-color image in the DS9 interface and the HI information for target J1053-62. Clearly visible in the field is a large spiral galaxy. The blue ellipse marks the galaxy parameters as defined by the user in *findgal*. The small magenta circle marks the position of a 2MASX source in the field, 2MASXJ10534560-6250026. In this case the 2MASX source is offset due to the faintness of the galaxy and the presence of a foreground star.

This PSF may be variable across the field. Second, the fitted PSF is used to remove stars in the neighbourhood of each detected galaxy.

4.6.1 PSF Determination

While, the shape of the PSF depends on the instrumental set-up, the dominant driver of the PSF shape is atmospheric seeing, which results in a generally Gaussian-shaped profile of point sources. Variations in the seeing cause deviations from a symmetric Gaussian, which may vary across the field of view. Saturated stars deviate from the Gaussian profile and very bright stars produce diffraction spikes. Determining an accurate PSF is very important for star removal. A further complication to accurate PSF modelling is high star density, where light from neighbouring stars may be present in the wings of what appears to be an isolated star. Routines such as KILLALL (Buta & McCall 1999) have been developed to ease the PSF-fitting and star removal in crowded fields. However, the implementation of these routines are manual and time-consuming. For our relatively large sample we require an automated routine. Dr Nagayama* developed an automated PSF fitting routine for the Norma Wall Survey which uses the DAOPHOT package in IRAF. I modified the script to run in PyRAF[†]. Here follows the algorithm:

1. A maximum of 50 unsaturated, isolated stars are selected. This set of stars is `{PSF model}`.
2. This set of stars is used to create an initial estimate of the field PSF, `PSF1`. `PSF1` is used to subtract all detected stars in the original image except for `{PSF model}`.
3. A new improved PSF, `PSF2`, is fitted using `{PSF model}` on the star-subtracted image. This ensures that any possible contamination in the wings of the PSF model stars by nearby stars is reduced, thereby resulting in an improved model PSF.
4. Step 3 is repeated to produce the final PSF, `PSF`.

4.6.2 Background Cleaning

Bright stars in the images may produce leakage along a column in the array. An effect of the reset anomaly also produces vertical gradients in some of the images. These vertical features are removed by subtracting the average of each column from that column. The median sky level is added back to the entire image.

4.6.3 Star Removal

An algorithm used for the removal of stars around each galaxy was also developed by Dr Nagayama. However, extensive modifications were made to improve the performance of the routine to prevent the removal of structures on the galaxy as well as spurious rings around the galaxy. The algorithm relies on some limited user input to verify the identification of

*Department of Astrophysics, Nagoya University

[†]PyRAF is a product of the Space Telescope Science Institute, which is operated by AURA for NASA

stars on the galaxy. The user is allowed the options of removing spurious detections or adding sources that were not detected. Stars are removed from a box around each galaxy, the size of which depends on the initial estimate of the size of the galaxy. This is done to decrease the total computation time.

The steps in the star subtraction process are described here:

1. The sky background and rms, σ , in the image is determined. Both are determined using `imstatistics` with 30 iterations with 3σ clipping.
2. The galaxy is modeled using `ellipse` and `bmodel`. This model is subtracted from the image with `imarith` resulting in the galaxy-subtracted image. Structures on the galaxy such as spiral arms may not be fully modelled and may result in residuals in the galaxy-subtracted image.
3. The bright stars in the galaxy-subtracted image are detected and removed. This is done using `findstars` which uses Source Extractor to detect all sources above 3.5σ of the background. The DAOPHOT tasks `phot` and `allstar` are used to measure the PSF photometry of these sources and then to remove them from the galaxy-subtracted image. `allstar` produces an output file containing the details of all successfully subtracted stars.
4. The faint stars are then detected and removed from the galaxy-subtracted image. The detection is done using `findstars` with a detection limit of 1.8σ . Within the radius of the galaxy only stars that are also detected using DAOPHOT's `daofind` with a threshold of 2σ are included in the list. This prevents the misidentification of residuals of structures as stars. Again PSF photometry is done with `phot` and the stars are removed from the galaxy-subtracted image using `allstar`.
5. The two `allstar` output files for the bright and faint stars are concatenated, and used in `substar` to remove these stars from the original image.
6. An additional step is taken to find and remove any residuals as a result of the imperfect fit of the PSF to every star in the image.
7. Steps 2 to 6 are iterated four times. Each iteration improves the galaxy model as the subtraction of stars on the galaxy is improved. This results in improved photometry of stars on the galaxy and therefore improved subtraction. In the last iteration the user is asked to confirm the source lists for the bright and faint stars.

A flowchart of the star-subtraction algorithm is shown in Fig. 4.12. Tasks and subroutines are shown in rectangles. Input/output is shown with rounded rectangles.

Figure 4.13 shows two examples of where the original star-subtraction routine resulted in residuals on the galaxy. This problem particularly affects galaxies that are difficult to model with `ellipse`. These include edge-on galaxies, which result in a row of residuals along the plane of the galaxy. Isophote twists produce a ring of residuals. Galaxies with

clear structure, especially strong spiral arms, are also affected and often strong residuals occur at the edges of bars in barred spiral galaxies. Comparison of the *central* panel which displays the results from the original method of subtraction, and the *right* panel illustrating the results from the improved method, demonstrates that we have overcome this problem.

4.6.4 Residual Cleaning

The PSF fitting is not perfect and does not exactly match the true shape of every star in the image. The star-subtraction process often leaves residuals of large negative flux where the PSF does not fit precisely. These ‘blemishes’ can affect the photometry so need to be removed. While residuals away from the galaxy are removed in the star-subtraction routine, those on the galaxy are removed manually. The IRAF task `imedit` was applied to remove these blemishes. A user interface implementing pyDS9 was developed allowing the user to define circular apertures of varying radius to non-interactively input into `imedit`. The smallest possible aperture is chosen. `imedit` measures the background level and any gradients within a small annulus around the aperture. This background map is used to replace the pixel values within the aperture. Large residuals, due to saturated stars, are more problematic. They require large apertures, typically a few pixels larger than the radius of the PSF.

4.6.5 Postage Stamp Creation

As part of the star-subtraction process, three-colour postage stamp images of the starry and the star-subtracted fields are generated. The images were colour stretched using the following recipe, based on that used by T. Jarrett for the 2MASS Near-Infrared Galaxy Morphology Atlas* (Jarrett 2000). The colour scale is stretched relative to the NIR colour of a “normal” galaxy ($J - K_s = 1^m0$ and $H - K_s = 0^m28$). This means that the true colour of the galaxy will be reflected in the three-colour image. The K_s peak flux is measured from the K_s band image. From this the J and H peak fluxes are deduced from the normal galaxy colours. These peak fluxes define the upper limits of the colour stretch. The lower limits are taken to be -7.5% of the peak flux.

The RGB images are generated using the `make_rgb_image` routine in APLpy[†] (Astronomical Plotting Library in Python) which is a Python module aimed at producing publication-quality plots of astronomical imaging data in FITS format. The blue scale is assigned to the J band, green to the H band and red to the K_s band. A logarithmic stretch is used in all bands. Normal galaxies will appear white because of their normal colours. Galaxies with $J - K_s > 1^m2$ will appear redder, and with $J - K_s < 1^m$ will appear blueish. Note that large extinction will result in redder colours. Figure 4.14 shows examples of postage stamps for six galaxies. J0716-18C is an edge-on slightly reddish galaxy characteristic of a large early type spiral galaxy. J0949-47B is a blueish galaxy and has a low surface

*http://www.ipac.caltech.edu/2mass/gallery/galmorph/2mass_galmorp.html

[†]<http://aplpy.sourceforge.net/>

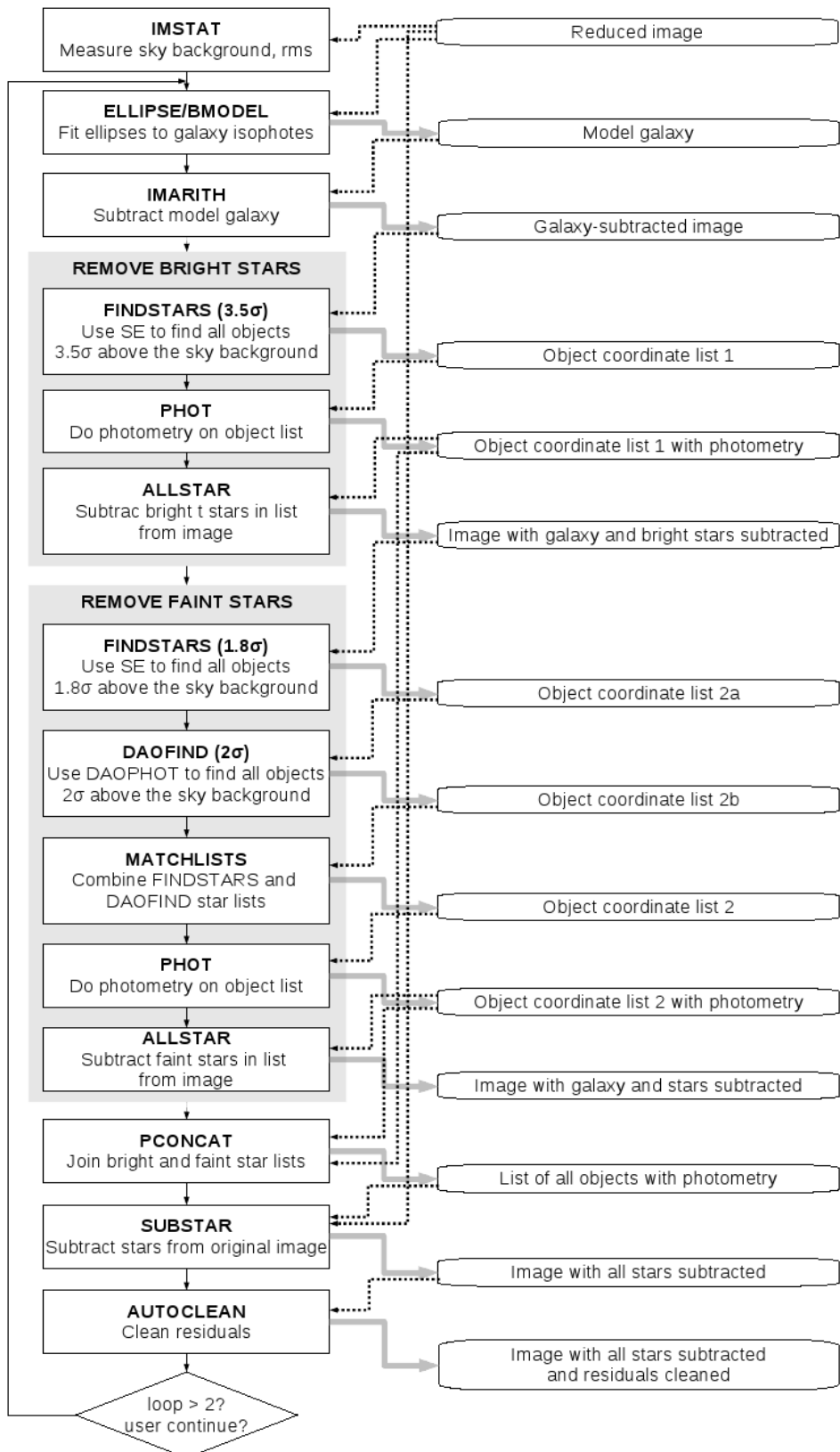


Figure 4.12: Flowchart of star subtraction algorithm

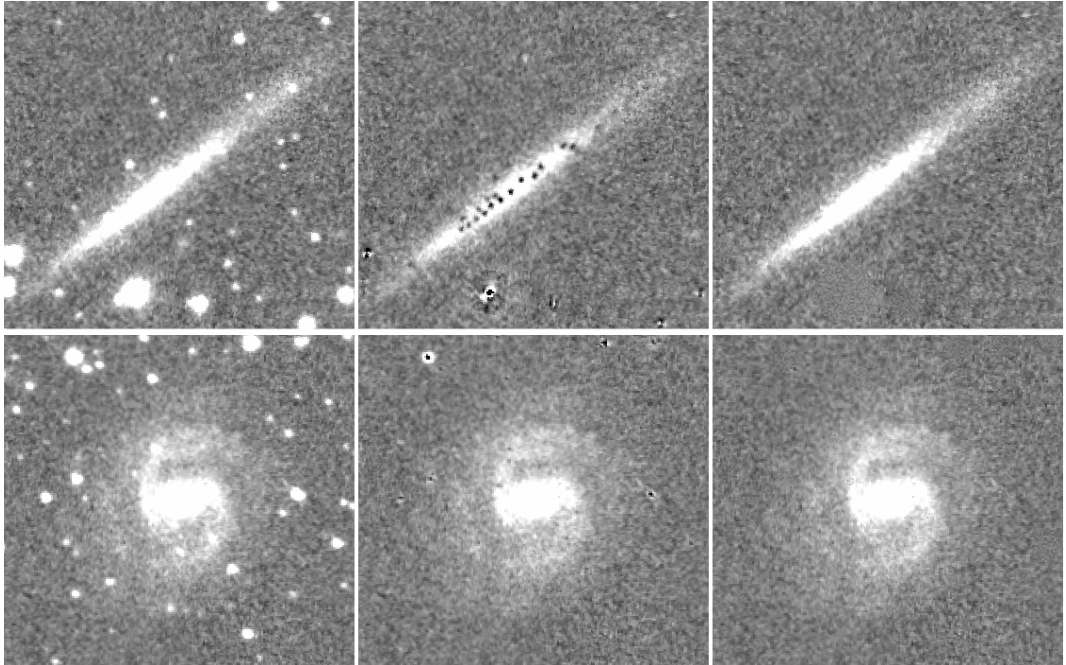


Figure 4.13: K_s band images showing the improved performance of star-subtraction routine for two galaxies: J0716-18C (*top row*) and J0903-41 (*bottom row*). The *left* panel shows the original starry images, the *middle* panel shows the results of the star-subtraction using the original routine and the *right* panel shows the results of the improved star-subtraction routine. The original routine leaves residuals on the galaxies which are not present with the new routines. Particularly affected are the planes of edge-on galaxies and substructure within galaxies.

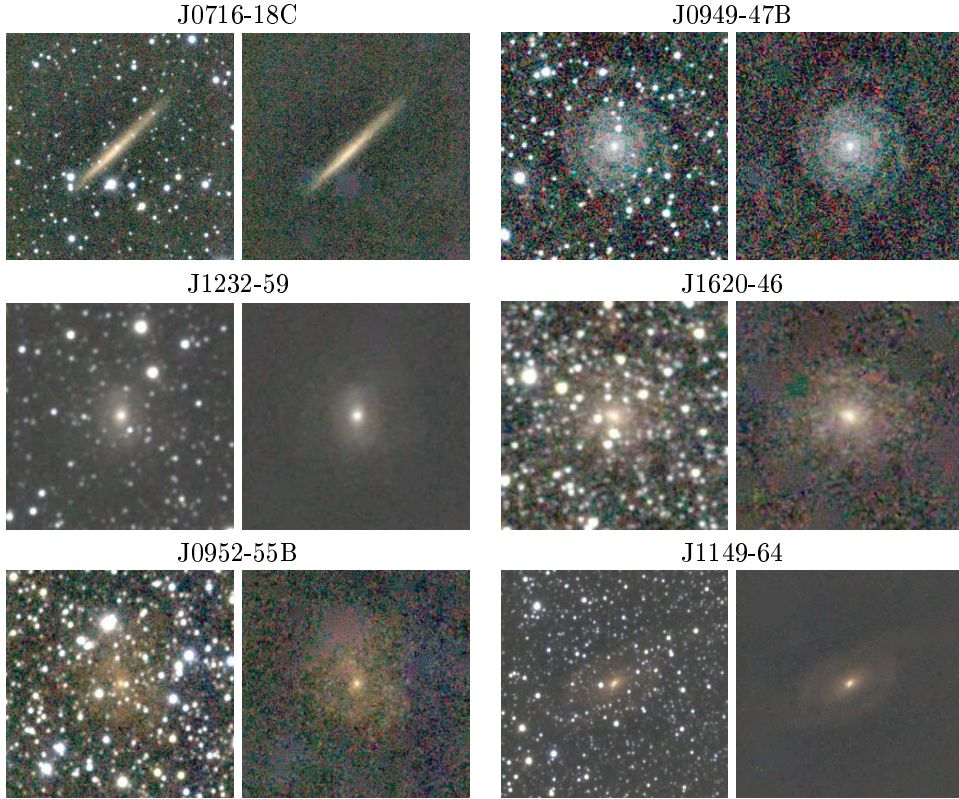


Figure 4.14: Examples of starry and star-subtracted postage stamp images. The colours of the galaxies are representative of the true NIR colours.

brightness. J1232-59 appears white and J1620-46 appears slightly redder as it lies behind more extinction. J0952-55B and J1149-64 both lie behind a heavy layer of dust and thus appear very red.

4.7 Surface Photometry

The extraction of simple parameters, such as total magnitude, mean surface brightness and isophotal radius of a galaxy is actually more complicated for larger galaxies than smaller galaxies. The larger number of pixels on which these galaxies lie increases the difficulty, in particular because the outer pixels are dominated by the sky. In general, larger galaxies require a full surface photometry study of their isophotes and shape. The use of elliptical isophotes, while they are the simplest shape to use, is justified by Kepler's first law. This is particularly true in elliptical galaxies (e.g. Jedrzejewski 1987). The first stage is the reduction of the two-dimensional image onto a one-dimensional profile determined by elliptical isophotes.

The following sections describe the surface photometry and the astrometric, geometric and photometric parameters derived thereby.

4.7.1 Astrometric Parameters

Source Positions

Two positional measurements are made. The first is the position of the peak pixel in the J band which is most sensitive, except in regions of very high extinction. The second is based on the intensity-weighted centroid of the $J + H + K_s$ “super” co-add image. The intensity-weighted mean or first order moment is given by

$$X = \bar{x} = \frac{\sum_{i \in S} I_i x_i}{\sum_{i \in S} I_i}, \text{ and} \quad (4.6)$$

$$Y = \bar{y} = \frac{\sum_{i \in S} I_i y_i}{\sum_{i \in S} I_i}, \quad (4.7)$$

where I_i is the intensity at pixel (x_i, y_i) of source S . x and y are in image coordinates and are transformed to J2000 and Galactic coordinates via the WCS solution of each field.

Ellipse Fitting and Object Orientation

Ellipses were fitted to each galaxy image using the IRAF task `ellipse`. The central coordinates, (X, Y) , are fixed while the position angle (ϕ , measured counterclockwise from the x -axis) and ellipticity ($\epsilon = 1 - b/a$) are fit at intervals in the semi-major axis. `ellipse` returns a table containing, amongst others, the intensity in counts enclosed within the ellipse, the position angle, the ellipticity and their errors at each semi-major axis step. The ellipticity and position angle characteristic of the galaxy are determined to be the average value in the outer part of the disk, between the 1σ and 2σ isophotes, where σ is the sky rms. Both the ellipticity and the position angle are usually stable in the outer disk. The ellipse parameters are determined in all three bands. The final position angle is transformed to J2000 coordinates.

4.7.2 SELF-sky Correction for Large Galaxies

The nature of the SELF-sky measurement (see Sect. 4.2.1 and Sect. 4.3.3) means that galaxies larger than the dither radius, overlap in the individual dithered frames, $\mathbf{self}_d^f(i)$. The final sky frame, $\mathbf{SELF}(i)$, therefore contains an extended residual in the region of the galaxy. The result is that too much sky is subtracted from the region around the galaxy causing the measured fluxes to be lower than they should be. This is clearly evident in the intensity profile of the galaxy as a dip in flux around the outer edges below the median sky level. The residual is such that it is largest in the centre of the galaxy, decreasing towards the outer parts. However, it cannot be measured directly at the centre of the galaxy. We therefore measure the shape of the recovery of the dip in the outer parts to the sky level and extrapolate to the centre. This is done by fitting a linear function to the intensity

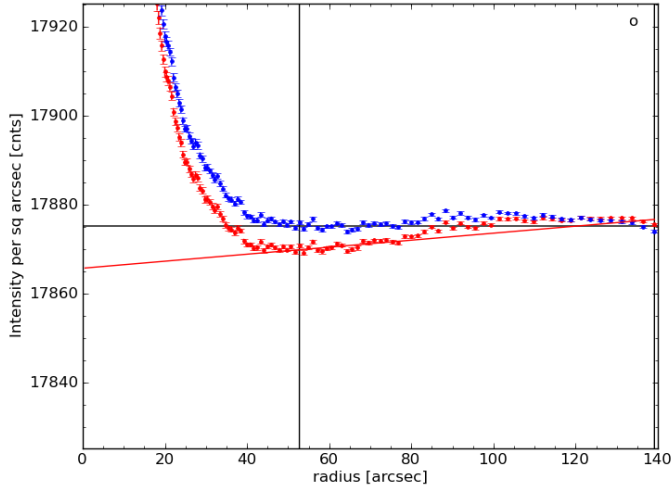


Figure 4.15: Example intensity profile with SELF-sky correction. The red profile shows the intensity profile before the correction. A linear function is fitted to the outer part of the profile from the minimum (red line) to the outer edge where the sky level is reached. The limits of the fit are shown with solid vertical lines. The horizontal line shows the measured median sky level in the image. The blue profile shows the corrected profile.

profile between the minimum intensity and the asymptotic sky value and adding this to the intensity profile. A linear function was chosen as it is the simplest function that describes the shape of the dip. It provides a first order correction while introducing as little error as possible from a higher order terms. The size of the correction at the centre of the galaxy can be up to 5 – 10 counts pixel⁻¹ for large bright galaxies.

A correction for this effect is made for galaxies which have both semi-major and -minor axes that are larger than the dither radius. Figure 4.15 shows as an example for one galaxy (J0748-26B) the *H* band intensity profile. The red profile is uncorrected. The red line shows the fit that has been made from the minimum in the profile to the outer edges. The fit region is demarcated by two vertical lines. The horizontal line shows the measured median sky value. The blue profile shows the corrected intensity profile.

The correction is applied to the image for further photometric analysis, using the determined elliptical parameters (centre, ellipticity and position angle).

4.7.3 Photometric Parameters

Radial Surface Brightness Profiles

The one-dimensional radial surface brightness profile (SBP) is measured with `ellipse` by holding the position angle and ellipticity fixed, in addition to the position. The SBPs of

each galaxy were fitted with a double Sérsic function,

$$\mu(a) = \mu_0 + 1.086 \left(\frac{a}{r_h} \right)^n + \mu_{0,2} + 1.086 \left(\frac{a}{r_{h,2}} \right)^{n,2}, \quad (4.8)$$

or in terms of intensities,

$$I(a) = I_0 \exp \left(\frac{a}{r_h} \right)^n + I_{0,2} \exp \left(\frac{a}{r_{h,2}} \right)^{n,2}. \quad (4.9)$$

The double Sérsic function is the most general profile that allows for the simultaneous fitting of both an inner bulge (usually following a de Vaucouleurs profile with $n = 4$) and an outer disk profile (exponential with $n = 1$).

A plot of the SBP in each band is produced which shows the measured SBP, the fitted SBP, the residuals, the fitted parameters and a grey-scale image and ellipse parameters. Examples of such SBP plots for J0748-26B are shown in Fig. 4.16. In each plot the upper panel shows the surface brightness, μ in mag arcsec^{-2} , as a function of semi-major axis, a in arcsec . The inset panel shows a grey-scale image of the galaxy, with the characteristic ellipse plotted in white. The parameters of the ellipse are given below the inset and the radius of the ellipse is determined to be the 1σ isophote, which is marked on the SBP by the horizontal and vertical dashed lines. The solid line shows the fitted profile, the parameters of which are printed in the top left of the plot. The lower panel shows the residuals, in mag arcsec^{-2} , of the fitted profile.

Following a similar analysis to Kirby et al. (2008b), extrapolation of the analytic double Sérsic function allows for an accurate estimate of the flux that remains undetected below the sky noise. The integrated flux between an outer radius, r_{out} , and $r = \infty$ is:

$$\Delta m = -2.5 \log \left(\frac{I_{\text{missing}}}{I_{\text{total}}} \right) \quad (4.10)$$

where

$$\begin{aligned} I_{\text{missing}} &= \int_0^{a_{\text{tot}}} 2\pi(1-\epsilon)I(a)a da \\ &= \int_0^{a_{\text{tot}}} 2\pi(1-\epsilon) \left[I_0 \exp \left(\frac{a}{r_h} \right)^n + I_{0,2} \exp \left(\frac{a}{r_{h,2}} \right)^{n,2} \right] a da \\ &= 2\pi(1-\epsilon) \left\{ \frac{I_0 r_h^2}{n} \Gamma \left[\frac{2}{n}, \left(\frac{r_{\text{tot}}}{r_h} \right)^n \right] + \frac{I_{0,2} r_{h,2}^2}{n,2} \Gamma \left[\frac{2}{n,2}, \left(\frac{r_{\text{tot}}}{r_{h,2}} \right)^{n,2} \right] \right\} \end{aligned} \quad (4.11)$$

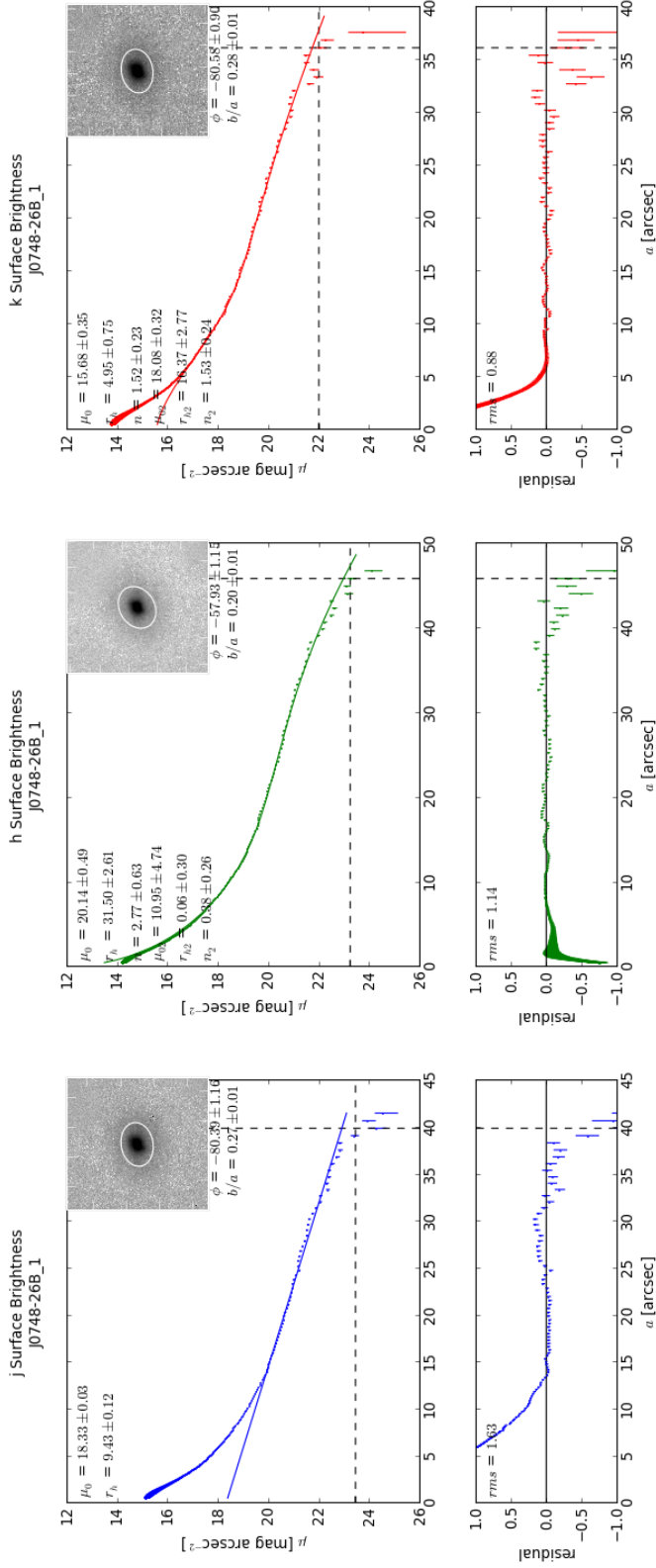


Figure 4.16: Example of radial SBP plots in the J (left), H (centre) and K_s (right) bands for galaxy J0748-26B. The best-fit double Sérsic function is shown as a solid line together with the residuals in the bottom panel. The rms of the fit, in mag arcsec $^{-2}$, is given in the top left corner of the bottom panel. The inset panel shows a greyscale image of the galaxy, with the characteristic ellipse. The parameters of the ellipse are given below the inset and the radius of the ellipse is determined to be the 1σ isophote, which is marked on the SBP by the horizontal and vertical dashed lines.

and

$$\begin{aligned}
 I_{\text{total}} &= \int_0^\infty 2\pi(1-\epsilon)I(a)a da \\
 &= \int_0^\infty 2\pi(1-\epsilon) \left[I_0 \exp\left(\frac{a}{r_h}\right)^n + I_{0,2} \exp\left(\frac{a}{r_{h,2}}\right)^{n,2} \right] a da \\
 &= 2\pi(1-\epsilon) \left\{ \frac{I_0 r_h^2}{n} \Gamma\left[\frac{2}{n}\right] + \frac{I_{0,2} r_{h,2}^2}{n,2} \Gamma\left[\frac{2}{n,2}\right] \right\}.
 \end{aligned} \quad (4.12)$$

$\Gamma[\alpha, x]$ is the incomplete gamma function and a_{tot} was taken to be the radius at which the surface brightness drops to 1σ . The observed total magnitude, m_{obs} , is the magnitude enclosed within this aperture. The total magnitude is then determined to be:

$$m_{\text{tot}} = m_{\text{obs}} - \Delta m. \quad (4.13)$$

Fixed Aperture Magnitudes

The simplest photometric measurement is for fixed circular apertures. Magnitudes are measured using a python routine for apertures of $3''$, $5''$, $7''$, $10''$ and $15''$.

Isophotal Magnitudes

Isophotal elliptical aperture photometry is performed in each band, using the `ellipse` task. The isophotal radius, r_μ , is the radius of the isophote at surface brightness μ . The isophotal magnitude, m_μ , is defined as the integrated magnitude within that radius. In each band the $\mu = 20$ mag arcsec $^{-2}$, $\mu = 21$ mag arcsec $^{-2}$ and $\mu = 22$ mag arcsec $^{-2}$ isophotal radii and magnitudes are calculated. The surface brightness profile is used to determine the radius at which a given surface brightness is reached.

Photometric Errors

The fundamental limits to the photometry depend on the accuracy of the background determination, the S/N within the aperture and the zeropoint calibration. The error, σ_F , on a flux within a given aperture, F , is the quadrature sum of the Poissonian source noise and the error in the sky background:

$$\sigma_F = \sqrt{F + N\sigma_{rms}^2}, \quad (4.14)$$

where N is the number of pixels in the aperture and σ_{rms} is the sky background

The ellipse fitting procedures will introduce additional errors, however, these are neglected here as they are expected to be less significant than the errors already mentioned.

Chapter 5

Near Infrared Galaxy Catalogue

This chapter presents the final catalogue of NIR galaxies identified as possible HI counterparts to the HIZOA galaxies. The parameters listed in the catalogue are described and the quality of the photometry is assessed by comparing it to the 2MASS photometry where available. To further assess the photometric quality of these data we also compare it to that from the Norma Wall Survey which was performed with the same telescope, instrument and exposure times, but with a different data reduction and photometry pipeline. The NIR colours of these galaxies are used to investigate the nature of extinction across the survey region. In the final two sections, the NIR counterparts for the HI sources are confirmed and an analysis of some of the HI and NIR properties of these galaxies is made.

5.1 Catalogue Parameters

The astrometric, geometric and photometric parameters described in the previous Chapter are all listed in the final galaxy catalogue. Various parameters pertaining to each observation, including the observation date, the seeing parameters and the magnitude zero points for all three bands are also given. A complete list with brief descriptions of all the parameters in the final catalogue is given below. The list shows the column number, followed by the column name and the description. The units or column format are shown in square brackets where applicable.

***Column 1 Designation:** Unique identifier [ZOAhmmss.sss±ddmmss.ss]

***Column 2 Jname:** HI catalogue name [Jhhmm±dd]

Column 3 Date: Observation date [ccyy-mm-dd]

Columns 4 & 5 RA, Dec: J2000 Equatorial coordinates [deg]

***Columns 6 & 6 1, b:** Galactic coordinates [deg]

***Columns 8 & 9 j_ell, j_ell_sig:** J band ellipticity ($\epsilon = 1 - b/a$) and error

***Columns 10 & 11 j_phi, j_phi_sig:** J band position angle (East of North) and error [deg]

Columns 12 & 13 `h_ell, h_ell_sig`: H band ellipticity ($\epsilon = 1 - b/a$) and error

Columns 14 & 15 `h_phi, h_phi_sig`: H band position angle (East of North) and error
[deg]

Columns 16 & 17 `k_ell, k_ell_sig`: K_s band ellipticity ($\epsilon = 1 - b/a$) and error

Columns 18 & 19 `k_phi, k_phi_sig`: K_s band position angle (East of North) and error
[deg]

Column 20 `r_j20e`: J_{20} isophotal radius [arcsec]

Columns 21 & 22 `j_m_j20e, j_msig_j20e`: J_{20} isophotal magnitude and error [mag]

Column 23 `r_h20e`: H_{20} isophotal radius [arcsec]

Columns 24 & 25 `h_m_j20e, h_msig_j20e`: H_{20} isophotal magnitude and error [mag]

Column 26 `r_k20e`: K_{s20} isophotal radius [arcsec]

Columns 27 & 28 `k_m_j20e, k_msig_j20e`: K_{s20} isophotal magnitude and error [mag]

Column 29 `r_j21e`: J_{21} isophotal radius [arcsec]

Columns 30 & 31 `j_m_j21e, j_msig_j21e`: J_{21} isophotal magnitude and error [mag]

Column 32 `r_h21e`: H_{21} isophotal radius [arcsec]

Columns 33 & 34 `h_m_j21e, h_msig_j21e`: H_{21} isophotal magnitude and error [mag]

Column 35 `r_k21e`: K_{s21} isophotal radius [arcsec]

Columns 36 & 37 `k_m_j21e, k_msig_j21e`: K_{s21} isophotal magnitude and error [mag]

Column 38 `r_j22e`: J_{22} isophotal radius [arcsec]

Columns 39 & 40 `j_m_j22e, j_msig_j22e`: J_{22} isophotal magnitude and error [mag]

Column 41 `r_h22e`: H_{22} isophotal radius [arcsec]

Columns 42 & 43 `h_m_j22e, h_msig_j22e`: H_{22} isophotal magnitude and error [mag]

Column 44 `r_k22e`: K_{s22} isophotal radius [arcsec]

Columns 45 & 46 `k_m_j22e, k_msig_j22e`: K_{s22} isophotal magnitude and error [mag]

***Column 47** `r_k20fe`: K_{s20} fiducial isophotal radius [arcsec]

***Columns 48 & 49** `j_m_k20fe, j_msig_k20fe`: J band K_{s20} fiducial isophotal magnitude and error [mag]

***Columns 50 & 51** `h_m_k20fe, h_msig_k20fe`: H band K_{s20} fiducial isophotal magnitude and error [mag]

***Columns 52 & 53** `k_m_k20fe, k_msig_k20fe`: K_s band K_{s20} fiducial isophotal magnitude and error [mag]

Column 54 `r_k20fe`: J_{21} fiducial isophotal radius [arcsec]

Columns 55 & 56 `j_m_j21fe, j_msig_j21fe`: J band J_{21} fiducial isophotal magnitude and error [mag]

Columns 57 & 58 `h_m_j21fe, h_msig_j21fe`: H band J_{21} fiducial isophotal magnitude and error [mag]

Columns 59 & 60 `k_m_j21fe, k_msig_j21fe`: K_s band J_{21} fiducial isophotal magnitude and error [mag]

***Column 61** `j_m_ext`: J band extrapolated total magnitude [mag]

***Column 62** `h_m_ext`: H band extrapolated total magnitude [mag]
***Column 63** `k_m_ext`: K_s band extrapolated total magnitude [mag]
***Column 64** `j_msig_ext`: J band extrapolated total magnitude error [mag]
***Column 65** `h_msig_ext`: H band extrapolated total magnitude error [mag]
***Column 66** `k_msig_ext`: K_s band extrapolated total magnitude error [mag]
Column 67 `j_dm_ext`: J band difference between total magnitude and J_{21} magnitude [mag]
Column 68 `h_dm_ext`: H band difference between total magnitude and H_{21} magnitude [mag]
Column 69 `k_dm_ext`: K_s band difference between total magnitude and K_{s21} magnitude [mag]
Columns 70 & 71 `j_m3, j_msig3`: J band 3'' aperture magnitude and error [mag]
Columns 72 & 73 `j_m5, j_msig5`: J band 5'' aperture magnitude and error [mag]
Columns 74 & 75 `j_m7, j_msig7`: J band 7'' aperture magnitude and error [mag]
Columns 76 & 77 `j_m10, j_msig10`: J band 10'' aperture magnitude and error [mag]
Columns 78 & 79 `j_m15, j_msig15`: J band 15'' aperture magnitude and error [mag]
Columns 80 & 81 `h_m3, h_msig3`: H band 3'' aperture magnitude and error [mag]
Columns 82 & 83 `h_m5, h_msig5`: H band 5'' aperture magnitude and error [mag]
Columns 84 & 85 `h_m7, h_msig7`: H band 7'' aperture magnitude and error [mag]
Columns 86 & 87 `h_m10, h_msig10`: H band 10'' aperture magnitude and error [mag]
Columns 88 & 89 `h_m15, h_msig15`: H band 15'' aperture magnitude and error [mag]
Columns 90 & 91 `k_m3, k_msig3`: K_s band 3'' aperture magnitude and error [mag]
Columns 92 & 93 `k_m5, k_msig5`: K_s band 5'' aperture magnitude and error [mag]
Columns 94 & 95 `k_m7, k_msig7`: K_s band 7'' aperture magnitude and error [mag]
Columns 96 & 97 `k_m10, k_msig10`: K_s band 10'' aperture magnitude and error [mag]
Columns 98 & 99 `k_m15, k_msig15`: K_s band 15'' aperture magnitude and error [mag]
Columns 100–102 `j_sb_core, h_sb_core, k_sb_core`: J , H and K_s central surface brightness [mag arcsec $^{-2}$]
Columns 103–105 `j_peak, h_peak, k_peak`: J , H and K_s peak flux [mag]
Columns 106–108 `j_back, h_back, k_back`: J , H and K_s background values [mag arcsec $^{-2}$]
Columns 109 & 110 `im_nx, im_ny`: Postage stamp x and y dimensions [pix]
Column 111 `Photflag`: Photometry quality flag [int]
Columns 112–114 `j_sbflag, h_sbflag, k_sbflag`: J , H and K_s surface brightness fit flag [int]
Columns 115–117 `j_magzp, h_magzp, k_magzp`: J , H and K_s magnitude zero point
Columns 118–120 `j_see, h_see, k_see`: J , H and K_s FWHM seeing [arcsec]
Columns 121–123 `j_expos, h_expos, k_expos`: J , H and K_s exposure time [sec]
***Column 124** `ebv`: Galactic reddening along the line of sight (Schlegel et al. 1998) [mag]
***Column 125** `SD`: Log of the stellar density for stars brighter than 14^m in K_s

A sample of the catalogue with only the columns marked with a * is given in Appendix A, Table A.1. This table contains the brightest, $K_{s20} < 11^m$, galaxies. The choice of including only the J band ellipticity in the sample catalogue was made because this parameter is used in Chapter 6 for the determination of the inclination of each galaxy. The longer wavebands are assumed to be increasingly biased to the bulge of the galaxies and so the J band should provide the best estimate of the inclination of the disk. The full catalogue is available in electronic form on the internet*.

5.2 Quality Control

5.2.1 Comparison with 2MASX

A comparison was made between the 2MASS and IRSF photometric parameters of the galaxies for which counterparts are available in the 2MASX catalogue. Of the 821 HIZOA galaxies within $v = 6000 \text{ km s}^{-1}$, 101 have counterparts in 2MASX, of which 82 have been observed with the IRSF. Sixty-nine of these galaxies have reliable 2MASS and IRSF photometry and can therefore be used to assess the quality of our photometry compared to 2MASS. In many cases, the 2MASS coordinates are offset from the IRSF coordinates because the source is centered on a nearby foreground star which has not been removed. Only sources with reliable IRSF photometry are compared, i.e. galaxies near the edge of the field are excluded.

The comparison is made for both the $5''$ aperture magnitudes and the $K_s = 20^m$ fiducial isophotal magnitudes in all three bands. The metric used is

$$\Delta m = m(\text{2MASS}) - m(\text{IRSF}). \quad (5.1)$$

Thus a positive quantity means that the 2MASS magnitude is fainter than the IRSF. All IRSF/SIRIUS magnitudes are transformed to the 2MASS standard via the transformation given in Eqs. 4.4. Figure 5.1 shows the comparison of the IRSF/SIRIUS and 2MASS magnitudes. The $5''$ aperture photometry in all three bands is compared in the *left* panel and the $K_s = 20^m$ fiducial isophotal magnitudes are compared in the *right* panel. In both figures the horizontal coloured strip shows the 1σ dispersion around the mean (horizontal dashed line). The mean and standard deviation is given in the top left corner of each plot. The mean offsets and standard deviations are summarised in Table 5.1. The offsets and dispersion are smaller for the $5''$ aperture than the isophotal magnitudes. This is to be expected given the smaller apertures used, although it may be more affected by the different methods used for determining the position. 2MASX uses the peak J band pixel while our photometry is based on the centroid of the super co-add image. Note that that seeing corrections are deemed negligible given the excellent observing conditions. On average, the IRSF isophotal magnitudes are fainter than the 2MASX magnitudes. This is not surprising because

*password-protected at <http://www.ast.uct.ac.za/~wendy/zoatf/nircat>, for access email the author (wendy*AT*ast.uct.ac.za)

of the higher resolution of IRSF/SIRIUS which improves the detection and subtraction of faint stars within the isophotal radius. The dispersion in all three bands is ~ 2 times that obtained by Riad (2010) when comparing IRSF/SIRIUS isophotal magnitudes (same instrumental set-up) to 2MASX. However, our larger dispersion may originate from the fact that our sample is composed mostly of spiral galaxies, many of which have extended faint disks, whereas Riad's sample contains many more elliptical galaxies. Note also that the $K_s = 20^m$ fiducial isophotal magnitudes are measured in differently determined apertures.

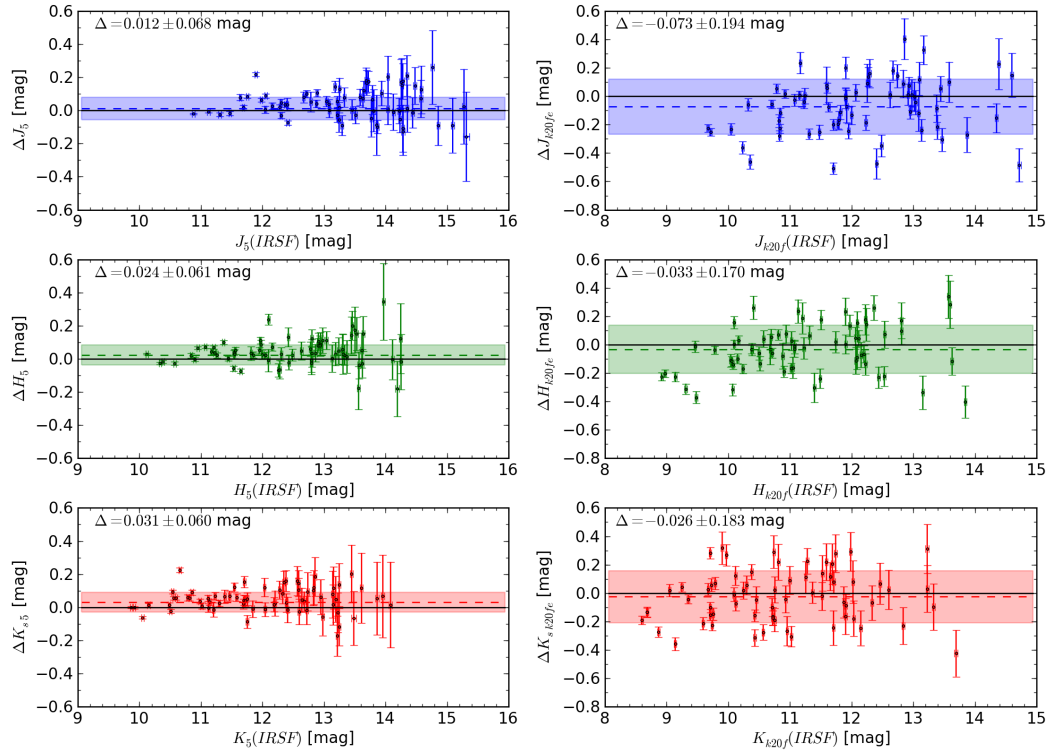


Figure 5.1: Comparison of the $5''$ circular aperture (left) and $K_s = 20^m$ fiducial isophotal (right) magnitudes in J (top), H (middle) and K_s (bottom) between the IRSF and 2MASX. The horizontal coloured strip shows the 1σ dispersion around the mean.

Table 5.1: Comparison of 2MASX and IRSF/SIRIUS $5''$ aperture and $K_s = 20^m$ fiducial isophotal magnitudes

Filter	$5''$ aperture		$K_s = 20^m$ fiducial	
	$\langle \Delta m \rangle$	σ	$\langle \Delta m \rangle$	σ
	[mag]	[mag]	[mag]	[mag]
J	0.012	0.068	-0.07	0.19
H	0.024	0.061	-0.03	0.17
K_s	0.031	0.060	-0.03	0.18

5.2.2 Comparison with Other IRSF Observations in the ZoA

We also compare the photometry of galaxies common to both our survey and the Norma Wall Survey (Riad 2010) which was conducted using IRSF/SIRIUS with the same instrumental set-up and observing parameters. Sixteen galaxies with reliable photometry in both catalogues were found. Here the metric used is

$$\Delta m = m(NWS) - m(IRSF). \quad (5.2)$$

Figure 5.2 shows the comparison of the 5'' and isophotal magnitudes of these galaxies. Table 5.2 lists the means and standard deviations of each comparison. The table also lists the standard deviations derived for the NWS using multiply-observed galaxies.

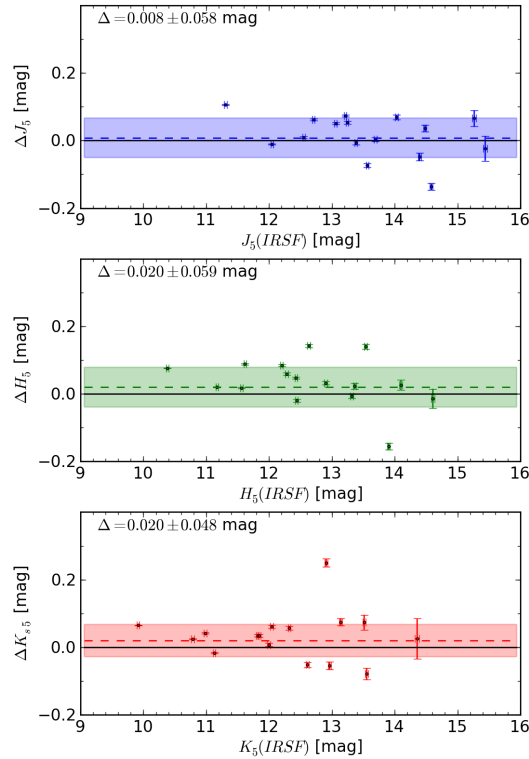


Figure 5.2: Comparison of the 5'' circular aperture magnitudes in J (top), H (middle) and K_s (bottom) between the IRSF and NWS. The horizontal coloured strip shows the 1 σ dispersion around the mean.

5.2.3 Internal Consistency

A small number of galaxies were observed in more than one field, 9 of which have reliable photometry. The overlap is largely due to two HI galaxies within 4' of each other and were thus observed twice with small positional offsets. For these galaxies we compare the 5'' aperture magnitudes derived from each image as an indication of the repeatability of the

Table 5.2: Comparison of 2MASX and IRSF/SIRIUS 5'' aperture magnitudes

Filter	5'' aperture		
	$\langle \Delta m \rangle$ [mag]	σ [mag]	σ_{NWS} [mag]
<i>J</i>	0.008	0.058	0.140
<i>H</i>	0.020	0.059	0.134
<i>K_s</i>	0.020	0.048	0.140

photometry and the photometric accuracy. Here the metric used is

$$\Delta m = m(\text{IRSF}_1) - m(\text{IRSF}_2). \quad (5.3)$$

Figure 5.3 shows the comparison of the 5'' aperture magnitudes of these galaxies. Table 5.3 lists the means and standard deviations of each comparison. The table also lists the standard deviations derived for the NWS using multiply-observed galaxies. We find that, despite the small size of this sample, the scatter is consistent with that of the NWS.

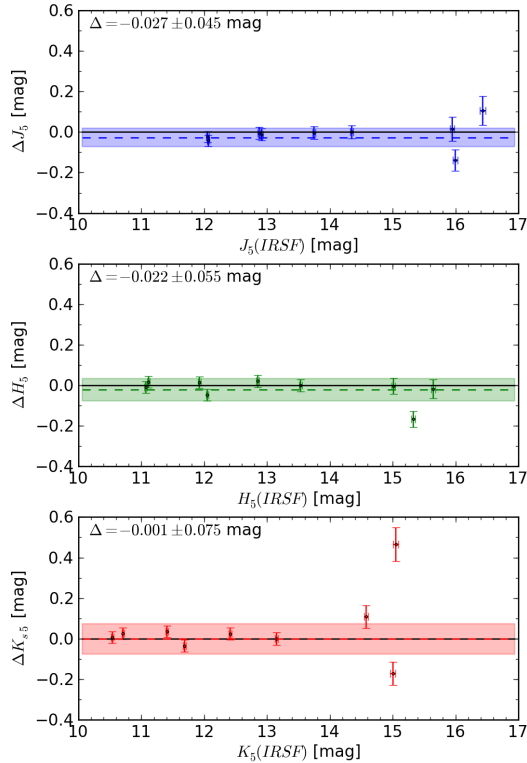


Figure 5.3: Comparison of the 5'' circular aperture magnitudes in *J* (top), *H* (middle) and *K_s* (bottom) for doubly-observed galaxies. The horizontal coloured strip shows the 1σ dispersion around the mean.

Table 5.3: Internal consistency of the 5'' aperture magnitudes

Filter	5'' aperture		
	$\langle \Delta m \rangle$	σ	σ_{NWS}
	[mag]	[mag]	[mag]
<i>J</i>	-0.027	0.045	0.140
<i>H</i>	-0.022	0.055	0.134
<i>K_s</i>	-0.001	0.075	0.140

5.3 Extinction and NIR Colours

The Schlegel et al. (1998) extinction maps derived from the DIRBE/IRAS data are not properly calibrated at low Galactic latitudes ($|b| < 5^\circ$) (see Sect. 1.1.1 for a full discussion of extinction including the DIRBE/IRAS extinction maps). Foreground contaminating sources are not removed from their maps at $|b| < 5^\circ$ which would lead to an overestimate of the extinction. Moreover, Schlegel et al. (1998) assume an extinction law with $R_V \sim 3.1$, while the dust composition of giant molecular clouds within the Galactic disk is likely to differ from less dense dust clouds further from the Galactic plane. Thus the extinction law and R_V parameter should vary across the Galactic plane. Higher density regions consisting of larger grains typically have $R_V \sim 5$. For these regions, the difference in extinction as a function of wavelength is lower (large grains are grey absorbers) and would also imply an overestimation of the total extinction for a given colour.

Despite these problems the DIRBE/IRAS maps remain the best means to estimate the extinction in this region of the sky. Several studies have shown that they do indeed overestimate the extinction. For example, Nagayama et al. (2004) measured the colour excess of giant stars in a region around PKS 1343-601 ($l, b = 309^\circ 7, 1^\circ 7$) and found the Schlegel values to be 33% too high. Schröder et al. (2007) looked at the $I - J$, $J - K_s$ and $I - K_s$ NIR colours of galaxies in the same region and concluded that the extinction is 87% of the DIRBE values, i.e. the DIRBE values overestimate the extinction by 15%. Other independent studies have shown the true extinction to be 67 – 87% of the DIRBE values (Arce & Goodman 1999, Choloniewski & Valentijn 2003, Dutra et al. 2003, Schröder et al. 2005, van Driel et al. 2009). Furthermore, in their study of Northern ZoA galaxies, van Driel et al. (2009) find that the overestimate depends on the amount of extinction, increasing from a factor of 0.86 for galaxies with B band extinction in the range $2 < A_B < 6$, to a factor of 0.69 for the more heavily extincted galaxies with $6 < A_B < 12$. Moreover, the consistency of their values with those derived in the Southern ZoA, closer to the Galactic bulge suggests little or no variation with Galactic longitude.

The colours of nearby galaxies provide an independent means to determine the extinction at low latitudes. To test the validity of the DIRBE/IRAS extinction we apply a correction based on these values and look for residuals in the resulting colours. Figure 5.4 shows the extinction-corrected NIR colours, $(J - H)^o$, $(H - K_s)^o$ and $(J - K_s)^o$, as a function of the K_s band extinction, A_{K_s} . The DIRBE/IRAS maps clearly overestimate the extinction at

these low latitudes. This is done for all NIR detections with reliable photometry in all three bands. The galaxies cover a wide range of Galactic latitude and longitude. The colours were determined from the 5'' aperture magnitudes. The dashed lines show a linear least squares fit to the data. There is a clear trend for the colours of galaxies at high extinction to be bluer than expected. The fits give:

$$\begin{aligned} (J - H)^o &= (-0.100 \pm 0.026)A_{K_s} + (0.680 \pm 0.012) & [\sigma = 0.12], \\ (H - K_s)^o &= (-0.152 \pm 0.025)A_{K_s} + (0.283 \pm 0.012) & [\sigma = 0.12], \text{ and} \\ (J - K_s)^o &= (-0.248 \pm 0.042)A_{K_s} + (0.964 \pm 0.019) & [\sigma = 0.19], \end{aligned} \quad (5.4)$$

where σ is the rms deviation of each fit.

To derive the true extinction as a function of the DIRBE/IRAS extinction we follow the method of Schröder et al. (2007), which is described briefly below.

A generic colour, Eqs. 5.4 may be written in terms of the K_s band extinction as

$$C^o = aA_{K_s} + b, \quad (5.5)$$

and the reddening law is given by

$$C = C^o + \left(\frac{E(C)}{A_{K_s}} \right) A_{K_s}, \quad (5.6)$$

for the DIRBE/IRAS correction and

$$C = \widetilde{C}^o + \left(\frac{E(C)}{A_{K_s}} \right) \widetilde{A}_{K_s}, \quad (5.7)$$

for the true extinction-corrected colour, where the true parameters are denoted by the tilde. $E(C)$ is the colour excess. Combining Eqs. 5.5 to 5.7 results in

$$\widetilde{C}^o = aA_{K_s} + b + \left(A_{K_s} - \widetilde{A}_{K_s} \right) \left(\frac{E(C)}{A_{K_s}} \right). \quad (5.8)$$

Since there is a clear trend in C with A_{K_s} , the true extinction cannot simply be a constant additive offset from the DIRBE/IRAS value. We therefore assume that the correction is a constant multiplicative factor, i.e.

$$\widetilde{A}_{K_s} = fA_{K_s}. \quad (5.9)$$

Substituting this into Eq. 5.8 yields

$$\widetilde{C}^o = \left[a + \frac{E(C)}{A_{K_s}} (1 - f) \right] A_{K_s} + b. \quad (5.10)$$

Now, in order for the true colour to be independent of extinction, the first term must be

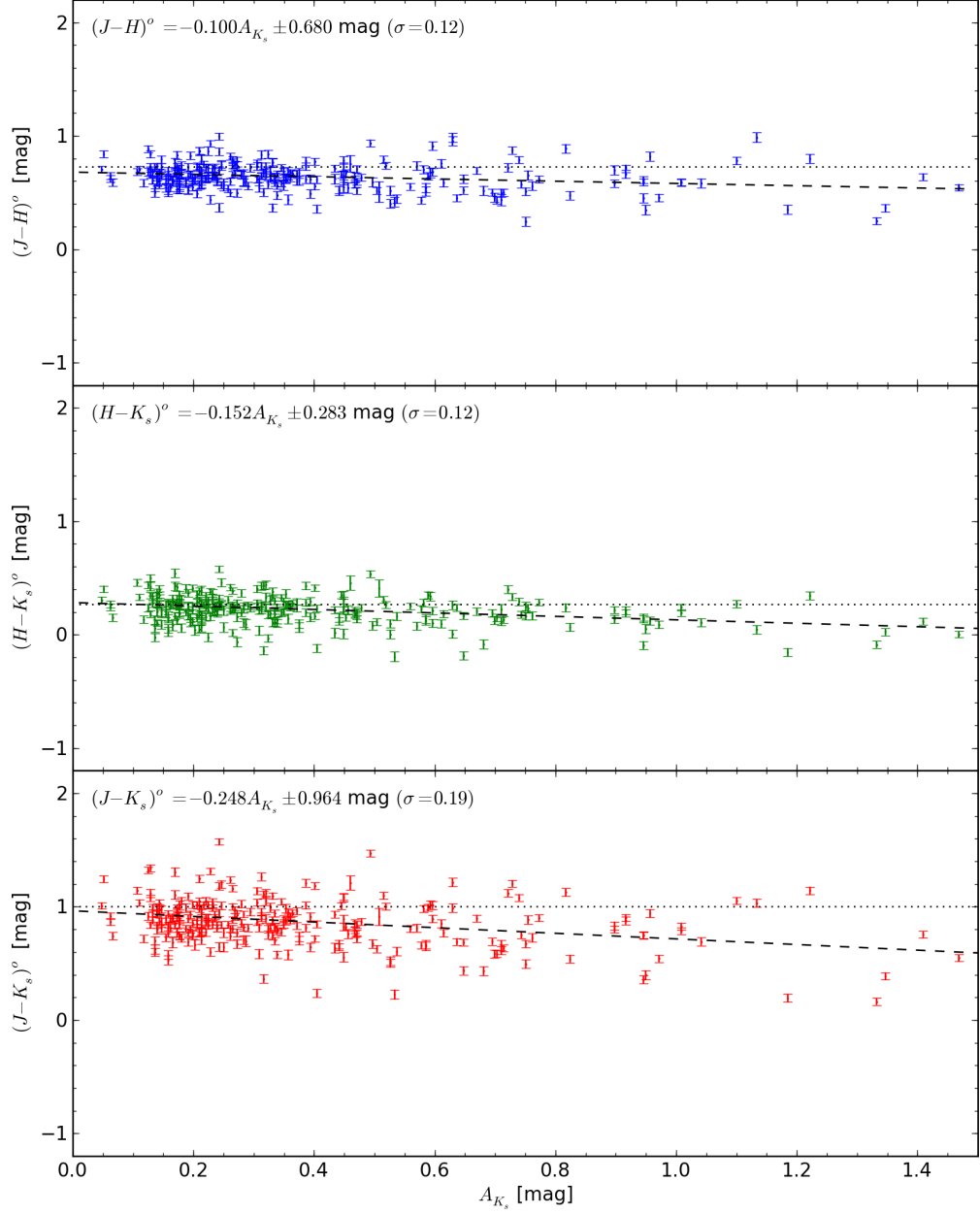


Figure 5.4: Extinction-corrected NIR colours plotted as a function of K_s band extinction derived from the DIRBE/IRAS maps (Schlegel et al. 1998), from *top* to *bottom*: $(J - H)^o$ (blue), $(H - K_s)^o$ (green) and $(J - K_s)^o$ (red). The colours are corrected for extinction based on the Schlegel et al. (1998) maps and Cardelli et al. (1989) extinction laws. The dashed lines in each panel show a least squares linear fit to the colours and the fitted linear equation is given in the top left corner. The dotted lines show the mean intrinsic NIR galaxy colours determined by Jarrett et al. (2003).

zero, i.e.

$$a + \frac{E(C)}{A_{K_s}} (1 - f) = 0, \quad (5.11)$$

which implies

$$f = a \left(\frac{E(C)}{A_{K_s}} \right)^{-1} + 1. \quad (5.12)$$

Therefore the slope of the linear fit (Eqs. 5.4) to the colour can be used to determine the correction factor f . For our fits we get

$$\begin{aligned} f_{(J-H)} &= 0.875 \pm 0.032, \\ f_{(H-K_s)} &= 0.723 \pm 0.046, \quad \text{and} \\ f_{(J-K_s)} &= 0.689 \pm 0.052, \end{aligned} \quad (5.13)$$

where the errors were determined via standard error propagation. While there are three values, only two are independent so we combine the first two (which have the lowest rms in the fits and which are consistent at the 2σ level), to conclude that

$$f = 0.82 \pm 0.03. \quad (5.14)$$

Thus, averaging across the entire southern ZoA, the true extinction is 18% lower than predicted by the DIRBE/IRAS values.

Because this sample covers such a large area, we can use it to investigate the extinction in different regions of the Galactic plane. In the following section we determine the correction factor in several latitude and longitude bins.

5.3.1 Variation with Galactic Latitude and Longitude

Figures 5.5 and 5.6 show the extinction factor derived for several Galactic longitude and latitude bins respectively. The size of the bins is restricted by the number of galaxies we have. Each bin contains 15–60 galaxies. From Fig. 5.5 we do not see any significant variation in the correction factor as a function of longitude. There is some variation within the errors. This is consistent with the results of van Driel et al. (2009), which suggest continuity of the overestimation across Galactic longitude. Initial work by Burstein and Heiles (see e.g. Heiles 1976, Burstein & Heiles 1978; 1982) suggested a variation with longitude based on the observed changes in the relationships between the H α gas-to-dust ratio and galaxy counts towards the Galactic bulge.

However, Fig. 5.6, indicates that there is significant variation with Galactic latitude, with the correction factor being smaller within the Galactic plane ($|b| < 1^\circ$) and smallest immediately below the plane ($-1^\circ < b < -3^\circ$). The sample size within each bin prevents a more detailed analysis to investigate whether this trend occurs at all longitudes. Despite this, the fact that the correction factor is smaller above the plane is clear. This appears to follow the asymmetry in the star density and the H α distribution about the Galactic plane,

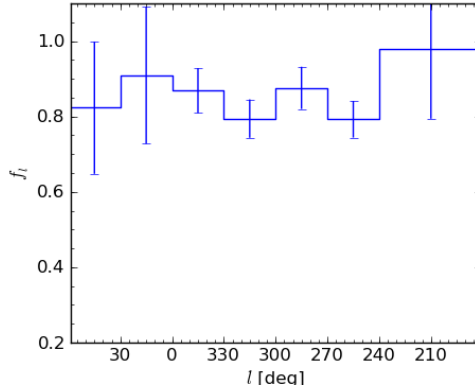


Figure 5.5: DIRBE/IRAS extinction correction factor as a function of Galactic longitude l .

which is consistent with the warp of the Galactic disk falling below the Galactic plane in the Southern hemisphere.

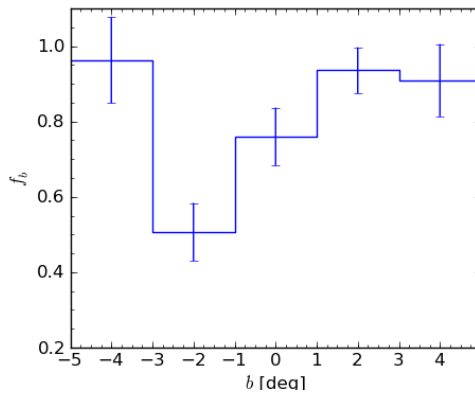


Figure 5.6: DIRBE/IRAS extinction correction factor as a function of Galactic latitude b .

5.4 Catalogue Statistics

5.4.1 Detection Rates

Of the 580 fields that were observed, galaxies were found in 422 fields. A total of 567 galaxies were identified. 141 fields had more than one galaxy identified as a possible counterpart. The identification of NIR counterparts to the H α sources is described in Sect. 5.5, including the likelihood of choosing the right counterpart. Figure 5.7 shows the spatial distribution of the detected galaxies. The small red points show the fields for which no counterpart was identified. The large blue points indicate the fields in which one or more possible H α counterparts were identified. Stellar mass density contours are overlaid for values of $\log N_{(K_s < 14^m)} = 3.5, 4.0, 4.5$ and 5.0 (yellow, orange, red and magenta respectively).

tively). An extinction contour is plotted in grey for $A_{K_s} = 3^{\text{m}}0$ Schlegel et al. (1998). At $\log N_{(K_s < 14^{\text{m}})} > 4.5$, the detection of galaxies correlates with the extinction level. The likelihood of a detection is clearly determined by the foreground stellar density and for a given stellar density decreases at higher extinction. Below the orange contour (i.e. $\log N_{(K_s < 14^{\text{m}})} < 4.0$), nearly all galaxies have NIR detections. The amount of non-detections increases slightly above the orange contour as the stellar density increases. Between the red and magenta contours ($4.5 < \log N_{(K_s < 14^{\text{m}})} < 5.0$), most galaxies have NIR detections, except where the extinction level is very high ($A_{K_s} > 3^{\text{m}}0$). However, for very high star density ($\log N_{(K_s < 14^{\text{m}})} > 5.0$, magenta contour), almost no counterparts are found. Comparison to Fig. 2.9 shows our improved ability to detect the NIR counterparts in regions of higher star density.

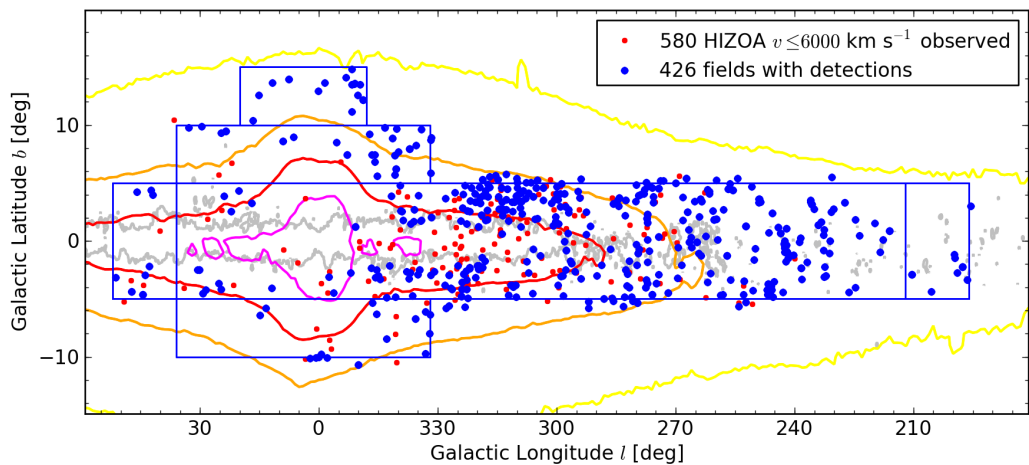


Figure 5.7: Spatial distribution of detected possible NIR counterparts. The small red points show the fields for which no counterpart was identified. The large blue points indicate the fields in which one or more possible HI counterparts were identified. 2MASS PSC stellar density contours are overplotted with values of $\log N_{(K_s < 14^{\text{m}})} = 3.5, 4.0, 4.5$ and 5.0 plotted in yellow, orange, red and magenta respectively. Very few detections are made at $\log N_{(K_s < 14^{\text{m}})} > 5.0$. An extinction contour is plotted in grey for $A_{K_s} = 3^{\text{m}}0$.

The Schlegel foreground extinction of the detected galaxies ranges between $0^{\text{m}}03$ and $4^{\text{m}}48$ with a mean extinction of $\langle 0^{\text{m}}34 \rangle$. Figure 5.8 shows the number of galaxies detected as a function of foreground extinction in the K_s band, A_{K_s} . The histogram shows only those galaxies with $A_{K_s} < 1^{\text{m}}5$. Of the detected galaxies, 0.90% have $A_{K_s} > 1^{\text{m}}5$. The mean extinction is plotted as a vertical dotted line. The stellar density of the detected galaxies ranges between 3.42 and 5.32 with a mean stellar density of $\langle 4.04 \rangle$. Figure 5.9 shows the distribution of detected galaxies as a function of the stellar density, $\log N_{K_s < 14^{\text{m}}}$.

5.4.2 Magnitude and Colour Distribution

This section presents the magnitude and colour distributions of the detected galaxies. Figure 5.10 shows the distribution of the observed (dotted histogram) and extinction-corrected

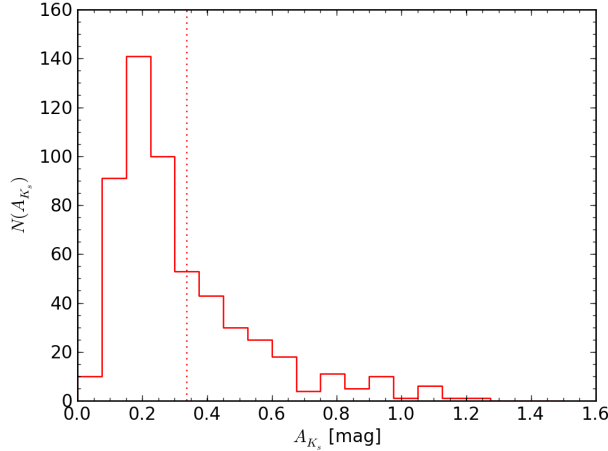


Figure 5.8: Number of galaxies detected as a function of K_s band extinction. Only galaxy counts for galaxies with $A_{K_s} < 1^m5$; 0.90% of the detected galaxies have $A_{K_s} > 1^m5$. The vertical dotted line shows the mean extinction of $\langle 0^m34 \rangle$.

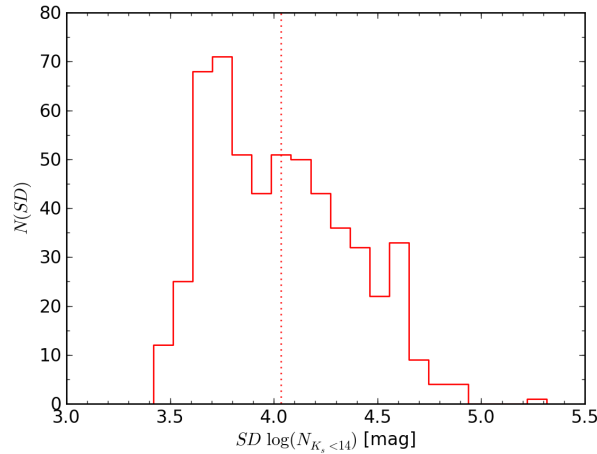


Figure 5.9: Number of galaxies detected as a function of stellar density. The vertical dotted line shows the mean stellar density of $\langle 4^m04 \rangle$.

(solid histogram) $K_s = 20$ mag arcsec $^{-2}$ fiducial isophotal magnitudes in J (blue), H (green) and K_s (red). The magnitudes are corrected for foreground extinction based on the DIRBE/IRAS maps, scaled by the factor 0.82 derived in Sect. 5.3. The mean observed and extinction-corrected magnitudes are listed in Table 5.4; the mean extinction-corrected magnitudes are 0 m 78, 0 m 52 and 0 m 33 brighter than the mean observed magnitudes in J , H and K_s respectively. For comparison the 2MASS completeness limits at high Galactic latitudes are for the J , H and K_s bands respectively: 14 m 7, 13 m 9 and 13 m 1 (Jarrett 2000).

Table 5.4: Mean observed and extinction-corrected $K_s = 20$ mag arcsec $^{-2}$ fiducial isophotal magnitudes

Filter	$\langle m \rangle$ [mag]	$\langle m^o \rangle$ [mag]
J	14.55	13.77
H	13.60	13.08
K_s	13.16	12.83

The 5'' aperture magnitudes are used to derive the NIR colours of the detected galaxies; the distribution of the observed colours is plotted in the *top* panel of Fig. 5.11 and that of the extinction-corrected colours in the *bottom* panel. $J - H$ is plotted in blue, $H - K_s$ in green and $J - K_s$ in red. The mean values of each colour are plotted as vertical dotted lines. It is evident that the distributions of observed colours are skewed towards the red end as a result of selective extinction. This is due to reddening by extinction. The extinction-corrected colour distributions are more symmetric and less dispersed. Table 5.5 lists the mean values of the observed and extinction-corrected colours as well as the dispersion of each distribution. For comparison, the mean colours of the 2MASS Large Galaxy Atlas (LGA), $\langle (J - H)^0 \rangle = 0^m73$, $\langle (H - K)^0 \rangle = 0^m27$ and $\langle (J - K)^0 \rangle = 1^m00$, are also given (Jarrett 2000, Jarrett et al. 2003). The mean extinction-corrected colours of $\langle (J - H)^0 \rangle = 0^m69$, $\langle (H - K)^0 \rangle = 0^m26$ and $\langle (J - K)^0 \rangle = 0^m95$ are consistent with those of the LGA. NIR colours vary only slightly with morphological type, so there is little dispersion introduced by different types present in this sample. Jarrett (2000) plot the NIR colour distributions for the LGA for different morphological types. The dispersion of the extinction-corrected colours of 0 m 1 – 0 m 2 is consistent with the dispersion in their distributions. The consistency between the mean values and dispersions of the extinction-corrected colours derived here and for the 2MASS LGA outside the ZoA adds credence to the new extinction correction derived in Sect. 5.3.

Table 5.5: Mean observed and extinction-corrected colours

Colour	$\langle C \rangle$ [mag]	σ_C [mag]	$\langle C^o \rangle$ [mag]	σ_{C^o}	$\langle C^o \rangle$ (LGA)
$J - H$	0.94	0.22	0.69	0.12	0.73
$H - K_s$	0.43	0.16	0.26	0.12	0.27
$J - K_s$	1.37	0.35	0.95	0.19	1.00

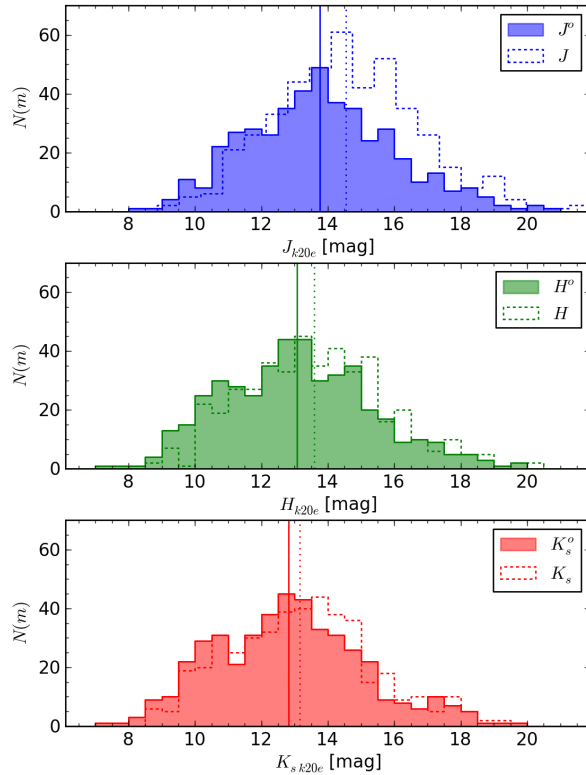


Figure 5.10: Distribution of $K_s = 20$ mag arcsec $^{-2}$ fiducial isophotal magnitudes in J (top, blue), H (middle, green) and K_s (bottom, red) in 0 m 5 bins. The dotted histograms show the observed magnitudes and the filled solid histograms show the extinction-corrected magnitudes. The vertical dotted lines indicate the mean observed values and the vertical solid lines show the mean extinction-corrected magnitudes.

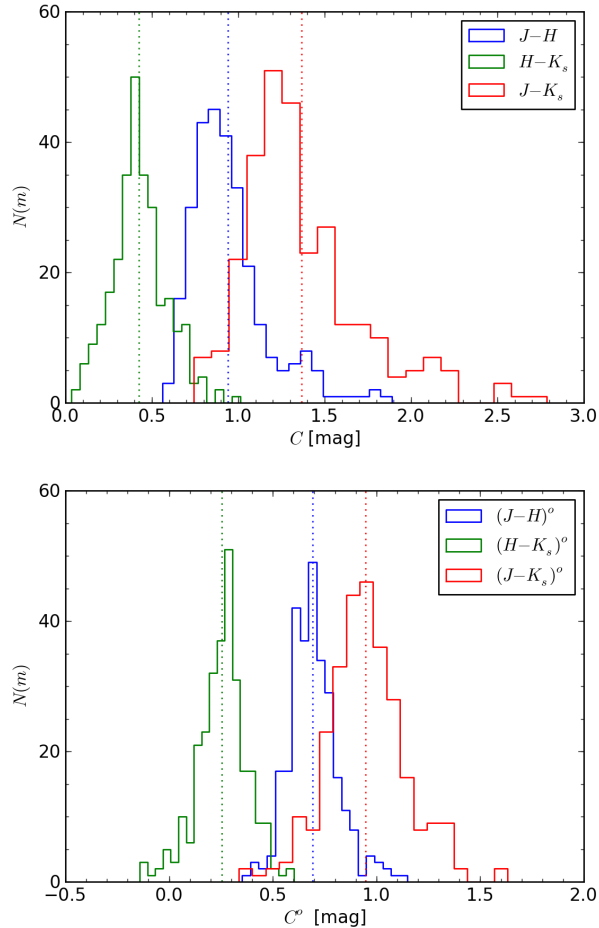


Figure 5.11: Histograms showing the distribution of NIR colours derived from the 5'' aperture magnitudes. The *top* panel shows the observed colour distributions which are skewed to the right (redder) due to selective extinction. The *bottom* panel shows the extinction-corrected colour distributions which are more symmetric. $J - H$ is shown in blue, $H - K_s$ in green and $J - K_s$ in red. Vertical dotted lines indicate the mean values of each distribution.

5.5 HI Counterpart Identification

The NIR catalogue contains all galaxies identified as possible HI counterparts. Visual inspection of the HI spectra of the 422 HI galaxies for which possible NIR counterparts were identified allowed for the confirmation of the counterpart for 356 (84%) HI galaxies. Both the HI spectra and NIR images were used to aid in the counterpart identification. For instance a galaxy with a clear double horn profile was identified as an edge-on NIR galaxy and one with a Gaussian-shaped profile was identified as a face-on galaxy. Of the 141 fields with more than one possible identified counterpart, a single counterpart could be confirmed for 75 fields, while the NIR counterpart for 66 fields remained ambiguous. In the cases of positive identification of the NIR counterpart, usually only the presence of a strong double horn profile and clearly inclined galaxy allowed for confirmation of the counterpart.

The offsets between the HI and IRSF positions for the confirmed counterparts are plotted in Fig. 5.12. The large circle shows an offset of $4'$, which is the pixel size of the HI data. 98% of the detections lie within $4'$ and 88% are within $3'$. Table 5.6 lists the number of counterparts found and the number confirmed within $3'$ and $4'$. The number confirmed is also given as a percentage of the number found, i.e. 62% of counterparts within $3'$ were confirmed, dropping to 55% within $4'$. As a comparison, for the two parts of HIZOA Northern Extension (NE), Donley et al. (2005) confirm 54 – 60% 2MASS counterparts within $3'$ and 52 – 67% within $5'$. Note that the size of the IRSF field precludes the consideration of all possible counterparts within $5'$, but Donley’s $5'$ values are reproduced here for completeness. In fact, in their final counterpart selection, Donley et al. (2005) exclude counterparts offset by $> 4'$ as statistically unlikely. Our detection rate is consistent with that of Donley et al. (2005) bearing in mind that these NIR data are deeper than 2MASS and is better able to penetrate both the dust and stars of the Milky Way, our counterpart detection rate of 62% within $3'$ is comparable to the NE 2MASS counterpart detection rates. Furthermore, the NE fields lie at lower extinction and star density than much of the rest of the HIZOA fields.

Table 5.6: Counterpart detection rates

	$< 3'$	$< 4'$
$N_{\text{counterparts found}}$	320	399
$N_{\text{counterparts confirmed}}$	198 (62%)	220 (55%)

5.5.1 Reliability

The possibility of a misidentification remains, even more so in high extinction regions, due to the fact that the real counterpart drops below the detection threshold. However, the probability of this is difficult to quantify. For the HIZOA Northern Extension, Donley et al. (2005) investigated the likelihood of identifying the “real” counterpart associated with the HI galaxy. They simulated a grid of artificial HI detections across the survey regions and

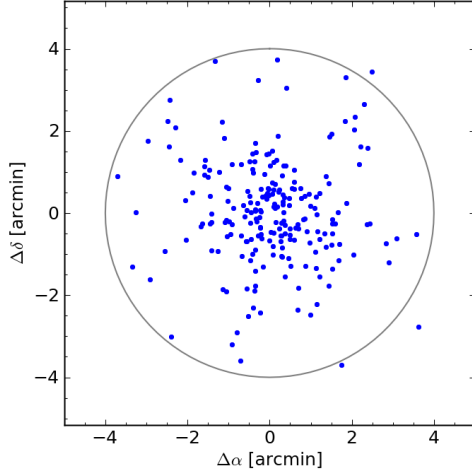


Figure 5.12: Positional offsets between HI positions and IRSF positions. The large circle shows an offset of $4'$, which is the pixel size of the HI data. 98% of the detections lie within $4'$, 88% within $3'$.

identified the *nearest* 2MASS counterpart to each source within $3'$ and $5'$. This allows the number of spurious counterparts to be determined that are expected for the real detections. The probability, P , that the detected counterpart is in fact related to the HI galaxy is given by:

$$P = \frac{N_{\text{counterparts}} - N_{\text{unrelated}}}{N_{\text{counterparts}}}, \quad (5.15)$$

where

$$N_{\text{unrelated}} = \frac{N_{\text{simulated galaxies with counterpart}}}{N_{\text{simulated galaxies}}} \times N_{\text{HI galaxies}}. \quad (5.16)$$

The probabilities varied for the two NE fields as a result of the different foreground extinction and varying density of galaxies in these two fields. They determined the expected percentage of real detections to be 79 – 88% within $3'$ and 59 – 77% within $5'$. Since the positional uncertainty of the Parkes HI sources depends on the S/N of the galaxy and the reliability of the counterparts is field dependent, these numbers provide a representation of the sample. Actual values for each galaxy should vary slightly, on the order of 10%.

5.6 Stellar and HI Properties

The sample of 356 confirmed counterparts is used here to investigate the relationships between the stellar properties based on the NIR magnitudes and the gas properties from the HI parameters of the galaxies. This information provides insights into galaxy evolution.

Figure 5.13 shows the HI mass, $\log M_{\text{HI}}$, as a function of the observed extinction-

corrected K_s band magnitude, K_s^o (*left panel*) and as a function of the absolute extinction-corrected K_s band magnitude, $M_{K_s}^{o,i}$ (*right panel*). The absolute magnitude is calculated based on the H α recession velocity:

$$M_{K_s}^{o,i} - 5 \log h_{75} = m_{K_s,obs} - A_{K_s} - I_{K_s} - 5 \log v_{rec} - 15, \quad (5.17)$$

where A_{K_s} is the Galactic extinction correction and I_{K_s} is the inclination-dependent internal extinction correction, applied as described in Sect. 1.1.1. Galaxies for which no possible NIR counterparts were identified are indicated with an upper limit to the magnitude which is calculated from the K_s band completeness limit of $K_s = 15^m4$ (NWS; Riad 2010) and corrected for foreground extinction. The apparent magnitude provides information on the observational sample. The faintest galaxies in the NIR are not recovered and they span a wide range of H α mass. The absolute magnitude plot sheds lights on the intrinsic properties of the sample. A correlation between the H α mass and K_s band magnitude can be seen.

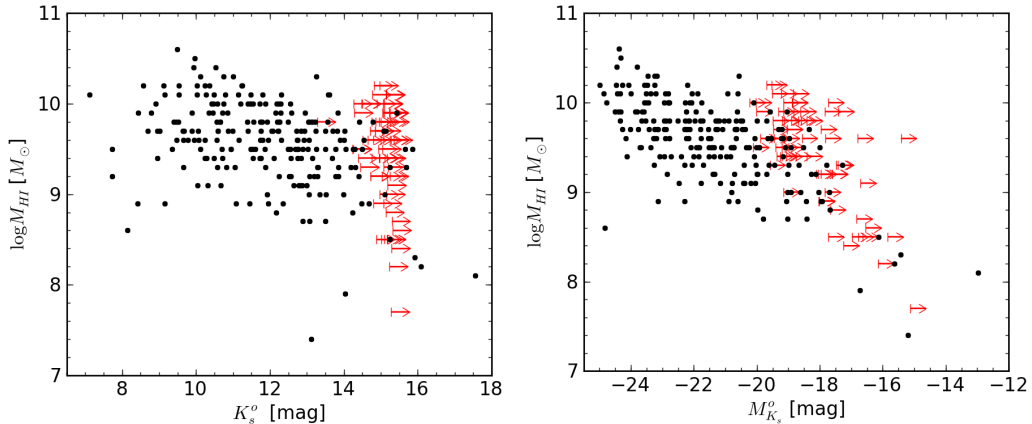


Figure 5.13: *Left* HI mass as a function of apparent K band magnitude. *Right* HI mass as a function of absolute K band magnitude.

It is more useful to examine the HI mass-to-light ratio and the relationship between the HI mass and the stellar mass. The K_s -band luminosity, in solar units, is given by

$$L_{K_s} = 10^{-0.4(M_{K_s} - M_{K_s,\odot})}, \quad (5.18)$$

where the $M_{K,\odot} = 3.32$ mag (Bell et al. 2003), and the stellar masses are estimated from the K_s luminosity using the relation from Bell et al. (2003)*:

$$\frac{M_*}{L_{K_s}} = 0.95 \pm 0.03. \quad (5.19)$$

Figure 5.14 shows the HI mass-to-light ratio as a function of K_s absolute magnitude (*left*

*This is an average value for the local Universe, calculated from the average stellar mass density and luminosity density.

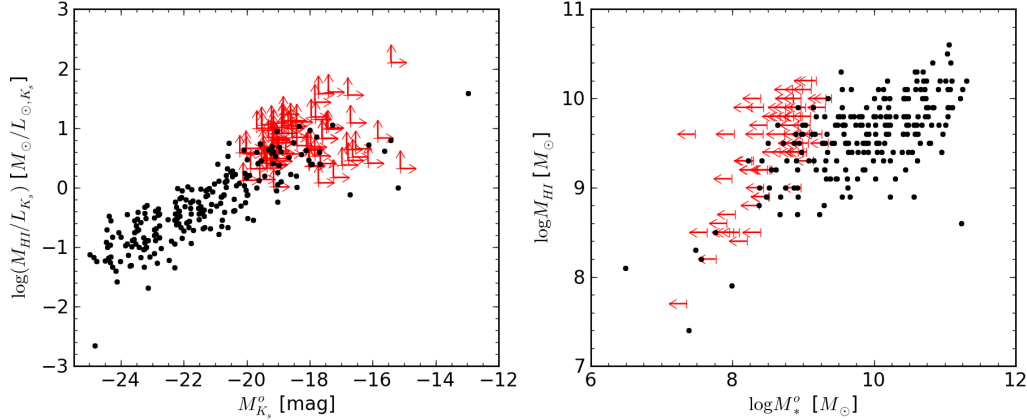


Figure 5.14: H I mass as a function of stellar mass.

panel). The two parameters plotted are dependent on each other so the direct relationship between the H I and stellar masses is also shown (*right* panel). Both these plots indicate how the gas and stars in galaxies are related to each other. Warren et al. (2006) proposed that for a given luminosity, a galaxy's mass-to-light ratio cannot exceed a certain value. The theoretical work by Taylor & Webster (2005) supports this suggestion that the mass of a galaxy determines the minimum amount of stars that can be formed. Kirby et al. (2008a) have done a similar analysis in the H band for dwarf galaxies. They include also a sample of galaxies from Virgo, thereby incorporating a variety of morphological types in their sample.

Chapter 6

Tully-Fisher Analysis

In this chapter the HI and NIR data of the HI-detected ZoA galaxies are used to derive a preliminary peculiar velocity flow field behind the Galactic plane through an analysis using the near infrared Tully-Fisher (NIR TF) method. This Chapter is divided into four parts: the first section (6.1) gives a brief overview of the use of the TF relation in peculiar velocity surveys as well as some of the key results from these studies; Section 6.2 details the implementation of the TF relation, with reference to the TF observables, the corrections made to the observed parameters, the derivation of an unbiased TF template relation and the determination of peculiar velocities; the third section (6.3) describes the selection of a TF sample and the subsequent peculiar velocity sample selection; and finally Sect. 6.4 presents the peculiar velocity flow field in the ZoA.

6.1 Previous Work

6.1.1 Early Work

Since its inception in the late 1970's, the TF relation has extensively been used to measure cosmological parameters as well as distances and peculiar velocities of galaxies. Most of the early work, such as that by Aaronson, Mould and collaborators (Aaronson et al. 1980b;c, Mould et al. 1980), was focused on the determination of the Hubble parameter, but also contributed significantly to the growing understanding of bulk flows in the universe, most notably the nature of the infall onto the Virgo cluster. Increasing evidence from these TF surveys and other techniques showed that Virgocentric infall could not be the sole cause of the peculiar motion of the LG over the uniform Hubble flow (Davis & Peebles 1983, Sandage & Tammann 1984, Yahil 1985). The development of CCD's for use in astronomy in the late 1980's allowed for greatly improved measurements of magnitudes for larger numbers of galaxies. Improved magnitudes reduces the errors in the resulting TF distances and large numbers of galaxies improves the statistical sampling of the peculiar velocity flow fields. Furthermore, Bothun & Mould (1987) showed a reduction in the intrinsic scatter of the NIR

TF relation based on I band CCD photometry, the longest wavelength band accessible to CCD's. Their I -band sample was also used to investigate bulk motions out to a velocity of 3000 km s^{-1} , but found no evidence for flows larger than 350 km s^{-1} perpendicular to the supergalactic plane, i.e. little evidence for large attractors other than the Virgo cluster. Whereas other independent studies (Shaya 1984, Tammann & Sandage 1985, Lilje et al. 1986) postulated the existence of another larger attractor towards Hydra-Centaurus supercluster.

It was the application of the $D_n - \sigma$ relation for ellipticals (Dressler et al. 1987) that led to the discovery of the Great Attractor (GA) by Lynden-Bell et al. (1988). Several independent large-scale peculiar velocity studies followed with results both challenging and supporting this claim. Moreover, Scaramella et al. (1989) suggested that much of the cause of the LG motion may be due to the more distant Shapley Concentration at $v \sim 14\,000 \text{ km s}^{-1}$. Willick (1990), using the R band TF sample of Aaronson et al. (1986), showed a coherent motion of the Perseus-Pisces (PP) supercluster towards the GA. Later, the R band TF sample of Courteau and Faber (Courteau et al. 1993) confirmed the extent of this PP inflow over a much larger region of the sky. The large area coverage and uniform selection of their sample allowed for easy comparison of peculiar velocities between different regions of the sky. Mould, Han and collaborators (Mould et al. 1991, Han 1992, Han & Mould 1992) obtained I band TF data distributed over much of the sky, but could not distinguish between the two models they fitted; one with a bulk flow towards the GA region and the other with infall onto both the GA and PP.

6.1.2 Large TF Samples

Large, uniform samples provide less biased determinations of the peculiar velocity flow field. The largest single TF dataset at the time was that of Mathewson and collaborators (Mathewson et al. 1992a, Mathewson & Ford 1994) consisting of I band photometry and HI and optical linewidths for 1355 galaxies in the southern sky. Samples can be increased by combining different datasets, however this introduces systematic errors resulting from the use of different methods of measuring the magnitudes and velocity widths and the application of different corrections to these measurements. Despite these problems, several large studies were started in an effort to combine the growing amount of available TF data from different sources into one *homogeneous* sample by attempting to account for the differences in the individual datasets.

Initial work by Burstein produced the Mark I and Mark II peculiar velocity catalogues which combined $D_n - \sigma$ elliptical data and TF data for spirals. However, some uncertainty remained in their distance catalogue because of the spatial separation of the ellipticals and spirals. The availability of newer, larger peculiar velocity samples allowed this to be extended to the Mark III Catalogue of Galaxy Peculiar Velocities (Willick et al. 1995; 1996; 1997). The Mark III incorporates data from the samples of Han, Mould and collaborators (Han 1992, Han & Mould 1992, Mould et al. 1991; 1993), Willick (Willick 1991), Courteau and Faber (Courteau 1992), Mathewson (Mathewson et al. 1992a) and Aaronson (Aaronson et al. 1982). This catalogue was analysed by Dekel et al. (1999) using the POTENT method resulting in

a measured bulk flow of over 300 km s^{-1} within 5000 km s^{-1} , towards $(l, b) = (314^\circ, 30^\circ)$. This bulk flow shows a coherent flow of most of the galaxies in the local Universe, including the PP, towards the GA and the Shapley Concentration.

The second study is the I band sample of Giovanelli and collaborators who chose to combine some existing data with extensive new observations. Their sample is separated into ~ 2000 field galaxies (the SFI; Giovanelli et al. 1994; 1995, Freudling et al. 1995, da Costa et al. 1996) and 782 galaxies in 24 clusters (the SCI; Giovanelli et al. 1997b, Haynes et al. 1999b;a). The cluster sample can be used to derive the TF template relation as well as study the amplitude of the motions of the clusters (Giovanelli et al. 1997a). Dekel et al.'s POTENT analysis of the SFI catalogue yielded flows which are consistent with the Mark III catalogue.

The largest peculiar velocity survey at the time was that of the Kinematics of the Local Universe project (KLUN; Bottinelli et al. 1990; 1992, di Nella et al. 1996, Theureau et al. 1998). The initial KLUN catalogue consisted of 6600 galaxies with B magnitudes and H α redshifts and linewidths. However, a significant fraction of the KLUN data were taken directly from the literature and the H α spectra have low velocity resolution.

These surveys were useful in revealing the main features of the bulk flows in the Universe, however some inconsistent results remained, in particular pertaining to the scale of the largest flows (Dekel et al. 1999). Much larger samples were needed to resolve these inconsistencies and to investigate the details of the large-scale structure in the local Universe. The newer generation peculiar velocity surveys include ~ 5000 or more galaxies and aim to provide the best fidelity data available, by combining existing data with extensive new observations. The KLUN survey was expanded to include some 20 000 spiral galaxies with new H α data from the Nançay radio telescope and with added B and I band data from DSS1 and DENIS (KLUN+; Theureau et al. 2005). More recently, a further extension of the KLUN project has been made to include the J , H and K_s NIR data from 2MASS (Theureau et al. 2007). The augmented SFI project (SFI++; Masters et al. 2006, Springob et al. 2007) includes significant amounts of new data and implements more careful determination of TF parameters. I band TF parameters for 4861 field and cluster galaxies are included in their sample.

Despite their significant extent, both the SFI++ and the KLUN+ are incomplete across the Galactic plane. The derivation of peculiar velocity fields from these samples therefore requires some form of interpolation to be done across this region of the sky (see e.g. Yahil et al. 1991, Lahav et al. 1994, Kolatt et al. 1995). Furthermore, the effect of the mass distribution within the ZoA on the local dynamics is still largely unknown, in particular the nature and extent of the GA.

6.1.3 The 2MASS Tully-Fisher Survey

Giovanelli's group has begun work on the 2MASS Tully-Fisher survey (2MTF; Masters et al. 2008, Masters 2008) which aims to measure TF distances for all bright inclined spirals in the 2MASS Redshift Survey (2MRS; Huchra et al. 2005). Because the magnitudes for the 2MTF

are provided from a single catalogue (2MASX), systematic errors as a result of homogenising data sets are avoided. The 2MTF will also obtain new high-fidelity HI measurements with even sky coverage and will provide better statistics for the study of the local peculiar velocity flow field. The use of the NIR TF will result in a reduction of the ZoA and therefore reduce the impact of the ZoA on peculiar velocity studies. However, since the 2MRS is restricted to $|b| > 5^\circ$ and $|b| > 10^\circ$ for $|l| < 30^\circ$, there is still a significant part of the sky that will remain unsampled in the 2MTF.

The aim of this thesis is to provide TF data for galaxies in the ZoA where the 2MTF will be undersampled. We use the TF template derived for the 2MTF and derive our TF data consistently with the 2MTF. This will enable these data to be incorporated into the 2MTF with limited uncertainty introduced by attempting to homogenise the two different samples. This is important to studies of the dynamics in the Universe and the continuity across the ZoA. Furthermore, it will be useful later to compare the peculiar velocity flow field derived here with the fields resulting from statistical interpolation. This will help test the interpolation methods used.

6.2 The Tully-Fisher Relation

The TF relation is introduced and the advantages of the NIR TF are discussed in Sect. 1.3.4. Two sets of data contribute to the TF relation; imaging data provides a measurement of the (distance-dependent) luminosity of the galaxy, and spectral data, in this case HI spectral data, provides a proxy for the (distance-independent) rotation speed of the galaxy. The absolute brightness and the rotation speed are related through the TF relation. In order to use the TF relation to measure galaxy distances a *template* is required. This TF template is derived from a sample of galaxies with known distances or a sample of cluster galaxies and provides the *calibrated* relation between the absolute magnitude and rotation width. The absolute brightness of a galaxy with unknown distance can be read off from the TF template given a measurement of its rotation width. This can be used with the galaxy's apparent brightness to determine the distance via the distance modulus.

The specific parameters used result in different determinations of the TF relation and thus it is important to use parameters and corrections that are consistent with those used in the derivation of the TF template. For example, the magnitudes used may be isophotal or total magnitudes and the widths may be the 50% or 20% linewidths or the calculated v_{max} . The TF template used here has been derived by Masters et al. (2008) (described in Sect. 6.2.2) and was chosen for its current availability and the fact that it covers all three NIR bands used in our survey, J , H and K_s . The raw data used and the corrections made here are chosen to be consistent as far as possible with the parameters and corrections made by Masters et al. (2008) in their derivation.

6.2.1 Tully-Fisher Observables

NIR Imaging Data

The luminosity of the galaxy is provided by NIR imaging. Chapters 4 and 5 described in detail the derivation of the NIR parameters to be used in the TF relation. The quantities of interest are the J , H and K_s extrapolated total magnitudes, m_J , m_H and m_{K_s} respectively, and the ellipticity, $\epsilon = 1 - b/a$, where b/a is the axis ratio. Note that the total magnitudes are chosen to be consistent with the TF template relations derived by Masters et al. (2008) that are already available.

The inclination, i , of the system is derived from the J band ellipticity ($\epsilon = \epsilon_J$), as it is assumed that it should best trace the inclination of the disk and be least affected by the bulge (Masters et al. 2008). The inclination is determined from

$$\cos^2 i = \frac{(1 - \epsilon)^2 - q_0^2}{1 - q_0^2}, \quad (6.1)$$

where $q_0 = 0.2$ is the intrinsic axis ratio of the galaxy for all types of galaxies. Normally a slightly lower value of $q_0 = 0.13$ is taken for later type Sb and Sc galaxies, but the lower value is chosen in order to mitigate the effect of the bulge on the most edge-on galaxies. A small correction for the effects of seeing on the axis ratio is made following Masters et al. (2003). The corrected axis ratio, a/b , is given by

$$\left(\frac{a}{b}\right)_{cor} = \left(\frac{a}{b}\right)_{obs} (1 - 0.02x + 0.21x^2 - 0.01x^3), \quad (6.2)$$

where $x = \text{FWHM} \left(\frac{a/b}{r_{20}}\right)_{obs}$, FWHM is the full width half maximum of the seeing disc and r_{20} is the radius of the $J = 20$ mag arcsec $^{-2}$ isophote. For small inclined galaxies a minimum of value of $b/a = 0.12$ is imposed to prevent overcorrection. The NIR images also provide an estimate of the Hubble type, T , of the galaxy. An initial visual inspection is made of each galaxy and it is classified as one of three classes: $T \leq 2$, $2 < T \leq 4$ and $T = 5$.

Magnitude Corrections

The magnitudes are corrected for extinction due to dust in our galaxy using the DIRBE/IRAS maps of Schlegel et al. (1998), but reduced by a factor of 0.82 (see Sect. 5.3) that corrects for the overestimation of the DIRBE values in the ZoA. The extinction in each IRSF/SIRIUS band is obtained by integrating the extinction law of Cardelli, Clayton, & Mathis (1989) over each of the J , H and K_s bandpasses (Cluver et al. 2008b):

$$\begin{aligned} A_J &= 0.863E(B - V), \\ A_H &= 0.570E(B - V), \\ A_{K_s} &= 0.368E(B - V). \end{aligned} \quad (6.3)$$

Note that the difference between these values and those given in Sect. 1.1.1 is due to the filters used. A correction for internal extinction is made as prescribed in Sect. 1.1.1 following the work of Masters et al. (2003).

We apply a small cosmological k correction* as in Masters et al. (2003; 2008) which is derived from the models of Poggianti (1997). In the three bands the k corrections are

$$\begin{aligned} k_J &= -0.68z, \\ k_H &= -0.40z, \\ k_{K_s} &= -1.52z, \end{aligned} \quad (6.4)$$

where z is the redshift determined from the H α spectra. For our galaxies, the k corrections are $< 0^m03$, which are insignificant compared to the size of the magnitude errors and extinction corrections.

Since the TF relation is found to depend slightly on the galaxy type, the magnitudes of earlier type galaxies are corrected to an Sc type ($T = 5$) using the prescription of Masters et al. (2008):

$$\begin{aligned} T_M &= 0.23 - 2.86(\log W - 2.5) & : & T \leq 2, \\ T_M &= 0.02 - 1.31(\log W - 2.5) & : & 2 \leq T \leq 4 \end{aligned} \quad (6.5)$$

in the J band,

$$\begin{aligned} T_M &= 0.21 - 2.92(\log W - 2.5) & : & T \leq 2, \\ T_M &= 0.01 - 1.26(\log W - 2.5) & : & 2 \leq T \leq 4 \end{aligned} \quad (6.6)$$

in the H band, and

$$\begin{aligned} T_M &= 0.19 - 3.16(\log W - 2.5) & : & T \leq 2, \\ T_M &= 0.01 - 1.46(\log W - 2.5) & : & 2 \leq T \leq 4 \end{aligned} \quad (6.7)$$

in the K_s band.

The corrected magnitude for each galaxy is thus given by:

$$m_{cor} = m_{obs} - A - I + k - T_M(W), \quad (6.8)$$

where m_{cor} is the corrected apparent magnitude, m_{obs} is the observed apparent magnitude, A is the Galactic foreground extinction, I is the internal extinction and k is the k correction. $T_M(W)$ is the linewidth-dependent type correction.

*The redshift implies that light received in a given passband centred on λ was actually emitted from a narrower passband centred on $\lambda_0 = \lambda/(1+z)$; for broadband photometry the k -correction provides the transformation between the observed frame and the rest frame, correcting for both the change in the width of the passband and for the shift in central wavelength (Humason, Mayall, & Sandage 1956, Oke & Sandage 1968). The correction can be expressed as a magnitude difference.

HI Spectral Data

The 21 cm HI spectral data are provided by the HIZOA survey and new narrowband observations. The HIZOA and narrowband data are described in Chapters 2 and 3 respectively. For the purposes of the TF analysis, the parameters of interest are the systemic velocity, v , and the velocity width. The linewidth used for the TF analysis is the width measured at 50% of the peak flux, w_{50} . The raw linewidth has to be corrected for instrumental broadening, Δ_s , the effects of turbulent motions, Δ_t , the inclination of the disk, i , and cosmological broadening.

The instrumental correction is always a small positive number that depends on the spectrometer channel separation, Δv , the signal-to-noise of the spectrum, SNR, and the type of smoothing. We use the correction derived by Springob et al. (2005):

$$\Delta_s = 2\Delta v \lambda, \quad (6.9)$$

where λ is a piece-wise defined function of SNR and channel separation:

$$\begin{aligned} \log(\text{SNR}) < 0.6 : \quad \lambda &= \lambda_1(\Delta v); \\ 0.6 < \log(\text{SNR}) \leq 1.1 : \quad \lambda &= \lambda_2(\Delta v) + \lambda'_2(\Delta v) \log(\text{SNR}); \quad \text{and} \\ \log(\text{SNR}) > 1.1 : \quad \lambda &= \lambda_3(\Delta v). \end{aligned} \quad (6.10)$$

For Hanning smoothing and channel separations larger than 11 km s^{-1} , the values of λ_i are $\lambda_1(\Delta v) = 0.227$, $\lambda_2(\Delta v) = -0.1532$, $\lambda'_2(\Delta v) = 0.623$ and $\lambda_3(\Delta v) = 0.533$.

The correction for turbulent motion accounts for non-circular motion of the HI gas, warps, bars and global asymmetries as well as small-scale dispersion particularly around spiral arms. Springob et al. (2005) give the merits of a simple linear correction as opposed to a correction subtracted in quadrature. A value of $\Delta_t = 6.5 \text{ km s}^{-1}$ is used.

Redshift effects cause the profile to be broadened by a factor of $1+z$, where $z = v/c$ is the redshift calculated from the systemic velocity. Finally the projection of the velocities onto the line-of-sight causes the observed width to be narrower by a factor of $\sin i$, where i is the inclination of the disk determined from the J band axis ratio.

The corrected linewidth is given by:

$$W = \left[\frac{w_{50} - \Delta_s}{1+z} - \Delta_t \right] \frac{1}{\sin i}. \quad (6.11)$$

6.2.2 2MTF Template

To use the TF relation to measure distances to galaxies a *template* is required which provides the calibrated relation between the absolute magnitude and rotation width. Ideally, the template sample should be unbiased or fully bias-corrected, the distances should be well known and not affected by (or properly corrected for) peculiar velocities. Furthermore, the photometric and spectroscopic data should come from the same source and be analysed

consistently. Errors in the parameters should be well understood. It is important to note that a biased template will result in biased peculiar velocity measurements.

Masters et al. (2008) have calculated a global template in the 2MASS J , H and K_s bands for use with the 2MTF. A *global* or *unbiased* template is constructed by removing all sample biases and can readily be used to determine TF distances without applying individual bias corrections. We provide here a description of the data sample, bias corrections and derivation of the TF template relations.

TF Sample

The Masters et al. (2008) sample is drawn from the Cornell HI digital archive (Springob et al. 2005) and the database of optical rotation curves (ORCs; see e.g. Catinella et al. 2005) that have counterparts in the 2MASS XSC. Of these sources, those that lie within the clusters with known distances used by Masters et al. (2006) are chosen for the derivation of the template relation. In the final TF template sample 65% of the galaxies are also found in the SFI++ sample (Masters et al. 2006), which was used to derive the I band TF template. The ORC linewidths were transformed to the 50% HI linewidth. The photometry is provided by the 2MASX total magnitudes in the J , H and K_s bands. The motivation for using the total magnitudes is that, in theory, they provide the best estimate of the total luminosity, hence mass, of the system. However, it should be noted that the depth of the 2MASS survey limits the determination of total magnitudes, particularly for LSB galaxies. The I band axis ratios, where available, are chosen in preference to the 2MASX J band ratio. In the cases where the 2MASX axis ratios are used, only galaxies with J band inclinations greater than 25° are included in the sample. Corrections are made to the rotational widths and magnitudes as described in the previous section. One important exception is that Masters et al. (2008) use the Galactic extinction correction given in Sect. 1.1.1:

$$\begin{aligned} A_J &= 0.902E(B-V), \\ A_H &= 0.576E(B-V), \\ A_K &= 0.367E(B-V), \end{aligned} \quad (6.12)$$

which are calculated by Schlegel et al. (1998) for the UKIRT J , H and K filters. Note that they do not use total-to-selective extinction ratios derived for the 2MASS filters. However, since their template galaxies lie in regions of low extinction the small extinction corrections are very small and the differences introduced by total-to-selective extinction ratios are smaller.

Bias Corrections

Masters et al. (2008) attempt to derive an unbiased TF template by making reasonable assumptions about the parent galaxy population to correct for observational biases in the sample population. For completeness, I briefly describe here how the biases for which they

correct arise:

1. Incompleteness bias correction. At the faint end of the TF relation bright galaxies lying above the TF relation are preferentially observed because the fainter galaxies fall below the detection threshold, while at the bright end all galaxies can be observed. This effect artificially raises the zero point of the derived TF relation and makes the slope shallower.
2. Mean distances to cluster. This bias is introduced because the TF relation uses magnitudes or the average of the log of the distance while the physical parameter is the log of the average distance of a cluster, which is a small fixed difference for each cluster.
3. Cluster size incompleteness. In a given cluster, dimmer galaxies are preferentially observed in the closer parts of the cluster. This is a small correction that depends on the size of the cluster and correction 1.
4. Morphological correction. The slope of the TF relation differs according to morphological type, being shallower for later types. The corrections they prescribe are given in the previous section, Eqs. 6.5 to 6.7.
5. Cluster peculiar velocity. The magnitudes are corrected for the peculiar velocity of each cluster so that the data from each cluster lie on the same TF relation.

TF Template Relation

A bivariate fit to the Masters et al. (2008) data after all the corrections have been applied yields the following TF relations in the J , H and K_s bands respectively:

$$\begin{aligned} M_J - 5 \log h &= -20.999 - 9.070(\log W - 2.5), \\ M_H - 5 \log h &= -21.833 - 9.016(\log W - 2.5), \\ M_{K_s} - 5 \log h &= -22.030 - 10.017(\log W - 2.5). \end{aligned} \quad (6.13)$$

Figure 6.1 shows a plot of the absolute magnitude as a function of the corrected linewidths of their TF calibration data. They observe a slight shallowing of the slope at both the very high and very low mass ends. Usually the deviation at the low mass end is to make the slope steeper as observed in the optical (Pierini & Tuffs 1999, Kannappan et al. 2002) and suggested in the I band (Masters et al. 2006). However, the shallower slope at the low mass end may be a result of the assumptions of the incompleteness bias correction. Moreover, distinguishing changes in the TF relation due to morphological type or luminosity (or H α mass) is difficult. At the high mass end the shallowing of the TF relation has also been reported in the I and K bands (Masters et al. 2006, Noordermeer & Verheijen 2007).

The scatter in their TF relation is found to depend on rotation width, being greater for narrower linewidths. They fit the scatter with a linear function and obtain for the observed

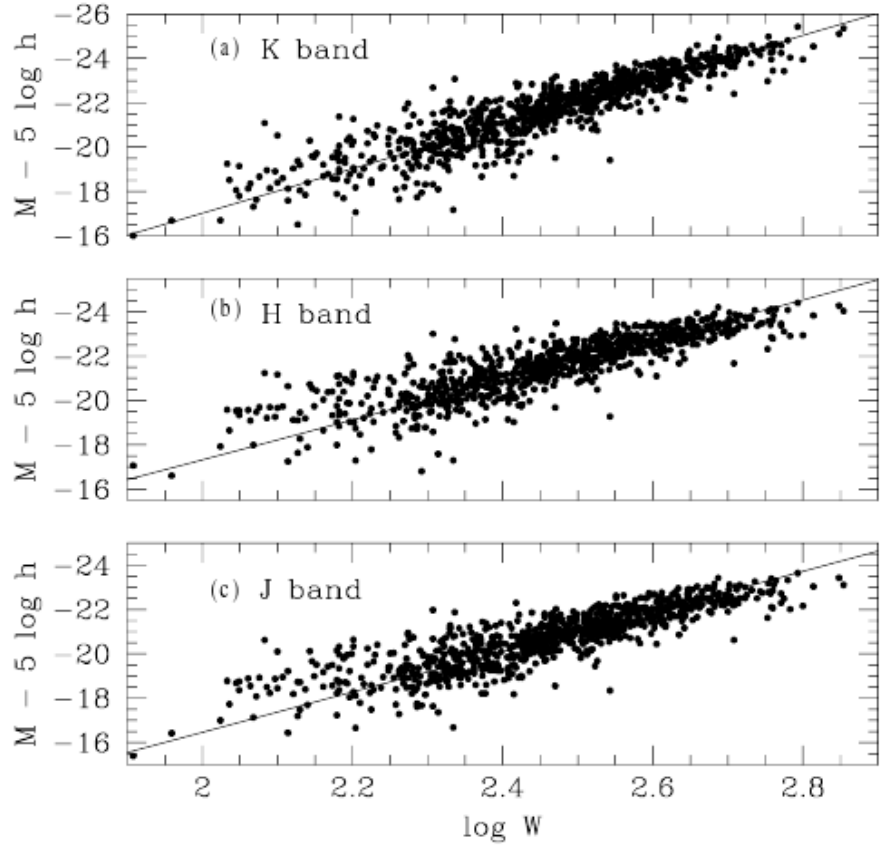


Figure 6.1: Global TF relation in the (a) K_s , (b) H and (c) J bands taken from Masters et al. (2008). The solid line shows the bivariate fit to their sample

scatter:

$$\begin{aligned}\epsilon_{obs,J} &= 0.56 - 0.66(\log W - 2.5), \\ \epsilon_{obs,H} &= 0.54 - 0.89(\log W - 2.5), \\ \epsilon_{obs,K_s} &= 0.54 - 0.87(\log W - 2.5).\end{aligned}\quad (6.14)$$

Accounting for measurement errors they calculate the intrinsic scatter in the TF relation to be:

$$\begin{aligned}\epsilon_{int,J} &= 0.39 - 0.78(\log W - 2.5), \\ \epsilon_{int,H} &= 0.38 - 1.14(\log W - 2.5), \\ \epsilon_{int,K_s} &= 0.35 - 1.17(\log W - 2.5).\end{aligned}\quad (6.15)$$

6.2.3 Derivation of Peculiar Velocities

This section summarises the corrections made to the observed parameters and provides the recipe for the determination of distances, d , and peculiar velocities, v_{pec} , from the TF relation. This is done in each of the J , H and K_s bands. The peculiar velocities are determined in the CMB frame so the heliocentric HI recession velocity, v_{hel} , is first transformed to the CMB frame using the model of Fixsen et al. (1996):

$$v_{cmb} = v_{hel} + v_{apex} [\sin b \sin b_{apex} + \cos b \cos b_{apex} \cos(l - l_{apex})], \quad (6.16)$$

where $v_{apex} = 371.0 \text{ km s}^{-1}$, $l_{apex} = 264^\circ 14$ and $b_{apex} = 48^\circ 26$ are the velocity and position (Galactic coordinates) components of the apex vector describing the relative motion of the Sun with respect to the CMB. The *corrected* absolute magnitude, M , calculated from the observed HI recession velocity in the CMB frame, v_{cmb} , is given by

$$M - 5 \log h = m_{cor} - 5 \log v_{cmb} - 15, \quad (6.17)$$

i.e.

$$M - 5 \log h = m_{obs} - A - I + k - T_M(W) - 5 \log v_{cmb} - 15. \quad (6.18)$$

The corrected linewidth W is

$$W = \left[\frac{w_{50} - \Delta_s}{1 + z} - \Delta_t \right] \frac{1}{\sin i}. \quad (6.19)$$

If the galaxy has no peculiar velocity, it should lie on the TF relation. This is, however, not generally true and the peculiar velocity of the galaxy introduces an offset from the TF relation:

$$\Delta M = M - M(W), \quad (6.20)$$

where $M(W)$ is the value of the TF relation for width W . Since $M \propto 5 \log(v_{cmb})$ and $M(W) \propto 5 \log(v_{cmb} - v_{pec})$, it can be shown that the peculiar velocity is given by

$$v_{pec,cmb} = v_{cmb} (1 - 10^{0.2\Delta M}). \quad (6.21)$$

From the definition of the peculiar velocity, $v_{pec} = v_{cmb} - H_0 d$, the distance of the galaxy is found to be:

$$d = \frac{v_{cmb}}{H_0} 10^{0.2\Delta M}. \quad (6.22)$$

Uncertainties

The uncertainties are calculated by standard propagation of the measurement errors. The error on the absolute magnitude is calculated from Eq. 6.18 as,

$$\sigma_M^2 = \sigma_{m_{obs}}^2 + \sigma_A^2 + \sigma_I^2 + \left(\frac{5}{v_{cmb} \ln 10} \right)^2 \sigma_{v_{cmb}}^2, \quad (6.23)$$

where the dominant term is the observational error on m_{obs} . The uncertainty associated with the corrected linewidth is calculated from Eq. 6.19 as

$$\sigma_W^2 = \left(\frac{1}{1+z} \right)^2 \sigma_{w_{50}}^2 + \left(W \frac{\cos i}{\sin i} \right)^2 \sigma_i^2. \quad (6.24)$$

where the terms due to uncertainties in the Δs , Δt and z have been assumed to be small compared to the observational error in the linewidth and inclination. The error in the inclination is determined from the ellipticity error using Eq. 6.1 to obtain,

$$\sigma_i^2 = \left(\frac{1-\epsilon}{1-q_0^2} \frac{1}{\cos i \sin i} \right)^2 \sigma_\epsilon^2. \quad (6.25)$$

The uncertainty in the offset from the TF relation is the quadrature sum of the uncertainty in the absolute magnitude, σ_M , and that of the TF magnitude, $\sigma_{M(W)}$, i.e.

$$\sigma_{\Delta M}^2 = \sigma_M^2 + \sigma_{M(W)}^2, \quad (6.26)$$

where the latter term depends on the error in the corrected linewidth and includes the intrinsic scatter in the TF relation, ϵ_{int} ,

$$\sigma_{M(W)}^2 = \left(\frac{b}{W \ln 10} \right)^2 \sigma_W^2 + \epsilon_{int}^2. \quad (6.27)$$

The error in the peculiar velocity, $\sigma_{v_{pec}}$, is given by:

$$\sigma_{v_{pec}}^2 = (1 - 10^{0.2\Delta M})^2 \sigma_{v_{cmb}}^2 + (0.2v_{cmb} 10^{0.2\Delta M} \ln 10)^2 \sigma_{\Delta M}^2. \quad (6.28)$$

Finally, the distance error is

$$\sigma_d^2 = \left(\frac{1}{H_0} 10^{0.2\Delta M} \right)^2 \sigma_{v_{cmb}}^2 + \left(0.2 \frac{v_{cmb}}{H_0} 10^{0.2\Delta M} \ln 10 \right)^2 \sigma_{\Delta M}^2. \quad (6.29)$$

6.3 The Peculiar Velocity Sample within the ZoA

In this section galaxies are selected from the NIR galaxy catalogue to obtain a sample of galaxies suitable for a TF analysis of the peculiar velocity field in the ZoA. We consider here only the 356 galaxies with *confirmed* NIR cross-identifications of the H α source (See Sect. 5.5 for the discussion on H α counterpart identification).

6.3.1 TF Sample

From the sample of confirmed counterparts we select a TF sample: only galaxies with good NIR photometry are considered, i.e. those that did not lie near the edge of a field and were not contaminated by a bright saturated star or by another galaxy. Thirteen galaxies were excluded based on poor photometry. The least inclined ($b/a > 0.72$) galaxies are excluded

as the inclination correction of the width and its associated errors are prohibitively large for these galaxies; of the 356 galaxies, 80 were excluded as face-on. A further 39 galaxies were excluded from the sample because the HIZOA w_{50} parameters were not available at the time of this writing. Finally, 30 galaxies had very small implied corrected linewidths $\log W < 1.9$; these were excluded as they lie outside the range of the 2MTF template relation.

The final TF sample consists of 196 galaxies which are listed in Appendix B, Table B.1, which gives the uncorrected photometric and spectroscopic parameters as well as the absolute magnitudes from the TF relation. The columns are:

Column 1 HI catalogue name

Column 2 & 3 Galactic co-ordinates, l and b

Column 4 HI recession velocity, v

Column 5 HI 50% linewidth uncorrected for inclination, w_{50}

Column 6 J band ellipticity, ϵ

Columns 7-9 observed extrapolated total magnitudes in J , H and K_s respectively, m_J , m_H , and m_{K_s} , before corrections for extinction

Column 10 50% linewidth corrected for inclination, instrumental, turbulent and cosmological broadening, w_{cor}

Columns 11-13 absolute magnitudes in J , H and K_s respectively, computed assuming the galaxy is at the distance given by its redshift and corrected for extinction

The 66 galaxies for which new narrowband HI observations are available are marked with an asterisk. The absolute magnitudes are plotted as a function of the corrected linewidths in Fig. 6.2 for the J (*top*, blue), H (*middle*, green) and K_s (*bottom*, red) bands. The solid lines show the 2MTF template relations of Masters et al. (2008) (eqs. 6.13) and the dotted lines show $3\times$ the intrinsic scatter in the 2MTF template relation (eqs. 6.15). Open circles indicate galaxies for which the implied peculiar velocity is greater than 2000 km s^{-1} . The figure shows that the majority of galaxies lie within $3\epsilon_{int}$ of the TF relation, however it does reveal a tendency for galaxies to lie above the TF relation, i.e. they are brighter than expected. While care has been taken in identifying the NIR counterparts, the large errors on the HI positions increase the difficulty of counterpart identification. The extreme outliers above the template relation may be a result of the misidentification of the NIR counterpart, most likely of a foreground galaxy or another NIR-bright galaxy in the field. It is also possible that a foreground star on or near the nucleus of the galaxy could not be removed, thereby causing the galaxy to be too bright. Finally, following inspection of the individual galaxies it was found that some do have disturbed HI-spectra, making them unsuitable for TF analysis. However, in their analysis of the SFI++, Springob et al. (2007) also see several extreme outliers above the I band TF relation at low widths. They suggest that these galaxies either have significant intrinsic offsets from the TF template or erroneous width or magnitude data. In the case of the former suggestion, these galaxies will be useful for galaxy evolution studies.

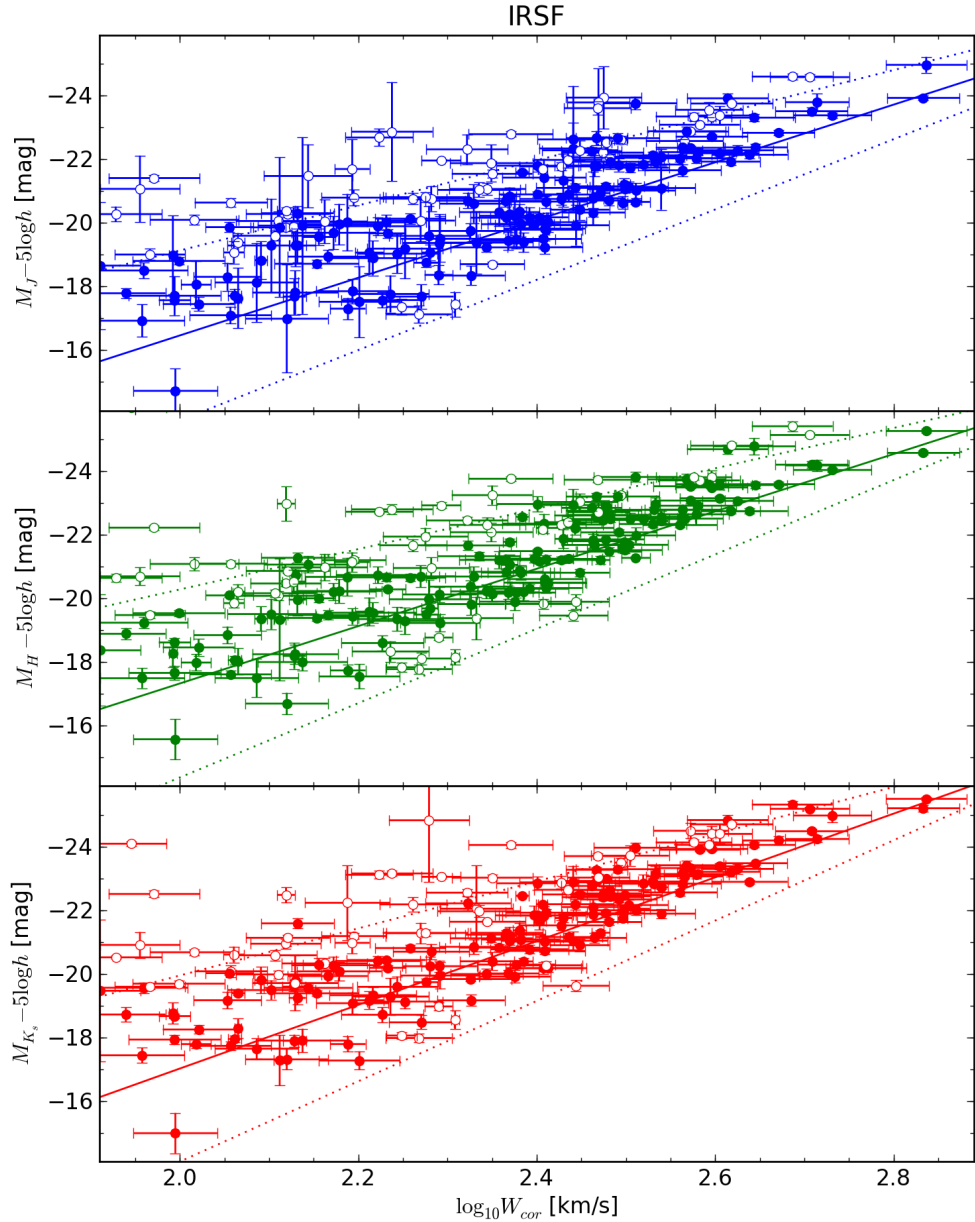


Figure 6.2: Tully-Fisher relation or absolute magnitude as a function of rotational width for galaxies in the ZoA in J (*top* in blue), H (*middle* in green) and K_s (*bottom* in red). Open circles indicate galaxies for which the implied peculiar velocity is greater than 2000 km s^{-1} . The solid lines show the 2MTF template relations of Masters et al. (2008) and the dotted lines show $3 \times$ the intrinsic scatter in the 2MTF template relation, $\pm 3\epsilon_{int}$.

6.3.2 Peculiar Velocity Sample

A further subsample is selected in order to study the peculiar velocity field. Discussed here are the properties of the peculiar velocity sample, in particular the inclusion of galaxies with large peculiar velocities and those with narrow linewidths. It is noted that very few galaxies have real peculiar velocities greater than 1000 km s^{-1} and very few galaxies outside of clusters have peculiar velocities much greater than 500 km s^{-1} (Springob et al. 2007).

Peculiar velocities are given for all 196 galaxies in the TF sample. These are listed in Appendix B, Table B.2, which gives the uncorrected photometric and spectroscopic parameters as well as the absolute magnitudes and peculiar velocities derived from the TF relation. The columns are:

Column 1 HI catalogue name

Column 2 & 3 Galactic co-ordinates, l and b

Column 4 HI recession velocity, v

Column 5 HI 50% linewidth uncorrected for inclination, w_{50}

Column 6 J band ellipticity, ϵ

Columns 7-9 observed extrapolated total magnitudes in J , H and K_s respectively, m_J , m_H , and m_{K_s} , before corrections for extinction

Column 10 50% linewidth corrected for inclination, instrumental, turbulent and cosmological broadening, w_{cor}

Columns 11-13 absolute magnitudes in J , H and K_s respectively, computed assuming the galaxy is at the distance given by its redshift and corrected for extinction

Column 14 the TF distance in velocity units, $H_0 d$

Column 15 peculiar velocity, v_{pec}

The 66 galaxies for which new narrowband HI observations are available are marked with an asterisk. These galaxies have significantly lower peculiar velocity errors because of the improved rotational widths.

Figure 6.3 shows the peculiar velocities for all 196 galaxies in the TF sample in the Galactic longitude – Hubble distance plane. Peculiar velocities are plotted on a colour scale with the greater positive velocities in redder colours and the greater negative velocities in bluer colours. The various symbols indicate the position of each galaxy with respect to the Galactic plane: upwards-pointing triangles lie above the plane ($0^\circ < b < 5^\circ$), downwards-pointing triangles lie below the plane ($-5^\circ < b < 0^\circ$). Near the Galactic bulge, in the GB extension of HIZOA, galaxies farther above the plane ($5^\circ < b < 15^\circ$) are plotted as open upwards-pointing triangles and those farther below the plane ($-10^\circ < b < -5^\circ$) are open downwards-pointing triangles. Galaxies with narrowband HI observations are plotted with black circles around the triangle. Note that the lack of galaxies with large positive peculiar velocities at larger distances is due to the observational limit $v_{obs} = 6000 \text{ km s}^{-1}$.

The distribution of peculiar velocities is shown in Figs. 6.4 to 6.6. In all figures the unfilled histogram is the distribution of *all* galaxies in the TF sample; it is clearly strongly

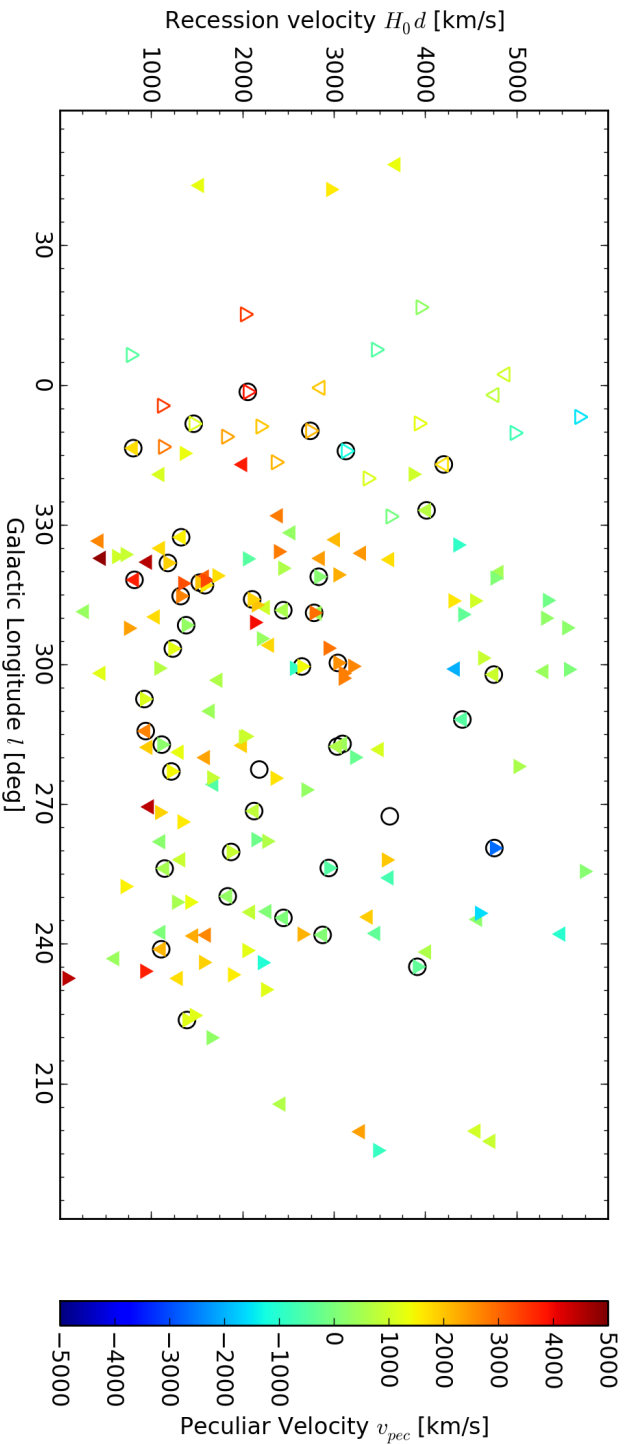


Figure 6.3: Peculiar velocities for all galaxies in the TF samples plotted in the Galactic longitude – Hubble distance plane. The colour scale shows the values of the peculiar velocities, with redder colours being more positive velocities and bluer colours being more negative velocities. The various symbols indicate the position of each galaxy with respect to the Galactic plane: upwards-pointing triangles lie above the plane ($0^\circ < b < 5^\circ$), downwards-pointing triangles lie below the plane ($-5^\circ < b < 0^\circ$). Near the Galactic bulge, in the GB extension of HIZOA, galaxies farther above the plane ($5^\circ < b < 15^\circ$) are plotted as open upwards-pointing triangles and those farther below the plane ($-10^\circ < b < -5^\circ$) are open downwards-pointing triangles. The points with large black circles around them have narrowband HI observations.

offset towards positive peculiar velocities. The measured peculiar velocities have a mean value of 993 km s^{-1} (shown by the vertical dotted line) and a dispersion of 1480 km s^{-1} . This large offset is reflected in the large numbers of galaxies lying above the TF relation in Fig. 6.2. This large average peculiar velocity is not unreasonable given the bulk flow of $v = 615 \pm 211 \text{ km s}^{-1}$ towards $(l, b) = (259^\circ, 4^\circ)$ found by Hudson et al. (2004). Moreover, the fairly broad distribution ($\sim 1000 \text{ km s}^{-1}$) of peculiar velocities is partly a result of the intrinsic scatter in the TF relation. For example, at $\log W = 2.5$, the intrinsic scatter in the TF relation is $\sim 0^{\mathrm{m}}4$. This gives peculiar velocities of the order of $400 - 800 \text{ km s}^{-1}$ in the velocity range $2000 - 4000 \text{ km s}^{-1}$.

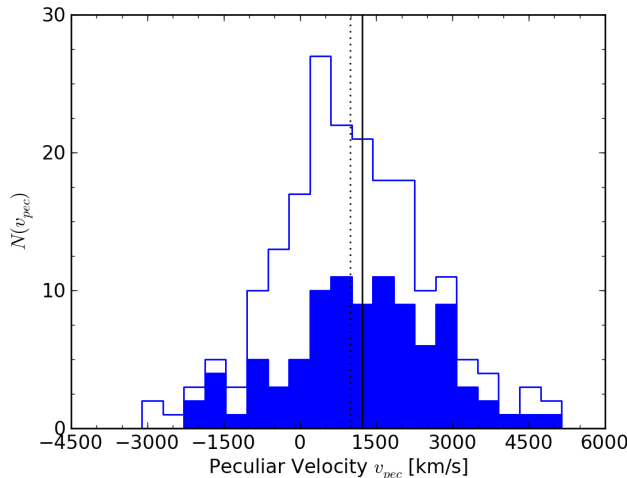


Figure 6.4: Peculiar velocity distribution of all galaxies (unfilled histogram). The mean value of the distribution, 993 km s^{-1} , is shown with a dotted vertical line and the dispersion is 1480 km s^{-1} . The filled histogram shows the measured peculiar velocities of the galaxies within $\pm 30^\circ$ of $l = 325^\circ$. The solid vertical line shows the mean value of 1230 km s^{-1} . The dispersion is similar to the entire distribution: 1480 km s^{-1} .

The question remains whether this mean and dispersion is representative of the whole sample so an investigation whether the large mean and scatter is a result of poor data or bias is done. To this end, histograms of the peculiar velocities for galaxies in the GA region (Fig. 6.4), for those with new narrowband HI observations (Fig. 6.5) as well as for the more massive ($\log W > 2.3$) HI galaxies (Fig. 6.6) are presented. The latter sample excludes the galaxies where the scatter around the Masters et al. (2008) template becomes asymmetric and may be biased.

From Fig. 6.3, there appears to be a region with larger positive peculiar velocities within $\sim 30^\circ$ of the GA centre ($290^\circ < l < 350^\circ$). The solid histogram in Fig. 6.4 shows these peculiar velocities; this distribution has a mean 1230 km s^{-1} and dispersion of 1480 km s^{-1} . The implication is that galaxies in the foreground of the GA have slightly larger peculiar velocities than the rest of the sample. In Fig. 6.5, the solid histogram shows the distribution of the narrowband peculiar velocities; they have a mean of 797 km s^{-1} and a dispersion of

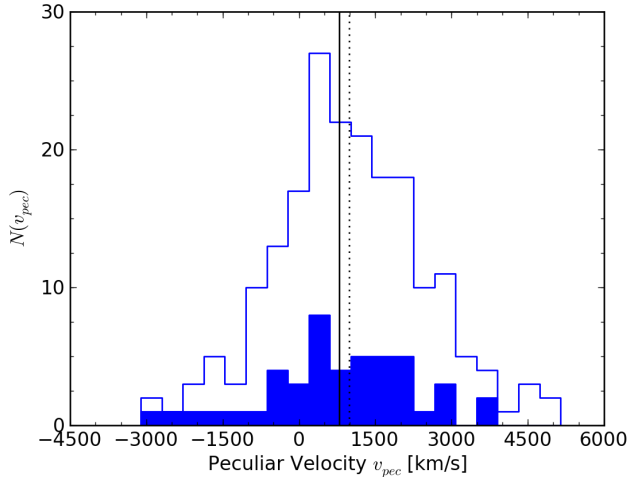


Figure 6.5: Peculiar velocity distribution of all galaxies (unfilled histogram). The mean value of the distribution, 993 km s^{-1} , is shown with a dotted vertical line and the dispersion is 1480 km s^{-1} . The filled histogram shows the measured peculiar velocities of the galaxies with narrowband observations. The solid vertical line shows the mean value of 797 km s^{-1} . The dispersion is similar to the entire distribution: 1490 km s^{-1} .

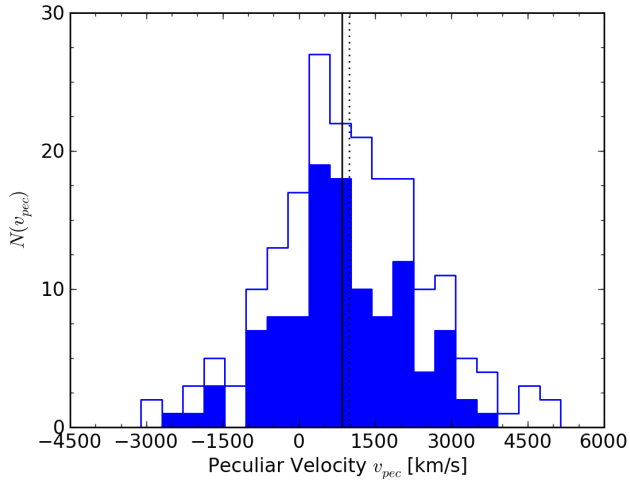


Figure 6.6: Peculiar velocity distribution of all galaxies (unfilled histogram). The mean value of the distribution, 993 km s^{-1} , is shown with a dotted line and the dispersion is 1480 km s^{-1} . The filled histogram shows the peculiar velocities of the galaxies with $\log W > 2.3$. The solid line shows the mean values of 768 km s^{-1} and the dispersion is 1240 km s^{-1} .

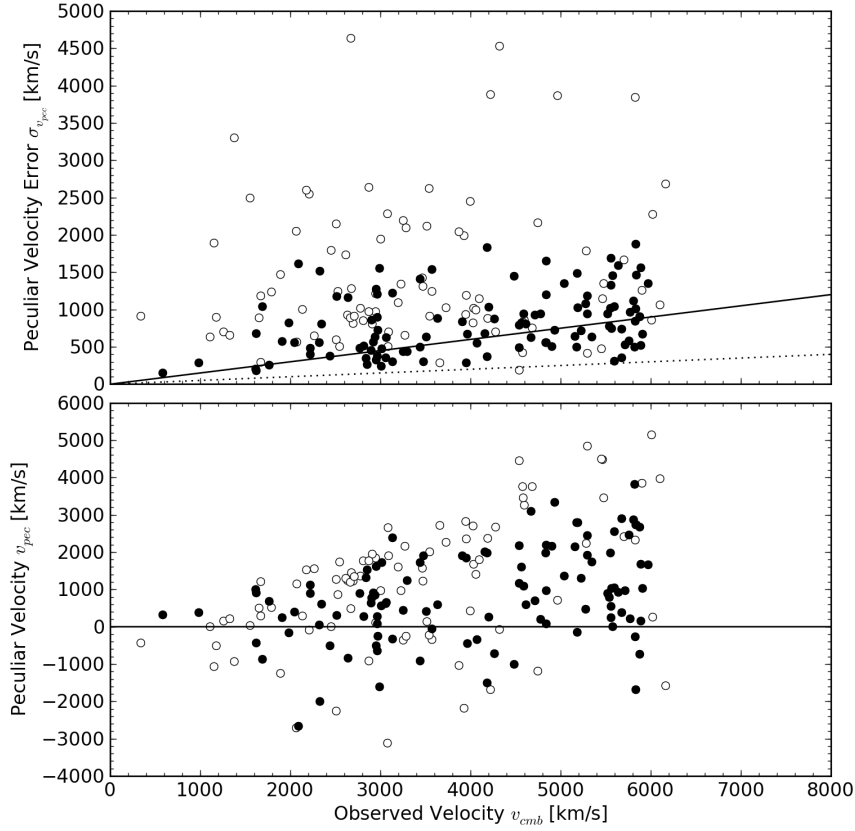


Figure 6.7: Peculiar velocities (*bottom*) and errors (*top*) as a function of observed velocity, v_{cmb} . The open circles show galaxies at the low mass end of the TF relation ($\log W < 2.3$). The solid line in the *top* plot shows an error on the peculiar velocity that is 15% of the recession velocity; the dotted line shows a 5% error. In the *bottom* panel it can be seen that the largest peculiar velocities are those low mass galaxies. No galaxies lie further than $v_{obs} \leq 6000 \text{ km s}^{-1}$, the selection cutoff for the NIR observations.

1490 km s^{-1} . Similarly, the sample of galaxies excluding those at the low mass end of the TF relation have peculiar velocities with a mean value of 768 km s^{-1} and a dispersion of 1240 km s^{-1} , shown in Fig. 6.6. The lower mean and dispersion in the latter case is explained by the fact that low mass galaxies are clearly biased towards higher peculiar velocities due to the flattening of the TF relation as described in the previous section (Sect. 6.2.2).

Figure 6.7 shows the peculiar velocities (*bottom* panel) and errors (*top* panel) as a function of the observed CMB velocity. The open circles show galaxies with $\log W < 2.3$ that lie at the low mass end of the TF relation where uncertainties pertaining to bias corrections become large and it is thought that the TF relation flattens. Especially at larger distances, the $\log W < 2.3$ galaxies appear to have larger peculiar velocities than those with wider linewidths. This is a result of the possible turnover in the TF relation as well as the increased numbers of outliers (see Sect. 6.3.1). As an indication of the scale of the errors,

the solid line in the *top* panel shows an error on the peculiar velocity of 15% of the distance; the dotted line is 5%. Note, however, that there is no indication that the errors scale with velocity. The sample of galaxies with $\lesssim 5\%$ errors have linewidths measured from the new narrowband H I spectra. The bottom panel indicates that with increasing observed velocity, it is more likely that we obtain an unusually large positive peculiar velocity. Since the peculiar velocity scales with the observed CMB velocity (Eq. 6.21), the same offset from the TF relation, resulting either from photometric errors or the intrinsic scatter in the TF relation, at a greater distance implies a larger peculiar velocity. The distribution is similar to that obtained by Masters (2005) of a local field TF sample from the SFI++ (see her Fig. 6.2), in particular the growing numbers of very large peculiar velocities for $v > 4000 \text{ km s}^{-1}$.

6.4 The Local Peculiar Velocity Field in the ZoA

The peculiar velocity sample is used to produce a map of the peculiar velocity flow field in the ZoA. The map is made by interpolating the peculiar velocity surface across the Galactic longitude – recession velocity plane. This is done using the `griddata` task in Python’s `matplotlib` package, which employs natural neighbor interpolation based on Delaunay triangulation. First, only the higher mass ($\log W > 2.3$ where the scatter about the TF template is symmetric) galaxies are considered and the peculiar velocities are limited to $|v_{pec}| < 2000 \text{ km s}^{-1}$. The map is presented in Fig. 6.8 where the peculiar velocities of individual galaxies are plotted as points and the filled contours show the smoothed peculiar velocity map. This map includes all galaxies within the Galactic plane, i.e. within $|b| < 5^\circ$. Peculiar velocities are indicated by the colour scale, with redder colours being more positive velocities and bluer colours being more negative velocities. Note that the interpolation around the Galactic bulge, $0^\circ < l < 60^\circ$, is unreliable due to the underdensity of available data there. This is a combined effect of the lower detection rate and the exclusion from the sample of those galaxies with poor photometry due to contamination by foreground stars. The black star marks the centre of the GA at $(l, v) = (320^\circ, 4500 \text{ km s}^{-1})$.

Figure 6.9 shows a similar plot, but this time for all the galaxies in the TF sample, i.e. including the galaxies at the low mass end of the TF relation as well as those with very large derived peculiar velocities. This plot is provided for completeness and it should be noted that there is a strong observational bias evident in the map. The selection criterion of $v_{obs} = 6000 \text{ km s}^{-1}$ means that for a given recession velocity $H_0 d$ we cannot measure peculiar velocities larger than $v_{obs} - H_0 d$. For example, at $H_0 d = 4000 \text{ km s}^{-1}$, the upper limit to the allowable peculiar velocity is 2000 km s^{-1} . The map does, however, indicate the larger peculiar velocities present in the foreground of the GA at $2000 - 3000 \text{ km s}^{-1}$, compared to the same distance in the longitude range $210^\circ < l < 270^\circ$.

Inspection of these two figures, but in particular Fig. 6.8 where the details of the flow field can be seen, shows that around $(l, v) \sim (240^\circ, 200 \text{ km s}^{-1})$ there is evidence of an outflow behind Puppis towards the Hydra-Antlia extension. Also infall onto Hydra-Antlia from behind at $v = 4000 \text{ km s}^{-1}$ can be seen across the Galactic longitudes $240^\circ < l < 270^\circ$.

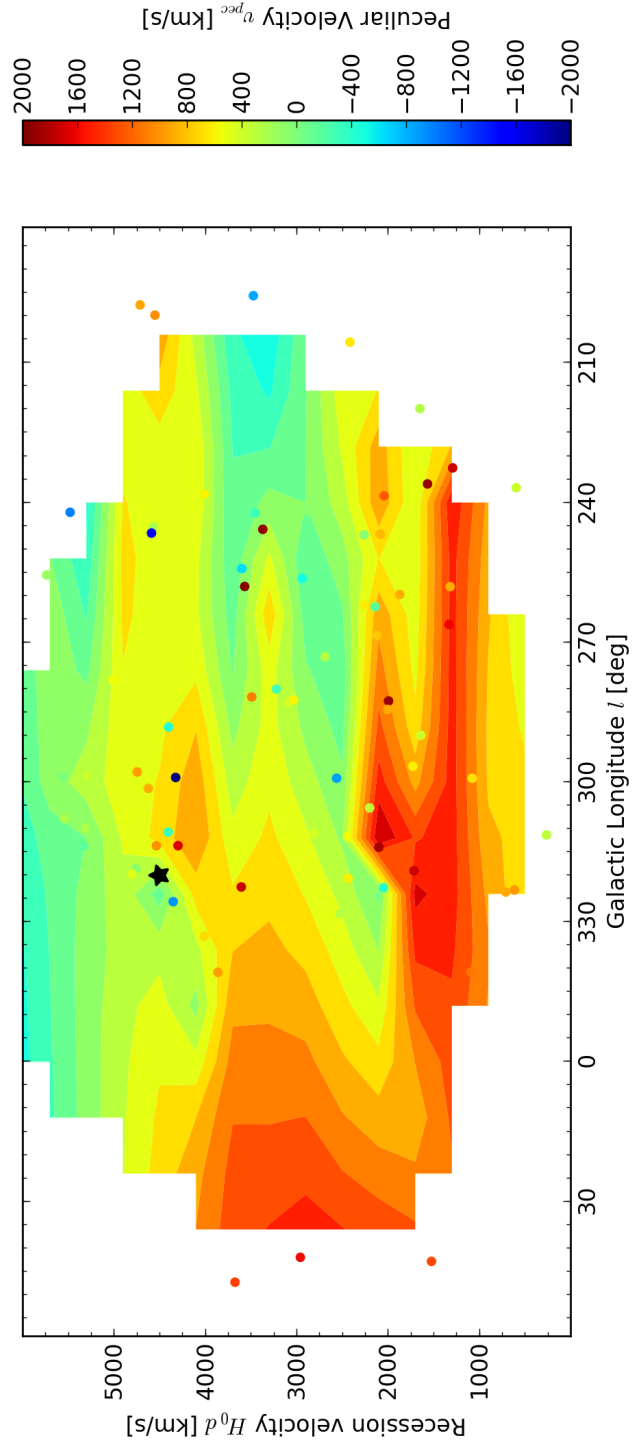


Figure 6.8: Smoothed peculiar velocity flow field obtained by interpolating the peculiar velocities across the Galactic longitude – recession velocity plane. Only galaxies with $\log W > 2.3$ and $|v_{pec}| < 2000 \text{ km s}^{-1}$ are included in this plot. The peculiar velocities of individual galaxies are plotted as points. The colour scale shows the values of the peculiar velocities, with redder colours being more positive velocities and bluer colours being more negative velocities. The centre of the GA is plotted as a large black star at $(l, v) = (320^\circ, 4500 \text{ km s}^{-1})$ (Kolatt et al. 1995).

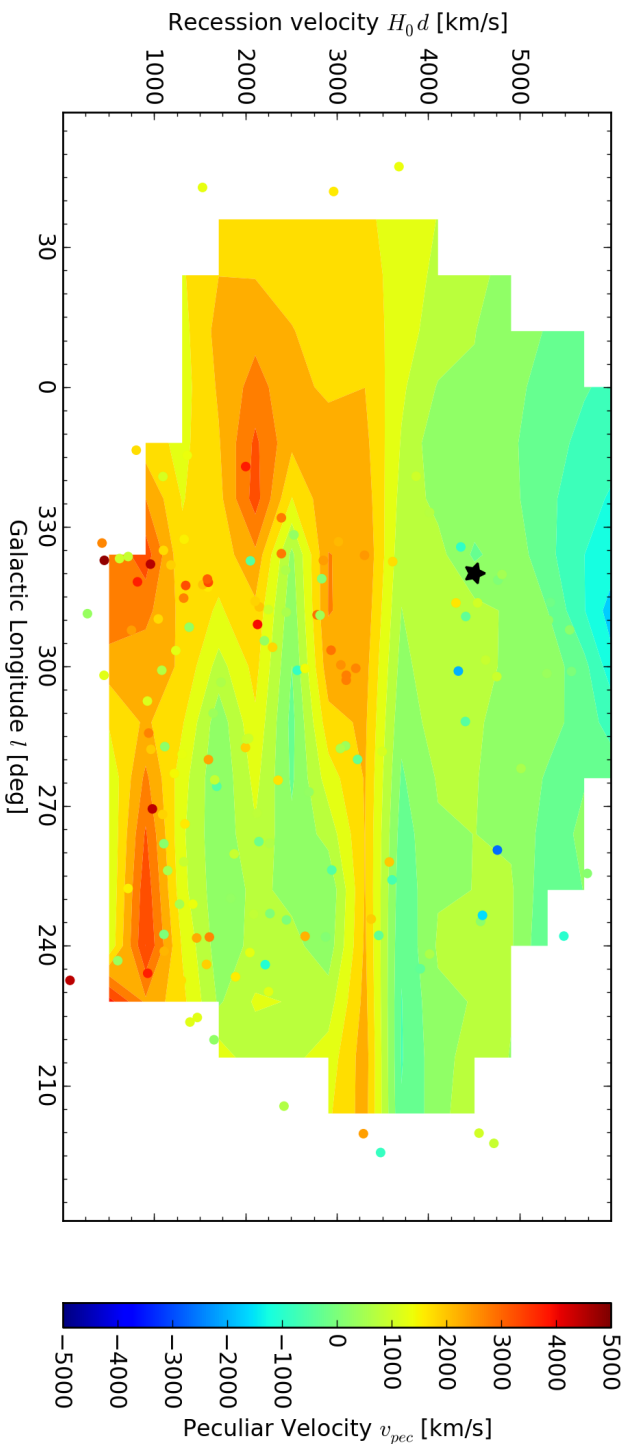


Figure 6.9: Smoothed peculiar velocity flow field obtained by interpolating the peculiar velocities across the Galactic longitude – recession velocity plane. Data from the entire TF sample are plotted for all peculiar velocities. Individual galaxies are plotted as points. The colour scale shows the values of the peculiar velocities, with redder colours being more positive velocities and bluer colours being more negative velocities. The centre of the GA is plotted as a large black star at $(l, v) = (320^\circ, 4500 \text{ km s}^{-1})$ (Kolatt et al. 1995).

Lynden-Bell et al. (1988) placed the GA at $(l, b, v) = (307^\circ, +9^\circ, 4500 \text{ km s}^{-1})$. Based on the larger sample including ellipticals and spirals, Kolatt et al. (1995) put it at $(l, b, v) = (320^\circ, 0^\circ, 4500 \text{ km s}^{-1})$, which is plotted as a large black star in Figs. 6.8 and 6.9. The blue region behind the GA appears to show evidence for backside infall onto the GA, i.e. the presence of negative peculiar velocities behind the GA region. This evidence bears further inspection given its location at the limits of the NIR survey and the observational bias towards smaller peculiar velocities. Notably, in Fig. 6.9, it can be seen that most of the large amplitude positive peculiar velocities lie in the foreground of the GA.

The peculiar velocity flow field is also plotted as a vector field in Fig. 6.10. All the galaxies within 5° of the Galactic plane are plotted in a plane where the positive Y -axis points to the Galactic centre. Galactic longitude increases counterclockwise. The GA centre is indicated by the blue star. The tails of the arrows are plotted at the TF distance c_z and the tips are plotted at the observed velocity v_{obs} , thus the length and direction of the arrow indicates the peculiar velocity (in km s^{-1}). Negative velocities point towards the origin, positive velocities, away. The amplitude of the peculiar velocities is restricted to 2000 km s^{-1} and galaxies with $\log W < 2.3$. The filled grey region is not covered by the HIZOA survey: $60^\circ < l < 190^\circ$. Data for all galaxies in the TF sample are plotted, with large peculiar velocities, $|v_{pec}| > 2000 \text{ km s}^{-1}$, plotted in grey. A strong flow towards the GA which is confined to the first quadrant of the plot can be seen.

6.4.1 One Attractor or Two?

One of the questions concerning the Local velocity flow field that remains unresolved is that of the Great Attractor versus the Shapley Concentration. Which is the dominant attractor in the Local flow field? Backside infall onto the GA was first suggested by Dressler & Faber (1990) but was refuted by Mathewson et al. (1992b) based on independent data. Analysis of the “Streaming Motions of Abell Clusters” sample (SMAC) showed a bulk motion that was inconsistent with the GA, and marginally supports infall onto Shapley (Hudson et al. 2004). Tonry et al. (2000) find an attractor closer and less massive than the original GA, $(l, b, v) = (289^\circ, 19^\circ, 3200 \pm 260 \text{ km s}^{-1})$, based on their sample of ~ 300 galaxies with distances from the method of surface brightness fluctuations. The SNIa data of Lucey et al. (2005) suggests significant flow towards Shapley. Decoupling the GA and Shapley flow is difficult, and thus constraining the relative contributions of the two structures has been controversial. The simplest approach is to consider spherically symmetric infall onto discrete attractors.

The mathematical model for the peculiar velocity at position \mathbf{r} generated by a single attractor at position \mathbf{d}_a is:

$$v_{pec,a}(\mathbf{r}) = \left(v_a \frac{\mathbf{r}_a}{d_a} \left[\frac{(d_a^2 + c_a^2)}{(r_a^2 + c_a^2)} \right]^{(n_a+1)/2} \right) \cdot \hat{\mathbf{r}}, \quad (6.30)$$

where d_a is the distance to the attractor, $\mathbf{r}_a = \mathbf{d}_a - \mathbf{r}$ is the vector connecting the point \mathbf{r}

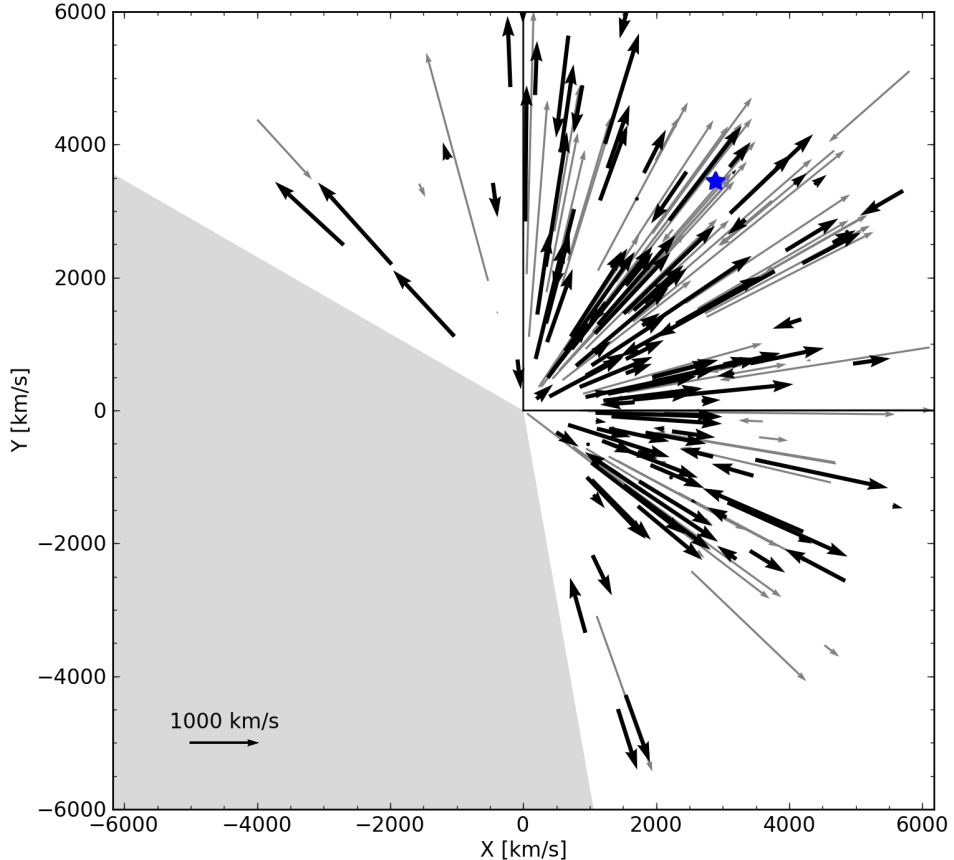


Figure 6.10: Peculiar velocities within 5° of the Galactic plane. The positive Y -axis points towards the Galactic centre. The tails of the arrows are plotted at the TF distance cz and the tips are plotted at the observed velocity v_{obs} , thus the length and direction of the arrow indicates the peculiar velocity (in km s^{-1}). Thin light grey arrows correspond to galaxies with $\log W < 2.3$ while the thicker black arrows are galaxies with $\log W > 2.3$. The centre of the GA is plotted as a large blue star at $(l, v) = (320^\circ, 4500 \text{ km s}^{-1})$ (Kolatt et al. 1995). The filled grey region is not covered by the HIZOA survey: $60^\circ < l < 190^\circ$.

and the attractor, c_a is the core radius and v_a is the velocity generated by the attractor at the origin.

Figure 6.11 shows the peculiar velocity for all galaxies in the TF sample as a function of the recession velocity H_0d . Galaxies near the GA are plotted in solid points, while others are plotted in open circles. The shaded region indicates the NIR observational limit at $v_{obs} = 6000 \text{ km s}^{-1}$; this limits our ability to fully determine the flow behind the GA. Also plotted are three attractor models. The first consists only of the GA (dotted green line). The GA of Faber & Burstein (1988) with $n_{GA} = 1.7$, $r_{GA} = 4200 \text{ km s}^{-1}$, $c_{GA} = 1430 \text{ km s}^{-1}$ and it is normalised to give a peculiar velocity at the LG of 500 km s^{-1} . The second model consists only of the Shapley Concentration (blue dashed line) with $n_{SC} = 1.7$, $r_{SC} = 14\,500 \text{ km s}^{-1}$, $c_{SC} = 2250 \text{ km s}^{-1}$. The final model is the sum of the GA and SC attractors, where the relative contribution is $50 \pm 10\%$ (red line and shaded region) (Smith et al. 2000). Note that amount of backside infall onto the GA in the GA+SC model depends strongly on the relative contributions of the two structures. The single SC model is inconsistent with the negative peculiar velocities observed at $H_0d > 3000 \text{ km s}^{-1}$. The GA only and GA+SC models cannot be distinguished from the available data; they depend crucially on the nature of the peculiar velocities beyond $H_0d = 4500 \text{ km s}^{-1}$ where this survey fails to measure positive peculiar velocities. However, it is clear that the GA does have a significant role in the local dynamics. The fact that there are significant negative peculiar velocities does suggest that, at least for this type of model, the contribution of the GA to the peculiar velocity of the LG is $> 40\%$. The extension of the NIR survey presented in this thesis to $v_{obs} = 8000 \text{ km s}^{-1}$ will determine more precisely the nature of the peculiar velocities beyond $H_0d = 4500 \text{ km s}^{-1}$. A lower amplitude of positive peculiar velocities beyond this point will imply a greater influence of the GA compared to the SC.

It is clear that the mass distribution in the Universe is more complex than simple attractor models, in fact infall onto attractors may occur mainly along filaments. Conflicting determinations of the mass density may result from this non-spherical infall onto these two structures. Moreover, there is evidence for a filamentary link between the Hydra-Centaurus and Shapley superclusters (Drinkwater et al. 2004) that may cause significant deviations from the simple attractor models in this region. In the future, non-parametric modeling of the local velocity field, such as the POTENT method (Dekel et al. 1990), will allow for fitting more complicated mass distributions.

6.5 Discussion

In this section, some of the systematic uncertainties that could affect these results are discussed. Methods of overcoming these uncertainties are suggested.

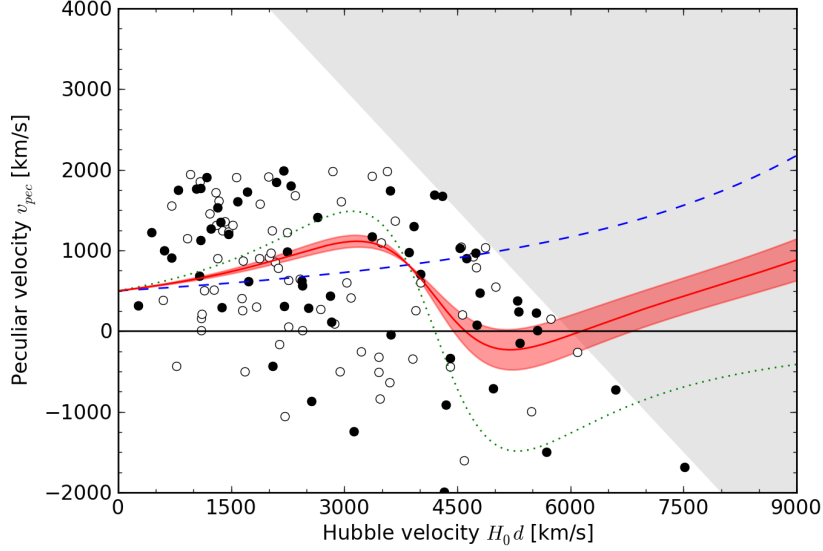


Figure 6.11: Peculiar velocities as a function of Hubble distance $H_0 d$ for all TF sample galaxies with peculiar velocities $|v_{pec}| < 2000 \text{ km s}^{-1}$ (open circles). Data for galaxies within $\sim 30^\circ$ of the GA centre ($290^\circ < l < 350^\circ$), are plotted in filled circles. The shaded region indicates the NIR observational limit at $v_{obs} = 6000$. Three attractor models are plotted for comparison: a single GA model (green dotted line), a single Shapley model (blue dashed line) and a double GA+Shapley model (red shaded region) with $50 \pm 10\%$ contribution to the LG peculiar motion.

6.5.1 Extinction

It is well known that the DIRBE/IRAS extinction maps (Schlegel et al. 1998) overestimate the extinction in the ZoA. In the derivation of the peculiar velocities, a single value of $f = 0.82$ was used to correct for this overestimation. However, it was shown in Sect. 5.3.1 that this correction factor varies with Galactic latitude, dropping as low as 0.51 in the range $-3^\circ < b < -1^\circ$. This has the effect of dimming the absolute magnitudes and reducing the derived peculiar velocities. Approximately 15 galaxies in the peculiar velocity sample lie within this range and their peculiar velocities may as a result be overestimated by $\sim 200 \text{ km s}^{-1}$. For future flow fields derived in the ZoA, it will be necessary to better constrain the DIRBE/IRAS overestimation. Larger samples across the ZoA containing NIR colours will enable this to be done.

6.5.2 Comparison to 2MASS TF Relation

The TF template relation used here is derived from 2MASS total magnitudes. Thus, it is necessary to ensure that the magnitudes used here are consistent with the 2MASS magnitudes.

The extrapolated total magnitudes obtained by 2MASS and the IRSF/SIRIUS pipeline are compared for the 82 galaxies observed with the IRSF that have counterparts in 2MASX.

We cannot transform the IRSF/SIRIUS magnitudes to the 2MASS standard due to the lack of colour terms*. Figure 6.12 shows this comparison. The mean offsets and standard deviations are listed in Table 6.1. It is noted that low resolution and depth of the 2MASS survey limits its performance in the ZoA, resulting in poorly determined magnitudes. The positive offsets indicate that the 2MASS magnitudes are fainter than those determined by our profile fits. This is due to the improved performance of our images and fitting which measures the surface brightness profile further out on the disk than 2MASS does. The offset is much larger for galaxies with large extended low surface brightness disks which are missed in 2MASS. This is likely substantiated by the fact that we do not see any trend with magnitude. It has been shown that even outside of the ZoA 2MASS underestimates the total magnitudes of dwarf and LSB galaxies by $0.^m5 - 2.^m0$ (Kirby et al. 2008b, de Swardt et al. 2010). This is particularly important in a HI selected sample. The offset in the determination of total magnitudes between 2MASS and the IRSF/SIRIUS may imply overly large peculiar velocities.

In using the IRSF/SIRIUS magnitudes in the 2MASS TF template relation, it should be ensured that there are no significant offsets produced by the different methods of determining the total magnitudes and the depth of the images. The TF relation for the 51 galaxies in the TF sample that have 2MASS counterparts is derived using both the 2MASS and IRSF/SIRIUS magnitudes. Figure 6.13 shows the absolute magnitudes plotted as a function of the corrected linewidths derived from the IRSF/SIRIUS magnitudes and inclinations (*left* panels) and derived from the 2MASS data (*right* panels). As in Fig. 6.2, the J band is plotted in the *top* panels (blue), the H band in the *middle* panels (green) and the K_s band in the *bottom* panels (red). The solid lines show the Masters et al. (2008) 2MTF template relations (eqs. 6.13) and the dotted lines show the intrinsic scatter in the 2MTF template relation (eqs. 6.15). Open circles indicate galaxies for which the implied peculiar velocity is greater than 2000 km s^{-1} . Note that the extreme outliers at the faint end of the TF relation appear in both panels. Table 6.2 shows the mean and standard deviation of the offsets from the 2MTF template relation for the IRSF/SIRIUS and 2MASS TF relations in J , H and K_s . Note that these values include the obvious outliers at the low mass end of the TF relation. The scatter is the same for both the IRSF/SIRIUS observations and the 2MASS data. The small difference, $\sim 0.^m3$, in the mean offsets is not significant given the asymmetric distribution of the offsets for both the IRSF/SIRIUS and 2MASS.

The applicability of the total magnitudes in a 2MASS TF template is questionable due to the large offsets in the photometry between 2MASS and the IRSF/SIRIUS. However, since the derivation of a template relation using isophotal magnitudes is beyond the scope of this thesis, we have used the Masters et al. (2008) 2MASS TF template relation that is already available and note that there may be a systematic offset introduced by the use of total magnitudes.

*Colours can only be calculated in a common aperture.

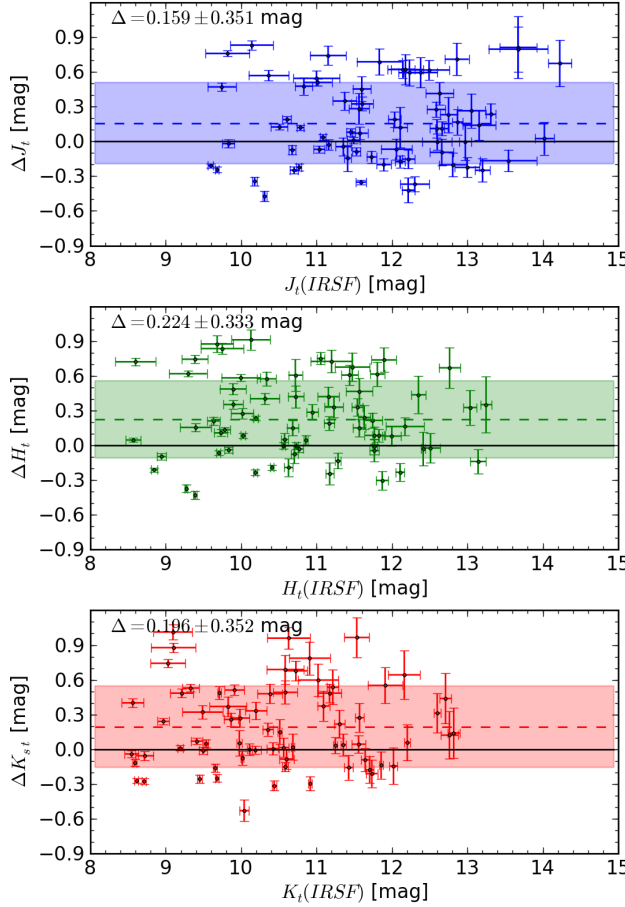


Figure 6.12: Comparison of the extrapolated total magnitudes in J (top), H (middle) and K_s (bottom) between the IRSF and 2MASX. The horizontal coloured strip shows the 1σ dispersion around the mean.

Table 6.1: Comparison of 2MASX and IRSF/SIRIUS total magnitudes

Filter	Total magnitude	
	$\langle \Delta m \rangle$	σ
	[mag]	[mag]
J	0.16	0.35
H	0.22	0.33
K_s	0.20	0.35

Table 6.2: Comparison of 2MASX and IRSF/SIRIUS TF offsets

Filter	IRSF/SIRIUS		2MASS	
	$\langle \Delta m \rangle$	σ	$\langle \Delta m \rangle$	σ
	[mag]	[mag]	[mag]	[mag]
J	-1.6	1.9	-1.2	1.9
H	-1.4	1.8	-1.1	1.8
K_s	-1.5	1.9	-1.2	1.9

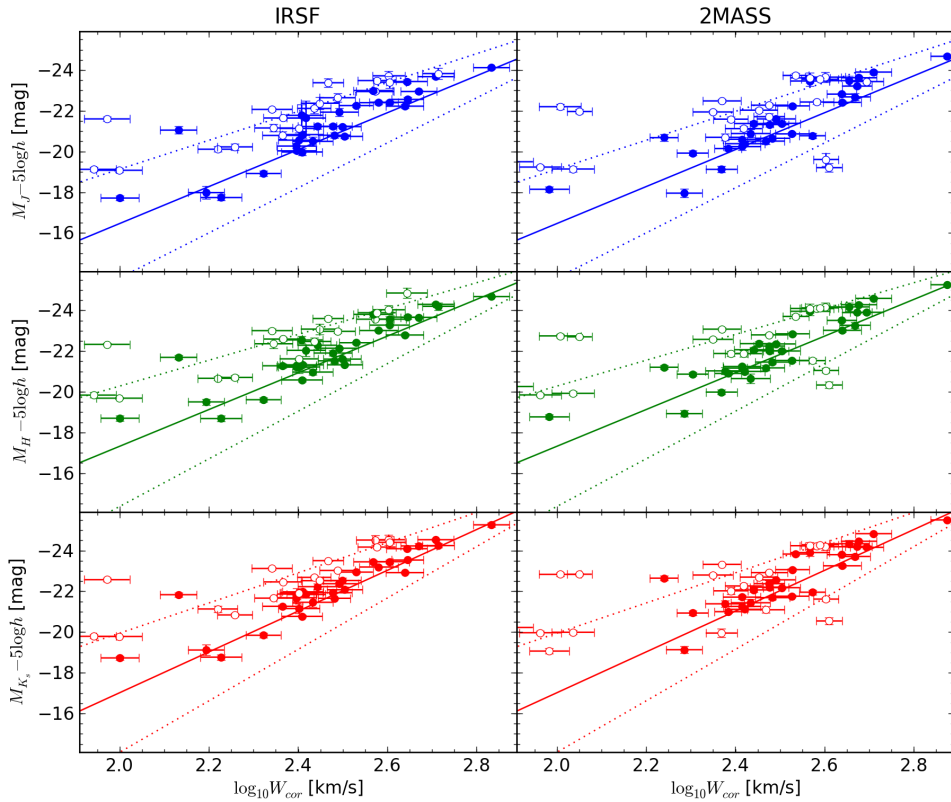


Figure 6.13: Comparison between the TF relations from IRSF magnitudes (*left*) and 2MASS magnitudes (*right*) for a subsample of galaxies that have counterparts in the 2MASX. The top panel is the J band (blue), the middle is H (green) and the bottom is K_s (red). The solid lines show the 2MTF template relations of Masters et al. (2008) and the dotted lines show the intrinsic scatter in the 2MTF template relation.

6.5.3 Further Work

The answer to the GA versus SC question remains unresolved. However, the GA has been shown to have a significant effect on the local peculiar velocity field. The extension of this survey to observed velocities larger than 6000 km s^{-1} , at least to 8000 km s^{-1} , in particular in the GA region, will better enable the mapping of the flow field behind the GA.

In addition, full non-parametric modelling of this peculiar flow field with a method such as POTENT, may help determine the nature of the obviously complex mass distribution in this region. This dataset can readily be merged with the 2MTF survey when it is completed and can be used both to complement and improve the sampling in the ZoA of that data, as well as to compare with the results of interpolation of the ZoA mass density field.

Chapter 7

Conclusions and Future Work

7.1 Summary

The high extinction and stellar density at low Galactic latitude results in optical and near infrared surveys becoming incomplete close to the Galactic plane and Galactic bulge. The 21 cm line of neutral hydrogen has proven to be the most effective at penetrating the ZoA. However, it provides little information about the stellar content of the galaxies. Data from other wavelengths are required for the determination of the stellar properties of these HI galaxies. It has been shown here that the deep NIR observations are well suited for such measurements in the ZoA as they are able to penetrate the dust of the Milky Way. Moreover the NIR traces out the old stellar population of these galaxies providing a good estimate of the stellar mass of the galaxy. The combination of HI survey data and deep NIR follow-up imaging in the NIR Tully-Fisher relation has allowed for the determination of a preliminary peculiar velocity flow field within the southern ZoA.

In this thesis we have presented new narrowband HI observations of a sample of HIZOA galaxies. These observations provide improved measurements of the linewidths for use in TF analysis of peculiar velocities. The relative errors in the HI linewidths from the narrowband observations are a factor of ~ 3.4 better than the HIZOA linewidth errors.

Deep NIR follow-up observations of HIZOA galaxies within 6000 km s^{-1} are presented. J , H and K_s images of 580 targets were obtained using the 1.4 m IRSF telescope with the SIRIUS camera. The combined three-colour NIR fields were visually searched for counterparts of the HI galaxies and following the identification of possible counterpart galaxies, careful subtraction of foreground stars was done. Surface photometry was performed on the star-subtracted images to produce a photometric catalogue of 567 NIR galaxies. A range of photometric parameters are determined for each source and used to compile the final NIR catalogue; these include the ellipticity, position angle, isophotal magnitudes and extrapolated total magnitudes in all three NIR bands. The NIR colours of all the detected galaxies were used to investigate the extinction in the Galactic plane. The ratio of the true extinction to the DIRBE/IRAS extinction (Schlegel et al. 1998) was found to be 0.82 across the HIZOA

survey region. This value showed no significant variation with Galactic longitude but did vary with Galactic latitude. The DIRBE/IRAS overestimate of extinction is greater at lower Galactic latitude and, furthermore, is asymmetric about the Galactic plane. The correction factor is smaller above the plane than below it. Near IR counterparts were confirmed for 356 HI galaxies and the HI and NIR data for these galaxies were used to investigate the relationship between the stellar and gas components. The HI mass-to-light ratio has an upper envelope for any given luminosity.

The HI spectral data and NIR photometry were used to measure the peculiar velocities for a subsample of inclined galaxies. Using the TF template derived by Masters et al. (2008) for the 2MTF, we combine the HI 50% velocity widths and the NIR total extrapolated magnitudes to obtain peculiar velocities and distances. The raw linewidths are corrected for inclination determined from the *J* band ellipticity and the raw magnitudes are corrected for Galactic and internal extinction. The new narrowband HI data provide significantly improved linewidths and consequently smaller errors for a subset of peculiar velocities. This allowed for the determination of a preliminary peculiar velocity flow field constructed directly for the first time from observations. A strong flow towards the Great Attractor (GA) is observed. This flow field also shows possible indications of backside infall onto the GA, showing that the GA does indeed play an important role in the motion of the Local Group.

7.2 Future Prospects

The success of this study demonstrates the feasibility of further TF peculiar velocity studies in the ZoA. There are several ways in which this project can be expanded.

The extension of this NIR survey to slightly more distant galaxies, $v_{obs} < 8000 \text{ km s}^{-1}$ will allow the peculiar velocities behind the GA to be mapped in more detail. This will better constrain the influence of the GA on the motions of galaxies in the Local Universe.

The problems associated with using total magnitudes both for 2MASS and within the ZoA have been highlighted. Further work can be undertaken to determine a TF template relation using 2MASS isophotal magnitudes which can, with the introduction of less uncertainty, be used in the ZoA. The continued work on the exploration of extinction within the ZoA and better constraints on the overestimation by the DIRBE/IRAS maps will reduce the uncertainties associated with extinction corrections.

We have used this HI and NIR dataset only to investigate the peculiar velocity field within the ZoA. It should be combined with other datasets, in particular the 2MASS Tully-Fisher survey, to map the local peculiar velocity field without having to rely on statistical interpolation techniques. Our dataset has been specifically chosen so that it can be readily combined with the 2MTF survey. However, it will also be insightful to compare this peculiar velocity flow field with that obtained in the ZoA through interpolation techniques.

This work demonstrates the ability of deep NIR imaging to detect HI galaxies in the ZoA. In particular, galaxies are detected in regions where the existing all-sky 2MASS survey fails to detect any galaxies due to prohibitive stellar densities. The complementary dataset

consisting of the NIR imaging and HI spectra will be useful in a number of applications. For example, the properties of galaxies in dynamically interesting structures in the ZoA, in particular the Local Void, can be studied. Some LV galaxies were detected in HIZOA; are the NIR and HI properties of these galaxies different to those in denser environments?

The dataset can be expanded to include mid infrared (MIR) counterparts. The MIR information can be used to measure the Spectral Energy Distributions (SEDs) of these galaxies. Fitting SEDs is a method that can more accurately determine the foreground extinction. This will be a useful extension of our study of extinction in the Galactic plane. MIR fluxes provide further information on other parameters such as the star formation rate which will expand our understanding of the relationships between the neutral gas, old stellar population and the young stellar population in galaxies. The GLIMPSE and MIPS GAL surveys by the Spitzer Telescope cover most of the inner Galactic plane ($|b| < 1^\circ$) and have some overlap with our survey. In the near future the NASA Wide Field Infrared Explorer (WISE) will survey the entire sky at $3.4\mu\text{m}$, $4.6\mu\text{m}$, $12.6\mu\text{m}$ and $22\mu\text{m}$, providing further MIR data for this analysis.

Additionally, with the advent of more sensitive HI and NIR instruments, the ability to extend this work to fainter and less massive galaxies will become possible. This will significantly increase the sample sizes, in particular within the ZoA but also across the whole sky. Improved sampling and more even coverage will allow for more accurate determinations of the cosmic peculiar velocity fields. Four-metre-class NIR telescopes such as VISTA will provide high resolution imaging overcoming some of the problems of star crowding near the Galactic bulge. Of particular interest will be the VISTA Hemisphere Survey (VHS), an ESO public survey which will map the entire Southern sky in J , H and K_s . While the depth of the survey may result in it becoming saturated by numerous faint stars at very low Galactic latitudes, $|b| < 2^\circ$, it will be able to detect fainter galaxies at higher latitudes. The new generation of radio telescopes, specifically the two SKA pathfinders, MeerKAT and ASKAP, will be able to detect fainter HI galaxies to measure linewidths. In particular, the Widefield ASKAP L-band Legacy All-Sky Blind surveY (WALLABY; Koribalski & López-Sánchez 2009) will survey the southern sky ($\sim 75\%$ of the sky) and will detect galaxies with HI content as low as $10^8 M_\odot$. All-sky surveys with the WSRT/APERTIF will extend this to include the northern sky. This thesis is a forerunner for larger projects such as these and clearly shows that such studies will be possible.

Appendix A

Catalogue and Postage Stamps

This appendix lists a sample of the parameters available in the NIR catalogue for the brightest, $K_{s20} < 11^m$, galaxies. The catalogue parameters listed here are chosen for their similarity to the major 2MASX parameters. The columns in Table A.1 are:

Column 1 Unique identifier [ZOAhhmmss.sss±ddmmss.ss]

Column 2 HI catalogue name [Jhhmm±dd]

Columns 3 & 4 Galactic co-ordinates [deg]

Columns 5 J band ellipticity ($\epsilon = 1 - b/a$) and error

Columns 6 J band position angle (East of North) and error [deg]

Column 7 K_{s20} fiducial isophotal radius [arcsec]

Columns 8–10 J , H and K_s band K_{s20} fiducial isophotal magnitude and error [mag]

Columns 11–13 J , H and K_s band extrapolated total magnitude [mag]

Column 14 Galactic reddening along the line of sight (Schlegel et al. 1998) [mag]

Column 15 Stellar density for stars brighter than 14^m in K_s

The galaxies are sorted by K_{s20} magnitude, from brightest to faintest. Table A.2 displays the three-colour postage stamps of the galaxies in Table A.1. The entire catalogue is available online at <http://www.ast.uct.ac.za/~wendy/zoatf/nircat>.

Table A.1: The brightest, $K_{s20} < 11^m$ galaxies in the NIR catalogue sorted by K_{s20} magnitude from the brightest to the faintest.

Designation	H1 Name	l	b	ϵ_J	ϕ_J	r_{k20fe}	J_{k20fe}	K_{s20fe}	H_{k20fe}	J_{tot}	H_{tot}	$K_{s,tot}$	$E(B-V)$	SD
		[deg]	[deg]	[deg]	["]	[mag]	[mag]	[mag]	[mag]	[mag]	[mag]	[mag]	[mag]	[mag]
ZOA151434.147-525921.52	J1514-53	323.594	4.043	0.77	-16.9	136.09	8.86 ± 0.02	7.91 ± 0.02	7.42 ± 0.02	8.96 ± 0.03	7.83 ± 0.03	7.34 ± 0.02	0.99	4.30
ZOA085728.473-391605.66	J0857-39	261.500	4.100	0.10	28.8	45.77	9.18 ± 0.02	8.32 ± 0.02	9.21 ± 0.02	8.06 ± 0.07	7.93 ± 0.03	0.72	3.61	
ZOA122238.290-583657.66	J1222-58	299.180	4.046	0.69	-27.0	60.30	9.71 ± 0.02	8.92 ± 0.02	9.68 ± 0.02	8.57 ± 0.10	8.58 ± 0.02	0.58	4.12	
ZOA145709.815-542331.46	J1457-54	320.654	4.096	0.51	51.6	53.80	10.04 ± 0.02	9.14 ± 0.02	8.69 ± 0.02	8.83 ± 0.08	8.94 ± 0.06	8.59 ± 0.02	0.85	4.21
ZOA094916.505-475511.27	J0949-47A	274.257	4.549	0.06	28.9	38.65	9.67 ± 0.02	8.97 ± 0.02	9.59 ± 0.04	8.85 ± 0.04	8.65 ± 0.03	0.35	3.80	
ZOA114606.371-562326.95	J1145-56	293.937	5.336	0.27	-48.5	54.68	9.99 ± 0.02	9.26 ± 0.02	8.82 ± 0.02	9.41 ± 0.20	8.45 ± 0.24	8.41 ± 0.11	0.39	3.84
ZOA135138.534-583515.22	J1351-58	310.724	3.370	0.52	32.3	47.27	10.23 ± 0.02	9.31 ± 0.02	8.87 ± 0.02	10.18 ± 0.03	9.27 ± 0.02	8.55 ± 0.09	0.97	4.29
ZOA143158.829-552758.82	J1431-55	316.912	4.653	0.05	82.6	34.39	10.32 ± 0.02	9.46 ± 0.02	9.05 ± 0.02	9.74 ± 0.19	8.60 ± 0.27	8.56 ± 0.15	0.85	4.09
ZOA074843.871-261445.62	J0748-26B	242.586	-0.239	0.32	-26.6	39.43	10.49 ± 0.02	9.64 ± 0.02	9.10 ± 0.02	10.31 ± 0.06	9.54 ± 0.03	8.60 ± 0.14	0.56	3.72
ZOA163211.878-280530.82	J1632-28	351.084	13.502	0.72	-52.8	81.48	10.28 ± 0.02	9.45 ± 0.02	9.10 ± 0.02	10.13 ± 0.06	9.28 ± 0.03	8.97 ± 0.02	0.61	3.54
ZOA141036.181-653457.76	J1410-65	310.997	-3.958	0.52	-87.4	46.18	10.35 ± 0.02	9.48 ± 0.02	9.14 ± 0.02	10.31 ± 0.03	9.39 ± 0.02	8.72 ± 0.12	0.60	4.33
ZOA074843.902-261446.34	J0748-26A	242.586	-0.239	0.30	-27.9	31.93	10.71 ± 0.02	9.78 ± 0.02	9.25 ± 0.02	9.82 ± 0.29	9.70 ± 0.03	8.97 ± 0.08	0.72	3.84
ZOA083439.531-400855.61	J0834-40	259.448	0.122	0.22	20.8	34.38	10.02 ± 0.02	9.52 ± 0.02	9.30 ± 0.02	9.41 ± 0.21	9.11 ± 0.12	8.54 ± 0.23	2.12	3.84
ZOA085838.795-423157.31	J0858-42	264.125	2.141	0.45	64.1	43.00	11.95 ± 0.02	10.10 ± 0.02	9.35 ± 0.02	11.89 ± 0.09	9.78 ± 0.07	9.19 ± 0.04	3.99	3.73
ZOA094952.868-563223.55	J0949-56	279.808	-2.054	0.24	-67.6	45.57	11.43 ± 0.02	10.29 ± 0.02	9.58 ± 0.02	11.03 ± 0.23	9.78 ± 0.12	9.01 ± 0.14	2.10	4.16
ZOA141933.720-580850.19	J1419-58B	314.363	2.755	0.59	19.7	52.89	11.00 ± 0.02	10.14 ± 0.02	9.59 ± 0.02	10.79 ± 0.08	10.02 ± 0.03	9.41 ± 0.03	1.52	4.36
ZOA163140.1118-280606.66	J1631-28	350.997	13.584	0.27	69.5	35.29	10.83 ± 0.02	10.07 ± 0.02	9.59 ± 0.02	10.70 ± 0.06	9.40 ± 0.20	9.45 ± 0.03	0.63	3.60
ZOA090033.110-392626.93	J0900-39	262.020	4.438	0.39	-53.3	37.83	10.79 ± 0.02	10.15 ± 0.02	9.67 ± 0.02	10.61 ± 0.06	10.19 ± 0.03	9.54 ± 0.03	0.67	3.61
ZOA161319.695-562349.17	J1613-56	328.261	-3.802	0.35	-70.7	40.49	10.93 ± 0.02	10.69 ± 0.02	9.68 ± 0.02	10.58 ± 0.13	9.82 ± 0.31	9.29 ± 0.09	0.54	4.42
ZOA162101.624-360831.49	J1621-36	343.413	9.765	0.55	54.2	38.44	10.84 ± 0.02	10.05 ± 0.02	9.71 ± 0.02	10.51 ± 0.11	9.83 ± 0.05	9.41 ± 0.08	0.71	3.79
ZOA074252.007-315959.79	J0742-31	246.532	0.52	31.9	26.61	11.15 ± 0.02	10.38 ± 0.02	9.71 ± 0.02	11.08 ± 0.04	10.41 ± 0.02	9.33 ± 0.11	0.83	3.76	
ZOA101212.032-623159.40	J1012-62	285.685	-5.121	0.62	41.4	39.84	10.84 ± 0.02	10.08 ± 0.02	9.71 ± 0.02	10.77 ± 0.04	9.73 ± 0.09	9.49 ± 0.05	0.29	4.04
ZOA114948.692-640006.93	J1149-64	296.241	-1.934	0.57	-63.4	42.66	11.73 ± 0.02	10.42 ± 0.02	9.73 ± 0.02	11.08 ± 0.29	9.84 ± 0.16	9.13 ± 0.16	2.44	4.38
ZOA141710.039-553238.77	J1416-55B	314.915	5.320	0.86	14.5	68.61	11.23 ± 0.02	10.10 ± 0.02	9.73 ± 0.02	11.16 ± 0.03	9.38 ± 0.17	9.21 ± 0.15	0.62	3.98
ZOA074141.201-223112.25	J0741-22	238.558	0.239	0.80	-20.1	48.26	11.31 ± 0.02	10.24 ± 0.02	9.74 ± 0.02	11.03 ± 0.07	9.30 ± 0.25	9.68 ± 0.02	0.66	3.74
ZOA161710.749-581844.59	J1617-58	327.304	-5.542	0.53	79.0	33.09	10.82 ± 0.02	10.04 ± 0.02	9.75 ± 0.02	10.68 ± 0.04	9.63 ± 0.08	9.65 ± 0.03	0.30	4.16
ZOA075220.625-250840.47	J0752-25A	242.052	1.022	0.56	35.4	33.38	10.92 ± 0.02	10.17 ± 0.02	9.79 ± 0.02	10.78 ± 0.05	10.02 ± 0.03	9.03 ± 0.23	0.38	3.68
ZOA175453.601-342057.64	J1755-34	356.554	-4.464	0.37	-15.7	33.98	11.04 ± 0.02	10.35 ± 0.02	9.83 ± 0.02	10.77 ± 0.16	9.73 ± 0.19	9.29 ± 0.16	0.70	4.86
ZOA182226.663-354035.70	J1822-35	357.559	-10.062	0.65	87.5	37.90	10.98 ± 0.02	10.14 ± 0.02	9.84 ± 0.02	10.76 ± 0.07	10.01 ± 0.04	9.09 ± 0.21	0.14	4.11
ZOA141604.868-651502.53	J1416-65	311.644	-3.821	0.48	69.7	36.60	11.23 ± 0.02	10.32 ± 0.02	9.89 ± 0.02	10.47 ± 0.26	10.10 ± 0.04	9.38 ± 0.14	0.77	4.31
ZOA105345.693-625013.17	J1053-62	289.556	-2.968	0.67	-20.5	65.48	11.60 ± 0.02	10.68 ± 0.02	9.90 ± 0.02	11.37 ± 0.16	10.57 ± 0.04	9.71 ± 0.02	0.83	4.23
ZOA133732.784-585414.06	J1337-58B	308.867	3.436	0.28	-16.5	33.07	11.33 ± 0.02	10.31 ± 0.02	9.92 ± 0.02	10.93 ± 0.13	9.93 ± 0.07	9.70 ± 0.04	1.09	4.30
ZOA191724.683-074909.02	J1917+07	42.853	-2.159	0.30	69.8	34.25	11.44 ± 0.02	10.40 ± 0.02	9.94 ± 0.02	11.18 ± 0.10	10.14 ± 0.07	9.90 ± 0.02	1.94	4.51
ZOA143927.759-552503.43	J1439-55	317.910	4.281	0.22	44.9	30.55	11.17 ± 0.02	10.41 ± 0.02	9.97 ± 0.02	10.83 ± 0.11	9.68 ± 0.21	9.10 ± 0.26	0.64	4.11
ZOA074901.358-261442.69	J0748-26A	242.618	-0.182	0.27	-79.5	26.65	11.49 ± 0.02	10.33 ± 0.02	9.99 ± 0.02	11.40 ± 0.06	9.68 ± 0.15	9.84 ± 0.03	0.72	3.84

Continued on Next Page...

Table A.1 – Continued

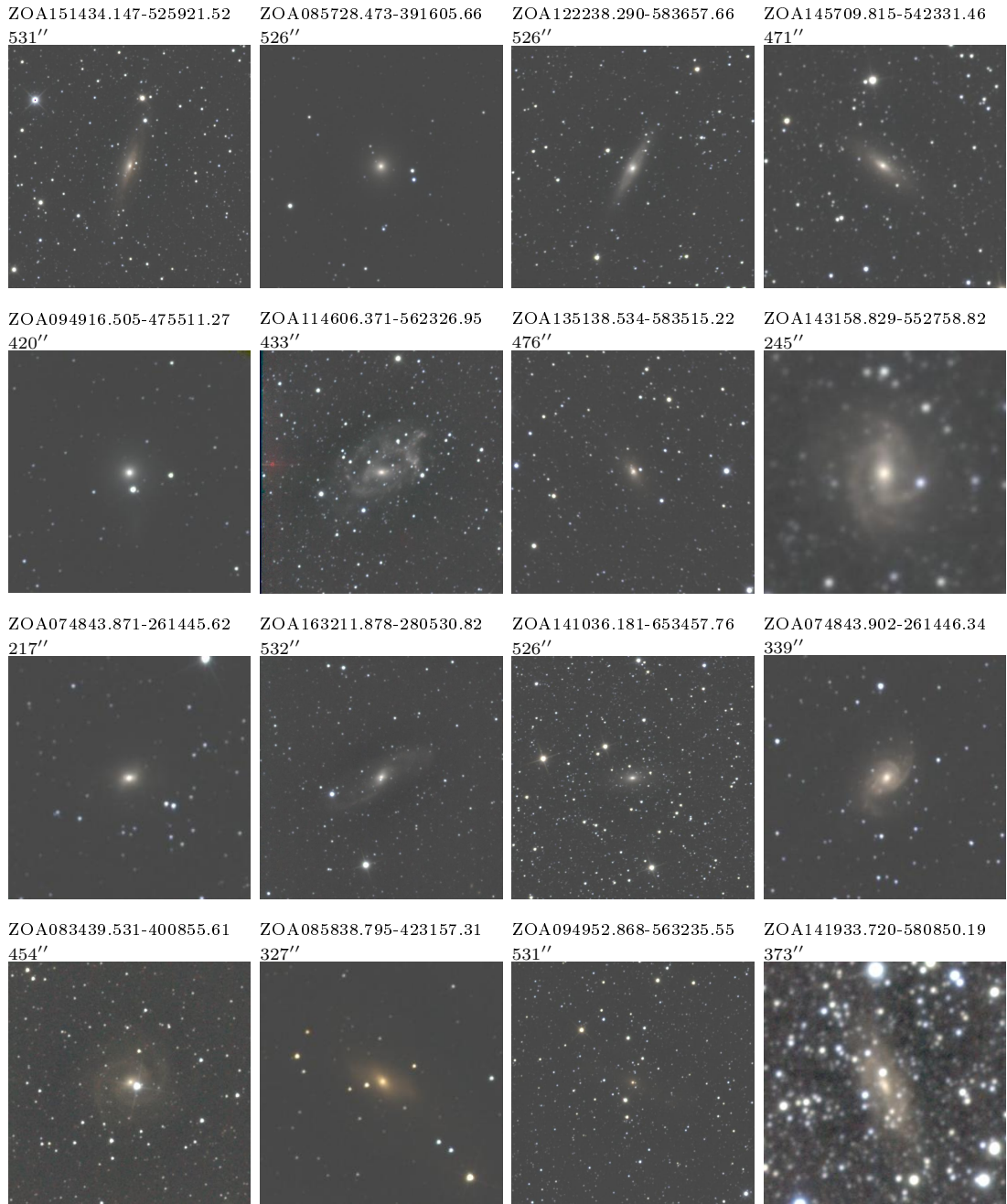
Designation	H _i Name	<i>l</i>	<i>b</i>	ϵ_J	ϕ_J	r_{k20fe} [deg]	J_{k20fe} ["]	H_{k20fe} [mag]	$K_{s\ k20fe}$ [mag]	J_{tot} [mag]	H_{tot} [mag]	$K_{s\ tot}$ [mag]	$E(B-V)$ [mag]	
ZOA164421-521-552937.33	J1644-55	331.917	-6.333	0.83	-59.2	41.24	11.41 ± 0.02	10.41 ± 0.02	10.04 ± 0.02	11.34 ± 0.04	10.07 ± 0.08	9.89 ± 0.03	0.34	4.13
ZOA182423-339-341054.15	J1824-34	339.399	-9.758	0.36	-76.4	25.92	11.08 ± 0.02	10.38 ± 0.02	10.09 ± 0.02	10.14 ± 0.28	9.89 ± 0.13	9.10 ± 0.29	0.13	4.08
ZOA154526-828-605931.93	J1545-61	322.508	-4.918	0.49	20.7	27.22	11.49 ± 0.02	10.58 ± 0.02	10.10 ± 0.02	11.48 ± 0.02	10.52 ± 0.02	9.99 ± 0.03	0.71	4.14
ZOA085828-676-451630.99	J0858-45B	266.181	0.325	0.29	-62.9	35.29	12.29 ± 0.02	10.94 ± 0.02	10.12 ± 0.02	12.06 ± 0.20	10.68 ± 0.08	10.01 ± 0.02	3.66	3.82
ZOA074901-332-261442.57	J0748-26B	242.618	-0.182	0.27	-80.4	23.76	11.35 ± 0.02	10.48 ± 0.02	10.12 ± 0.02	10.97 ± 0.12	9.50 ± 0.18	10.04 ± 0.02	0.56	3.72
ZOA133724-550-585221.57	J1337-58B	308.555	3.469	0.68	36.9	34.33	11.48 ± 0.02	10.51 ± 0.02	10.12 ± 0.02	11.41 ± 0.04	10.02 ± 0.15	9.97 ± 0.03	1.09	4.30
ZOA085809-386-454812.51	J0858-45A	266.544	-0.062	0.30	45.3	28.25	12.14 ± 0.02	10.95 ± 0.02	10.12 ± 0.02	11.85 ± 0.16	10.65 ± 0.10	9.97 ± 0.03	2.74	3.89
ZOA154710.889-590408.56	J1547-59	323.868	-3.538	0.39	-80.3	47.97	11.32 ± 0.02	10.70 ± 0.02	10.13 ± 0.02	10.68 ± 0.23	10.45 ± 0.08	9.95 ± 0.03	0.64	4.34
ZOA160441.177-413947.62	J1604-41	337.221	7.994	0.35	6.8	28.11	11.25 ± 0.02	10.55 ± 0.02	10.18 ± 0.02	10.74 ± 0.15	10.51 ± 0.02	9.96 ± 0.05	0.65	3.89
ZOA1406227.300-575142.26	J1406-57	312.799	3.566	0.27	12.4	32.83	11.57 ± 0.02	10.62 ± 0.02	10.18 ± 0.02	10.91 ± 0.25	10.23 ± 0.10	9.16 ± 0.28	0.73	4.17
ZOA182700.997-243159.00	J1827-20	11.924	-4.088	0.70	17.6	41.25	11.59 ± 0.02	10.62 ± 0.02	10.20 ± 0.02	11.35 ± 0.07	10.48 ± 0.03	10.11 ± 0.03	0.83	4.69
ZOA103718.096-545610.12	J1037-54	284.401	3.036	0.66	49.0	54.55	11.48 ± 0.02	10.61 ± 0.02	10.22 ± 0.02	10.92 ± 0.21	10.13 ± 0.07	10.03 ± 0.02	0.74	4.00
ZOA065802-880-052040.60	J0657-05B	218.441	-0.969	0.13	-5.5	23.79	11.82 ± 0.02	10.70 ± 0.02	10.25 ± 0.02	11.73 ± 0.07	9.75 ± 0.28	10.11 ± 0.04	1.28	3.49
ZOA151548.734-600404.37	J1515-60B	320.387	-2.083	0.17	-84.5	32.38	12.09 ± 0.02	10.84 ± 0.02	10.25 ± 0.02	11.65 ± 0.21	10.54 ± 0.07	9.99 ± 0.06	3.62	4.61
ZOA080953.826-4141-36.58	J0809-41	258.049	-4.600	0.84	-22.4	66.41	12.03 ± 0.02	10.82 ± 0.02	10.25 ± 0.02	11.88 ± 0.10	10.64 ± 0.05	9.87 ± 0.10	1.22	3.75
ZOA160449.497-414301.20	J1604-41	337.204	7.937	0.44	-29.4	36.21	11.42 ± 0.02	10.71 ± 0.02	10.29 ± 0.02	11.17 ± 0.09	10.51 ± 0.04	10.08 ± 0.04	0.65	3.89
ZOA183155.989-314742.59	J1831-31	2.280	-10.134	0.35	76.3	32.63	11.24 ± 0.02	10.57 ± 0.02	10.30 ± 0.02	10.36 ± 0.27	9.89 ± 0.18	9.87 ± 0.10	0.17	4.05
ZOA120920.790-622912.31	J1209-62	298.092	-0.011	0.36	-78.7	22.97	13.08 ± 0.02	11.21 ± 0.02	10.31 ± 0.02	12.36 ± 0.16	11.65 ± 0.05	10.04 ± 0.06	3.83	4.55
ZOA141232.785-563433.93	J1412-56A	313.972	4.547	0.46	-62.7	42.52	11.43 ± 0.02	10.62 ± 0.02	10.32 ± 0.02	10.83 ± 0.20	10.25 ± 0.08	10.06 ± 0.05	0.65	4.15
ZOA165136.176-492305.15	J1651-49	337.328	-3.257	0.29	43.0	25.41	11.73 ± 0.02	10.58 ± 0.02	10.36 ± 0.02	11.55 ± 0.07	9.88 ± 0.20	9.93 ± 0.12	1.10	4.49
ZOA084421.997-344138.52	J0844-34	256.286	4.969	0.46	52.8	25.12	11.60 ± 0.02	10.81 ± 0.02	10.38 ± 0.02	11.45 ± 0.06	10.73 ± 0.02	9.91 ± 0.13	0.35	3.59
ZOA062226.284+043123.63	J0622+04	205.582	-4.359	0.60	50.0	26.29	11.63 ± 0.02	10.71 ± 0.02	10.43 ± 0.02	11.02 ± 0.19	10.56 ± 0.02	10.19 ± 0.07	0.59	3.48
ZOA070934.590-052541.37	J0709-05	219.831	1.542	0.57	39.5	40.95	11.71 ± 0.02	10.50 ± 0.02	10.43 ± 0.02	11.59 ± 0.07	10.19 ± 0.03	9.49 ± 0.27	0.47	3.64
ZOA133148.660-651639.13	J1331-65	307.140	-2.736	0.28	-7.6	22.16	11.92 ± 0.02	10.88 ± 0.02	10.46 ± 0.02	11.56 ± 0.14	10.70 ± 0.04	9.98 ± 0.13	1.28	4.37
ZOA072545.358-175252.65	J0725-17	232.689	-0.782	0.05	-1.5	23.32	11.96 ± 0.02	10.93 ± 0.02	10.46 ± 0.02	11.76 ± 0.09	10.67 ± 0.07	10.19 ± 0.06	1.40	3.72
ZOA154205.067-584505.33	J1541-58	323.541	-2.884	0.41	-66.5	24.11	11.86 ± 0.02	10.86 ± 0.02	10.47 ± 0.02	11.39 ± 0.16	10.56 ± 0.09	9.85 ± 0.18	1.27	4.42
ZOA085813.978-455054.03	J0858-45A	266.587	-0.082	0.66	-54.4	27.82	12.58 ± 0.02	11.15 ± 0.02	10.52 ± 0.02	12.38 ± 0.10	11.05 ± 0.02	10.19 ± 0.09	2.74	3.89
ZOA074625.418-83249.78	J0746-18B	235.663	3.179	0.72	-81.2	32.17	11.72 ± 0.02	10.79 ± 0.02	10.55 ± 0.02	11.02 ± 0.21	10.24 ± 0.11	10.28 ± 0.07	0.47	3.55
ZOA141552.098-585534.39	J1415-58	313.652	2.177	0.79	-48.4	41.70	12.60 ± 0.02	11.29 ± 0.02	10.56 ± 0.02	12.03 ± 0.24	11.13 ± 0.04	10.44 ± 0.03	1.98	4.47
ZOA074625.307-183248.33	J0746-18A	235.663	3.179	0.72	-30.2	33.73	11.71 ± 0.02	10.90 ± 0.02	10.57 ± 0.02	11.53 ± 0.05	10.90 ± 0.26	10.44 ± 0.03	0.47	3.63
ZOA103157.298-634230.12	J1031-63	288.208	-4.898	0.54	59.9	28.90	11.69 ± 0.02	10.96 ± 0.02	10.58 ± 0.02	11.39 ± 0.10	10.68 ± 0.06	10.18 ± 0.10	0.47	4.01
ZOA162949.964-264644.24	J1629-26	351.743	14.764	0.44	27.2	23.59	11.68 ± 0.02	11.00 ± 0.02	10.59 ± 0.02	11.57 ± 0.04	10.73 ± 0.08	10.42 ± 0.04	0.48	3.55
ZOA090323.536-411817.06	J0903-41	263.782	3.614	0.20	-71.6	30.93	12.01 ± 0.02	11.11 ± 0.02	10.64 ± 0.02	11.53 ± 0.19	10.84 ± 0.07	10.09 ± 0.12	1.10	3.61
ZOA154066.589-504740.98	J1540-50	328.095	3.648	0.30	27.5	17.85	11.91 ± 0.02	11.03 ± 0.02	10.71 ± 0.02	11.15 ± 0.24	10.34 ± 0.13	10.35 ± 0.07	0.83	4.35
ZOA072729.171-235733.44	J0727-23	238.235	-3.312	0.68	-32.7	32.01	12.23 ± 0.02	11.08 ± 0.02	10.72 ± 0.02	12.11 ± 0.06	10.86 ± 0.03	10.42 ± 0.08	1.18	3.96
ZOA162808.701-290547.96	J1628-29	349.704	13.499	0.60	68.2	23.09	11.78 ± 0.02	11.02 ± 0.02	10.72 ± 0.02	11.49 ± 0.09	10.77 ± 0.06	10.58 ± 0.04	0.44	3.59

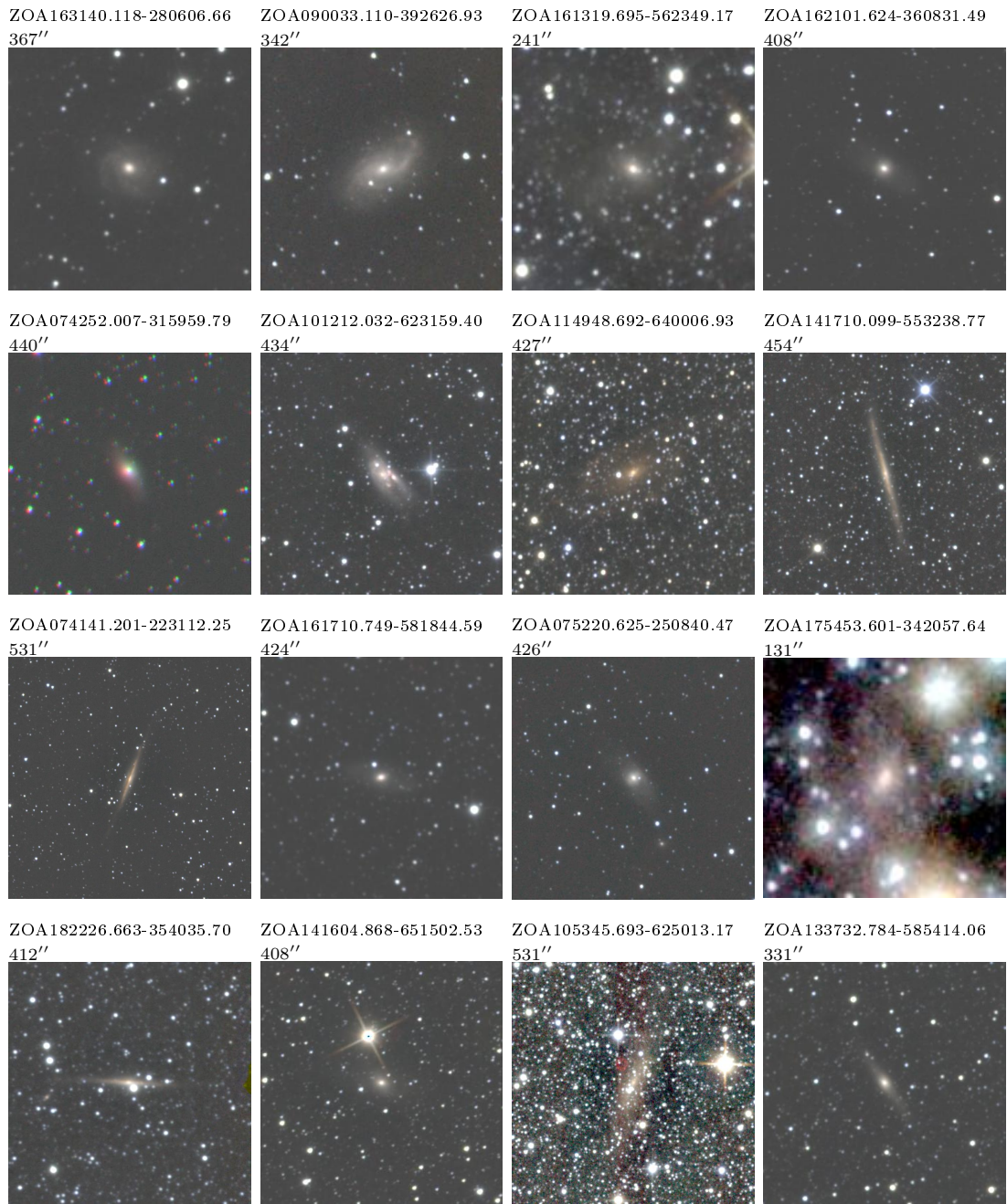
Continued on Next Page...

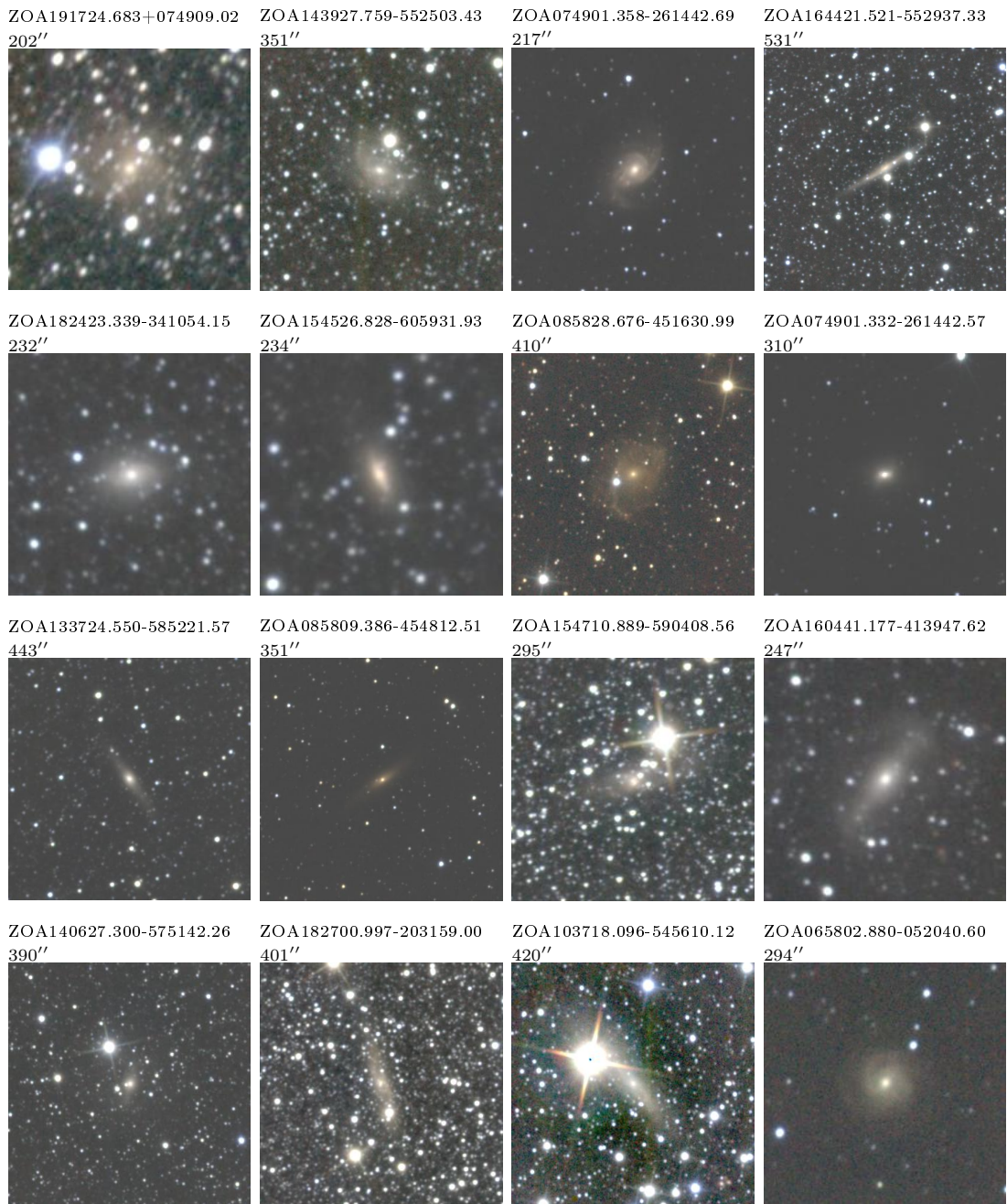
Table A.1 – Continued

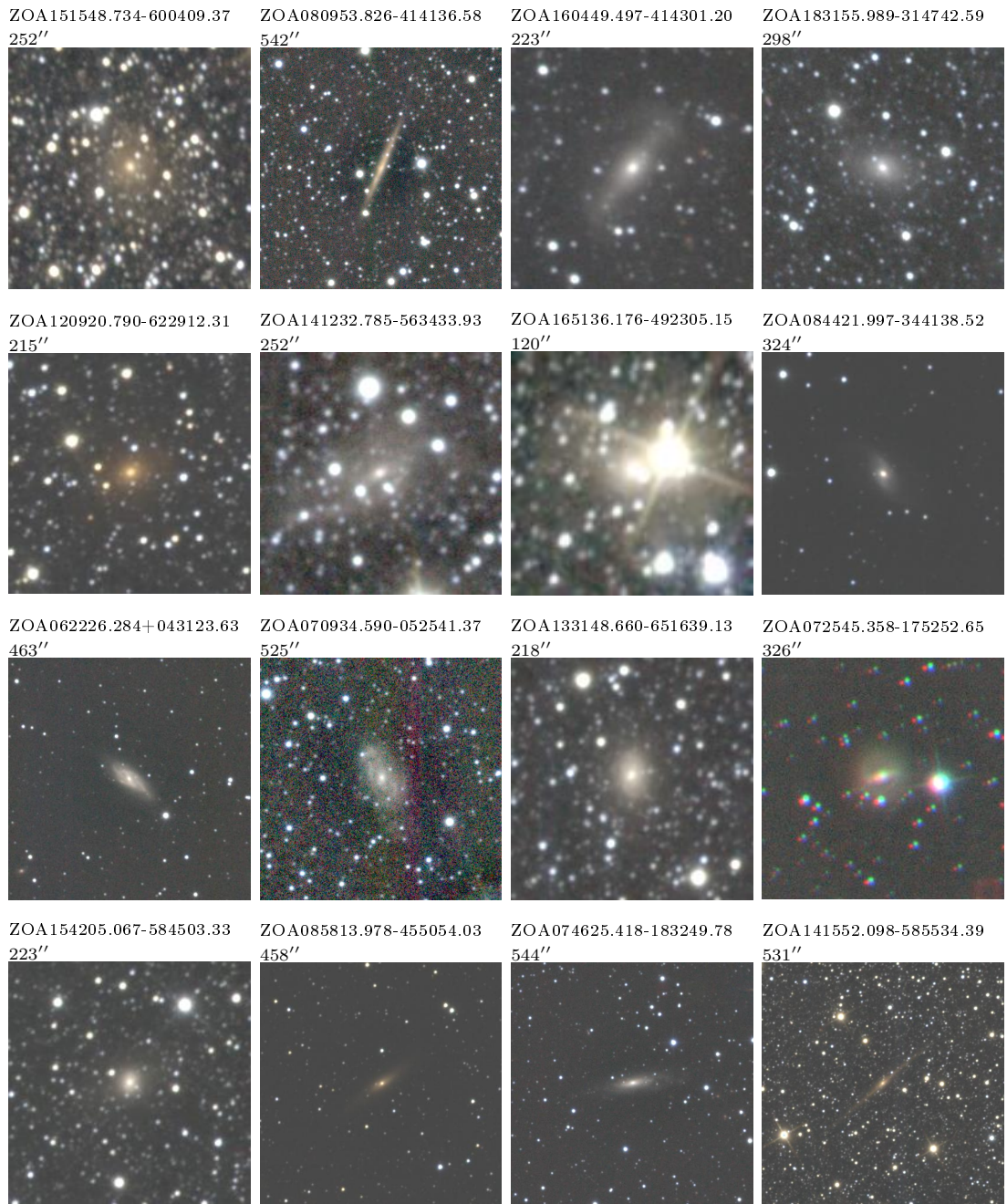
Designation	H/I Name	<i>l</i>	<i>b</i>	ϵ_J	ϕ_J	r_{k20fe} [deg]	r_{k20fe} ['']	J_{k20fe} [mag]	H_{k20fe} [mag]	$K_{s\,k20fe}$ [mag]	J_{tot} [mag]	H_{tot} [mag]	$K_{s\,tot}$ [mag]	$E(B-V)$ [mag]	<i>SD</i>
ZOA150125.899-572319.39	J1501-57	319.767	1.171	0.45	26	30.57	12.59 ± 0.02	11.16 ± 0.02	10.73 ± 0.02	11.98 ± 0.26	10.73 ± 0.09	10.49 ± 0.05	2.57	4.65	
ZOA101345.674-521712.71	J1013-52B	280.032	3.431	0.33	30.1	29.52	11.91 ± 0.02	11.13 ± 0.02	10.74 ± 0.02	11.60 ± 0.12	10.72 ± 0.10	10.51 ± 0.03	0.48	3.88	
ZOA160627.540-573350.42	J1606-57	326.778	-4.022	0.76	-61.4	36.95	12.02 ± 0.02	11.14 ± 0.02	10.75 ± 0.02	11.93 ± 0.04	11.03 ± 0.02	10.57 ± 0.04	0.57	4.29	
ZOA130612.957-573322.76	J1305-57	304.921	5.258	0.15	-55.2	25.51	11.79 ± 0.02	11.05 ± 0.02	10.75 ± 0.02	11.35 ± 0.10	10.63 ± 0.06	9.83 ± 0.25	0.36	3.89	
ZOA074058.810-320421.92	J0740-32	246.798	-4.610	0.59	-0.8	33.90	11.90 ± 0.02	11.07 ± 0.02	10.76 ± 0.02	11.57 ± 0.10	10.31 ± 0.19	10.20 ± 0.14	0.65	3.63	
ZOA161616.704-400313.56	J1616-40	339.945	7.663	0.63	-55.5	33.03	11.98 ± 0.02	11.13 ± 0.02	10.77 ± 0.02	11.74 ± 0.09	10.80 ± 0.07	10.60 ± 0.03	0.95	3.98	
ZOA151340.684-544527.41	J1513-54	322.561	2.600	0.41	-39.3	26.18	12.21 ± 0.02	11.39 ± 0.02	10.81 ± 0.02	11.78 ± 0.15	11.13 ± 0.07	10.71 ± 0.02	1.73	4.44	
ZOA120821.250-652931.97	J1208-65	298.480	-2.994	0.34	-8.2	25.60	12.25 ± 0.02	11.21 ± 0.02	10.81 ± 0.02	12.11 ± 0.09	10.72 ± 0.09	10.69 ± 0.02	0.95	4.22	
ZOA122948.708-610705.31	J1229-61	300.322	1.644	0.35	73.0	20.22	12.40 ± 0.02	11.48 ± 0.02	10.85 ± 0.02	11.74 ± 0.22	10.80 ± 0.20	9.95 ± 0.25	1.89	4.40	
ZOA152947.742-591535.65	J1530-59	321.559	-2.370	0.33	79.9	20.69	12.24 ± 0.02	11.22 ± 0.02	10.86 ± 0.02	11.43 ± 0.27	11.05 ± 0.04	10.43 ± 0.12	1.27	4.61	
ZOA150742.472-605347.07	J1507-60	318.756	-2.282	0.61	63.5	28.61	12.59 ± 0.02	11.46 ± 0.02	10.86 ± 0.02	12.46 ± 0.10	10.51 ± 0.30	10.46 ± 0.07	1.30	4.61	
ZOA171943.078-411834.03	J1719-41	346.750	-2.324	0.43	-43.8	26.74	13.42 ± 0.02	11.59 ± 0.02	10.91 ± 0.02	13.08 ± 0.29	10.97 ± 0.18	10.50 ± 0.09	2.60	4.64	
ZOA180031.811-040052.11	J1800-03	23.450	0.67	-66.7	24.19	12.52 ± 0.02	11.49 ± 0.02	10.92 ± 0.02	12.32 ± 0.08	10.74 ± 0.21	10.85 ± 0.02	1.37	3.79		
ZOA140156.320-554729.98	J1401-55	312.783	5.726	0.51	-27.5	29.53	12.00 ± 0.02	11.23 ± 0.02	10.93 ± 0.02	11.00 ± 0.31	10.13 ± 0.25	10.56 ± 0.07	0.45	3.97	
ZOA145256.359-564700.09	J1452-56	319.026	2.243	0.80	-32.3	37.24	12.64 ± 0.02	11.52 ± 0.02	10.93 ± 0.02	12.27 ± 0.14	11.20 ± 0.09	10.60 ± 0.09	1.60	4.49	
ZOA134229.543-610124.62	J1342-61	309.077	1.238	0.18	46.4	18.39	13.34 ± 0.02	11.81 ± 0.02	10.93 ± 0.02	11.91 ± 0.58	11.42 ± 0.11	10.04 ± 0.25	2.99	4.65	
ZOA142042.940-580645.01	J1420-58	314.518	2.737	0.13	-39.1	21.30	12.37 ± 0.02	11.70 ± 0.02	10.94 ± 0.02	11.53 ± 0.32	10.71 ± 0.32	10.25 ± 0.18	1.57	4.47	
ZOA131509.704-585612.15	J1314-58	305.995	3.794	0.27	33.3	23.57	12.36 ± 0.02	11.15 ± 0.02	10.95 ± 0.02	12.05 ± 0.14	10.25 ± 0.18	10.21 ± 0.19	0.92	4.13	
ZOA171727.684-430657.76	J1717-43A	345.029	-3.019	0.21	-20.0	17.75	12.77 ± 0.02	11.64 ± 0.02	10.95 ± 0.02	12.71 ± 0.06	11.54 ± 0.04	10.73 ± 0.04	2.02	4.51	
ZOA153931.522-593438.04	J1539-59B	322.782	-3.348	0.66	-53.5	28.19	12.40 ± 0.02	11.40 ± 0.02	10.95 ± 0.02	12.21 ± 0.09	11.17 ± 0.05	10.60 ± 0.10	0.98	4.38	
ZOA084521.622-421845.17	J0845-42	262.590	0.394	0.42	-83.3	23.31	13.54 ± 0.03	11.29 ± 0.02	10.97 ± 0.02	12.45 ± 0.67	10.33 ± 0.13	10.48 ± 0.06	3.08	3.83	
ZOA140610.192-575210.01	J1406-57	312.760	3.569	0.71	44.9	20.08	12.24 ± 0.02	11.34 ± 0.02	10.97 ± 0.02	12.29 ± 0.02	11.09 ± 0.08	10.79 ± 0.06	0.73	4.17	
ZOA112513.679-603601.55	J1125-60	292.542	0.521	0.20	-12.9	15.63	13.11 ± 0.02	11.73 ± 0.02	10.98 ± 0.02	12.76 ± 0.17	11.42 ± 0.08	10.76 ± 0.04	1.34	4.42	
ZOA134436.279-581309.28	J1344-58	309.903	3.931	0.24	-45.9	18.50	12.20 ± 0.02	11.38 ± 0.02	11.00 ± 0.02	11.80 ± 0.14	10.81 ± 0.04	10.94	4.18		

Table A.2: NIR postage stamps

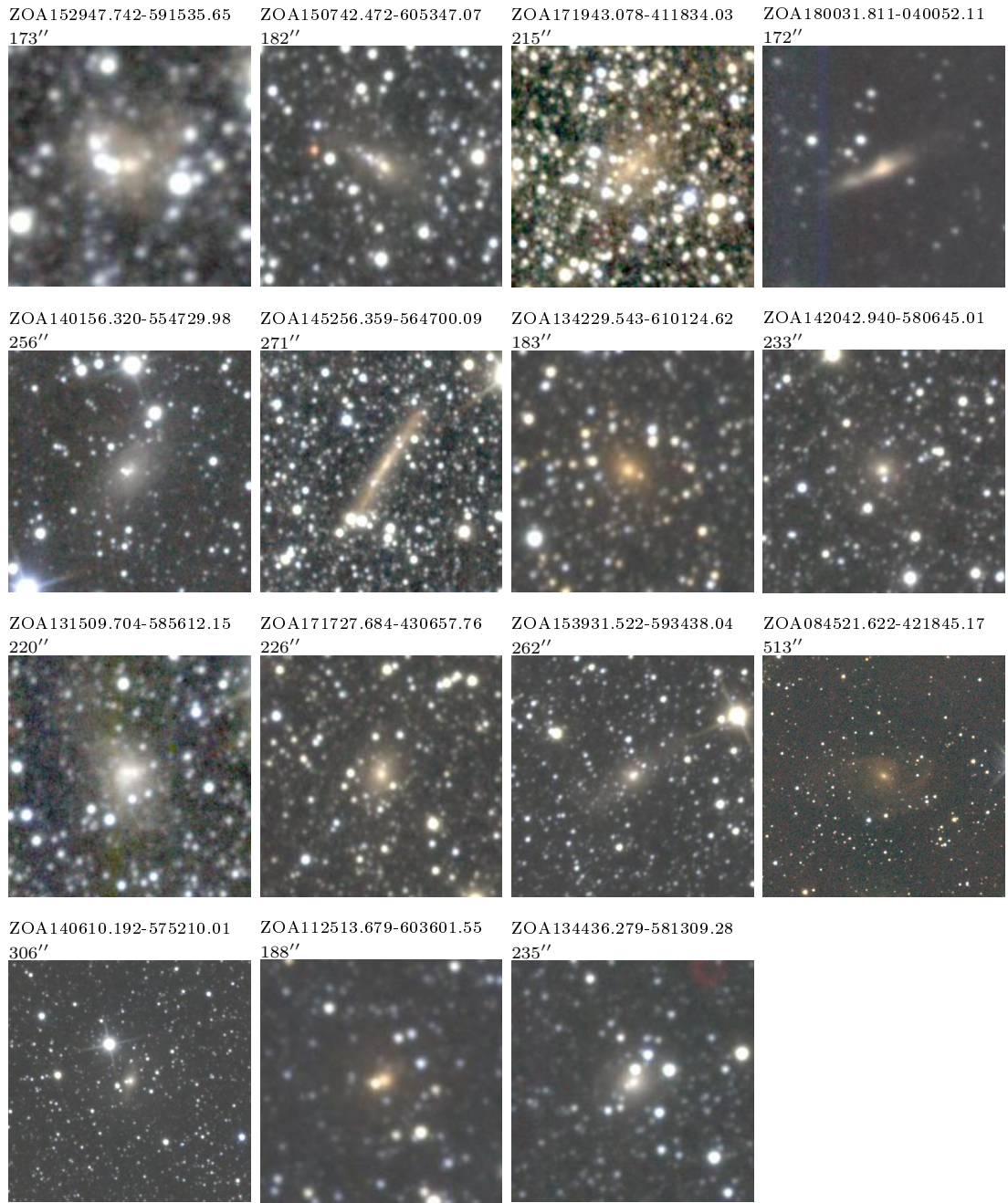












Appendix B

Tully-Fisher Sample

This appendix gives the full tables referred to in Chapter 6. These tables are also available online at <http://www.ast.uct.ac.za/~wendy/zotaf/>.

Table B.1 gives the uncorrected photometric and spectroscopic parameters as well as the absolute magnitudes from the TF relation for all confirmed counterparts. The columns are:

Column 1 HI catalogue name

Column 2 & 3 Galactic co-ordinates, l and b

Column 4 HI recession velocity, v

Column 5 HI 50% linewidth uncorrected for inclination, w_{50}

Column 6 J band ellipticity, ϵ

Columns 7-9 observed extrapolated total magnitudes in J , H and K_s respectively, m_J , m_H , and m_{K_s} , before corrections for extinction

Column 10 50% linewidth corrected for inclination, instrumental, turbulent and cosmological broadening, w_{cor}

Columns 11-13 absolute magnitudes in J , H and K_s respectively, computed assuming the galaxy is at the distance given by its redshift and corrected for extinction

Table B.1: TF Sample

Name	<i>l</i> [deg]	<i>b</i> [deg]	<i>v</i> [km s ⁻¹]	<i>w</i> ₅₀ [km s ⁻¹]	ϵ	<i>m</i> _{<i>J</i>} [mag]	<i>m</i> _{<i>H</i>} [mag]	<i>m</i> _{<i>K</i>_{<i>s</i>}} [mag]	<i>w</i> _{<i>cor</i>} [km s ⁻¹]	<i>M</i> _{<i>J</i>} [mag]	<i>M</i> _{<i>H</i>} [mag]	<i>M</i> _{<i>K</i>_{<i>s</i>}} [mag]
J0614+12	197.59	-2.23	5553	217.0	0.47	13.74	12.84	12.22	232.3	-20.16	-20.84	-21.29
J0621+11	199.66	-1.50	5599	188.0	0.49	13.50	13.09	13.13	191.3	-20.77	-20.95	-20.69
J0622+04	205.58	-4.36	2958	306.0	0.60	11.20	10.77	10.37	310.3	-21.82	-22.08	-22.34
J0622+11B	199.78	-1.15	5493	366.0	0.58	12.17	11.95	11.21	367.8	-22.58	-22.51	-23.06
J0630+16	195.62	3.04	2532	258.0	0.54	12.51	11.90	12.06	258.6	-20.02	-20.49	-20.18
J0700-13	226.27	-4.41	5651	197.0	0.63	14.89	14.32	9.33	190.2	-19.59	-19.97	-24.83
J0709-05	219.83	1.54	1722	252.0	0.57	11.82	10.38	9.65	249.6	-19.94	-21.25	-21.84
J0712-09*	223.64	0.46	2441	97.0	0.36	13.42	12.19	11.90	98.6	-17.57	-18.62	-18.67
J0716-18B	232.05	-3.01	5822	244.0	0.61	15.02	13.79	13.22	240.9	-19.96	-20.81	-21.08
J0716-18C	232.57	-3.11	2816	267.0	0.88	13.26	11.43	10.93	251.7	-21.80	-22.97	-22.84
J0719-09	224.61	1.80	2497	181.0	0.81	13.58	12.47	12.39	166.8	-19.90	-20.73	-20.40
J0727-23	238.23	-3.31	4407	412.0	0.68	12.33	11.04	10.59	402.3	-22.19	-23.15	-23.38
J0730-22	236.82	-1.85	773	276.0	0.77	10.94	9.43	9.37	255.9	-21.43	-22.35	-21.83
J0732-16	232.59	0.94	4320	80.0	0.32	14.57	13.58	12.92	88.3	-28.56	-26.00	-24.09
J0733-13	230.16	2.72	3253	151.0	0.59	13.81	13.16	12.53	146.5	-18.94	-19.48	-19.93
J0734-14	230.85	2.49	3295	181.0	0.59	13.98	13.50	13.06	175.3	-19.03	-19.35	-19.59
J0735-17	233.35	1.64	3244	99.0	0.29	14.58	13.81	13.23	113.1	-18.31	-18.84	-19.17
J0736-18	234.11	1.33	4463	119.0	0.84	14.62	13.27	13.16	103.9	-20.10	-21.08	-20.68
J0737-31*	245.57	-4.83	2240	127.0	0.62	13.96	13.27	12.92	113.9	-17.10	-17.61	-17.74
J0740-22*	238.83	-0.10	3049	138.0	0.52	12.78	12.03	11.34	131.4	-19.86	-20.47	-20.95
J0740-30A	245.75	-4.18	5079	323.0	0.80	13.24	12.37	12.02	303.0	-22.05	-22.62	-22.63
J0740-32	246.80	-4.61	2723	278.0	0.59	11.79	10.50	10.37	277.3	-21.10	-22.22	-22.19
J0741-22	238.56	0.24	3068	466.0	0.80	11.28	9.47	9.85	440.1	-23.31	-24.78	-24.05
J0741-26	241.69	-1.54	3506	142.0	0.75	14.10	13.74	13.38	129.0	-20.06	-20.08	-19.98
J0741-30B	245.26	-3.52	4558	349.0	0.55	12.01	11.57	11.21	363.4	-22.03	-22.31	-22.56
J0742-26	242.23	-1.78	2913	247.0	0.60	12.99	12.62	11.94	246.5	-20.18	-20.30	-20.77
J0742-31	246.93	-4.23	2103	305.0	0.52	11.28	10.61	9.50	315.2	-21.06	-21.52	-22.48
J0743-18*	235.07	2.72	3337	172.0	0.40	14.22	13.34	12.94	188.7	-18.75	-19.49	-19.74
J0744-25	241.88	-0.96	4049	158.0	0.36	12.25	11.10	10.38	182.5	-20.76	-21.67	-22.18
J0744-26*	241.92	-0.99	2736	278.0	0.41	11.95	11.14	10.70	314.6	-21.22	-21.77	-22.03
J0747-18	236.01	3.37	3243	506.0	0.82	10.04	8.99	8.82	485.7	-24.60	-25.41	-25.32
J0747-25	242.10	-0.33	4252	216.0	0.29	13.22	12.69	12.50	280.5	-20.42	-20.81	-20.90
J0747-26A	242.46	-0.56	882	145.0	0.37	12.51	10.78	10.95	156.1	-17.85	-19.43	-19.08
J0748-18	235.96	3.50	917	166.0	0.58	12.83	12.70	12.80	158.9	-17.52	-17.28	
J0752-25A	242.05	1.02	4603	361.0	0.56	10.98	10.22	9.20	373.7	-22.87	-23.52	-24.50

Continued on Next Page...

Table B.1 – Continued

Name	<i>l</i> [deg]	<i>b</i> [deg]	<i>v</i> [km s ⁻¹]	<i>w</i> ₅₀ [km s ⁻¹]	ϵ	<i>m_J</i> [mag]	<i>m_H</i> [mag]	<i>m_{K_s}</i> [mag]	<i>w_{cor}</i> [km s ⁻¹]	<i>M_J</i> [mag]	<i>M_H</i> [mag]	<i>M_{K_s}</i> [mag]
J0754-38	254.17	-5.59	2749	270.0	0.67	13.20	12.30	11.88	256.2	-19.82	-20.49	-20.72
J0801-29	246.56	0.72	2749	249.0	0.52	13.52	12.96	12.42	255.6	-19.50	-19.82	-20.18
J0801-33*	250.20	-1.62	1901	177.0	0.69	13.78	12.96	12.98	163.1	-19.07	-19.58	-19.17
J0804-32	249.93	-0.66	1970	131.0	0.67	13.97	14.35	13.89	121.9	-18.13	-17.49	-17.65
J0809-41	258.05	-4.60	1997	316.0	0.84	12.10	10.83	10.03	292.8	-21.80	-22.61	-22.92
J0810-39*	256.17	-3.34	1421	123.0	0.82	15.36	14.92	14.62	104.3	-18.06	-17.98	-17.79
J0818-29A	248.95	3.59	1531	99.0	0.62	14.06	13.41	13.24	90.8	-16.93	-17.49	-17.44
J0818-29B	248.95	3.59	2520	165.0	0.84	13.87	13.33	13.16	150.9	-19.96	-20.23	-20.08
J0818-33	252.31	1.28	2016	104.0	0.65	13.21	12.33	11.74	91.1	-18.51	-19.24	-19.56
J0826-44	261.93	-3.56	1027	184.0	0.74	13.85	12.67	12.41	164.5	-18.89	-19.55	-19.33
J0839-34	255.55	4.36	5623	235.0	0.38	12.92	12.47	12.50	272.8	-20.89	-21.24	-21.16
J0840-37	258.01	2.65	5291	315.0	0.78	13.17	12.61	12.32	297.8	-22.21	-22.46	-22.41
J0842-44	263.32	-1.23	3754	188.0	0.49	14.70	13.53	13.07	195.5	-19.37	-20.12	-20.24
J0844-34*	256.29	4.97	2167	295.0	0.46	11.65	10.93	10.08	324.2	-20.66	-21.27	-22.04
J0844-35	256.82	4.47	2240	156.0	0.32	14.43	13.89	13.39	186.4	-17.69	-18.11	-18.47
J0844-39	260.38	1.84	1808	158.0	0.35	15.47	14.40	13.84	185.2	-17.13	-17.78	-17.98
J0845-42	262.39	0.39	1730	305.0	0.42	12.71	10.49	10.64	346.2	-21.10	-22.57	-21.89
J0848-39*	260.57	2.58	1831	171.0	0.30	14.73	13.76	13.13	203.5	-17.44	-18.16	-18.56
J0856-37*	259.73	5.22	2500	250.0	0.72	12.70	11.50	11.74	234.2	-20.85	-21.78	-21.19
J0856-48*	268.51	-2.08	2666	268.0	0.61	12.20	11.26	11.05	269.0	-21.34	-21.87	-21.75
J0858-45B	266.18	0.33	2699	232.0	0.29	12.28	10.87	10.18	293.1	-22.67	-23.20	-23.27
J0900-39	262.02	4.44	2627	295.0	0.39	10.79	10.40	9.71	338.8	-22.13	-22.34	-22.90
J0907-48	269.41	-0.51	5219	181.0	0.63	12.53	11.95	11.07	172.9	-22.87	-23.15	
J0917-53	274.25	-2.87	947	179.0	0.59	13.19	11.95	11.60	168.7	-17.58	-18.60	-18.71
J0920-44	268.21	3.77	2677	168.0	0.71	13.95	12.85	10.79	154.1	-20.02	-20.68	-22.23
J0923-42*	267.39	5.43	2979	137.0	0.51	14.95	14.30	14.39	134.4	-17.69	-18.19	-17.89
J0927-55	277.14	-3.67	1153	140.0	0.53	13.97	14.05	13.17	131.8	-16.99	-16.69	-17.31
J0932-44	270.05	4.96	5740	101.0	0.69	14.41	13.76	13.46	84.8	-20.28	-20.64	-20.52
J0944-59	281.14	-4.83	2400	144.0	0.73	14.62	14.02	13.65	126.7	-19.29	-19.51	-19.49
J0946-46	273.06	5.21	2693	289.0	0.81	13.19	12.46	11.78	267.8	-20.75	-21.21	-21.52
J0950-49	275.56	3.30	3772	164.0	0.39	12.42	11.77	11.48	181.3	-20.13	-20.65	-20.81
J0951-59	281.72	-4.01	4371	338.0	0.69	13.25	12.21	11.48	330.6	-21.84	-22.49	-22.86
J0953-49	275.65	3.86	2265	97.0	0.34	14.97	13.84	13.96	105.0	-17.45	-18.46	-18.25
J0955-60*	282.94	-4.84	3295	253.0	0.58	12.96	11.82	11.19	253.0	-20.18	-21.17	-21.66
J0956-59*	282.37	-3.85	3417	252.0	0.76	14.44	13.22	12.77	234.1	-20.29	-21.05	-21.03
J0958-55	279.99	-0.36	3714	160.0	0.85	15.33	13.74	13.71	145.3	-20.05	-20.98	-20.33

Continued on Next Page...

Table B.1 – Continued

Name	<i>l</i> [deg]	<i>b</i> [deg]	<i>v</i> [km s ⁻¹]	<i>w</i> ₅₀ [km s ⁻¹]	ϵ	<i>m</i> _J [mag]	<i>m</i> _H [mag]	<i>m</i> _{K_s [mag]}	<i>w</i> _{cor} [km s ⁻¹]	<i>M</i> _J [mag]	<i>M</i> _H [mag]	<i>M</i> _{K_s [mag]}
J1000-58A	282.19	-2.85	2685	118.0	0.67	13.08	11.96	11.42	99.7	-18.81	-19.53	-19.69
J1002-57	281.73	-1.70	2642	244.0	0.40	13.64	15.26	12.79	276.1	-22.34	-19.46	-21.04
J1003-49*	277.01	4.72	2410	105.0	0.44	12.96	13.56	12.86	98.2	-18.99	-18.27	-18.76
J1004-58	282.59	-2.41	3682	290.0	0.51	11.74	12.01	11.60	298.6	-23.94	-22.76	-22.53
J1006-49*	277.44	5.04	2402	125.0	0.38	12.13	12.57	14.46	129.4	-19.87	-19.33	-17.28
J1006-50B	278.09	4.11	5298	298.0	0.59	12.80	11.96	11.82	300.2	-21.15	-21.85	-21.90
J1009-51*	278.83	4.01	2818	146.0	0.32	15.08	14.52	14.18	177.1	-17.36	-17.84	-18.06
J1012-62*	285.69	-5.12	3450	207.0	0.62	10.97	9.92	9.67	196.2	-21.96	-22.92	-23.05
J1013-52B	280.03	3.43	2714	251.0	0.33	11.80	10.92	10.69	302.8	-20.71	-21.47	-21.63
J1018-51	279.96	4.86	4057	203.0	0.48	13.87	13.80	11.04	215.0	-19.38	-19.38	-22.05
J1024-54*	282.78	2.23	1079	135.0	0.74	13.03	12.37	12.05	115.2	-17.71	-18.06	-17.95
J1031-63*	288.18	-4.95	3760	316.0	0.82	13.69	13.14	12.71	296.2	-20.94	-21.21	-21.29
J1037-54	284.40	3.04	2671	313.0	0.66	11.11	10.33	10.21	303.9	-21.92	-22.49	-22.44
J1039-54	284.54	3.57	2752	117.0	0.67	13.71	13.55	13.01	98.7	-17.71	-17.66	-17.93
J1053-62	289.96	-2.97	1837	271.0	0.67	11.57	10.78	9.88	257.4	-20.67	-21.23	-21.92
J1130-58*	292.56	2.53	1842	149.0	0.62	13.10	11.41	12.17	134.8	-19.29	-20.74	-19.79
J1153-63	296.60	-1.74	2144	188.0	0.36	13.17	12.45	11.84	213.5	-20.61	-20.69	-20.85
J1203-64*	297.82	-2.45	5519	352.0	0.65	13.13	12.34	11.75	346.3	-22.07	-22.43	-22.72
J1204-59 A	297.04	2.40	5616	238.0	0.75	13.68	13.08	13.62	223.4	-21.88	-22.08	-21.12
J1208-65	298.48	-2.99	5484	364.0	0.34	12.34	10.90	10.86	441.6	-22.38	-23.56	-23.48
J1209-62	298.09	-0.01	1461	127.0	0.36	13.11	11.23	10.19	135.5	-20.31	-21.28	-21.59
J1213-65	299.01	-3.02	2139	238.0	0.35	12.52	12.34	12.44	278.0	-19.93	-19.89	-19.62
J1214-58	298.09	4.08	5607	287.0	0.81	13.71	12.86	11.94	267.6	-21.78	-22.32	-22.87
J1219-66	299.69	-3.77	4036	170.0	0.52	15.64	14.91	13.76	172.2	-17.77	-18.33	-19.29
J1221-57	298.92	4.92	5348	323.0	0.64	13.34	12.58	11.94	318.6	-21.14	-21.68	-22.16
J1221-59	299.17	2.95	1473	185.0	0.34	13.59	11.79	12.17	212.0	-18.35	-19.82	-19.17
J1222-58	299.18	4.05	1542	374.0	0.69	9.89	8.76	8.79	369.7	-22.88	-23.74	-23.41
J1223-61*	299.56	1.46	3845	163.0	0.42	14.13	13.17	12.96	170.9	-19.67	-20.28	-20.19
J1225-59	299.60	3.52	5658	238.0	0.38	12.37	11.77	11.39	272.3	-21.98	-22.40	-22.64
J1229-58*	300.07	4.69	5651	293.0	0.48	13.80	12.59	12.29	313.5	-20.64	-21.61	-21.75
J1229-61*	300.32	1.64	5387	328.0	0.35	11.94	11.00	10.12	394.4	-23.34	-23.81	-24.40
J1239-59	301.37	3.24	5308	379.0	0.62	12.42	11.48	11.09	380.3	-22.23	-22.91	-23.14
J1255-58	303.48	4.54	5596	217.0	0.54	13.03	11.66	12.20	221.1	-21.07	-22.31	-21.64
J1255-59*	303.41	3.51	2296	162.0	0.76	14.20	13.41	12.76	143.2	-19.56	-20.00	-20.29
J1302-64	304.11	-1.22	3910	174.0	0.57	14.51	13.06	12.68	170.4	-20.02	-20.66	-20.43
J1312-60	305.53	1.89	2318	238.0	0.31	12.81	11.22	10.56	290.6	-20.78	-21.83	-22.10

Continued on Next Page...

Table B.1 – Continued

Name	<i>l</i>	<i>b</i>	<i>v</i>	<i>w</i> ₅₀	ϵ	<i>m</i> _{<i>J</i>}	<i>m</i> _{<i>H</i>}	<i>m</i> _{K_s}	<i>w</i> _{cor}	<i>M</i> _{<i>J</i>}	<i>M</i> _{<i>H</i>}	<i>M</i> _{K_s}
	[deg]	[deg]	[km s ⁻¹]	[km s ⁻¹]		[mag]	[mag]	[mag]	[km s ⁻¹]	[mag]	[mag]	[mag]
J1327-57	307.77	5.04	2929	255.0	0.74	11.26	9.95	9.27	234.9	-22.79	-23.76	-24.05
J1329-58	307.85	3.66	5573	388.0	0.48	12.32	11.34	11.00	421.9	-22.28	-23.06	-23.30
J1332-58*	308.42	4.35	1473	104.0	0.28	13.52	12.97	12.47	116.2	-17.64	-18.02	-18.28
J1337-58C	309.01	4.10	5907	130.0	0.30	13.78	13.17	13.05	156.6	-20.80	-21.20	-21.19
J1342-57*	309.92	4.97	3727	182.0	0.46	14.32	13.76	13.40	194.9	-18.37	-18.77	-18.97
J1343-57	309.93	4.61	5360	207.0	0.37	13.72	12.72	12.35	241.2	-19.97	-20.81	-21.07
J1346-58A	310.19	3.86	3677	218.0	0.43	13.22	13.34	13.16	237.4	-20.23	-19.90	-19.91
J1351-58	310.72	3.37	3881	635.0	0.52	10.38	9.47	8.72	680.9	-23.93	-24.57	-25.20
J1355-59A*	311.07	2.58	5495	329.0	0.77	13.28	12.18	11.49	311.9	-22.61	-23.25	-23.50
J1356-58	311.32	3.34	5978	186.0	0.33	15.68	14.04	13.64	223.8	-18.71	-20.15	-20.39
J1401-55	312.78	5.73	3967	274.0	0.51	11.20	10.33	10.75	280.8	-22.28	-23.03	-22.49
J1405-66	310.20	-4.83	2659	159.0	0.79	12.06	12.17	13.24	139.2	-21.48	-21.06	-19.56
J1410-65	311.00	-3.96	3099	437.0	0.52	10.51	9.58	8.89	468.5	-22.83	-23.59	-24.19
J1412-56A*	313.97	4.55	3769	276.0	0.46	11.01	10.46	10.24	300.7	-22.52	-22.90	-22.98
J1413-57	313.75	3.37	5007	332.0	0.68	13.72	12.36	12.05	324.4	-21.02	-21.98	-22.00
J1413-65	311.33	-3.81	435	254.0	0.44	7.27	6.60	6.35	276.0	-22.63	-22.93	-22.90
J1414-58	313.64	2.76	5798	249.0	0.57	13.51	12.61	12.03	251.5	-20.90	-21.49	-21.84
J1415-58	313.65	2.18	5393	71.30	0.79	12.23	11.32	10.61	686.2	-24.97	-25.26	-25.50
J1416-65*	311.64	-3.82	2859	337.0	0.48	10.65	10.31	9.56	366.0	-22.38	-22.53	-23.16
J1419-57*	314.67	3.81	3849	167.0	0.62	11.88	12.16	12.05	156.0	-21.70	-21.14	-20.97
J1423-65	312.21	-4.69	3083	155.0	0.75	14.29	13.30	12.88	142.3	-18.72	-19.39	-19.39
J1429-54*	317.01	5.54	3018	122.0	0.39	13.73	13.04	12.39	123.3	-18.83	-19.36	-19.80
J1434-55	317.42	4.85	2005	85.0	0.48	12.90	13.02	11.66	81.4	-18.66	-18.37	-19.47
J1437-56	317.38	3.80	4431	143.0	0.69	14.17	13.27	12.58	132.2	-20.28	-20.86	-21.13
J1441-57*	317.56	2.60	3384	151.0	0.78	13.83	12.69	13.07	134.1	-19.88	-20.53	-19.60
J1442-54*	318.83	5.32	2778	185.0	0.49	13.93	13.12	12.42	190.6	-19.07	-19.68	-20.23
J1444-55	318.55	3.96	4672	237.0	0.33	13.57	11.94	11.75	290.6	-20.33	-21.80	-21.87
J1448-57	318.06	1.78	4780	221.0	0.64	12.30	11.74	11.29	209.8	-22.31	-22.45	-22.55
J1451-55A	319.23	3.24	5126	165.0	0.38	14.53	13.59	12.79	186.2	-20.07	-20.69	-21.28
J1452-56	319.03	2.24	3287	334.0	0.80	12.48	11.39	10.77	309.4	-22.66	-23.20	-23.29
J1457-54	320.65	4.10	2900	475.0	0.50	10.03	9.14	8.76	510.4	-23.51	-24.20	-24.48
J1501-60*	318.16	-1.73	4436	124.0	0.34	14.38	11.30	11.47	131.5	-20.38	-22.98	-22.48
J1503-54*	321.78	3.49	2938	135.0	0.69	14.83	13.62	14.07	116.2	-19.38	-20.21	-19.39
J1507-60	318.76	-2.28	4537	233.0	0.61	12.71	10.68	10.62	223.9	-21.54	-23.25	-23.02
J1509-52	323.16	4.81	1464	346.0	0.79	8.95	8.56	8.04	323.9	-23.76	-23.82	-23.96
J1514-53	323.59	4.04	1471	431.0	0.76	9.17	8.02	7.51	411.1	-23.92	-24.69	-24.83

Continued on Next Page...

Table B.1 – Continued

Name	<i>l</i> [deg]	<i>b</i> [deg]	<i>v</i> [km s ⁻¹]	<i>w</i> ₅₀ [km s ⁻¹]	ϵ	<i>m</i> _J [mag]	<i>m</i> _H [mag]	<i>m</i> _{K_s} [mag]	<i>w</i> _{cor} [km s ⁻¹]	<i>M</i> _J [mag]	<i>M</i> _H [mag]	<i>M</i> _{K_s} [mag]
J1515-60A	319.74	-2.45	5150	362.0	0.58	13.24	11.71	11.40	366.2	-21.66	-22.79	-22.83
J1518-55	322.68	1.48	1480	248.0	0.51	14.17	11.99	10.98	256.6	-19.24	-20.61	-21.01
J1523-60	320.45	-3.13	3158	201.0	0.61	13.54	13.61	12.68	195.7	-19.50	-19.23	-19.95
J1525-51	325.65	4.18	3299	184.0	0.30	13.76	12.80	12.79	233.4	-19.44	-20.19	-20.01
J1526-54	324.22	1.70	5058	237.0	0.32	11.82	12.21	11.42	294.6	-23.79	-22.71	-23.02
J1530-59	321.96	-2.37	5329	146.0	0.33	11.61	11.27	10.61	167.2	-22.69	-22.72	-23.11
J1539-44	331.78	8.71	3434	224.0	0.69	13.58	12.74	12.99	211.6	-19.75	-20.37	-19.84
J1539-59B	322.78	-3.35	5179	110.0	0.66	12.42	11.37	10.77	93.6	-21.41	-22.22	-22.51
J1543-60	322.76	-4.20	5186	230.0	0.68	13.12	12.62	11.78	216.4	-21.04	-21.33	-21.97
J1545-61	322.51	-4.92	5238	365.0	0.49	11.69	10.72	10.16	394.4	-22.71	-23.49	-23.93
J1546-57	324.92	-2.15	2756	89.0	0.35	14.86	13.44	13.24	87.0	-17.79	-18.89	-18.72
J1547-59	323.87	-3.54	5652	341.0	0.39	10.85	10.67	10.13	392.0	-23.0	-23.56	-24.05
J1605-57	326.49	-4.14	2990	93.0	0.37	11.09	11.37	10.95	90.2	-21.07	-20.69	-20.91
J1606-57	326.78	-4.02	5065	398.0	0.76	12.13	11.23	10.74	382.3	-23.09	-23.71	-23.90
J1613-56	328.26	-3.80	2722	318.0	0.35	10.77	10.02	9.47	379.0	-22.03	-22.64	-23.11
J1616-40	339.95	7.66	4438	344.0	0.63	11.95	11.00	10.78	339.8	-22.08	-22.78	-22.83
J1617-58*	327.30	-5.54	2767	240.0	0.53	10.89	9.83	9.83	242.0	-21.59	-22.56	-22.45
J1621-36	343.41	9.77	4447	370.0	0.55	10.70	10.04	9.59	376.7	-23.35	-23.81	-24.13
J1626-40	340.83	5.70	4755	236.0	0.67	13.97	12.78	12.90	228.0	-20.34	-21.21	-20.82
J1628-29	349.70	13.50	4180	426.0	0.60	11.69	10.97	10.76	435.2	-22.14	-22.74	-22.89
J1629-26	351.74	14.76	5143	334.0	0.44	11.77	10.93	10.60	373.5	-22.36	-23.07	-23.32
J1630-30	348.89	12.21	4109	207.0	0.79	13.91	12.51	12.84	188.4	-20.81	-21.94	-21.29
J1632-28	351.08	13.50	4104	518.0	0.72	10.33	9.48	9.15	508.0	-24.58	-25.13	-25.19
J1632-29B*	350.15	12.58	4820	276.0	0.76	12.80	12.08	11.75	255.0	-21.70	-22.17	-22.18
J1636-26	353.14	14.07	4109	239.0	0.46	13.70	13.02	12.95	257.4	-19.79	-20.33	-20.27
J1639-36*	345.83	6.79	1817	158.0	0.60	14.43	13.79	13.49	154.3	-17.31	-17.74	-17.79
J1640-35	346.71	7.39	3878	84.0	0.33	14.00	13.33	12.94	92.6	-19.01	-19.48	-19.59
J1642-29*	351.68	11.16	2596	155.0	0.79	13.89	13.00	13.33	135.4	-19.29	-19.96	-19.24
J1642-37	345.32	5.63	2643	162.0	0.69	13.67	12.83	12.36	148.7	-19.69	-20.21	-20.27
J1644-55	331.92	-6.33	5114	441.0	0.83	11.56	10.25	10.06	415.3	-23.75	-24.80	-24.70
J1648-54*	333.08	-6.07	4656	253.0	0.67	13.35	12.72	12.08	240.3	-20.36	-20.87	-21.36
J1651-22*	358.52	13.66	5853	119.0	0.46	15.21	14.31	13.47	115.0	-19.07	-19.85	-20.60
J1654-56	332.12	-7.98	4912	149.0	0.65	15.54	15.04	13.43	134.7	-17.81	-18.24	-19.71
J1702-27	355.55	8.49	4546	107.0	0.37	12.41	11.89	12.75	114.1	-20.64	-21.09	-20.08
J1711-47	340.77	-4.79	2186	232.0	0.78	12.56	11.27	10.32	210.4	-20.70	-21.66	-22.21
J1712-15	7.58	13.96	2937	206.0	0.47	12.88	11.77	11.89	220.7	-19.23	-20.22	-19.99

Continued on Next Page...

Table B.1 – Continued

Name	<i>l</i> [deg]	<i>b</i> [deg]	<i>v</i> [km s ⁻¹]	<i>w</i> ₅₀ [km s ⁻¹]	ϵ	<i>m</i> _{<i>J</i>} [mag]	<i>m</i> _{<i>H</i>} [mag]	<i>m</i> _{K_s} [mag]	<i>w</i> _{cor} [km s ⁻¹]	<i>M</i> _{<i>J</i>} [mag]	<i>M</i> _{<i>H</i>} [mag]	<i>M</i> _{K_s} [mag]
J1719-45	342.92	-4.91	5793	254.0	0.39	10.71	10.42	10.34	293.8	-23.61	-23.73	-23.70
J1727-18	6.44	8.94	346	107.0	0.51	13.59	12.53	12.95	98.9	-14.72	-15.57	-14.99
J1732-43*	346.44	-5.37	2539	111.0	0.36	12.04	11.70	11.58	113.6	-19.87	-20.09	-20.02
J1733-09	15.16	12.63	5502	138.0	0.65	14.43	13.63	12.94	127.8	-19.60	-20.16	-20.58
J1734-44*	345.48	-6.28	5825	219.0	0.42	14.69	13.77	13.48	242.7	-19.39	-20.20	-20.39
J1736-47*	342.94	-8.44	5878	328.0	0.52	12.31	11.18	10.95	341.1	-21.91	-22.95	-23.13
J1744-09	16.68	10.39	4245	238.0	0.33	12.13	11.97	12.33	291.6	-21.79	-21.68	-21.13
J1803-03	24.65	9.30	3616	175.0	0.48	14.40	13.93	13.78	178.8	-19.19	-19.29	-19.13
J1822-35	357.86	-10.06	5604	542.0	0.65	10.95	10.22	9.26	538.6	-23.38	-24.04	-24.97
J1824-34	359.40	-9.76	4901	335.0	0.36	10.31	10.11	9.28	402.9	-23.38	-23.55	-24.40
J1826-33	0.05	-9.98	5900	315.0	0.28	12.24	11.37	10.90	414.3	-21.93	-22.74	-23.21
J1831-31	2.28	-10.13	5992	426.0	0.35	10.55	10.10	10.05	517.8	-23.80	-24.18	-24.24
J1841-18	14.83	-6.37	1670	159.0	0.88	12.26	13.90	13.57	137.3	-19.92	-18.00	-17.90
J1852+10	42.42	4.45	4906	238.0	0.59	14.43	13.54	13.25	238.4	-19.49	-20.18	-20.29
J1853+09	41.98	3.96	4729	320.0	0.58	12.38	11.36	9.98	319.6	-21.74	-22.51	-23.71
J1917+07	42.85	-2.16	3033	226.0	0.30	11.39	10.33	10.08	289.3	-22.25	-22.84	-22.76
J1933+10	47.32	-4.37	5255	240.0	0.66	13.25	12.55	12.38	231.6	-20.69	-21.22	-21.23

NOTES:

*Galaxies with new narrowband observations.

Table B.2 gives the uncorrected photometric and spectroscopic parameters as well as the absolute magnitudes from the TF relation and peculiar velocities for the peculiar velocity sample in Chapter 6. The columns are:

Column 1 H_I catalogue name

Column 2 & 3 Galactic co-ordinates, l and b

Column 4 H_I recession velocity, v

Column 5 H_I 50% linewidth uncorrected for inclination, w_{50}

Column 6 J band ellipticity, ϵ

Columns 7-9 observed extrapolated total magnitudes in J , H and K_s respectively, m_J , m_H , and m_{K_s} , before corrections for extinction

Column 10 50% linewidth corrected for inclination, instrumental, turbulent and cosmological broadening, w_{cor}

Columns 11-13 absolute magnitudes in J , H and K_s respectively, computed assuming the galaxy is at the distance given by its redshift and corrected for extinction

Column 14 the TF distance in velocity units, $H_0 d$

Column 15 peculiar velocity, v_{pec}

Table B 2: Peculiar Velocity Sample

Name	<i>l</i> [deg]	<i>b</i> [deg]	<i>v</i> [km s ⁻¹]	<i>w</i> ₅₀ [km s ⁻¹]	ϵ	<i>m</i> _J [mag]	<i>m</i> _H [mag]	<i>m</i> _{K_s} [mag]	<i>w</i> _{cor} [km s ⁻¹]	<i>M</i> _J [mag]	<i>M</i> _H [mag]	<i>M</i> _{K_s} [mag]	<i>c</i> _z [km s ⁻¹]	<i>v</i> _{pec} [km s ⁻¹]
J0614+12	197.59	-2.23	5553	217.0	0.47	13.74	12.84	12.22	232.3	-20.16	-20.84	-21.29	4712 ± 623	928 ± 607
J0621+11	199.66	-1.50	5599	188.0	0.49	13.50	13.09	13.13	191.3	-20.77	-20.95	-20.69	3284 ± 700	2415 ± 697
J0622+04	205.58	-4.36	2958	306.0	0.60	11.20	10.77	10.37	310.3	-21.82	-22.08	-22.34	2414 ± 374	651 ± 350
J0622+11B	199.78	-1.15	5493	366.0	0.58	12.17	11.95	11.21	367.8	-22.58	-22.51	-23.06	4549 ± 719	1045 ± 706
J0630+16	195.62	3.04	2532	258.0	0.54	12.51	11.90	12.06	258.6	-20.02	-20.49	-20.18	3472 ± 611	-835 ± 570
J0709-05	219.83	1.54	1722	252.0	0.57	11.82	10.38	9.65	249.6	-19.94	-21.25	-21.84	1649 ± 310	258 ± 272
J0712-09*	223.64	0.46	2441	97.0	0.36	13.42	12.19	11.90	98.6	-17.57	-18.62	-18.67	1385 ± 42	1246 ± 42
J0716-18B	232.05	-3.01	5822	244.0	0.61	15.02	13.79	13.22	240.9	-19.96	-20.81	-21.08	5743 ± 1182	273 ± 1170
J0716-18C	232.57	-3.11	2816	267.0	0.88	13.26	11.43	10.93	251.7	-21.80	-22.97	-22.84	1290 ± 250	1721 ± 259
J0719-09	224.61	1.80	2497	181.0	0.81	13.58	12.47	12.39	166.8	-19.90	-20.73	-20.40	1466 ± 310	1231 ± 306
J0727-23	238.23	-3.31	4407	412.0	0.68	12.33	11.04	10.59	402.3	-22.19	-23.15	-23.38	4008 ± 601	605 ± 583
J0730-22	236.82	-1.85	773	276.0	0.77	10.94	9.43	9.37	255.9	-21.43	-22.35	-21.83	595 ± 207	388 ± 192
J0732-16	232.59	0.94	4320	80.0	0.32	14.57	13.58	12.92	88.3	-28.56	-26.00	-24.09	72 ± 12	4463 ± 171
J0733-13	230.16	2.72	3253	151.0	0.59	13.81	13.16	12.53	146.5	-18.94	-19.48	-19.93	2245 ± 388	1226 ± 377
J0734-14	230.85	2.49	3295	181.0	0.59	13.98	13.50	13.06	175.3	-19.03	-19.35	-19.59	3364 ± 1043	149 ± 1030
J0735-17	233.35	1.64	3244	99.0	0.29	14.58	13.81	13.23	113.1	-18.31	-18.84	-19.17	1883 ± 376	1581 ± 372
J0736-18	234.11	1.33	4463	119.0	0.84	14.62	13.27	13.16	103.9	-20.10	-21.08	-20.68	923 ± 182	3760 ± 226
J0737-31*	245.57	-4.83	2240	127.0	0.62	13.96	13.27	12.92	113.9	-17.10	-17.61	-17.74	2441 ± 422	9 ± 422
J0740-22*	238.83	-0.10	3049	138.0	0.52	12.78	12.03	11.34	131.4	-19.86	-20.47	-20.95	1103 ± 134	2168 ± 134
J0740-30A	245.75	-4.18	5079	323.0	0.80	13.24	12.37	12.02	303.0	-22.05	-22.62	-22.63	3369 ± 545	1924 ± 538
J0740-32	246.80	-4.61	2723	278.0	0.59	11.79	10.50	10.37	277.3	-21.10	-22.22	-22.19	2082 ± 350	854 ± 331
J0741-22	238.56	0.24	3068	466.0	0.80	11.28	9.47	9.85	440.1	-23.31	-24.78	-24.05	2041 ± 369	1251 ± 359
J0741-26	241.69	-1.54	3506	142.0	0.75	14.10	13.74	13.38	129.0	-20.06	-20.08	-19.98	1459 ± 286	2268 ± 297
J0741-30B	245.26	-3.52	4558	349.0	0.55	12.01	11.57	11.21	363.4	-22.03	-22.31	-22.56	4567 ± 627	208 ± 605
J0742-26	242.23	-1.78	2913	247.0	0.60	12.99	12.62	11.94	246.5	-20.18	-20.30	-20.77	3452 ± 602	-318 ± 571
J0742-31	246.93	-4.23	2103	305.0	0.52	11.28	10.61	9.50	315.2	-21.06	-21.52	-22.48	2261 ± 350	57 ± 396
J0743-18*	235.07	2.72	3337	172.0	0.40	14.22	13.34	12.94	188.7	-18.75	-19.49	-19.74	3907 ± 96	-341 ± 96
J0744-25	241.88	-0.96	4049	158.0	0.36	12.25	11.10	10.38	182.5	-20.76	-21.67	-22.18	1597 ± 215	2675 ± 232
J0744-26*	241.92	-0.99	2736	278.0	0.41	11.95	11.14	10.70	314.6	-21.22	-21.77	-22.03	2870 ± 55	90 ± 55
J0747-18	236.01	3.37	3243	506.0	0.82	10.04	8.99	8.82	485.7	-24.60	-25.41	-25.32	1566 ± 262	1911 ± 267
J0747-25	242.10	-0.33	4252	216.0	0.29	13.22	12.69	12.50	280.5	-20.42	-20.81	-20.90	5477 ± 696	-998 ± 664
J0747-26A	242.46	-0.56	882	145.0	0.37	12.51	10.78	10.95	156.1	-17.85	-19.43	-19.08	1100 ± 290	9 ± 233
J0748-18	235.96	3.50	917	166.0	0.58	12.83	12.70	12.80	158.9	-17.52	-17.55	-17.28	2209 ± 1222	-1058 ± 1186
J0752-25A	242.05	1.02	4603	361.0	0.56	10.98	10.22	9.20	373.7	-22.87	-23.52	-24.50	2645 ± 375	2192 ± 371
J0754-38	254.17	-5.59	2749	270.0	0.67	13.20	12.30	11.88	256.2	-19.82	-20.49	-20.72	3597 ± 617	-633 ± 581

Continued on Next Page...

Table B.2 – Continued

Name	<i>l</i>	<i>b</i>	<i>v</i>	<i>w</i> ₅₀	<i>ε</i>	<i>m</i> _J	<i>m</i> _H	<i>m</i> _{K_s}	<i>w</i> _{cor}	<i>M</i> _J	<i>M</i> _H	<i>M</i> _{K_s}	<i>c_z</i>	<i>v_{pec}</i>
	[deg]	[deg]	[km s ⁻¹]	[km s ⁻¹]		[mag]	[mag]	[mag]	[km s ⁻¹]	[mag]	[mag]	[mag]	[km s ⁻¹]	[km s ⁻¹]
J0801-29	246.56	0.72	2749	249.0	0.52	13.52	12.96	12.42	255.6	-19.50	-19.82	-20.18	4587 ± 795	-1599 ± 755
J0801-33*	250.20	-1.62	1901	177.0	0.69	13.78	12.96	12.98	163.1	-19.07	-19.58	-19.17	1831 ± 374	302 ± 374
J0804-32	249.93	-0.66	1970	131.0	0.67	13.97	14.35	13.89	121.9	-18.13	-17.49	-17.65	2282 ± 1429	-76 ± 1418
J0809-41	258.05	-4.60	1997	316.0	0.84	12.10	10.83	10.03	292.8	-21.80	-22.61	-22.92	1318 ± 247	902 ± 235
J0810-39*	256.17	-3.34	1421	123.0	0.82	15.36	14.92	14.62	104.3	-18.06	-17.98	-17.79	1141 ± 228	508 ± 228
J0818-29A	248.95	3.59	1531	99.0	0.62	14.06	13.41	13.24	90.8	-16.93	-17.49	-17.44	1271 ± 367	515 ± 349
J0818-29B	248.95	3.59	2520	165.0	0.84	13.87	13.33	13.16	150.9	-19.96	-20.23	-20.08	1416 ± 463	1359 ± 463
J0818-33	252.31	1.28	2016	104.0	0.65	13.21	12.33	11.74	91.1	-18.51	-19.24	-19.56	708 ± 154	1556 ± 187
J0826-44	261.93	-3.56	1027	184.0	0.74	13.85	12.67	12.41	164.5	-18.89	-19.55	-19.33	1099 ± 351	157 ± 318
J0839-34	255.55	4.36	5623	235.0	0.38	12.92	12.47	12.50	272.8	-20.89	-21.24	-21.16	5734 ± 701	153 ± 680
J0840-37	258.01	2.65	5291	315.0	0.78	13.17	12.61	12.32	297.8	-22.21	-22.46	-22.41	3567 ± 580	1982 ± 573
J0842-44	263.52	-1.23	3754	188.0	0.49	14.70	13.53	13.07	195.5	-19.37	-20.12	-20.24	3568 ± 1635	427 ± 1628
J0844-34*	256.29	4.97	2167	295.0	0.46	11.65	10.93	10.08	324.2	-20.66	-21.27	-22.04	2938 ± 72	-503 ± 71
J0844-35	256.82	4.47	2240	156.0	0.32	14.43	13.89	13.39	186.4	-17.69	-18.11	-18.47	4752 ± 797	-2246 ± 742
J0844-39	260.38	1.84	1808	158.0	0.35	15.47	14.40	13.84	185.2	-17.13	-17.78	-17.98	4767 ± 727	-2704 ± 648
J0845-42	262.39	0.39	1730	305.0	0.42	12.71	10.49	10.64	346.2	-21.10	-22.57	-21.89	2140 ± 674	-161 ± 648
J0848-39*	260.57	2.58	1831	171.0	0.30	14.73	13.76	13.13	203.5	-17.44	-18.16	-18.56	4750 ± 399	-2660 ± 399
J0856-37*	259.73	5.22	2500	250.0	0.72	12.70	11.50	11.74	234.2	-20.85	-21.78	-21.19	1869 ± 108	902 ± 108
J0856-48*	268.51	-2.08	2666	268.0	0.61	12.20	11.26	11.05	269.0	-21.34	-21.87	-21.75	2120 ± 612	782 ± 612
J0858-45B	266.18	0.33	2699	232.0	0.29	12.28	10.87	10.18	293.1	-22.67	-23.20	-23.27	1330 ± 156	1617 ± 165
J0900-39	262.02	4.44	2627	295.0	0.39	10.79	10.40	9.71	338.8	-22.13	-22.34	-22.90	2259 ± 280	636 ± 248
J0907-48	269.41	-0.51	5219	181.0	0.63	12.53	11.95	11.07	172.9	-22.87	-22.80	-23.15	974 ± 933	4489 ± 944
J0917-53	274.25	-2.87	947	179.0	0.59	13.19	11.95	11.60	168.7	-17.58	-18.60	-18.71	1679 ± 410	-503 ± 335
J0920-44	268.21	3.77	2677	168.0	0.71	13.95	12.85	10.79	154.1	-20.02	-20.68	-22.23	1086 ± 808	1855 ± 813
J0923-42*	267.39	5.43	2979	137.0	0.51	14.95	14.30	14.39	134.4	-17.69	-18.19	-17.89	3605 ± 589	-354 ± 589
J0944-59	281.14	-4.83	2400	144.0	0.73	14.62	14.02	13.65	126.7	-19.29	-19.51	-19.49	1300 ± 1239	1312 ± 1239
J0946-46	273.06	5.21	2693	289.0	0.81	13.19	12.46	11.78	267.8	-20.75	-21.21	-21.52	2687 ± 492	274 ± 467
J0950-49	275.56	3.30	3772	164.0	0.39	12.42	11.77	11.48	181.3	-20.13	-20.65	-20.81	2349 ± 300	1680 ± 292
J0951-59	281.72	-4.01	4371	338.0	0.69	13.25	12.21	11.48	330.6	-21.84	-22.49	-22.86	3489 ± 613	1097 ± 600
J0953-49	275.65	3.86	2265	97.0	0.34	14.97	13.84	13.96	105.0	-17.45	-18.46	-18.25	1656 ± 272	869 ± 254
J0955-60*	282.94	-4.84	3295	253.0	0.58	12.96	11.82	11.19	253.0	-20.18	-21.17	-21.66	3088 ± 100	417 ± 100
J0956-59*	282.37	-3.85	3417	164.0	0.76	14.44	13.22	12.77	234.1	-20.39	-21.05	-21.03	3031 ± 272	601 ± 272
J0958-55	279.99	-0.36	3714	160.0	0.85	15.33	13.74	13.71	145.3	-20.05	-20.98	-20.33	1587 ± 563	2362 ± 568
J1000-58A	282.19	-2.85	2685	118.0	0.67	13.08	11.96	11.42	99.7	-18.81	-19.53	-19.69	958 ± 192	1948 ± 217
J1003-49*	277.01	4.72	2410	105.0	0.44	12.96	13.56	12.86	98.2	-18.99	-18.27	-18.76	1214 ± 593	1458 ± 593
J1004-58	282.59	-2.41	3682	290.0	0.51	11.74	12.01	11.60	298.6	-23.94	-22.76	-22.53	1993 ± 610	1912 ± 610

Continued on Next Page...

Table B.2 – Continued

Name	<i>l</i>	<i>b</i>	<i>v</i>	<i>w</i> ₅₀	ϵ	<i>m</i> _{<i>J</i>}	<i>m</i> _{<i>H</i>}	<i>m</i> _{<i>K_s</i>}	<i>w</i> _{<i>cor</i>}	<i>M</i> _{<i>J</i>}	<i>M</i> _{<i>H</i>}	<i>M</i> _{<i>K_s</i>}	<i>c</i> _{<i>Z</i>}	<i>v</i> _{<i>pec</i>}
	[deg]	[deg]	[km s ⁻¹]	[km s ⁻¹]		[mag]	[mag]	[mag]	[km s ⁻¹]	[mag]	[mag]	[mag]	[km s ⁻¹]	[km s ⁻¹]
J1006-50B	278.09	4.11	5298	298.0	0.59	12.80	11.96	11.82	300.2	-21.15	-21.85	-21.90	5008 ± 725	549 ± 708
J1009-51*	278.83	4.01	28.8	146.0	0.32	15.08	14.52	14.18	177.1	-17.36	-17.84	-18.06	6183 ± 289	-3108 ± 289
J1012-62*	285.69	-5.12	3450	207.0	0.62	10.97	9.92	9.67	196.2	-21.96	-22.92	-23.05	934 ± 36	2720 ± 36
J1013-52B	280.03	3.43	2714	251.0	0.35	11.80	10.92	10.69	302.8	-20.71	-21.47	-21.63	3220 ± 384	-252 ± 335
J1024-54*	282.78	2.23	1079	135.0	0.74	13.03	12.37	12.05	115.2	-17.71	-18.06	-17.95	1110 ± 28	214 ± 28
J1031-63*	288.18	-4.95	3760	316.0	0.82	13.69	13.14	12.71	296.2	-20.94	-21.21	-21.29	4400 ± 116	-439 ± 115
J1037-54	284.40	3.04	2671	313.0	0.66	11.11	10.33	10.21	303.9	-21.92	-22.49	-22.44	2002 ± 342	915 ± 325
J1039-54	284.54	3.57	2752	117.0	0.67	13.71	13.55	13.01	98.7	-17.71	-17.66	-17.93	2027 ± 615	974 ± 607
J1053-62	289.96	-2.97	1837	271.0	0.67	11.57	10.78	9.88	257.4	-20.67	-21.23	-21.92	1640 ± 303	405 ± 272
J1130-58*	292.56	2.53	1842	149.0	0.62	13.10	11.41	12.17	134.8	-19.29	-20.74	-19.79	920 ± 196	1152 ± 196
J1153-63	296.60	-1.74	2144	188.0	0.36	13.17	12.45	11.84	213.5	-20.61	-20.69	-20.85	1725 ± 423	619 ± 406
J1203-64*	297.82	-2.45	5519	352.0	0.65	13.13	12.34	11.75	346.3	-22.07	-22.43	-22.44	4744 ± 138	969 ± 138
J1204-59A	297.04	2.40	5616	238.0	0.75	13.68	13.08	13.62	223.4	-21.88	-22.08	-21.12	3095 ± 764	2740 ± 763
J1208-65	298.48	-2.99	5484	364.0	0.34	12.34	10.90	10.86	441.6	-22.38	-23.56	-23.48	5292 ± 541	381 ± 517
J1209-62	298.09	-0.01	1461	127.0	0.36	13.11	11.23	10.19	135.5	-20.31	-21.28	-21.59	445 ± 79	1221 ± 142
J1213-65	299.01	-3.02	2139	238.0	0.35	12.52	12.34	12.44	278.0	-19.93	-19.89	-19.62	4322 ± 967	-1996 ± 924
J1214-58	298.09	4.08	5607	287.0	0.81	13.71	12.86	11.94	267.6	-21.78	-22.32	-22.87	3096 ± 521	2735 ± 519
J1219-66	299.69	-3.77	4036	170.0	0.52	15.64	14.91	13.76	172.2	-17.77	-18.33	-19.39	5897 ± 1956	-1679 ± 1942
J1221-57	298.92	4.92	5348	323.0	0.64	13.34	12.58	11.94	318.6	-21.14	-21.68	-22.16	5561 ± 866	13 ± 848
J1221-59	299.17	2.95	1473	185.0	0.34	13.59	11.79	12.17	212.0	-18.35	-19.82	-19.17	2560 ± 497	-871 ± 431
J1222-58	299.18	4.05	1542	374.0	0.69	9.89	8.76	8.79	369.7	-22.88	-23.74	-23.41	1077 ± 202	686 ± 185
J1223-61*	299.56	1.46	3845	163.0	0.42	14.13	13.17	12.96	170.9	-19.67	-20.28	-20.19	2644 ± 96	1410 ± 95
J1225-59	299.60	3.52	5658	238.0	0.38	12.37	11.77	11.39	272.3	-21.98	-22.40	-22.64	3200 ± 417	2676 ± 413
J1229-58*	300.07	4.69	5651	293.0	0.48	13.80	12.59	12.29	313.5	-20.64	-21.61	-21.75	6599 ± 159	-726 ± 159
J1229-61*	300.32	1.64	5387	328.0	0.35	11.94	11.00	10.12	394.4	-23.34	-23.81	-24.40	3037 ± 126	2557 ± 126
J1239-59	301.37	3.24	5308	379.0	0.62	12.42	11.48	11.09	380.3	-22.23	-22.91	-23.14	4621 ± 650	899 ± 634
J1255-58	303.48	4.54	5596	217.0	0.54	13.03	11.66	12.20	221.1	-21.07	-22.31	-21.64	2929 ± 457	2879 ± 457
J1255-59*	303.41	3.51	2296	162.0	0.76	14.20	13.41	12.76	143.2	-19.56	-20.00	-20.29	1230 ± 70	1273 ± 70
J1302-64	304.11	-1.22	3910	174.0	0.57	14.51	13.06	12.68	170.4	-20.02	-20.66	-20.43	2289 ± 376	1804 ± 371
J1312-60	305.53	1.89	2318	238.0	0.31	12.81	11.22	10.56	290.6	-20.78	-21.83	-22.10	2200 ± 935	313 ± 923
J1327-57	307.77	5.04	2929	255.0	0.74	11.26	9.95	9.27	234.9	-22.79	-23.76	-24.05	745 ± 127	2386 ± 178
J1329-58	307.85	3.66	5573	388.0	0.48	12.32	11.34	11.00	421.9	-22.28	-23.06	-23.30	5541 ± 725	228 ± 706
J1332-58*	308.42	4.35	1473	104.0	0.28	13.52	12.97	12.47	116.2	-17.64	-18.02	-18.28	1377 ± 544	294 ± 544
J1337-58C	309.01	4.10	5907	130.0	0.30	13.78	13.17	13.05	156.6	-20.80	-21.20	-21.19	2125 ± 243	3977 ± 261
J1342-57*	309.92	4.97	3727	182.0	0.46	14.32	13.76	13.40	194.9	-18.37	-18.77	-18.97	6094 ± 320	-2171 ± 319
J1343-57	309.93	4.61	5360	207.0	0.37	13.72	12.72	12.35	241.2	-19.97	-20.81	-21.07	5310 ± 677	244 ± 656

Continued on Next Page...

Table B.2 – Continued

Name	<i>l</i>	<i>b</i>	<i>v</i>	<i>w</i> ₅₀	<i>ε</i>	<i>m</i> _J	<i>m</i> _H	<i>m</i> _{K_s}	<i>w</i> _{cor}	<i>M</i> _J	<i>M</i> _H	<i>M</i> _{K_s}	c ₂₂	<i>v</i> _{pec}
	[deg]	[deg]	[km s ⁻¹]	[km s ⁻¹]		[mag]	[mag]	[mag]	[km s ⁻¹]	[mag]	[mag]	[mag]	[km s ⁻¹]	[km s ⁻¹]
J1346-58A	310.19	3.86	3677	218.0	0.43	13.22	13.34	13.16	237.4	-20.23	-19.90	-19.91	4893 ± 1086	-1026 ± 1065
J1351-58	310.72	3.37	3881	635.0	0.52	10.38	9.47	8.72	680.9	-23.93	-24.57	-25.20	4404 ± 567	-337 ± 355
J1355-59A*	311.07	2.58	5495	329.0	0.77	13.28	12.18	11.49	311.9	-22.61	-23.25	-23.50	2777 ± 44	2899 ± 44
J1356-58	311.32	3.34	5978	186.0	0.33	15.68	14.04	13.64	223.8	-18.71	-20.15	-20.39	7734 ± 1002	-1572 ± 979
J1401-55	312.78	5.73	3967	274.0	0.51	11.20	10.33	10.75	280.8	-22.28	-23.03	-22.49	2144 ± 376	2013 ± 374
J1405-66	310.20	-4.83	2659	159.0	0.79	12.06	12.17	13.24	139.2	-21.48	-21.06	-19.56	1038 ± 368	1768 ± 378
J1410-65	311.00	-3.96	3099	437.0	0.52	10.51	9.58	8.89	468.5	-22.83	-23.59	-24.19	2809 ± 378	439 ± 348
J1412-56A*	313.97	4.55	3769	276.0	0.46	11.01	10.46	10.24	300.7	-22.52	-22.90	-22.98	2099 ± 37	1851 ± 37
J1413-57	313.75	3.37	5007	332.0	0.68	13.72	12.36	12.05	324.4	-21.02	-21.98	-22.00	5330 ± 949	-147 ± 932
J1413-65	311.33	-3.81	435	254.0	0.44	7.27	6.60	6.35	276.0	-22.63	-22.93	-22.90	263 ± 115	321 ± 127
J1414-58	313.64	2.76	5798	249.0	0.57	13.51	12.61	12.03	251.5	-20.90	-21.49	-21.84	4297 ± 583	1675 ± 572
J1415-58	313.65	2.18	5393	713.0	0.79	12.23	11.32	10.61	686.2	-24.97	-25.26	-25.50	4534 ± 746	1030 ± 733
J1416-65*	311.64	-3.82	2859	337.0	0.48	10.65	10.31	9.56	366.0	-22.38	-22.53	-23.16	2440 ± 73	567 ± 73
J1419-57*	314.67	3.81	3849	167.0	0.62	11.88	12.16	12.05	156.0	-21.70	-21.14	-20.97	1316 ± 367	2708 ± 367
J1423-65	312.21	-4.69	3083	155.0	0.75	14.29	13.30	12.88	142.3	-18.72	-19.39	-19.39	2243 ± 388	982 ± 372
J1429-54*	317.01	5.54	3018	122.0	0.39	13.73	13.04	12.39	123.3	-18.83	-19.36	-19.80	1582 ± 305	1611 ± 305
J1437-56	317.38	3.80	4431	143.0	0.69	14.17	13.27	12.58	132.2	-20.28	-20.86	-21.13	1338 ± 221	3258 ± 248
J1441-57*	317.56	2.60	3384	151.0	0.78	13.83	12.69	13.07	134.1	-19.88	-20.53	-19.60	1526 ± 244	2018 ± 244
J1442-54*	318.83	5.32	2778	185.0	0.49	13.93	13.12	12.42	190.6	-19.07	-19.68	-20.23	2828 ± 158	118 ± 158
J1444-55	318.55	3.96	4672	237.0	0.33	13.57	11.94	11.75	290.6	-20.33	-21.80	-21.87	4756 ± 580	78 ± 554
J1448-57	318.06	1.78	4780	221.0	0.64	12.30	11.74	11.29	209.8	-22.31	-22.45	-22.55	1586 ± 330	3348 ± 346
J1451-55A	319.23	3.24	5126	165.0	0.38	14.53	13.59	12.79	186.2	-20.07	-20.69	-21.28	3037 ± 929	2246 ± 926
J1452-56	319.03	2.24	3287	334.0	0.80	12.48	11.39	10.77	309.4	-22.66	-23.20	-23.29	1713 ± 304	1726 ± 304
J1457-54	320.65	4.10	2900	475.0	0.50	10.03	9.14	8.76	510.4	-23.51	-24.20	-24.48	2434 ± 331	622 ± 303
J1501-60*	318.16	-1.73	4436	124.0	0.34	14.38	11.30	11.47	131.5	-20.38	-22.98	-22.48	811 ± 80	3762 ± 80
J1506-54*	321.78	3.49	2938	135.0	0.69	14.83	13.62	14.07	116.2	-19.38	-20.21	-19.39	1177 ± 55	1910 ± 55
J1507-60	318.76	-2.28	4537	233.0	0.61	12.71	10.68	10.62	223.9	-21.54	-23.25	-23.32	1576 ± 274	3093 ± 291
J1509-52	323.16	4.81	1464	346.0	0.79	8.95	8.56	8.04	323.9	-23.76	-23.82	-23.96	614 ± 128	1000 ± 153
J1514-53	323.59	4.04	1471	431.0	0.76	9.17	8.02	7.51	411.1	-23.92	-24.69	-24.83	708 ± 140	907 ± 153
J1515-60A	319.74	-2.45	5150	362.0	0.58	13.24	11.71	11.40	366.2	-21.66	-22.79	-22.83	4801 ± 725	477 ± 708
J1518-55	322.68	1.48	1480	248.0	0.51	14.17	11.99	10.98	256.6	-19.24	-20.61	-21.01	2047 ± 392	-431 ± 328
J1523-60	320.45	-3.13	3158	201.0	0.61	13.54	13.61	12.68	195.7	-19.50	-19.23	-19.95	3532 ± 1149	-253 ± 1134
J1525-51	325.65	4.18	3299	184.0	0.30	13.76	12.80	12.79	233.4	-19.44	-20.19	-20.01	4350 ± 557	-913 ± 514
J1526-54	324.22	1.70	5058	237.0	0.32	11.82	12.21	11.42	294.6	-23.79	-22.71	-23.02	2386 ± 785	2804 ± 786
J1530-59	321.96	-2.37	5329	146.0	0.33	11.61	11.27	10.61	167.2	-22.69	-22.72	-23.11	953 ± 120	4496 ± 184
J1539-44	331.78	8.71	3434	224.0	0.69	13.58	12.74	12.99	211.6	-19.75	-20.37	-19.84	3614 ± 663	-45 ± 640

Continued on Next Page...

Table B.2 – Continued

Name	<i>l</i>	<i>b</i>	<i>v</i>	<i>w</i> ₅₀	ϵ	<i>m</i> _{<i>J</i>}	<i>m</i> _{<i>H</i>}	<i>m</i> _{<i>K_s</i>}	<i>w</i> _{<i>cor</i>}	<i>M</i> _{<i>J</i>}	<i>M</i> _{<i>H</i>}	<i>M</i> _{<i>K_s</i>}	<i>c</i> _{<i>Z</i>}	<i>v_{pec}</i>
	[deg]	[deg]	[km s ⁻¹]	[km s ⁻¹]		[mag]	[mag]	[mag]	[km s ⁻¹]	[mag]	[mag]	[mag]	[km s ⁻¹]	[km s ⁻¹]
J1539-59B	322.78	-3.35	51.79	110.0	0.66	12.42	11.37	10.77	93.6	-21.41	-22.22	-22.51	448 ± 85	4843 ± 179
J1543-60	322.76	-4.20	51.86	230.0	0.68	13.12	12.62	11.78	216.4	-21.04	-21.33	-21.97	2845 ± 506	2449 ± 504
J1545-61	322.51	-4.92	52.58	365.0	0.49	11.69	10.72	10.16	394.4	-22.71	-23.49	-23.93	3604 ± 433	1739 ± 421
J1546-57	324.92	-2.15	2756	89.0	0.35	14.86	13.44	13.24	87.0	-17.79	-18.89	-18.72	1095 ± 193	1771 ± 211
J1547-59	323.87	-3.54	5652	341.0	0.39	10.85	10.67	10.13	392.0	-23.56	-23.59	-24.05	3296 ± 395	2463 ± 390
J1605-57	326.49	-4.14	2990	93.0	0.37	11.09	11.37	10.95	90.2	-21.07	-20.69	-20.91	423 ± 201	2661 ± 250
J1606-57	326.78	-4.02	5065	398.0	0.76	12.13	11.23	10.74	382.3	-23.09	-23.71	-23.90	3011 ± 459	2148 ± 453
J1613-56	328.26	-3.80	2722	318.0	0.35	10.77	10.02	9.47	379.0	-22.03	-22.64	-23.11	2523 ± 378	288 ± 345
J1616-40	339.95	7.66	4438	344.0	0.63	11.95	11.00	10.78	339.8	-22.08	-22.78	-22.83	3364 ± 500	1171 ± 485
J1617-58*	327.30	-5.54	2767	240.0	0.53	10.89	9.83	9.83	242.0	-21.59	-22.56	-22.45	1321 ± 9	1530 ± 9
J1621-36	343.41	9.77	4447	370.0	0.55	10.70	10.04	9.59	376.7	-23.35	-23.81	-24.13	2358 ± 335	2181 ± 333
J1626-40	340.83	5.70	4755	236.0	0.67	13.97	12.78	12.90	228.0	-20.34	-21.21	-20.82	3861 ± 847	978 ± 836
J1628-29	349.70	13.50	4180	426.0	0.60	11.69	10.97	10.76	435.2	-22.14	-22.74	-22.89	4973 ± 700	-709 ± 671
J1629-26	351.74	14.76	5143	334.0	0.44	11.77	10.93	10.60	373.5	-22.36	-23.07	-23.32	3923 ± 455	1300 ± 438
J1630-30	348.89	12.21	4109	207.0	0.79	13.91	12.51	12.84	188.4	-20.81	-21.94	-21.29	1814 ± 354	2375 ± 359
J1632-28	351.08	13.50	4104	518.0	0.72	10.33	9.48	9.15	508.0	-24.58	-25.13	-25.19	2190 ± 333	1991 ± 330
J1632-29B*	350.15	12.58	4820	276.0	0.76	12.80	12.08	11.75	255.0	-21.70	-22.17	-22.18	2735 ± 28	2162 ± 28
J1636-26	353.14	14.97	4109	239.0	0.46	13.70	13.02	12.95	257.4	-19.79	-20.33	-20.27	5680 ± 883	-1499 ± 854
J1639-36*	345.83	6.79	1817	158.0	0.60	14.43	13.79	13.49	154.3	-17.31	-17.74	-17.79	3125 ± 255	-1240 ± 254
J1640-35	346.71	7.39	3878	84.0	0.33	14.00	13.33	12.94	92.6	-19.01	-19.48	-19.59	1124 ± 145	2821 ± 184
J1642-29*	351.68	11.16	2596	155.0	0.79	13.89	13.00	13.33	135.4	-19.29	-19.96	-19.24	1459 ± 238	1201 ± 238
J1642-37	345.32	5.63	2643	162.0	0.69	13.67	12.83	12.36	148.7	-19.69	-20.21	-20.27	1356 ± 375	1352 ± 375
J1644-55	331.92	-6.33	5114	441.0	0.83	11.56	10.25	10.06	415.3	-23.75	-24.80	-24.70	2385 ± 382	2791 ± 385
J1648-54*	333.08	-6.07	4656	253.0	0.67	13.35	12.72	12.08	240.3	-20.36	-20.87	-21.36	4008 ± 143	707 ± 143
J1651-22*	358.52	13.66	5853	119.0	0.46	15.21	14.31	13.47	115.0	-19.07	-19.85	-20.60	2051 ± 154	3849 ± 154
J1654-56	332.12	-7.98	4912	149.0	0.65	15.54	15.04	13.43	134.7	-17.81	-18.24	-19.71	4252 ± 1979	713 ± 1974
J1702-27	355.55	8.49	4546	107.0	0.37	12.41	11.89	12.75	114.1	-20.64	-21.09	-20.08	1112 ± 168	3469 ± 209
J1711-47	340.77	-4.79	2186	232.0	0.78	12.56	11.27	10.32	210.4	-20.70	-21.66	-22.21	1090 ± 228	1130 ± 229
J1712-15	7.58	13.96	2937	206.0	0.47	12.88	11.77	11.89	220.7	-19.23	-20.22	-19.99	3454 ± 530	-506 ± 491
J1719-45	342.92	-4.91	5753	254.0	0.39	10.71	10.42	10.34	293.8	-23.61	-23.73	-23.70	1995 ± 236	3822 ± 256
J1727-18	6.44	8.94	346	107.0	0.51	13.59	12.53	12.95	98.9	-14.72	-15.57	-14.99	772 ± 553	-435 ± 445
J1732-43*	346.44	-5.37	2839	111.0	0.36	12.04	11.70	11.58	113.6	-19.87	-20.09	-20.02	797 ± 46	1749 ± 46
J1733-09	15.16	12.63	5502	138.0	0.65	14.43	13.63	12.94	127.8	-19.60	-20.16	-20.58	2020 ± 349	3456 ± 360
J1734-44*	345.48	-6.28	5825	219.0	0.42	14.69	13.77	13.48	242.7	-19.39	-20.20	-20.39	7514 ± 463	-1682 ± 463
J1736-47*	342.94	-8.44	5878	328.0	0.52	12.31	11.18	10.95	341.1	-21.91	-22.95	-23.13	4196 ± 160	1688 ± 160
J1744-09	16.68	10.39	4245	238.0	0.33	12.13	11.97	12.33	291.6	-21.79	-21.68	-21.13	3943 ± 531	259 ± 506

Continued on Next Page...

Table B.2 – Continued

Name	<i>l</i>	<i>b</i>	<i>v</i>	<i>w</i> ₅₀	ϵ	<i>m</i> _J	<i>m</i> _H	<i>m</i> _{K_s}	<i>w</i> _{cor}	<i>M</i> _J	<i>M</i> _H	<i>M</i> _{K_s}	c _z	<i>v</i> _{pec}
	[deg]	[deg]	[km s ⁻¹]	[km s ⁻¹]		[mag]	[mag]	[mag]	[km s ⁻¹]	[mag]	[mag]	[mag]	[km s ⁻¹]	[km s ⁻¹]
J1803-03	24.65	9.30	361.6	175.0	0.48	14.40	13.93	13.78	178.8	-19.19	-19.29	-19.13	3755 ± 1564	-218 ± 1533
J1822-35	357.86	-10.06	5604	542.0	0.65	10.95	10.22	9.26	538.6	-23.38	-24.04	-24.97	4750 ± 715	790 ± 699
J1824-34	359.40	-9.76	4901	335.0	0.36	10.31	10.11	9.28	402.9	-23.38	-23.55	-24.40	2846 ± 409	1986 ± 403
J1826-33	0.05	-9.98	5900	315.0	0.28	12.24	11.37	10.90	414.3	-21.93	-22.74	-23.21	6090 ± 562	-263 ± 532
J1831-31	2.28	-10.13	5992	426.0	0.35	10.55	10.10	10.05	517.8	-23.80	-24.18	-24.24	4870 ± 598	1039 ± 581
J1852+10	42.42	4.45	4906	238.0	0.59	14.43	13.54	13.25	238.4	-19.49	-20.18	-20.29	5929 ± 1009	-1185 ± 987
J1853+09	41.98	3.96	4729	320.0	0.58	12.38	11.36	9.98	319.6	-21.74	-22.51	-23.71	2958 ± 504	1608 ± 495
J1917+07	42.85	-2.16	3033	226.0	0.30	11.39	10.33	10.08	289.3	-22.25	-22.84	-22.76	1523 ± 167	1315 ± 160
J1933+10	47.32	-4.37	5255	240.0	0.66	13.25	12.55	12.38	231.6	-20.69	-21.22	-21.23	3673 ± 587	1364 ± 575

NOTES:

*Galaxies with new narrowband observations.

Bibliography

- Aaronson, M., Bothun, G., Mould, J., Huchra, J., Schommer, R. A., & Cornell, M. E. 1986, ApJ, 302, 536
- Aaronson, M., Huchra, J., & Mould, J. 1979, ApJ, 229, 1
- Aaronson, M., Huchra, J., Mould, J., Schechter, P. L., & Tully, R. B. 1982, ApJ, 258, 64
- Aaronson, M., Mould, J., & Huchra, J. 1980a, ApJ, 237, 655
- . 1980b, ApJ, 237, 655
- Aaronson, M., Mould, J., Huchra, J., Sullivan, I. W. T., Schommer, R. A., & Bothun, G. D. 1980c, ApJ, 239, 12
- Arce, H. G. & Goodman, A. A. 1999, ApJ, 512, L135
- Arnaboldi, M., Neeser, M. J., Parker, L. C., Rosati, P., Lombardi, M., Dietrich, J. P., & Hummel, W. 2007, The Messenger, 127, 28
- Bardeen, J. M., Steinhardt, P. J., & Turner, M. S. 1983, Phys. Rev. D, 28, 679
- Barnes, D. G., Staveley-Smith, L., de Blok, W. J. G., Oosterloo, T., Stewart, I. M., Wright, A. E., Banks, G. D., Bhathal, R., et al. 2001, MNRAS, 322, 486
- Beard, S. M., MacGillivray, H. T., & Thanisch, P. F. 1990, MNRAS, 247, 311
- Bell, E. F., McIntosh, D. H., Katz, N., & Weinberg, M. D. 2003, ApJS, 149, 289
- Bertin, E. 1996, SExtractor User's Manual v2.5
- Bertin, E. & Arnouts, S. 1996, A&AS, 117, 393
- Bertschinger, E. & Dekel, A. 1989, ApJ, 336, L5
- Bond, J. R. & Efstathiou, G. 1987, MNRAS, 226, 655
- Bothun, G. D. & Mould, J. R. 1987, ApJ, 313, 629
- Bottinelli, L., Durand, N., Fouque, P., Garnier, R., Gouguenheim, L., Paturel, G., & Teerikorpi, P. 1992, A&AS, 93, 173

- Bottinelli, L., Gouguenheim, L., Fouque, P., & Paturel, G. 1990, A&AS, 82, 391
- Burstein, D. 2005, in Astronomical Society of the Pacific Conference Series, Vol. 329, Nearby Large-Scale Structures and the Zone of Avoidance, ed. A. P. Fairall & P. A. Woudt, 111
- Burstein, D. & Heiles, C. 1978, ApJ, 225, 40
- . 1982, AJ, 87, 1165
- Buta, R. J. & McCall, M. L. 1999, ApJS, 124, 33
- Cameron, L. M. 1990, A&A, 233, 16
- Cardelli, J. A., Clayton, G. C., & Mathis, J. S. 1989, ApJ, 345, 245
- Carter, B. S. & Meadows, V. S. 1995, MNRAS, 276, 734
- Catinella, B., Haynes, M. P., & Giovanelli, R. 2005, AJ, 130, 1037
- Chamaraux, P., Cayatte, V., Balkowski, C., & Fontanelli, P. 1990, A&A, 229, 340
- Choloniewski, J. & Valentijn, E. A. 2003, Acta Astron., 53, 265
- Cluver, M. E., Jarrett, T. H., Appleton, P. N., Kraan-Korteweg, R. C., Woudt, P. A., Koribalski, B. S., Donley, J. L., Wakamatsu, K., & Nagayama, T. 2008a, ApJ, 686, L17
- . 2008b, ApJ, 686, L17
- Cohen, M., Wheaton, W. A., & Megeath, S. T. 2003, AJ, 126, 1090
- Conklin, E. K. 1969, Nature, 222, 971
- Courteau, S. 1992, PASP, 104, 976
- Courteau, S., Faber, S. M., Dressler, A., & Willick, J. A. 1993, ApJ, 412, L51
- da Costa, L. N., Freudling, W., Wegner, G., Giovanelli, R., Haynes, M. P., & Salzer, J. J. 1996, ApJ, 468, L5+
- Davis, M., Huchra, J., Latham, D. W., & Tonry, J. 1982, ApJ, 253, 423
- Davis, M. & Peebles, P. J. E. 1983, ARA&A, 21, 109
- de Lapparent, V., Geller, M. J., & Huchra, J. P. 1986, ApJ, 302, L1
- de Swardt, B., Kraan-Korteweg, R. C., & Jerjen, H. 2010, MNRAS, 407, 955
- de Vaucouleurs, G. 1958, Nature, 182, 1478
- Dekel, A. 1994, ARA&A, 32, 371
- Dekel, A., Bertschinger, E., & Faber, S. M. 1990, ApJ, 364, 349

- Dekel, A., Eldar, A., Kolatt, T., Yahil, A., Willick, J. A., Faber, S. M., Courteau, S., & Burstein, D. 1999, *ApJ*, 522, 1
- di Nella, H., Paturel, G., Walsh, A. J., Bottinelli, L., Gouguenheim, L., & Theureau, G. 1996, *A&AS*, 118, 311
- Djorgovski, S. & Davis, M. 1987, *ApJ*, 313, 59
- Donley, J. L. et al. 2005, *AJ*, 129, 220
- Dressler, A. & Faber, S. M. 1990, *ApJ*, 354, L45
- Dressler, A., Lynden-Bell, D., Burstein, D., Davies, R. L., Faber, S. M., Terlevich, R., & Wegner, G. 1987, *ApJ*, 313, 42
- Drinkwater, M. J., Parker, Q. A., Proust, D., Slezak, E., & Quintana, H. 2004, *PASA*, 21, 89
- Dutra, C. M., Ahumada, A. V., Clariá, J. J., Bica, E., & Barbuy, B. 2003, *A&A*, 408, 287
- Dutra, C. M., Santiago, B. X., & Bica, E. 2002, *A&A*, 381, 219
- Emerson, J., McPherson, A., & Sutherland, W. 2006, *The Messenger*, 126, 41
- Emerson, J. P., Sutherland, W. J., McPherson, A. M., Craig, S. C., Dalton, G. B., & Ward, A. K. 2004, *The Messenger*, 117, 27
- Epchtein, N., de Batz, B., Capoani, L., Chevallier, L., Copet, E., Fouqué, P., Lacombe, P., Le Bertre, T., et al. 1997, *The Messenger*, 87, 27
- Erdoğdu, P., Lahav, O., Huchra, J. P., Colless, M., Cutri, R. M., Falco, E., George, T., Jarrett, T. H., Jones, D. H., Macri, L. M., Mader, J., Martimbeau, N., Pahre, M. A., Parker, Q. A., Rassat, A., & Saunders, W. 2006a, *MNRAS*, 373, 45
- Erdoğdu, P. et al. 2006b, *MNRAS*, 368, 1515
- Ewen, H. I. & Purcell, E. M. 1951, *Nature*, 168, 356
- Faber, S. M. & Burstein, D. 1988, Motions of galaxies in the neighborhood of the local group, ed. Rubin, V. C. & Coyne, G. V., 115–167
- Fairall, A. P. 1998, Large-scale Structures in the Universe (Wiley)
- Fairall, A. P., Woudt, P. A., & Kraan-Korteweg, R. C. 1998, *A&AS*, 127, 463
- Fixsen, D. J., Cheng, E. S., Gales, J. M., Mather, J. C., Shafer, R. A., & Wright, E. L. 1996, *ApJ*, 473, 576
- Freudling, W., da Costa, L. N., Wegner, G., Giovanelli, R., Haynes, M. P., & Salzer, J. J. 1995, *AJ*, 110, 920

- Gibson, B. K., Stetson, P. B., Freedman, W. L., Mould, J. R., Kennicutt, J. R. C., Huchra, J. P., Sakai, S., Graham, J. A., et al. 2000, *ApJ*, 529, 723
- Giovanelli, R., Haynes, M. P., Herter, T., Vogt, N. P., da Costa, L. N., Freudling, W., Salzer, J. J., & Wegner, G. 1997a, *AJ*, 113, 53
- Giovanelli, R., Haynes, M. P., Herter, T., Vogt, N. P., Wegner, G., Salzer, J. J., da Costa, L. N., & Freudling, W. 1997b, *AJ*, 113, 22
- Giovanelli, R., Haynes, M. P., Salzer, J. J., Wegner, G., da Costa, L. N., & Freudling, W. 1994, *AJ*, 107, 2036
- . 1995, *AJ*, 110, 1059
- Glass, I. S. 1999, *Handbook of Infrared Astronomy* (Cambridge University Press)
- Guth, A. H. & Pi, S. 1982, *Physical Review Letters*, 49, 1110
- Han, M. 1992, *ApJ*, 395, 75
- Han, M. & Mould, J. R. 1992, *ApJ*, 396, 453
- Hauser, M. G., Kelsall, T., Moseley, J. S. H., Silverberg, R. F., Murdock, T., Toller, G., Spiesman, W., & Weiland, J. 1991, in *American Institute of Physics Conference Series*, Vol. 222, After the first three minutes, ed. S. S. Holt, C. L. Bennett, & V. Trimble, 161–178
- Hawking, S. W. 1982, *Physics Letters B*, 115, 295
- Haynes, M. P., Giovanelli, R., Chamaraux, P., da Costa, L. N., Freudling, W., Salzer, J. J., & Wegner, G. 1999a, *AJ*, 117, 2039
- Haynes, M. P., Giovanelli, R., Salzer, J. J., Wegner, G., Freudling, W., da Costa, L. N., Herter, T., & Vogt, N. P. 1999b, *AJ*, 117, 1668
- Heiles, C. 1976, *ApJ*, 204, 379
- Henning, P. A., Kraan-Korteweg, R. C., Rivers, A. J., Loan, A. J., Lahav, O., & Burton, W. B. 1998, *AJ*, 115, 584
- Henning, P. A., Kraan-Korteweg, R. C., & Staveley-Smith, L. 2005, in *Astronomical Society of the Pacific Conference Series*, Vol. 329, *Nearby Large-Scale Structures and the Zone of Avoidance*, ed. A. P. Fairall & P. A. Woudt, 199
- Henry, P. S. 1971, *Nature*, 231, 516
- Herschel, J. F. W. 1864, *Royal Society of London Philosophical Transactions Series I*, 154, 1
- Høg, E., Fabricius, C., Makarov, V. V., Urban, S., Corbin, T., Wycoff, G., Bastian, U., Schwekendiek, P., & Wicenec, A. 2000, *A&A*, 355, L27

- Holtzman, J. A. 1989, ApJS, 71, 1
- Hubble, E. 1929, Proceedings of the National Academy of Science, 15, 168
- Hubble, E. P. 1925, The Observatory, 48, 139
- . 1936, Realm of the Nebulae
- Huchra, J. et al. 2005, in Astronomical Society of the Pacific Conference Series, Vol. 329, Nearby Large-Scale Structures and the Zone of Avoidance, ed. A. P. Fairall & P. A. Woudt, 135
- Hudson, M. J. 1993a, MNRAS, 265, 43
- . 1993b, MNRAS, 265, 72
- Hudson, M. J., Smith, R. J., Lucey, J. R., & Branchini, E. 2004, MNRAS, 352, 61
- Humason, M. L., Mayall, N. U., & Sandage, A. R. 1956, AJ, 61, 97
- Jarrett, T. H. 2000, PASP, 112, 1008
- . 2004, Publications of the Astronomical Society of Australia, 21, 396
- Jarrett, T. H., Chester, T., Cutri, R., Schneider, S., Rosenberg, J., Huchra, J. P., & Mader, J. 2000a, AJ, 120, 298
- Jarrett, T. H., Chester, T., Cutri, R., Schneider, S., Skrutskie, M., & Huchra, J. P. 2000b, AJ, 119, 2498
- Jarrett, T. H., Chester, T., Cutri, R., Schneider, S. E., & Huchra, J. P. 2003, AJ, 125, 525
- Jarvis, J. F. & Tyson, J. A. 1981, AJ, 86, 476
- Jedrzejewski, R. I. 1987, in IAU Symposium, Vol. 127, Structure and Dynamics of Elliptical Galaxies, ed. P. T. de Zeeuw, 37–44
- Jerjen, H. & Tammann, G. A. 1993, A&A, 276, 1
- Joeveer, M. & Einasto, J. 1978, in IAU Symposium, Vol. 79, Large Scale Structures in the Universe, ed. M. S. Longair & J. Einasto, 241–250
- Kannappan, S. J., Fabricant, D. G., & Franx, M. 2002, AJ, 123, 2358
- Kerr, F. J. & Henning, P. A. 1987, ApJ, 320, L99
- Kerr, F. J. & Hindman, J. V. 1953, AJ, 58, 218
- Kirby, E., Jerjen, H., Ryder, S., & Driver, S. 2008a, Deepest Near-IR Surface Photometry of Galaxies in the Local Sphere of Influence, ed. Jerjen, H. & Koribalski, B. S., 49–
- Kirby, E. M., Jerjen, H., Ryder, S. D., & Driver, S. P. 2008b, AJ, 136, 1866

- Kocevski, D. D. & Ebeling, H. 2006, *ApJ*, 645, 1043
- Kochanek, C. S., Pahre, M. A., Falco, E. E., Huchra, J. P., Mader, J., Jarrett, T. H., Chester, T., Cutri, R., & Schneider, S. E. 2001, *ApJ*, 560, 566
- Kogut, A., Lineweaver, C., Smoot, G. F., Bennett, C. L., Banday, A., Boggess, N. W., Cheng, E. S., de Amici, G., et al. 1993, *ApJ*, 419, 1
- Kolatt, T., Dekel, A., & Lahav, O. 1995, *MNRAS*, 275, 797
- Koribalski, B. S. & López-Sánchez, Á. R. 2009, *MNRAS*, 400, 1749
- Koribalski, B. S., Staveley-Smith, L., Kilborn, V. A., Ryder, S. D., Kraan-Korteweg, R. C., Ryan-Weber, E. V., Ekers, R. D., Jerjen, H., et al. 2004, *AJ*, 128, 16
- Kraan-Korteweg, R. C. 2000, *A&AS*, 141, 123
- Kraan-Korteweg, R. C. 2005, in *Reviews in Modern Astronomy*, Vol. 18, *Reviews in Modern Astronomy*, ed. S. Röser, 48–75
- Kraan-Korteweg, R. C., Cayette, V., Balkowski, C., Fairall, A. P., & Henning, P. A. 1994a, in *Astronomical Society of the Pacific Conference Series*, Vol. 67, *Unveiling Large-Scale Structures Behind the Milky Way*, ed. C. Balkowski & R. C. Kraan-Korteweg, 99
- Kraan-Korteweg, R. C., Cayette, V., Balkowski, C., Fairall, A. P., & Henning, P. A. 1994b, in *Astronomical Society of the Pacific Conference Series*, Vol. 67, *Unveiling Large-Scale Structures Behind the Milky Way*, ed. C. Balkowski & R. C. Kraan-Korteweg, 99–+
- Kraan-Korteweg, R. C. & Huchtmeier, W. K. 1992, *A&A*, 266, 150
- Kraan-Korteweg, R. C. & Jarrett, T. 2005, in *Astronomical Society of the Pacific Conference Series*, Vol. 329, *Nearby Large-Scale Structures and the Zone of Avoidance*, ed. A. P. Fairall & P. A. Woudt, 119
- Kraan-Korteweg, R. C. & Lahav, O. 2000, *A&A Rev.*, 10, 211
- Lahav, O., Fisher, K. B., Hoffman, Y., Scharf, C. A., & Zaroubi, S. 1994, *ApJ*, 423, L93+
- Lahav, O., Santiago, B. X., Webster, A. M., Strauss, M. A., Davis, M., Dressler, A., & Huchra, J. P. 2000, *MNRAS*, 312, 166
- Landowitz, L. F. & Marshall, L. 1960, *Nature*, 187
- Lilje, P. B., Yahil, A., & Jones, B. J. T. 1986, *ApJ*, 307, 91
- Loeb, A. & Narayan, R. 2008, *MNRAS*, 386, 2221
- Lucey, J., Radburn-Smith, D., & Hudson, M. 2005, in *Astronomical Society of the Pacific Conference Series*, Vol. 329, *Nearby Large-Scale Structures and the Zone of Avoidance*, ed. A. P. Fairall & P. A. Woudt, 21–+

- Lynden-Bell, D., Lahav, O., & Burstein, D. 1989, MNRAS, 241, 325
- Lynden-Bell, D. et al. 1988, ApJ, 326, 19
- Martin, A. M., Papastergis, E., Giovanelli, R., Haynes, M. P., Springob, C. M., & Stierwalt, S. 2010, ApJ, 723, 1359
- Masters, K. L. 2005, PhD thesis, Cornell University, United States – New York
- Masters, K. L. 2008, in Astronomical Society of the Pacific Conference Series, Vol. 395, Frontiers of Astrophysics: A Celebration of NRAO's 50th Anniversary, ed. A. H. Bridle, J. J. Condon, & G. C. Hunt, 137
- Masters, K. L., Giovanelli, R., & Haynes, M. P. 2003, AJ, 126, 158
- Masters, K. L., Springob, C. M., Haynes, M. P., & Giovanelli, R. 2006, ApJ, 653, 861
- Masters, K. L., Springob, C. M., & Huchra, J. P. 2008, AJ, 135, 1738
- Mathewson, D. S. & Ford, V. L. 1994, ApJ, 434, L39
- Mathewson, D. S., Ford, V. L., & Buchhorn, M. 1992a, ApJS, 81, 413
- . 1992b, ApJ, 389, L5
- Meyer, M. J., Zwaan, M. A., Webster, R. L., Staveley-Smith, L., Ryan-Weber, E., Drinkwater, M. J., Barnes, D. G., Howlett, M., et al. 2004, MNRAS, 350, 1195
- Mould, J., Aaronson, M., & Huchra, J. 1980, ApJ, 238, 458
- Mould, J. R., Akeson, R. L., Bothun, G. D., Han, M., Huchra, J. P., Roth, J., & Schommer, R. A. 1993, ApJ, 409, 14
- Mould, J. R., Staveley-Smith, L., Schommer, R. A., Bothun, G. D., Hall, P. J., Han, M. S., Huchra, J. P., Roth, J., Walsh, W., & Wright, A. E. 1991, ApJ, 383, 467
- Nagashima, C., Nagayama, T., Nakajima, Y., Tamura, M., Sugitani, K., Nagata, T., Hirao, T., Nakaya, H., Yanagisawa, K., & Sato, S. 1999, in Proceedings of Star Formation, ed. T. Nakamoto, 397–398
- Nagayama, T., Nagashima, C., Nakajima, Y., Nagata, T., Sato, S., Nakaya, H., Yamamuro, T., Sugitani, K., & Tamura, M. 2003, in Instrument Design and Performance for Optical/Infrared Ground-based Telescopes (SPIE), ed. M. Iye & A. F. M. Moorwood, Vol. 4841, 459–464
- Nagayama, T., Woudt, P. A., Nagashima, C., Nakajima, Y., Kato, D., Kurita, M., Nagata, T., Nakaya, H., Tamura, M., Sugitani, K., Wakamatsu, K., & Sato, S. 2004, MNRAS, 354, 980

- Nagayama, T., Woudt, P. A., Wakamatsu, K., Nishiyama, S., Nagashima, C., Kato, D., Nagata, T., Nakaya, H., Sugitani, K., Tamura, M., & Sato, S. 2006, MNRAS, 368, 534
- Neugebauer, G., Habing, H. J., van Duinen, R., Aumann, H. H., Baud, B., Beichman, C. A., Beintema, D. A., Boggess, N., et al. 1984, ApJ, 278, L1
- Noordermeer, E. & Verheijen, M. A. W. 2007, MNRAS, 381, 1463
- O'Donnell, J. E. 1994, ApJ, 422, 158
- Oke, J. B. & Sandage, A. 1968, ApJ, 154, 21
- Peebles, P. J. E. 1976, ApJ, 205, 318
- Percival, W. J. 2005, A&A, 443, 819
- Persson, S. E., Murphy, D. C., Krzeminski, W., Roth, M., & Rieke, M. J. 1998, AJ, 116, 2475
- Pierini, D. & Tuffs, R. J. 1999, A&A, 343, 751
- Poggianti, B. M. 1997, A&AS, 122, 399
- Proctor, R. 1887, The Universe of Stars (London: Longman, Green and Co.), 41
- Ramsay, S. K., Mountain, C. M., & Geballe, T. R. 1992, MNRAS, 259, 751
- Riad, I. F. 2010, PhD thesis, University of Cape Town
- Riad, I. F., Kraan-Korteweg, R. C., & Woudt, P. A. 2010, MNRAS, 401, 924
- Riess, A. G., Strolger, L., Tonry, J., Casertano, S., Ferguson, H. C., Mobasher, B., Challis, P., Filippenko, A. V., et al. 2004, ApJ, 607, 665
- Rowan-Robinson, M., Lawrence, A., Saunders, W., Crawford, J., Ellis, R., Frenk, C. S., Parry, I., Xiaoyang, X., Allington-Smith, J., Efstathiou, G., & Kaiser, N. 1990, MNRAS, 247, 1
- Sandage, A. & Tammann, G. A. 1984, Nature, 307, 326
- Sault, R. J., Teuben, P. J., & Wright, M. C. H. 1995, in Astronomical Society of the Pacific Conference Series, Vol. 77, Astronomical Data Analysis Software and Systems IV, ed. R. A. Shaw, H. E. Payne, & J. J. E. Hayes, 433
- Scaramella, R., Baiesi-Pillastrini, G., Chincarini, G., Vettolani, G., & Zamorani, G. 1989, Nature, 338, 562
- Scaramella, R., Vettolani, G., & Zamorani, G. 1991, ApJ, 376, L1
- Schlegel, D. J., Finkbeiner, D. P., & Davis, M. 1998, ApJ, 500, 525

- Schröder, A. C., Kraan-Korteweg, R. C., Mamon, G. A., & Woudt, P. A. 2005, in Astronomical Society of the Pacific Conference Series, Vol. 329, Nearby Large-Scale Structures and the Zone of Avoidance, ed. A. P. Fairall & P. A. Woudt, 167
- Schröder, A. C., Mamon, G. A., Kraan-Korteweg, R. C., & Woudt, P. A. 2007, *A&A*, 466, 481
- Shafi, N. 2008, Master's thesis, University of Cape Town
- Shane, C. D. & Wirtanen, C. A. 1967, *Publ. Lick Obs.* XXII, Pt 1
- Shapley, H. 1930, *Harvard College Observatory Bulletin*, 874, 9
- Shapley, H. 1961, *Galaxies* (Cambridge: Harvard University Press), 159
- Shaya, E. J. 1984, *ApJ*, 280, 470
- Skelton, R. E., Woudt, P. A., & Kraan-Korteweg, R. C. 2009, *MNRAS*, 396, 2367
- Smith, R. J., Hudson, M. J., Lucey, J. R., Schlegel, D. J., & Davies, R. L. 2000, in Astronomical Society of the Pacific Conference Series, Vol. 201, Cosmic Flows Workshop, ed. S. Courteau & J. Willick, 39–+
- Springel, V., White, S. D. M., Jenkins, A., Frenk, C. S., Yoshida, N., Gao, L., Navarro, J., Thacker, R., Croton, D., Helly, J., Peacock, J. A., Cole, S., Thomas, P., Couchman, H., Evrard, A., Colberg, J., & Pearce, F. 2005, *Nature*, 435, 629
- Springob, C. M., Haynes, M. P., Giovanelli, R., & Kent, B. R. 2005, *ApJS*, 160, 149
- Springob, C. M., Masters, K. L., Haynes, M. P., Giovanelli, R., & Marinoni, C. 2007, *ApJS*, 172, 599
- Starobinsky, A. A. 1982, *Physics Letters B*, 117, 175
- Staveley-Smith, L. 1997, *Publications of the Astronomical Society of Australia*, 14, 111
- Staveley-Smith, L., Juraszek, S., Koribalski, B. S., Ekers, R. D., Green, A. J., Haynes, R. F., Henning, P. A., Kesteven, M. J., et al. 1998, *AJ*, 116, 2717
- Staveley-Smith, L., Wilson, W. E., Bird, T. S., Disney, M. J., Ekers, R. D., Freeman, K. C., Haynes, R. F., Sinclair, M. W., et al. 1996, *Publications of the Astronomical Society of Australia*, 13, 243
- Stein, P., Jerjen, H., & Federspiel, M. 1997, *A&A*, 327, 952
- Strauss, M. A., Yahil, A., Davis, M., Huchra, J. P., & Fisher, K. 1992, *ApJ*, 397, 395
- Strutskie, M. F. 2006, *AJ*, 131, 1163
- Tabur, V. 2007, *PASA*, 24, 189

- Tammann, G. A. & Sandage, A. 1985, ApJ, 294, 81
- Taylor, E. N. & Webster, R. L. 2005, ApJ, 634, 1067
- Theureau, G., Coudreau, N., Hallet, N., Hanski, M., Alsac, L., Bottinelli, L., Gouguenheim, L., Martin, J., & Paturel, G. 2005, A&A, 430, 373
- Theureau, G., Hanski, M. O., Coudreau, N., Hallet, N., & Martin, J. 2007, A&A, 465, 71
- Theureau, G., Rauzy, S., Bottinelli, L., & Gouguenheim, L. 1998, A&A, 340, 21
- Tonry, J. & Schneider, D. P. 1988, AJ, 96, 807
- Tonry, J. L., Blakeslee, J. P., Ajhar, E. A., & Dressler, A. 2000, ApJ, 530, 625
- Tonry, J. L. & Davis, M. 1981, ApJ, 246, 680
- Trumpler, R. J. 1930, PASP, 42, 214
- Tully, R. B. 2007, in Bulletin of the American Astronomical Society, Vol. 38, Bulletin of the American Astronomical Society, 240
- Tully, R. B. & Fisher, J. R. 1977, A&A, 54, 661
- . 1987, Atlas of Nearby Galaxies, ed. Tully, R. B. & Fisher, J. R.
- Tully, R. B. et al. 2008, ApJ, 676, 184
- van Driel, W., Schneider, S. E., Kraan-Korteweg, R. C., & Monnier Ragaigne, D. 2009, A&A, 505, 29
- Wakamatsu, K., Hasegawa, T., Karoji, H., Sekiguchi, K., Menzies, J. W., & Malkan, M. 1994, in Astronomical Society of the Pacific Conference Series, Vol. 67, Unveiling Large-Scale Structures Behind the Milky Way, ed. C. Balkowski & R. C. Kraan-Korteweg, 131
- Wakamatsu, K. & Malkan, M. A. 1981, PASJ, 33, 57
- Warren, B. E., Jerjen, H., & Koribalski, B. S. 2006, AJ, 131, 2056
- Wheelock, S. L., Gautier, T. N., Chillemi, J., Kester, D., McCallon, H., Oken, C., White, J., Gregorich, D., Boulanger, F., & Good, J. 1994, NASA STI/Recon Technical Report N, 95, 22539
- Willick, J. A. 1990, ApJ, 351, L5
- . 1991, PhD thesis, California Univ., Berkeley.
- . 2000, ArXiv Astrophysics e-prints: arXiv:astro-ph/0003232
- Willick, J. A., Courteau, S., Faber, S. M., Burstein, D., & Dekel, A. 1995, ApJ, 446, 12

- Willick, J. A., Courteau, S., Faber, S. M., Burstein, D., Dekel, A., & Kolatt, T. 1996, ApJ, 457, 460
- Willick, J. A., Courteau, S., Faber, S. M., Burstein, D., Dekel, A., & Strauss, M. A. 1997, ApJS, 109, 333
- Wong, O. I., Ryan-Weber, E. V., Garcia-Appadoo, D. A., Webster, R. L., Staveley-Smith, L., Zwaan, M. A., Meyer, M. J., Barnes, D. G., et al. 2006, MNRAS, 371, 1855
- Woudt, P. A. 1998, PhD thesis, , Univ. of Cape Town, South Africa, (1998)
- Woudt, P. A. & Kraan-Korteweg, R. C. 2001, A&A, 380, 441
- Yahil, A. 1985, in European Southern Observatory Conference and Workshop Proceedings, Vol. 20, European Southern Observatory Conference and Workshop Proceedings, ed. O.-G. Richter & B. Binggeli, 359–373
- Yahil, A., Strauss, M. A., Davis, M., & Huchra, J. P. 1991, ApJ, 372, 380
- Zwaan, M. A., Meyer, M. J., Staveley-Smith, L., & Webster, R. L. 2005, MNRAS, 359, L30

